

Proximal-Field Radiation Sensors for Dynamically Controllable and Self-Correcting Integrated Radiators

Thesis by
Amirreza Safaripour

In Partial Fulfillment of the Requirements for the
degree of
Doctor of Philosophy

The logo for the California Institute of Technology (Caltech), featuring the word "Caltech" in a bold, orange, sans-serif font.

CALIFORNIA INSTITUTE OF TECHNOLOGY
Pasadena, California

2017
Defended April 5, 2017

© 2017

Amirreza Safaripour
ORCID: 0000-0001-9758-6156

All rights reserved

To Mom, Dad, Ali, and Samira.

ACKNOWLEDGEMENTS

Pursuing a doctoral degree is an extremely long yet rewarding journey and if it was not for the help and support of numerous individuals, I would have not been able to get to this point. During this journey, I truly learned how profoundly the interactions with people we come across with in life can shape our mind, and lead to significant changes in our future opportunities.

Mr. Farhad Saber and Mr. Ali Roshan, who taught me several courses in mathematics during high school, were two of such people in my life. With their incredible teaching methods, they taught me how to approach math problems correctly, enjoy solving them, and always look for more problems to solve. They guided me to develop an engineering mindset for which I am always thankful to them.

After I was admitted to Sharif University of Technology for my undergraduate studies, it was the one and only Prof. Sharifbakhtiar's electronics classes that left no doubt for me that THIS was what I wanted to do for my entire life. I truly fell in love with electronics through his lectures. In his classes, not only did we explore the astonishing world of electronics, but also I learned engineering discipline and professional commitment, which has stuck with me ever since and I am always grateful for it. Also, I was fortunate enough to work with Prof. Fotowat as his teaching assistant for many of the classes he taught. I learned precious lessons in science and life from him during the unforgettable meetings we had. The numerous good memories and jokes from our discussions will stay with me forever. I would like to thank him for all the academic and professional support he provided for me during my studies at Sharif which were essential to navigate me to Caltech.

I am proud to have worked with Prof. Ali Hajimiri as my advisor at Caltech, who has truly been a source of inspiration for me. He always encouraged me to explore new ideas and challenges and taught me to think outside the box and to focus on innovation and long-term impact. He always believed in me during the ups and downs of my research, and through his encouragements he infused confidence in me to push my own boundaries. Due to his unique way of managing the group, we all count on him both as an advisor and as a friend. In addition to the invaluable technical advice, Ali has provided me with a great deal of support and guidance on a personal level as well, and during the difficult times he was like an elder brother to me. I have always enjoyed our discussions about life, culture, ethics, philosophy,

politics, etc., and the lessons I have learned from them would definitely last a lifetime. I would like to thank him for his mentorship, encouragement, friendship, and unreserved support.

My gratitude also goes towards my candidacy and defense committee members, Prof. Azita Emami, Dr. Sander Weinreb, Prof. David Rutledge, Prof. Changhuei Yang, and Prof. Hyuck Choo, for their inspirational interactions, scholarly advice, and timely suggestions. I am indebted to Dr. Weinreb and Prof. Emami for allowing me to use their laboratory facilities as well as equipment.

I would like to specifically thank my former labmates Steve and Kaushik (K2) for their true friendship and great help, as well as the invaluable lessons I learned from them through countless technical discussions we had. The unforgettable memories from all the fun activities as well as the sleepless nights during the several tapeouts will always remain with me. I would also like to thank all current and former members of CHIC lab whom I had the pleasure of working with, including Behrooz, Florian, Costis, Kaushik (K1), Firooz, Alex, Matan, Aroutin, Brian, Reza, Parham, Elliott, Austin, Chris, and M. Reza, as well as the current and former members of MICS lab who helped me a great deal over these past years, including Manuel, Meisam, Saman, Juhwan, Mayank, Matt, Krishna, Abhinav, Milad, and Aryan. I would like to extend my gratitude to our group administrator, Michelle, for her continued support, and our department administrators, Tanya and Carol, who have always been kind and helpful. I would also like to especially thank Laura and Daniel for making Caltech a welcoming place for me as an international student.

I did not have the chance to visit home during my studies at Caltech, and unfortunately my family could not come here for visit either. In this situation, looking back at all the ups and downs over these past years, there is no doubt that it would not have been possible to survive the graduate life if it was not for my beloved friends here in Southern California. I have had the fortune of knowing Paniz, Mohammad, Tina, Ashkan, Maani, Hannaneh, Nariman, Hessam, and Mahsa, who have always been there for me with genuine love and continuous support whenever I needed them. They are indeed more than just my friends. To me, they are family and I will always be thankful to them for all the help, love, and good memories. Also, a tip of hat to all my good friends across the globe, particularly Negar, Alborz, Rozhin, Bahram, Mahdi, Niloufar, Azadeh, Hamidreza, Parinaz, Javad, Gilda, Diana, Amer, Babak, Yasamin, Jamshid, Hengameh, Ardalan, Behnaz, Hassan, and Paniz, who truly proved that friendship goes beyond distance.

Finally and most importantly, I would like to thank my parents for their endless love and unconditional support in every single step I took in my entire life, and for the opportunities they provided for me to pursue my dreams. None of this would have been possible if it was not for them. I cannot thank them enough for their patience and encouragements throughout these years. I'm also thankful to my brother, Ali, for always paving the path for me so that I can easily follow his lead, and to my little sister, Samira, whose love and energy have always been the strongest driving force for me in life.

ABSTRACT

One of the major challenges in the design of integrated radiators at mm-wave frequencies is the generation of surface waves in the dielectric substrate by the on-chip antennas. Since dielectric substrates are excellent surface waveguides with a fundamental mode with no cutoff frequency, there is always some energy trapped in them due to the surface waves and the excited substrate modes. This phenomenon is a significant cause of reduced radiation efficiency for mm-wave integrated radiators. However, in this thesis, we use this as an opportunity. We show that the excited substrate modes in the dielectric substrate of an integrated antenna contain valuable information regarding its far-field radiation properties. We introduce Proximal-Field Radiation Sensors (PFRS) as a number of small sensing antennas that are placed strategically on the same substrate as the integrated antenna and measure electromagnetic waves in its immediate proximity. These sensors extract the existing information in the substrate modes and use it to predict the far-field radiation properties of the integrated antenna in real-time based on in-situ measurements in the close proximity of the antennas, without any need to use additional test equipment and without removing the antenna from its operating environment or interfering with its operation in a wireless system. In other words, PFRS enables self-calibration, self-correction, and self-monitoring of the performance of the integrated antennas. Design intuition and a variety of data processing schemes for these sensors are discussed. Two proof-of-concept prototypes are fabricated on printed circuit board (PCB) and integrated circuit (IC) and both verify PFRS capabilities in prediction of radiation properties solely based on in-situ measurements.

Dynamically controllable integrated radiators would significantly benefit from PFRS. These radiators are capable of controlling their radiation parameters such as polarization and beam steering angle through their actuators and control units. In these cases, PFRS serves as a tool for real-time monitoring of their radiation parameters, so that without direct measurement of the far-field properties through bulky equipment the required information for the control units and the actuators are provided.

Dynamically controllable integrated radiators can be designed using the additional design space provided by Multi-Port Driven (MPD) radiator methodology. After a review of advantages of MPD design over the traditional single-port design, we show that a slot-based MPD radiator would have the additional advantage of reduced exclusive use area compared to the original wire-based MPD radiator, through

demonstration of a 134.5-GHz integrated slot-based MPD radiator with a measured single-element EIRP of +6.0 dBm and a total radiated power of -1.3 dBm.

We discuss how MPD methodology enables the new concept of Dynamic Polarization Control, as a method to ensure polarization matching of the transmitter antenna to the receiver antenna, regardless of the polarization and orientation of the receiver antenna in space. A DPC antenna design using the MPD methodology is described and a 105.5-GHz 2×1 integrated DPC radiator array with a maximum EIRP of +7.8 dBm and a total radiated power of 0.9 mW is presented as the first demonstration of an integrated radiator with DPC capability. This prototype can control the polarization angle across the entire tuning range of 0° to 180° while maintaining axial ratios above 10 dB, and control the axial ratio from 2.4 dB (near circular) to 14 dB (linear). We also demonstrate how simultaneous two-dimensional beam steering and DPC capabilities can even match the polarization to a mobile receiver antenna through a prototype 123-GHz 2×2 integrated DPC radiator array with a maximum EIRP of +12.3 dBm, polarization angle control across the full range of 0° to 180° as well as tunable axial ratio down to 1.2 dB and beam steering of up to 15° in both dimensions. We also use slot-based DPC antennas to fabricate a 120-GHz integrated slot-based DPC radiator array, expected to have a maximum EIRP of +15.5 dBm.

We also introduce a new modulation scheme called Polarization Modulation (Pol-M) as a result of DPC capability, where the polarization itself is used for encoding the data. Pol-M is a spatial modulation method and is orthogonal to the existing phase and amplitude modulation schemes. Thus, it could be added on top of those schemes to enable creation of 4-D data constellations, or it can be used as the only basis for modulation to increase the stream security by misleading the undesired receivers. We discuss how DPC antenna enables Pol-M and also present PCB prototypes for Pol-M transmitter and receiver units operating at 2.4 GHz.

PUBLISHED CONTENT AND CONTRIBUTIONS

- [1] A. Safaripour, M. R. Hashemi, and A. Hajimiri, “Proximal-field radiation sensors”, to appear in *IEEE MTT-S International Microwave Symposium (IMS)*, Jun. 2017,
A. Safaripour conceived of the project, conducted the research, designed and manufactured the system, performed the system measurements with M. R. Hashemi’s assistance, and authored the manuscript.
- [2] A. Safaripour, S. M. Bowers, K. Dasgupta, and A. Hajimiri, “Dynamic polarization control of two-dimensional integrated phased arrays”, *IEEE Transactions on Microwave Theory and Techniques*, vol. 64, no. 4, pp. 1066–1077, Apr. 2016. DOI: 10.1109/TMTT.2016.2530704,
A. Safaripour authored the manuscript, performed the system measurements, and was responsible for the electromagnetic design of the antennas, passives, and matching networks, as well as the entire integrated circuitry other than the distribution network and the digital to analog converters, which were designed by S. M. Bowers and K. Dasgupta, respectively.
- [3] —, “A 2×2 dynamic polarization-controlling integrated phased array”, in *IEEE Radio Frequency Integrated Circuits Symposium (RFIC)*, May 2015, pp. 219–222. DOI: 10.1109/RFIC.2015.7337744,
A. Safaripour authored the manuscript, performed the system measurements, and was responsible for the electromagnetic design of the antennas, passives, and matching networks, as well as the entire integrated circuitry other than the distribution network and the digital to analog converters, which were designed by S. M. Bowers and K. Dasgupta, respectively.
- [4] S. M. Bowers, A. Safaripour, and A. Hajimiri, “Dynamic polarization control”, *IEEE Journal of Solid-State Circuits*, vol. 50, no. 5, pp. 1224–1236, May 2015. DOI: 10.1109/JSSC.2015.2403313,
A. Safaripour designed the entire drive and control circuitry including the oscillators, amplifiers, phase rotators, locking network, as well as electromagnetic structures such as inductors and matching networks, and participated in the writing of the manuscript, while S. M. Bowers was responsible for the electromagnetic design of the array, performance analysis, system measurements, and preparing the manuscript.
- [5] —, “An integrated slot-ring traveling-wave radiator”, *IEEE Transactions on Microwave Theory and Techniques*, vol. 63, no. 4, pp. 1154–1162, Apr. 2015. DOI: 10.1109/TMTT.2015.2405921,
A. Safaripour was responsible for the entire integrated circuit design including the oscillator and amplifiers, as well as the electromagnetic design of the passives and matching networks, and participated in the writing of the

manuscript while S. M. Bowers was in charge of the antenna design, system measurements, and preparing the manuscript.

- [6] ———, “Dynamic polarization control of integrated radiators”, in *IEEE Radio Frequency Integrated Circuits Symposium (RFIC)*, Jun. 2014, pp. 291–294. doi: 10.1109/RFIC.2014.6851723,
A. Safaripour designed the entire drive and control circuitry including the oscillators, amplifiers, phase rotators, locking network, as well as electromagnetic structures such as inductors and matching networks, and participated in the writing of the manuscript, while S. M. Bowers was responsible for the electromagnetic design of the array, system measurements, and preparing the manuscript.
- [7] ———, “An integrated traveling-wave slot radiator”, in *IEEE Radio Frequency Integrated Circuits Symposium (RFIC)*, Jun. 2014, pp. 369–372. doi: 10.1109/RFIC.2014.6851744,
A. Safaripour was responsible for the entire integrated circuit design including the oscillator and amplifiers, as well as the electromagnetic design of the passives and matching networks, and participated in the writing of the manuscript while S. M. Bowers was in charge of the antenna design, system measurements, and preparing the manuscript.
- [8] S. Bowers, K. Dasgupta, A. Safaipour, and A. Hajimiri, *Dynamic polarization modulation and control*, US Patent 9,485,076, Nov. 2016,
A. Safaripour participated in the conception of the idea, the design of proof-of-concept architectures, and the writing of the manuscript.
- [9] S. Bowers, A. Safaripour, and A. Hajimiri, *Sensing radiation metrics through mode-pickup sensors*, US Patent App. 13/766,667, Mar. 2014,
A. Safaripour participated in the conception of the idea, designed proof-of-concept architectures, developed the data analysis methods, and participated in the writing of the manuscript.
- [10] M. Varonen, A. Safaripour, D. Parveg, P. Kangaslahti, T. Gaier, and A. Hajimiri, “200-GHz CMOS amplifier with 9-dB noise figure for atmospheric remote sensing”, *Electronics Letters*, vol. 52, no. 5, pp. 369–371, Mar. 2016. doi: 10.1049/el.2015.3337,
A. Safaripour was responsible for designing the device layout methodology for optimal high-frequency performance.
- [11] D. Parveg, M. Varonen, A. Safaripour, S. Bowers, T. Tikka, P. Kangaslahti, T. Gaier, A. Hajimiri, and K. A. I. Halonen, “A 180-GHz CMOS down-converter MMIC for atmospheric remote sensing applications”, in *IEEE Topical Meeting on Silicon Monolithic Integrated Circuits in RF Systems (SiRF)*, Jan. 2017, pp. 64–67. doi: 10.1109/SIRF.2017.7874372,
A. Safaripour was responsible for the design of the voltage-controlled oscillator and its associated buffers in the LO path, and participated in the writing of the manuscript.

- [12] D. Parveg, M. Varonen, P. Kangaslahti, A. Safaripour, A. Hajimiri, T. Tikka, T. Gaier, and K. A. I. Halonen, “CMOS I/Q subharmonic mixer for millimeter-wave atmospheric remote sensing”, *IEEE Microwave and Wireless Components Letters*, vol. 26, no. 4, pp. 285–287, Apr. 2016. doi: [10.1109/LMWC.2016.2537786](https://doi.org/10.1109/LMWC.2016.2537786),
A. Safaripour participated in the design of the LO path and was also responsible for the post-processing of the IC to enable system measurements.

CONTENTS

Acknowledgements	iv
Abstract	vii
Published Content and Contributions	ix
Contents	xii
List of Figures	xiv
List of Tables	xxviii
Chapter I: Introduction	1
1.1 Contributions	2
1.2 Organization	3
Chapter II: Integrated Antennas: Motivations and Challenges	5
2.1 Integrated Antennas for Wireless Systems	5
2.2 Surface Waves in Integrated Antennas Substrate	8
2.3 Effects of Process and Environmental Variations	11
2.4 Indirect Measurement of Far-Field Radiation Properties	13
Chapter III: Proximal-Field Radiation Sensors	18
3.1 Introduction	18
3.2 Integrated Antennas on Dielectric Substrates	19
3.3 Proximal-Field Sensing	22
3.4 PFRS Data Capture Fundamentals	29
3.5 PFRS Data Processing	42
3.5.1 Symmetry-based Methods	43
3.5.2 Statistical Methods	54
3.5.3 Simulation-based Methods	58
3.6 PFRS Implementation on a PCB prototype	64
3.6.1 Prototype Design	65
3.6.2 Data Interpretation	65
3.6.3 Measurements	69
3.7 PFRS Implementation on an IC prototype	72
3.7.1 System Architecture	73
3.7.2 Radiator Design	75
3.7.3 PFRS Design	79
3.7.4 Measurements	81
3.8 Conclusions	84
Chapter IV: Multi-Port Driven Antennas	87
4.1 Introduction	87
4.2 Multi-Port vs. Single-Port Antennas	88
4.2.1 Limitations of Single-Port Antennas	89
4.2.2 Advantages of Multi-Port Antennas	90
4.3 Integrated Multi-Port Driven Slot Ring Traveling-Wave Radiator	90

4.3.1	Slot Antenna Design	91
4.3.2	Circuit Implementation	96
4.3.3	Measurements	104
4.4	MPD Antennas for Dynamic Control	108
4.5	Conclusions	109
Chapter V:	Dynamic Polarization Control and Modulation	111
5.1	Introduction	111
5.2	Electromagnetic Polarization	113
5.3	Dynamic Polarization Control	115
5.3.1	Concept	115
5.3.2	DPC Antenna	117
5.3.3	A 2×1 Integrated DPC Radiator Array	124
5.3.4	A 2×2 Integrated DPC Radiator Array	141
5.3.5	A 2×2 Integrated Slot-Based DPC Radiator Array	163
5.4	Polarization Modulation	165
5.4.1	Prototype: Transmitter and Receiver Architectures for Pol-M	170
5.4.2	Pol-M with the 2×2 Integrated DPC Radiator Array	175
5.5	Conclusions	175
Chapter VI:	Conclusions	177
Bibliography	179

LIST OF FIGURES

<i>Number</i>	<i>Page</i>
2.1 Operation principle of Distributed Active Radiator (DAR) [5].	6
2.2 Block diagram of the Multi-Port Driven (MPD) antenna [6].	6
2.3 Die photo of the (a) transmitter chip and (b) receiver chip for a coherent imaging system [8].	7
2.4 Transmitting antenna on a dielectric substrate showing the rays trapped as surface waves with the critical angle $\theta_C = 30^\circ$ appropriate for fused quartz ($\epsilon_r = 4$) [23].	8
2.5 Normalized power versus substrate thickness for (a) dipole on quartz substrate, (b) dipole on silicon or GaAs substrate, (c) slot on quartz substrate, and (d) slot on silicon or GaAs substrate [22].	9
2.6 Operation of a silicon lens to minimize substrate modes and to radiate the highest power down through the bottom of the substrate [12].	10
2.7 3-D depiction of the use of a dielectric superstrate (quartz in this case) to couple electromagnetic power up from the metal stack to antennas printed on top of the superstrate [17].	10
2.8 Average number dopant atoms as a function of technology node [33].	12
2.9 Line edge roughness shown in SEM images of an example process [35].	12
2.10 Threshold voltage variation over technology node [36].	12
2.11 Exterior fields of radiating antenna [40].	14
2.12 Specific expressions for scanning with ideal dipole on a plane, cylinder, and sphere [40].	15
2.13 Magnetically coupled in-situ probes for patch antennas operating at 20 GHz [45].	16
3.1 Generation of surface waves inside the dielectric substrate of an integrated antenna.	19
3.2 Complexity of an exemplary far-field measurement setup for a mm-wave integrated radiator operating at 120 GHz.	20
3.3 A simplified diagram for a far-field measurement range with AUT used as the receiver antenna and a known antenna used as the transmitter antenna.	20

3.4	A simplified diagram for a planar near-field measurement setup.	21
3.5	Example of a far-field measurement setup in anechoic chamber.	22
3.6	Proximal-Field Radiation Sensing (PFRS) concept where small sensing antennas measure certain properties of electromagnetic fields in the immediate proximity of the transmitting antennas.	23
3.7	Few examples of different antenna types to be used as PFRS.	24
3.8	Example of a self-correcting integrated radiator as a result of radiator integration with PFRS and digital processing units.	25
3.9	A 2×1 multi-port driven integrated radiator array with six slot-ring multi-port PFRS antennas.	25
3.10	Possible undesired mechanisms that could affect PFRS performance: (a) coupling to strongly driven points by the drive circuitry and (b) incident electromagnetic on the system from external sources.	26
3.11	Amplitude read-outs of the PFRS antenna located at the center versus the relative phase difference between the two radiating antennas.	27
3.12	Arrange of metallic contacts in the simulation setup to evaluate coupling of PFRS to strongly driven points on the chip.	27
3.13	Coupling strength of all PFRS antennas to the driving signal amplitude at the strongly driven points through substrate.	28
3.14	Simulation setup for evaluation of PFRS sensitivity to electromagnetic waves incident on the chip from a half-wavelength dipole antenna placed at 2λ distance above the chip.	28
3.15	Signals picked up by PFRS antennas for 0 dBm input power to the dipole antenna.	29
3.16	Rectangular waveguide configuration to evaluate various types of PFRS antennas when three PFRS units are located at points L , C , and R	30
3.17	Field components of the first ten propagating waveguide modes across the dashed line on top surface.	31
3.18	Y-oriented linear-slot antenna used as PFRS.	32
3.19	Outputs of the Y-oriented slots versus frequency for each excited mode.	33
3.20	X-oriented linear-slot antenna used as PFRS.	34
3.21	Outputs of the X-oriented slots versus frequency for each excited mode.	35
3.22	Field components of the first ten propagating waveguide modes across a line $10\ \mu\text{m}$ below the top metal surface.	36
3.23	Y-oriented dipole antenna used as PFRS.	37

3.24	Outputs of the Y-oriented dipoles versus frequency for each excited mode.	38
3.25	Combined TE/TM sensor for the waveguide.	39
3.26	Outputs of the TE/TM sensors versus frequency for each excited mode.	40
3.27	Hertzian dipole excitation on a chip with (a) TE sensors and (b) TM sensors.	41
3.28	(a) Outputs of the TE sensors and (b) outputs of the TM sensors for Hertzian dipole excitation.	41
3.29	A 2×1 multi-port driven radiator array with 13 slot-ring PFRS antennas.	43
3.30	In-phase drive of the transmitting antennas for optimum broadside radiation.	44
3.31	Simulated patterns of (a) gain and (b) directivity for optimum broadside radiation.	44
3.32	Simulated gain of the 2×1 array with relative phase error of (a) $\theta = +40^\circ$ and (b) $\theta = -40^\circ$ while $\Phi_{QA} = \Phi_{QA} = 0^\circ$	45
3.33	Outputs of the PFRS antennas versus the relative phase error, θ , and the color codes for the outputs of each PFRS.	46
3.34	Difference between the signals at the left and right ports of the central PFRS antenna.	47
3.35	Circular symmetry of the electromagnetic structure.	47
3.36	Outputs of the PFRS antennas versus quadrature phase error Φ_{QA} in Radiator A and the color codes for the outputs of each PFRS.	48
3.37	A 2×2 multi-port driven integrated radiator array with nine slot-ring multi-port PFRS antennas. Due to circular symmetry, the total 36 PFRS outputs can be divided into nine sets where all four output ports in each set are expected to have the exact same signal.	49
3.38	Sensitivity of the standard deviations of all nine sets to the relative phase error θ_D	50
3.39	Sum of the standard deviations for all nine sets as well as the relative strength of the radiated signal as θ_D varies.	51
3.40	A 2×2 multi-port driven integrated radiator array with 13 PFRS antennas.	51
3.41	Switching between horizontal and vertical polarization of the radiated electric field for $\Delta\psi = 0^\circ$ and $\Delta\psi = 180^\circ$, respectively.	52

3.42	Amplitude read-outs of the slot-ring PFRS antenna located at the center versus $\Delta\psi$ for all four radiating antennas. All radiating antennas are driven in phase.	53
3.43	Amplitude read-outs of the slot-ring PFRS antenna located at the center versus $\Delta\psi$ for all four radiating antennas, with relative phase difference between the right and left radiating antennas to steer the beam.	53
3.44	Simulated gain patterns of the 2×2 array when $\Delta\psi = 180^\circ$ for the two cases of broadside and off-axis radiation.	54
3.45	Example of Principal Component Analysis (PCA) on a 2-D data set.	55
3.46	Magnitude of the principal components associated with θ_D calculated using (a) both phases and amplitudes and (b) only amplitudes of the PFRS read-outs.	57
3.47	Application of an exemplary phase error correction algorithm to a random combination of relative phase errors θ_A , θ_B , θ_C , and θ_D , using the first principal component for each parameter.	57
3.48	Sniff antenna.	59
3.49	Example of an electromagnetic simulation setup using orthogonal dipole sniff antennas with the integrated radiator chip to extract mathematical relationships required for pattern prediction.	60
3.50	Comparison between the normalized predicted pattern using simulated PFRS read-outs and normalized simulated pattern by HFSS in (a) $\phi = 0^\circ$ and (b) $\phi = 90^\circ$ planes for broadside radiation.	62
3.51	Comparison between the normalized predicted pattern using simulated PFRS read-outs and normalized simulated pattern by HFSS in (a) $\phi = 0^\circ$ and (b) $\phi = 90^\circ$ planes for off-axis radiation.	62
3.52	Arrangement of sniff antennas on a planar surface on top of the integrated radiator chip in simulation to be used for plane-wave decomposition.	64
3.53	(a) Heat map for the relative magnitude of the reconstructed electric field on the planar surface using sniffers' voltages and (b) decomposition of the field into plane waves propagating at different angles, showing a maximum at $f_x = f_y = 0$, i.e. broadside radiation.	64
3.54	The prototype PCB antenna array with two transmitting patch antennas and four folded-slot PFRS antennas.	65

3.55	Symmetrically-placed sensors to detect the phase difference between the driving signals of the two patch antennas.	66
3.56	Simulation setups to relate PFRS read-outs to the polarization of radiated field (a) in an arbitrary direction, and (b) across an entire plane.	67
3.57	Simulation setup to investigate the impact of a disturbing metallic reflector on the performance of PFRS: (a) 3-D view and (b) top view.	68
3.58	Comparison of the reflector impact on the normalized gain patterns for $\phi = 90^\circ$ plane based on (a) HFSS simulation and (b) prediction by simulated PFRS read-outs.	68
3.59	Measured and simulated input reflection coefficients of (a) the patch and (b) PFRS antennas.	69
3.60	PFRS performance is evaluated through comparison between (a) simulation of radiation pattern through HFSS, (b) direct measurement of radiation pattern in a far-field measurement setup, and (c) prediction of radiation pattern through measured PFRS read-outs.	70
3.61	Normalized simulated, measured, and predicted gain patterns based on PFRS read-outs in (a) $\phi = 0^\circ$ and (b) $\phi = 90^\circ$ planes for in-phase drive.	71
3.62	Normalized simulated, measured, and predicted gain patterns based on PFRS read-outs in $\phi = 90^\circ$ plane for (a) 90° , (b) -90° and (c) 180° of phase difference between the patch antennas.	71
3.63	Normalized simulated, measured, and predicted (a) co-polarization and (b) cross-polarization gain patterns in $\phi = 90^\circ$ plane for in-phase drive.	72
3.64	Measured and simulated amplitude response of S_1 and S_2	72
3.65	Simplified block diagram of the 2×1 integrated linear-slot radiator with four PFRS antennas.	73
3.66	Detailed block diagram of the 2×1 integrated linear-slot radiator with four PFRS antennas.	74
3.67	(a) Electromagnetic structure of the 2×1 integrated linear-slot radiator and (b) simulated gain pattern.	75
3.68	(a) Electromagnetic structure of the integrated radiator's packaging and (b) simulated gain pattern.	76
3.69	(a) Schematic of the quadrature oscillators and (b) the simulated quadrature outputs of all four oscillators.	77

3.70	Schematic of the buffers. All buffers use the same cascode topology but the devices widths are scaled up as the power increases in the buffer chain.	78
3.71	Schematic of the phase rotator consisting of two Gilbert cells to allow arbitrary weighted summation of I and Q signals.	78
3.72	Simulated waveforms of the driving signals for (a) linear-slot antenna on the left and (b) linear-slot antenna on the right when their phase difference is controlled from 0° to 360°	79
3.73	3-D structure of the folded-slot PFRS antenna.	79
3.74	Simulated magnitude of the signals picked up by PFRS antennas when the phase difference between the two antennas is swept from 0° (setting index = 0) to 360° . (setting index = 16)	80
3.75	Downconversion scheme for coherent detection of PFRS signals. . . .	80
3.76	(a) LO distribution network to PFRS locations for downconversion and (b) detection circuitry located next to PFRS antenna.	81
3.77	Circuit schematics for (a) mixer $M1$, (b) mixer $M2$, (c) amplifier at f_0 , (d) mixer $M3$, and (e) buffer for distribution of off-chip low-frequency reference at f_0	82
3.78	Measurement of the radiation frequency of the 2×1 integrated linear-slot radiator array versus the tuning voltage of the quadrature oscillators.	83
3.79	Comparison between calibrated measured read-outs of PFRS for both I and Q channels of each sensor and simulated downconverted signals versus the phase difference between the two radiating antennas. The difference between two consequent phase rotator settings is roughly equal to 22.5°	83
3.80	Electromagnetic simulation setup to extract relationship between PFRS antennas and far-field radiation pattern of E_θ in $\phi = 0^\circ$ plane.	84
3.81	Normalized simulated gain pattern from HFSS and predicted gain pattern based on measured PFRS read-outs in (a) $\phi = 0^\circ$ and (b) $\phi = 90^\circ$ planes for 0° phase difference between the two linear-slot antennas.	85
3.82	Normalized simulated gain pattern from HFSS and predicted gain pattern based on measured PFRS read-outs in (a) $\phi = 0^\circ$ and (b) $\phi = 90^\circ$ planes for $+90^\circ$ phase difference between the two linear-slot antennas.	85

3.83	Normalized simulated gain pattern from HFSS and predicted gain pattern based on measured PFRS read-outs in (a) $\phi = 0^\circ$ and (b) $\phi = 90^\circ$ planes for -90° phase difference between the two linear-slot antennas.	85
4.1	Example of traditional single-port radiator with lossy matching networks and independent design of individual blocks [6].	88
4.2	Multi-port driven radiator design methodology for integrated radiation where drivers directly feed multiple ports of the antenna [6] . . .	89
4.3	Example of EM duality for a dipole antenna, with the cross-section of the beam, and \mathbf{E} and \mathbf{H} fields shown. The dual complement of this is the slot dipole, where the series source of the dipole has been replaced with an orthogonal source across the slot, and the \mathbf{E} and \mathbf{H} fields have been normalized and swapped.	92
4.4	Electromagnetic Duality for the MPD slot ring antenna converts a four-series port wire ring antenna into a four-port slot ring driven in quadrature, producing a traveling wave around the ring and circular polarization in the far field.	93
4.5	Current distribution on the four-series port ring antenna when two of the ports are at their maximum amplitude, while the other two have zero amplitude. This current distribution then rotates around the ring in a traveling-wave fashion over one oscillation period.	94
4.6	3-D depiction of the traveling-wave slot radiator, with quadrature driver circuitry at the center of the chip that drives across the metal slot at four ports. The inner ground plane extends orthogonally across the slot out to the edge of the chip to provide a bond pad to sink the dc current, and the outer ac ground plane is biased at VDD to provide dc power to the driver circuitry through the antenna feeds.	95
4.7	Block diagram showing the driver circuitry and the slot ring antenna. A quadrature oscillator sits at the center of the chip and is amplified through three buffer amplifier stages before being routed out to the antenna ports across the slot.	97
4.8	Schematic of the quadrature voltage-controlled oscillator (VCO), which generates the four required phases by coupling two cross-coupled VCOs through two coupling mechanisms. (a) Resistive network at the tails ($R_C = R_T = 10 \Omega$). (b) Weak quadrature coupling through parallel transistors ($W_{M_c} = 3 \mu\text{m}$ and $W_{M_x} = 30 \mu\text{m}$).	98

4.9	3-D structure of the custom microstrip-line-based tank inductors. Each of the two structures corresponds to one differential inductor with two VDD taps, which is attached to one of the two cross-coupled VCOs.	100
4.10	Isolation between one of the input ports of the upper inductor (port 1) and all six ports of the lower inductor (ports 7–12). Isolation is more than 42 dB over a wide frequency range.	100
4.11	Equivalent-circuit model for each differential tank inductor. The topology of the model is chosen based on physical structure and nature of the coupling between different segments of the inductor. Component values are optimized by Agilent ADS to minimize modeling error.	101
4.12	Comparison between S-parameters of the EM simulation of the inductor and S-parameters of the optimized equivalent-circuit model of the inductor. The circuit model is well matched to EM simulation over a wide frequency range.	102
4.13	Equivalent-circuit model is used with extracted layout of quadrature oscillator's transistors and resistors to simulate oscillation frequency.	102
4.14	Simulated output waveforms of the quadrature oscillator. Quadrature waveforms verify correct operation of the two coupling mechanisms.	103
4.15	Schematic of the amplifier chain consisting of three cascode stages with 20-, 40-, and 60- μm widths, respectively.	104
4.16	Die photograph of the traveling-wave slot ring radiator with a break-out view of the antenna, driver circuitry, and areas of fill exclude. . .	105
4.17	Device packaging to enable wire-bond connection of dc supply while radiating out from the backside of the chip.	105
4.18	Measurement setup for the traveling-wave slot radiator for: (a) absolute power calibration and (b) spectral measurement.	106
4.19	Measured calibrated spectrum of the received signal shows -25.1-dBm captured power, which corresponds to an EIRP of 6.0 dBm at 134.5 GHz when considering the distance and gain of the receive antenna. . . .	107
4.20	Orthogonal elevation planes of the simulated and measured radiation pattern when: (a) $\phi = 0^\circ$ and (b) $\phi = 90^\circ$	108

5.1	Effects of polarization mismatch on coupling transmit/receive antenna pairs. Maximum coupling occurs for polarization matched antenna pairs (top), no coupling for completely mismatched pairs (middle) and partial coupling for partially mismatched pairs (bottom).	112
5.2	Definitions of the polarization parameters for the general elliptical polarization.	114
5.3	Examples of polarization mismatch in wireless communication links: (a) due to antenna mismatch, (b) due to orientation change between the transmitter and receiver in mobile systems.	115
5.4	A radiator with Dynamic Polarization Control (DPC) can transmit any polarization angle and polarization axial ratio in order to maintain polarization matching with a receive antenna of any polarization or orientation in space.	116
5.5	(a) DPC antenna ensures polarization matching between the transmitter and receiver regardless of receiver antenna type and (b) solves polarization mismatch in mobile systems when used in 2-D phased arrays.	117
5.6	Four-spoke Multi-Port Driven (MPD) antenna for dynamic polarization control.	118
5.7	Operation principle of the original DPC antenna based on superposition of two orthogonal linear polarizations.	119
5.8	Realization of any arbitrary elliptical polarization with two orthogonal linear polarizations, as well as (b) graphical representation of the extreme cases of linear and (c) circular polarizations.	120
5.9	Modified MPD antenna of circumference $g\lambda$ used for polarization control. The phases and amplitudes of the drives of spokes A and B are controlled independently from each other, while ports on opposite ends of each spoke are driven differentially with the same amplitude.	121
5.10	Analysis setup for superposition subpart A when broken up to consider just (a) the signal ring or (b) just the spokes. The port impedances from subpart B are in parallel to the virtual shorts and thus do not affect the current distribution due to subpart A.	122
5.11	Standing current wave distribution when $1 < g < \pi/2$ for subparts A and B.	124

- 5.12 Block layout of the 2×1 radiator array. A central QVCO and locking network located between the two antennas locks the core circuitry located at the center of each antenna, with polarization control of the far field electric field achieved through amplitude and phase control of each individual antenna. 125
- 5.13 Block Diagram of the driver circuitry of the 2×1 radiator phased array with DPC. The central QVCO is amplified before distribution to phase rotators within each radiator core, which are then injected into the radiator core oscillators before being amplified and sent to the antennas. 126
- 5.14 Schematic of the central QVCO with two coupling mechanisms: Resistive network at the tail ($R_c = R_t = 15\Omega$) and quadrature coupling through transistors ($W_{M_q} = 0.5\mu\text{m}$, $W_{M_c} = 20\mu\text{m}$). The “Y” resistive network can be simplified through its “ Δ ” equivalent for analysis. . . 128
- 5.15 Simulated phase noise at 1 MHz offset and the ratio of second harmonic to fundamental of the QVCO vs. coupling resistance (R'_c) for three different widths ($0.5\mu\text{m}$, $1\mu\text{m}$, $1.5\mu\text{m}$) of coupling transistors along with the time-domain waveforms for $R'_c = 0\Omega$ and $R'_c = 40\Omega$ when $W_{M_q} = 0.5\mu\text{m}$ 129
- 5.16 Schematic of Gilbert cell based phased rotator. In-phase and quadrature signals from the locking network are weighted arbitrarily and added in current domain to generate the desired output phase to lock cores’ oscillator ($W = 2\mu\text{m}$ for tail transistors, $W = 1\mu\text{m}$ for upper transistors). 131
- 5.17 Simulated output current of phase rotator for eight different settings. Control voltages are set to generate 45° separated phases while keeping the amplitudes constant. 131
- 5.18 Schematic of the amplifier chain consisting of a differential common-source stage ($W = 5\mu\text{m}$) and two differential cascode stages ($W = 15\mu\text{m}$ and $W = 30\mu\text{m}$). Gain of the chain is controlled through the biasing circuit. 132
- 5.19 Additional non-idealities including the effects of extending the spokes out to an upper ground plane pulled back $\lambda/4$ from the antenna as well as a standard substrate around $\lambda/4$ thick mounted on a PCB with a lower ground plane. 134

5.20	Simulated radiation gain pattern of the 2×1 array in circularly polarized mode and linearly polarized mode for planes $\phi = 0^\circ$ (a) and $\phi = 90^\circ$ (b) show similar patterns and maximum gains within 0.3 dBi of each other.	135
5.21	Measurement setup for the 2×1 radiator with DPC.	136
5.22	Calibrated measured spectrum of the DPC radiator array in linearly polarized mode has a maximum EIRP of +7.8 dBm at 105.5 GHz.	137
5.23	Measured radiation pattern for two elevation planes when $\phi = 0^\circ$ (a) and $\phi = 90^\circ$ (b) for broadside radiation as well as beam steering in both directions in the $\phi = 0^\circ$ dimension.	137
5.24	Orientation of coordinate system (a) as well as three directions used in demonstration of DPC: $\theta = 0^\circ$ (b), $\theta = 20^\circ$, $\phi = 0^\circ$ (c), and $\theta = 30^\circ$, $\phi = 90^\circ$ (d).	138
5.25	Two demonstrations of DPC: tuning of the polarization angle while maintaining linear polarization (a), and tuning of the axial ratio while maintaining constant polarization angle (b).	139
5.26	Measured tuning of polarization angle while maintaining linear polarization (axial ratios above 10 dB) show full tuning range from 0° to 180° in three different directions.	139
5.27	Measured tuning of polarization axial ratio while maintain near constant polarization angles in three directions show tuning range from 2.4 dB through 14 dB.	139
5.28	Die photo of 2×1 radiator array with DPC.	140
5.29	Block diagram of the 2×2 DPC integrated phased array.	141
5.30	Modifications of the DPC antenna by adding two additional ground spokes to allow low-loss transmission lines for the locking signals while maintaining the symmetry of the structure.	142
5.31	Effect of the 5th and 6th spokes on polarization angle tuning. (a) Polarization angle is set by the drive settings and the (b) simulated polarization angle, (c) axial ratio, and (d) antenna array gain show more accuracy and symmetry for six-spoke DPC antennas.	144
5.32	Effect of the 5th and 6th spokes on axial ratio tuning. (a) Axial ratio is set by the phase difference of the drive sets, and the (b) simulated polarization angle, (c) axial ratio, and (d) antenna array gain show more accuracy and symmetry for six-spoke DPC antennas.	145

5.33	Simulated antenna gain patterns for the 2×2 DPC radiator array in circularly polarized mode and linearly polarized mode for planes: (a) $\phi = 0^\circ$ and (b) $\phi = 90^\circ$ show maximum gain of 0.4 dBi in the broadside direction.	146
5.34	Detailed block diagram of the drive circuitry for each DPC antenna with independent phase and gain control units for the two subparts, as well as independent control for each antenna with respect to the other antennas in the array.	147
5.35	Detailed block diagram of the drive circuitry for each DPC antenna with independent phase and gain control units for the two subparts, as well as independent control for each antenna with respect to the other antennas in the array.	147
5.36	Detailed block diagram of the drive circuitry for each DPC antenna with independent phase and gain control units for the two subparts, as well as independent control for each antenna with respect to the other antennas in the array.	148
5.37	Schematic of the buffer chain that controls the gain of each subpart in the antenna drive circuitry with a maximum simulated gain of 10.2 dB.	149
5.38	Variations of the single-ended input impedances of the DPC antenna for: (a) $0^\circ < \Delta\psi < 360^\circ$ when $V_A = V_B$ and (b) $0.2 < V_B/V_A < 5$ when $\Delta\psi = 0^\circ$	150
5.39	Block diagram of the locking network.	151
5.40	Schematic of the central QVCO and its simulated time-domain output waveforms.	153
5.41	Schematics of the 5-bit DACs with (a) single-ended and (b) differential outputs, as well as the (c) simulated output voltage for the single-ended DAC and (d) differential DAC.	154
5.42	Measurement setup for the 2×2 DPC radiator array. A 2-D stepper motor on the transmitter side and a 1-D stepper motor on the receiver side allow independent polarization measurement of the radiated signal at any desired direction.	155
5.43	Definitions of the angles θ , ϕ , and α that are controlled by the stepper motors. θ and ϕ are controlled by the 2-D stepper motor on the transmitter side and α is controlled by the 1-D stepper motor on the receiver side.	155
5.44	Die photograph of the 2×2 DPC radiator array.	156

5.45	(a) Measured calibrated spectrum of the radiated signal and (b) measured radiation patterns in two orthogonal planes show a tone at 122.88 GHz with a maximum EIRP of +12.3 dBm in the broadside direction.	159
5.46	(a) Ideal scenario for polarization angle tuning of the linear polarization across the full 0° to 180° range and (b) measured axial ratio for the optimized linear polarizations at different polarization angles.	159
5.47	Axial ratio tuning of the transmitted polarization to obtain elliptical and circular polarization. Normalized plots of projected power at (a) different polarization angles in broadside for expected target polarizations and (b) measured polarizations after optimization.	160
5.48	Radiation patterns corresponding to 2-D beam steering: (a) for the linear polarization mode, (b) simultaneous beam steering and polarization angle control, and (c) simultaneous beam steering and axial ratio control.	161
5.49	Measured and target polarizations corresponding to 2-D beam steering for the: (a) linear polarization mode, (b) simultaneous beam steering and polarization angle control, and (c) simultaneous beam steering and axial ratio control.	162
5.50	Block diagram of the 2×2 slot-based DPC radiator.	164
5.51	Electromagnetic design of the slot-based DPC antenna.	164
5.52	(a) HFSS simulation setup for the 2×2 integrated slot-based radiator and the simulated gain patterns for (b) linear polarization mode and (c) circular polarization mode.	166
5.53	DPC radiator can switch between different polarizations at symbol rate, T_{sym} , to transfer data through Polarization Modulation.	167
5.54	Projections of a 4-D constellation on orthogonal planes of the 4-D space for an exemplary 4-D data constellation resulted by performing simultaneous quadrature modulation schemes on two orthogonal polarizations.	168
5.55	Simplified block diagram of a transmitter capable of simultaneous phase, amplitude, and polarization modulation.	169
5.56	One possible implementation of a transmitter capable of performing Pol-M.	169
5.57	System architecture for the prototype polarization modulation (a) transmitter and (b) receiver.	171

5.58	Patch antenna simulations showing port isolation as well as gain patterns for X and Y polarizations with maximum gain of 2.7 dB. . .	172
5.59	Implementation details of (a) transmitter and (b) receiver units for Pol-M.	173
5.60	Measurement setup for Pol-M transmitter and receiver units.	173
5.61	Transmitter stand-alone measurements showing (a) power variation across angle of the receiving horn and (b) dynamic polarization control over the first quadrant.	174
5.62	Receiver stand-alone measurements showing (a) received power variation across angle of the transmitting horn and (b) received polarizations having different magnitudes as well as angles.	174
5.63	Pre-loaded polarization symbols for 2×2 integratd DPC radiator array.	175

LIST OF TABLES

<i>Number</i>	<i>Page</i>
4.1 Comparison with integrated radiating sources in silicon without external dielectrics	108
5.1 Comparison with integrated radiating sources in silicon without external dielectrics	140
5.2 Comparison of integrated radiating sources in silicon without external dielectrics.	163

Chapter 1

INTRODUCTION

Today, wireless systems play a significant role in almost all aspects of our lives, including communications, medical applications, security, etc. The key component to enable wireless connectivity for these applications is the antenna, the element that performs transmission and reception of electromagnetic (EM) waves. The physical size of an efficient antenna in a wireless system is proportional to the wavelength of the EM waves. This means that as the frequency of operation of the wireless link increases the dimensions of the required antenna will reduce. Thus, at low radio frequencies, large passive antennas are used to transfer electromagnetic energy while at millimeter-wave and THz frequencies the antennas become so small that they can easily fit within an area with dimensions in the order of millimeters or even few hundred microns. On the other hand, recent advancements in integrated circuit technologies have resulted in fabrication of transistors capable of operating at high mm-wave frequencies. Considering the small sizes of the antennas required for operating at mm-wave frequencies, this has opened up new design and application spaces for integrated mm-wave wireless systems as well as a new set of challenges associated with the integration of the radiating antennas and supporting circuitry on the same substrate. We address both of these topics in our research.

We investigate the creation of surface waves in the dielectric substrates as the major issue limiting the performance of integrated antennas. When an antenna is implemented on a dielectric substrate, it serves as a source for generation of surface waves. Since dielectric substrates are excellent surface waveguides, these waves get trapped inside the substrate and do not contribute to efficient radiation, which in turn reduces the radiation efficiency of integrated antennas. However, we use this challenge as an opportunity. We approach the trapped electromagnetic energy and the existing surface waves as a source for additional information. We show that the excited substrate modes contain valuable information regarding the far-field radiation properties of the integrated antenna and use them to extract the radiation properties. This enables in-situ measurement of electromagnetic waves in immediate proximity of the transmitting antennas that allows monitoring of the far-field radiation and can be used for self-calibration and self-correction purposes. The techniques we use are applicable to both printed circuit board (PCB) antennas as well as integrated

circuit (IC) antennas. However, the significance of such capabilities can particularly be seen in IC domain. In mm-wave integrated radiators, the integration of antenna and the driving circuitry on the same substrate enables new design methodologies compared to discrete design and allows implementation of novel electromagnetic radiators whose far-field radiation parameters can be dynamically controlled using the supporting circuitry. In this thesis, we have also advanced the state of the art for such integrated radiators and explore several designs of integrated antennas that take advantage of dynamic control over radiation parameters.

1.1 Contributions

In this dissertation:

- The concept of Proximal-Field Radiation Sensors (PFRS) is introduced as a means for calculation of far-field radiation properties of integrated antennas based on local measurements. This capability enables self-calibration, self-correction, and self-monitoring of the performance of integrated antennas in real-time. We have shown that the substrate modes excited by the surface waves inside the substrate indeed contain valuable information regarding the far-field radiation properties. These sensors are implemented as a number of small sensing antennas integrated on the same substrate as the transmitting antenna and measure certain properties of the electromagnetic field in immediate proximity of the radiating antennas. Fundamentals of the operation and various methods for processing the PFRS read-outs are presented through a variety of examples. Two proof-of-concept prototypes in printed circuit board (PCB) and integrated circuit (IC) platform are designed and fabricated.
- Slot-based Multi-Port Driven (MPD) radiator is presented as an efficient way to reduce the exclusive use area of the MPD antennas through low fill requirement. A proof-of-concept MPD slot ring radiator is designed and fabricated based on the original MPD radiator by using electromagnetic duality and similar to the original design performs power transfer and power combining.
- Dynamic Polarization Control (DPC) is introduced as the method of setting the polarization of the far-field electric field generated by a radiating antenna entirely electronically in order to maintain polarization matching with the receiving antenna regardless of its polarization or orientation in space. Simultaneous two-dimensional beam steering and dynamic polarization control

in an integrated radiator are discussed as a comprehensive method to entirely control the radiated beam to ensure polarization matching to a mobile receiver. Two proof-of-concept prototypes of 2×1 and 2×2 integrated DPC phased arrays, as well as a 2×2 integrated Slot-based DPC phased array, are designed and fabricated.

- Polarization Modulation (Pol-M) concept is presented as a major advantage of DPC radiators. Pol-M is completely orthogonal to the existing phase and amplitude modulation schemes, and can be used for increasing the security of the communication link and as an additional degree of freedom to create (4-D) constellations. A prototype PCB transmitter and receiver capable of Pol-M are designed and fabricated. Also, capability of the 2×2 DPC radiator array to perform Pol-M is discussed.

Specifically, the following projects are the highlights of the research that resulted in these four topics:

- A 5-GHz 2×1 PCB patch antennas with PFRS
- A 72-GHZ 2×1 integrated linear-slot radiator with PFRS
- A 134.5-GHz integrated MPD slot ring traveling-wave radiator
- A 105.5-GHz 2×1 integrated DPC radiator phased array
- A 123-GHz 2×2 integrated DPC radiator phased array,
- A 120-GHz 2×2 integrated Slot-based DPC radiator phased array
- A 2.4-GHz PCB prototype of Pol-M transmitter and receiver units

1.2 Organization

This thesis is organized as follows. A review of the motivations, achievements, and challenges in the design, characterization, and real-time correction of integrated antennas is presented in Chapter 2. After that, Chapter 3 introduces PFRS concept for indirect measurement of far-field radiation pattern of integrated antennas to enable self-calibration, self-correction, and self-monitoring of the performance, especially in dynamically controllable integrated antennas. Through a variety of examples operation principle and data processing schemes for PFRS are described, followed by two proof-of-concept prototypes of integrated antennas with PFRS in

both PCB and IC domains. Chapter 4 discusses the advantages of MPD antennas versus single-port antennas and presents an integrated slot-based MPD radiator with the added benefit of lower exclusive use area for the antenna design. It is also described how MPD antennas form the building block for dynamic control in integrated radiators. In Chapter 5, DPC concept is introduced and it is shown how a DPC antenna is designed based on the MPD antenna. Several proof-of-concept implementations of integrated DPC radiator arrays are demonstrated. Pol-M is also presented as a new modulation scheme and its advantages are discussed, followed by A PCB prototype for transmitter and receiver units capable of Pol-M. Finally, Chapter 6 includes the concluding remarks and summarizes the presented material.

*Chapter 2***INTEGRATED ANTENNAS: MOTIVATIONS AND CHALLENGES****2.1 Integrated Antennas for Wireless Systems**

Wireless systems are used for a variety of applications such as communications and data transfer between two points, radars, imaging, spectroscopy, etc. Although the building blocks of wireless systems could significantly vary depending on the application of interest, they all have one thing in common: the antenna, i.e., the means for radiating and receiving electromagnetic waves. Antennas are one of the key elements in any wireless systems. Traditionally, at low frequencies, the final output of a transmitter system is taken to a relatively large discrete antenna for radiation. This is directly due to the fact that for efficient radiation of an antenna, its size should be in the order of the wavelength [1]. As the frequency of operation increases due to advancements in transistor fabrication technologies, the size of the antenna becomes comparable to the dimensions of the transmitter or receiver circuitry. At millimeter-wave frequencies, this enables the integration of the antenna on the same dielectric substrate as the supporting circuitry, either a printed circuit board (PCB), a thin film, or an integrated circuit (IC). In other words, integrated antennas are the next step in the natural evolution of integrated circuits in the mm-wave frequencies.

In IC domain, since the parameters that determine the cost of the IC are different compared to discrete domain, new design methodologies can be used for implementation of on-chip antennas. Integrating the radiating antennas and the driving circuitry on the same substrate opens up a new opportunity for holistic design of novel electromagnetic structures and their supporting circuitry. One such example is the distributed active radiator (DAR) [2]–[5], shown in Figure 2.1. The DAR consists of a self-oscillating active electromagnetic structure, comprising two loops which sustain out-of-phase currents at the fundamental frequency and in-phase currents at the second harmonic. The fundamental signal thus gets spatially filtered, while the second harmonic is radiated selectively, thereby consolidating signal generation, frequency multiplication, radiation of desired harmonic, and filtration of undesired harmonics simultaneously in a small silicon footprint.

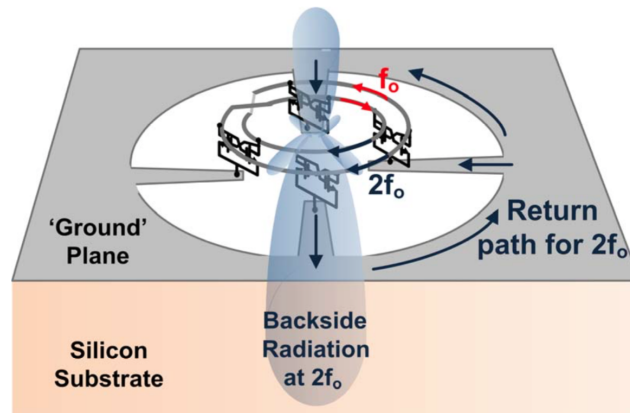


Figure 2.1: Operation principle of Distributed Active Radiator (DAR) [5].

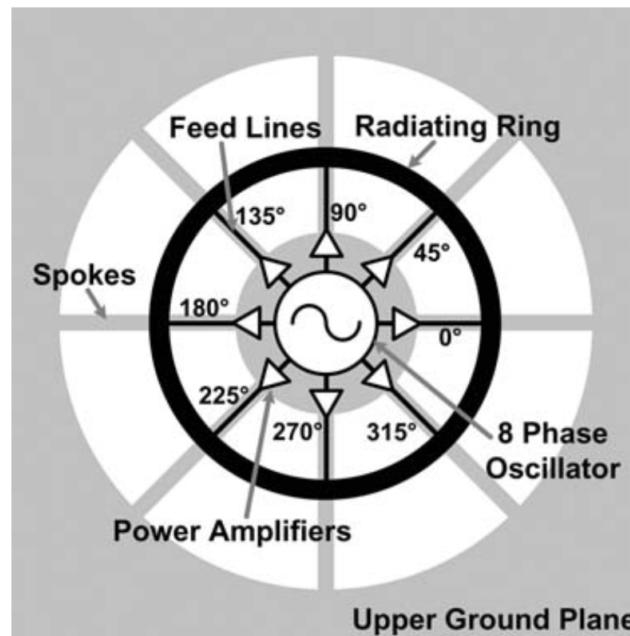


Figure 2.2: Block diagram of the Multi-Port Driven (MPD) antenna [6].

Another example for using the new design space provided in integrated circuit domain is Multi-Port Driven (MPD) antenna [6], [7], shown in Figure 2.2, which reduces costly losses by eliminating independent elements for power combination, output impedance matching networks, and power transfer by engineering current patterns on a chip based on the desired far field pattern.

Once the fabrication of such novel electromagnetic designs with their drive circuitry is enabled on integrated circuits platform, they can also be integrated with the entire required circuitry of a wireless system to serve a specific application. In Figure 2.3,

the die photo of such a wireless system for coherent imaging application [8] is shown. As it can be seen in this figure, integrated radiators can also be implemented as arrays of antennas, which allows for control over the direction of the radiated beam. Other radiation parameters may also be controlled through use of reconfigurable antennas and dynamic control over the driving circuitry [9].

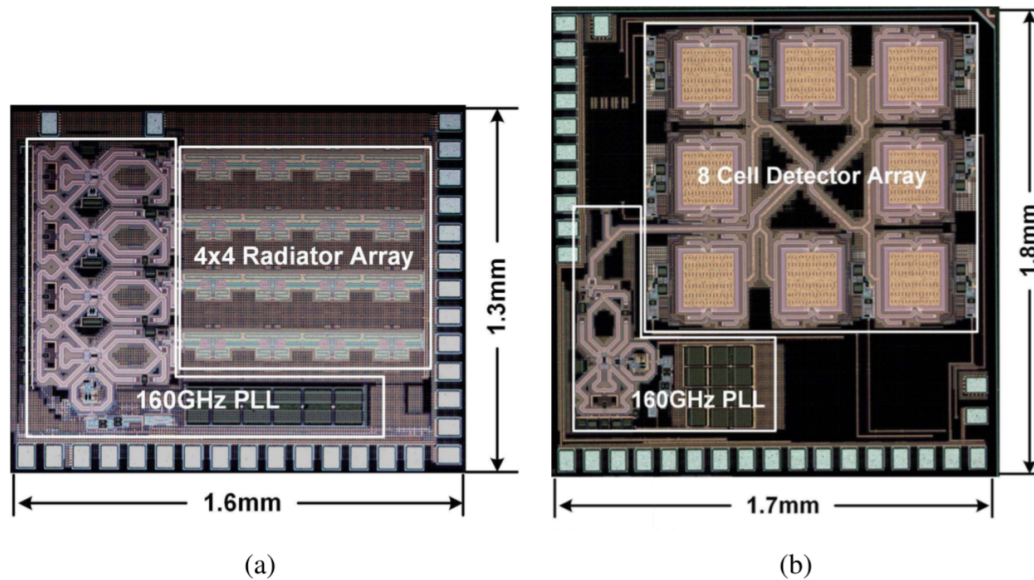


Figure 2.3: Die photo of the (a) transmitter chip and (b) receiver chip for a coherent imaging system [8].

Integrated antennas must be carefully designed and properly modeled to achieve acceptable performance. Design considerations for implementation of integrated antennas are very different compared to discrete antennas, due to the different platform they are fabricated in. They have been investigated for decades to provide a clear understanding of design methodologies and analysis of their advantages and limitations [10]–[21]. The key issue is that since they often sit at the interface of the substrate dielectric and free space (or any other medium depending on the application), their performance compared to free-space antennas is very different. Although such a configuration increases the integration level and thus lowers the costs of wireless systems, it adds to the complexity of the antenna design and could potentially degrade the performance. The major advantages of integrated antennas such as low weight, conformality to a given surface, and low cost are usually counterbalanced by limited power (due to limited thermal capacity of the substrate material) and low radiation efficiency.

2.2 Surface Waves in Integrated Antennas Substrate

Presence of the substrate plays a significant role in the design and performance of integrated antennas. When an antenna is implemented at the interface between a dielectric substrate and free space, its radiated power no longer divides equally above and below the interface. In fact, these antennas intend to initially radiate most of their energy into the lossy substrate due to the higher dielectric constant compared to air. This is the primary reason for the lower efficiency of integrated antennas. Shown in Figure 2.4 from the ray point of view, the rays that are incident at an angle larger than the critical angle (θ_C) are completely reflected and trapped in the substrate as surface waves [22]–[29]. In other words, dielectric substrates are excellent surface waveguides and the integrated antenna serves as a source of surface waves and excites different substrate modes whose cutoff frequency is below the frequency of radiation. This phenomenon critically affects the radiation patterns, efficiency, and the antenna impedance.

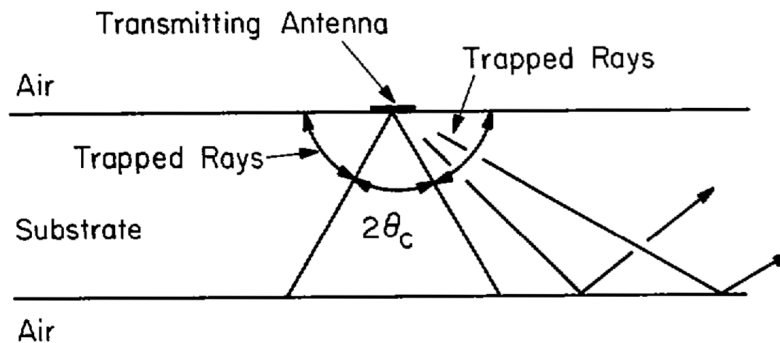


Figure 2.4: Transmitting antenna on a dielectric substrate showing the rays trapped as surface waves with the critical angle $\theta_C = 30^\circ$ appropriate for fused quartz ($\epsilon_r = 4$) [23].

Various parameters such as dimensions of the substrate, frequency of radiation, and the structure of the antenna itself determine which substrate modes are excited by the generated surface waves. As an example, Figure 2.5 shows the various substrate modes that get excited for a dipole antenna as well as a slot antenna implemented on quartz and GaAs substrates as a function of the ratio of substrate thickness (h) to the wavelength (λ_0). Although the modes shown on these plots are specific to those particular configurations, they provide a general understanding over the trend of excited modes as substrate thickness increases.

Various methods have been offered to reduce the loss associated with the excited

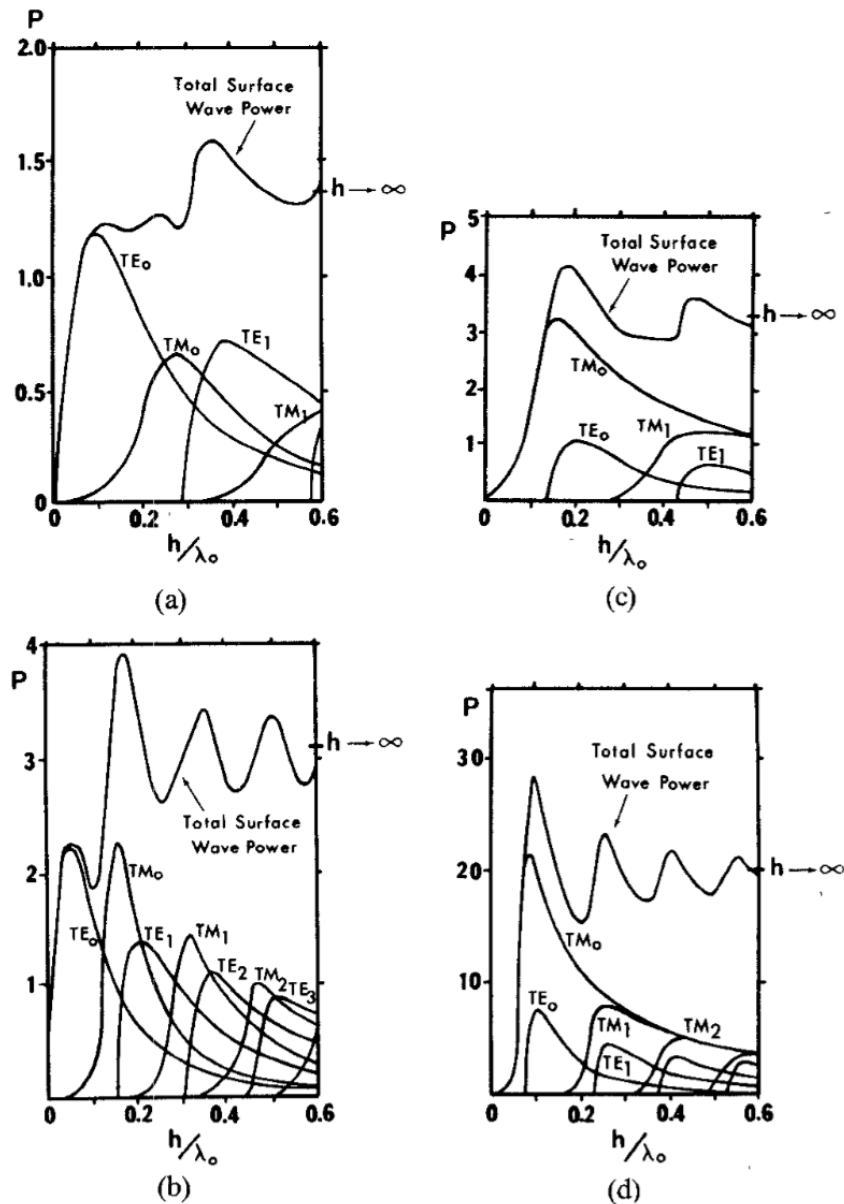


Figure 2.5: Normalized power versus substrate thickness for (a) dipole on quartz substrate, (b) dipole on silicon or GaAs substrate, (c) slot on quartz substrate, and (d) slot on silicon or GaAs substrate [22].

substrate modes. However, they involve expensive post-processing and use of additional material, which contradicts the integrated nature of the system. Two of such methods are mounting the integrated radiator on a silicon lens [12]–[14] and use of superstrates [17], [18]. A silicon lens, as can be seen in Figure 2.6, effectively extends the substrate dielectric such that the radiated electromagnetic waves face a normal interface between the silicon-air interface at all angles. A superstrate, shown

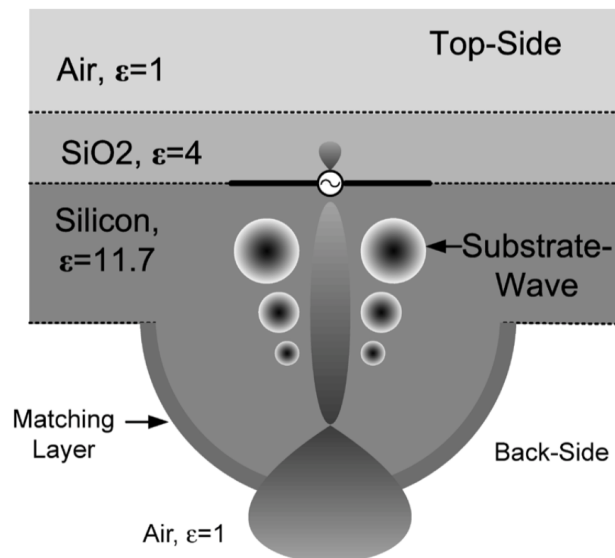


Figure 2.6: Operation of a silicon lens to minimize substrate modes and to radiate the highest power down through the bottom of the substrate [12].

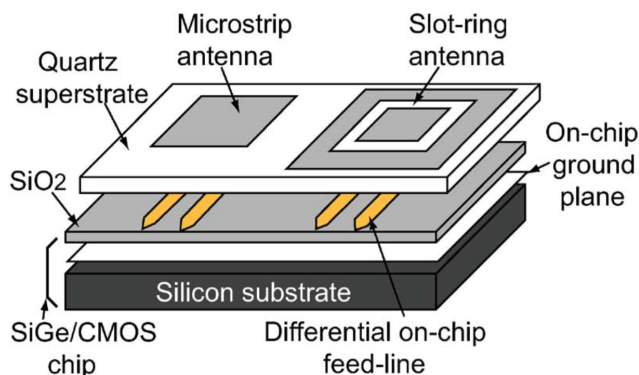


Figure 2.7: 3-D depiction of the use of a dielectric superstrate (quartz in this case) to couple electromagnetic power up from the metal stack to antennas printed on top of the superstrate [17].

in Figure 2.7, is a high dielectric constant slab that is mounted on top of the IC and because of its higher dielectric constant most of the power couples up and radiates through the superstrate. While these methods are effective in reducing the excited substrate modes and direct more energy towards the free space, they are bulky and expensive, and increase the cost of the mm-wave integrated radiator.

Looking for a better understanding to provide design intuition for an integrated solution to this problem, in [30] it was shown that to maximize broadside radiation from a set of currents on a plane in free space, the currents should be engineered

in such a way that at any instant, most of the current is facing the same direction. Similarly, it has been shown in [31] that careful engineering of the currents on the surface of the substrate and using multiple antenna elements in an array can cancel out most of the substrate modes to the first order. The theoretical optimal 2-D surface-current configuration that collectively suppresses surface waves and maximizes radiation efficiency with the desirable radiation pattern has been shown in [29]. Although this methodology provides significant insight for the design of integrated radiators with improved radiation efficiency and reduces the energy trapped in the substrate, some substrate modes still get excited in the substrate and impose limitation on the achievable radiation efficiency.

2.3 Effects of Process and Environmental Variations

In addition to the specific design and performance considerations for integrated radiators, similar to any other integrated circuit, their performance is also affected by process and environmental variations. Although transistor scaling has enabled implementation of mm-wave integrated radiators due to availability of faster devices and improved performance, it also brings up additional concerns such as more susceptibility to process variations, both between chips and between individual transistors on the same chip. The major sources for these variations are Random Dopant Fluctuations (RDF) in the transistor channel and Line Edge Roughness (LER) [32].

RDF deals with the dopant number and their random positioning in the channel of a MOSFET transistor. As transistors become smaller, the number of dopant atoms in their channel becomes smaller too [33]. This is shown in Figure 2.8. It has been experimentally demonstrated [34] that the threshold voltage fluctuation is mainly caused by charge fluctuation in the depletion layer. This means that RDF directly affects the threshold voltage of individual transistors and thus acts a major source for process variation.

LER is associated with line-width control in fabrication process and is caused by lithographic and etching steps. Figure 2.9 shows example SEM images of fabricated lines and the width variation caused by LER [35]. This phenomenon directly impacts the overlap capacitance and other device parameters such as drain induced barrier lowering (DIBL) and threshold voltage, and thus directly contributes to performance variation across a chip as well as between different samples of the chip.

Figure 2.10 shows the variation of threshold voltage of a transistor versus the channel

length as a result of RDF and LER [36]. It can be seen that this variation is smaller and thus easier to manage at larger process technology nodes compared to the advanced smaller nodes.

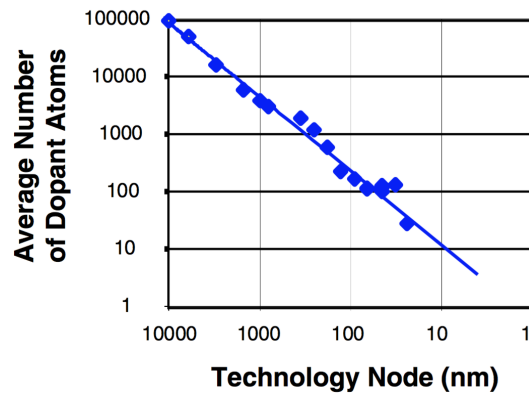


Figure 2.8: Average number dopant atoms as a function of technology node [33].

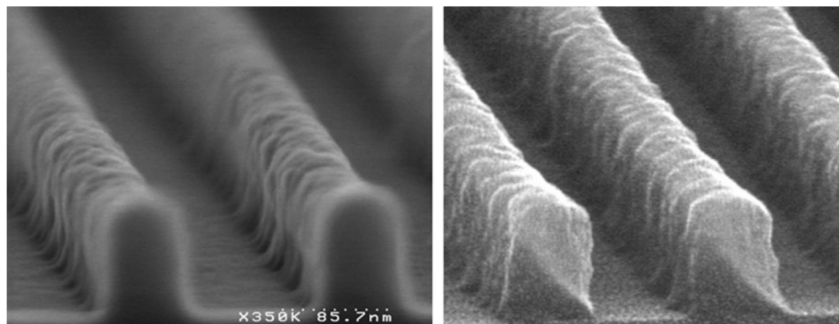


Figure 2.9: Line edge roughness shown in SEM images of an example process [35].

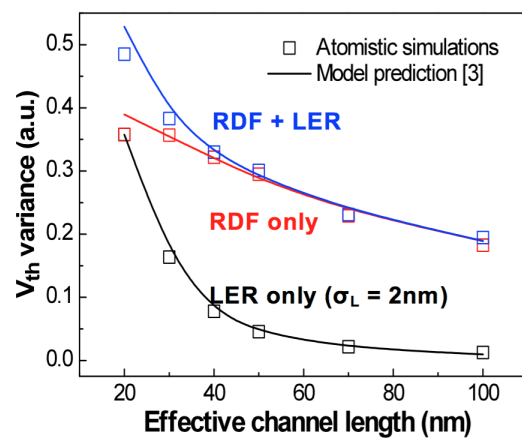


Figure 2.10: Threshold voltage variation over technology node [36].

In addition to these static process variations, other dynamic and time varying changes would also impact the performance of mm-wave integrated circuits. Such variations include temperature variations across the same die or in the environment over time, transistor aging, electro-migration, etc. Also, in the case of driving circuit of mm-wave integrated antennas, load impedance variations due to change in voltage standing wave ratio (VSWR) [37], [38] caused by interaction with objects in the near field of the antenna as well as dynamic switching between multiple settings, introduce additional variations to the performance. This is particularly important in integrated antenna arrays where mutual coupling between individual elements adds to the undesired impact of such interactions.

All these variations in the performance of the integrated radiators need to be dealt with. For static variations, a one-time calibration may be sufficient to compensate for the errors. However, dynamic variations require more complex correction schemes performed frequently or even in real time for compensation.

2.4 Indirect Measurement of Far-Field Radiation Properties

Once the integrated radiators are fabricated, they need to be characterized and their operation must be tested before they are used in the desired wireless application. The actual implemented antenna structures should be verified in measurement to match the expectations from electromagnetic models, and any discrepancies between them should be compensated to the possible extent through the existing actuation schemes. This includes the calibration of systematic modeling errors as well as process variation across each unit. However, a one-time calibration would not address the dynamic variations. Even if an integrated radiator's operation is verified and it is calibrated for the systematic errors and static process variations, still its performance might be affected by dynamic variations in the environment that occur during its operation in the actual system. This means that ideally the calibration schemes should be performed multiple times during the operation or even in real time.

Any correction method is based on the measured performance of the integrated radiator. Testing, characterization, and performance evaluation of integrated radiators at mm-wave frequencies are usually performed through a far-field measurement setup, that is, placing a receiver antenna with known characteristics at a relatively long distance (compared to the wavelength) away from the integrated radiator. Full control over the relative orientation and angle of the receiving antenna with re-

spect to the transmitting antenna while keeping their separation constant allows for complete characterization of the far-field radiation properties of the transmitter. If the measured radiation properties are not optimal, the data from this setup can also be used through a processing unit to form a closed-loop system that enables optimization as well as calibration and correction for systematic errors. However, since this setup is bulky and relies on direct measurement of the far-field radiation properties in the far-field region of the antenna, it cannot be used for monitoring of the performance of the integrated radiator and real-time calibration of dynamic variations in its operating environment for the specific wireless application.

There are also indirect measurement methods that capture the far-field radiation properties without directly measuring them in the far-field region. In fact, these methods have been investigated for a long time [39]–[41] for a variety of reasons. Figure 2.11 shows the definitions of different regions surrounding an antenna.

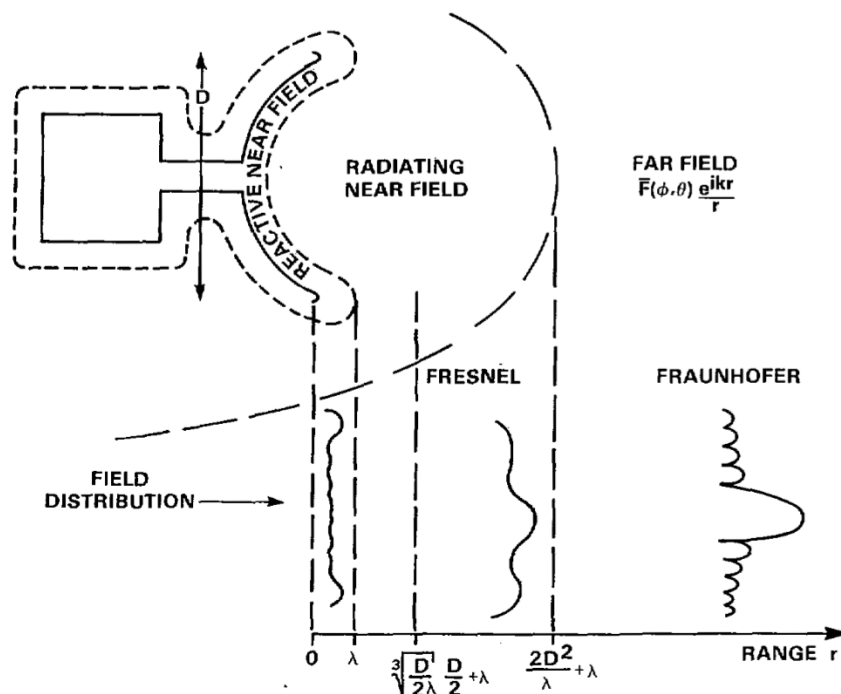
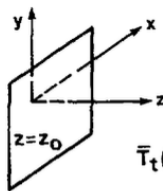


Figure 2.11: Exterior fields of radiating antenna [40].

It many cases it was impossible or impractical to move an antenna from its operating environment to a far-field range, or the desired amount of pattern data required too much time to capture on a far-field range. Such issues motivated a new set of methods to determine the far-field radiation patterns of an antenna from measurements made in the radiating near-field region. In these methods, a scanning probe is used to

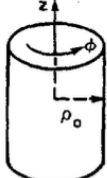
PLANAR



$$\bar{E}_t(x, y, z) = \frac{1}{2\pi} \int_{-\infty}^{\infty} \int_{-\infty}^{\infty} \bar{T}_t(k_x, k_y) e^{i\gamma z} e^{ik_x x} e^{ik_y y} dk_x dk_y$$

$$\bar{T}_t(k_x, k_y) = \frac{e^{-i\gamma z_0}}{2\pi} \int_{-\infty}^{\infty} \int_{-\infty}^{\infty} \bar{E}_t(x, y, z_0) e^{-ik_x x} e^{-ik_y y} dx dy$$

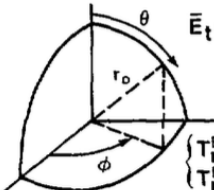
CYLINDRICAL



$$\bar{E}_t(\rho, \phi, z) = \frac{1}{2\pi} \sum_{m=-\infty}^{\infty} \int_{-\infty}^{\infty} \left\{ \bar{H}_m(\gamma, \rho) \cdot \bar{T}_m(\gamma) \right\} e^{im\phi} e^{i\gamma z} d\gamma$$

$$\bar{T}_m(\gamma) = \frac{1}{2\pi} \bar{H}_m^{-1}(\gamma, \rho_0) \cdot \int_{-\infty}^{\infty} \int_0^{2\pi} \bar{E}_t(\rho_0, \phi, z) e^{-im\phi} e^{-i\gamma z} d\phi dz$$

SPHERICAL



$$\bar{E}_t(r, \phi, \theta) = \sum_{n=1}^{\infty} \sum_{m=-n}^n \left[\bar{T}_{nm}^E h_n^{(1)}(kr) \bar{M}_{nm}(\theta) + \bar{T}_{nm}^M g_n^{(1)}(kr) \bar{N}_{nm}(\theta) \right] e^{im\phi}$$

$$\begin{cases} \bar{T}_{nm}^E \\ \bar{T}_{nm}^M \end{cases} = \begin{cases} -h_n^{(1)}(kr_0)^{-1} \\ g_n^{(1)}(kr_0)^{-1} \end{cases} \int_0^{\pi} \int_0^{2\pi} \begin{cases} \bar{N}_{nm}(\theta) \\ \bar{M}_{nm}(\theta) \end{cases} \cdot \hat{r} \times \bar{E}(r_0, \phi, \theta) e^{-im\phi} \sin\theta d\phi d\theta$$

Figure 2.12: Specific expressions for scanning with ideal dipole on a plane, cylinder, and sphere [40].

measure the electric field over a planar, cylindrical, or spherical surface in the radiating near-field region and then a mathematical transformation of measured near-field data accurately produces the far-field patterns, shown in Figure 2.12. These methods, once performed properly, capture all the information that a far-field measurement setup can provide and thus can be used for the exact same purposes. However, there are several issues such as correction of the measured field due to distortion by the probe and the trade-off between probe sensitivity and scanning resolution that need to be taken into account with these methods.

Although determination of far-field radiation patterns based on near-field measurements still requires use of bulky equipment and does not enable real-time monitoring of the integrated radiator performance, it motivates designing new indirect methods

based on local field measurements in the vicinity of the antennas. This is particularly useful in integrated radiators where the presence of dielectric substrate provides a great platform for in-situ measurement of the fields. Such capability could eventually be used as a tool for real-time in-situ calibration and performance monitoring. Although self-correcting methods have been previously investigated for other integrated circuits and systems [42]–[44], there is a very small body of research on implementation of in-situ probes for self-monitoring of integrated radiator performance to refer to. Here, we briefly discuss a previously published attempt for in-situ calibration of integrated arrays of antennas. In [45], magnetically coupled in-situ probes that excite the fundamental mode of a 20-GHz patch antenna are investigated to serve as a calibration tool. Two probes for each element are designed to detect mutual coupling and finite array effects in an integrated array of patch antennas, as shown in Figure 2.13.

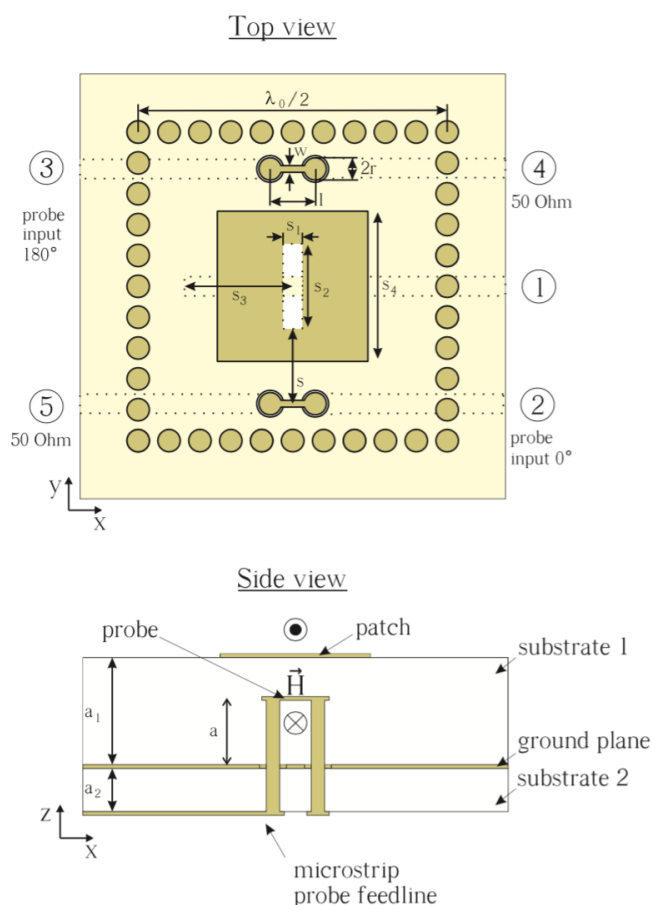


Figure 2.13: Magnetically coupled in-situ probes for patch antennas operating at 20 GHz [45].

In this work, the excitation of in-situ probes is used to excite the fundamental mode of the patch antennas. Due to the arrangement, the two probes have to be excited out of phase. It is shown that only with an opposite phase excitation of the two probes a symmetrical radiation can be obtained which emulates the patch radiation in normal operation mode and implies that mutual coupling and finite array effects are taken into account. Measurement results to show the probes operation on a single patch antenna are presented and simulations have been used to investigate this concept in a 2×2 array. A similar approach with measured results for a 4×1 array of circularly polarized patch antennas is presented in [46].

PROXIMAL-FIELD RADIATION SENSORS

3.1 Introduction

Dielectric substrates provide a crucial role in electronic and communications systems. They provide a variety of platforms such as printed circuit boards (PCB) and integrated circuits (IC) that allow implementation of these systems. They also serve as a basis to fabricate microwave and electromagnetic structures. Antennas are one type of such structures that are essential in wireless communications systems.

Focusing on the transmitter in a wireless communications system, the implementation cost at the desired frequency of operation determines what platform should be used for driving circuit and antenna fabrication. Also, the trade-offs between cost and performance determine whether or not using discrete components is affordable. At RF and mm-wave frequencies, usually the required performance and the complexity of power transfer methods enforce integration of transmitting antennas on the substrate. They might be implemented on the PCB substrate or even be fully integrated on the same IC substrate with the transmitter circuitry. In both cases, various design considerations must be taken into account to achieve an acceptable performance.

Once the antenna is fabricated on a dielectric substrate a new set of challenges are faced. These challenges range from sensitivity of the antenna performance to design parameters and the error caused by their variation, to testing and characterizing the antenna performance.

In this chapter, we first investigate the challenges associated with the design of integrated antennas on a dielectric substrate and review the existing methods for antenna characterization and their limitations in section 3.2. In section 3.3, we introduce Proximal-Field Radiation Sensors (PFRS) that are integrated with the transmitting antennas on the same substrate as a new concept that can be used to monitor radiating antennas' performance, both for error correction and characterization purposes. Section 3.4 provides some intuition on the fundamentals of operation of these sensors and demonstrates how they can capture meaningful information. Various examples of processing schemes for analyzing the data from PFRS sensors are discussed in section 3.5. Design and measurement results of proof-of-concept prototypes, both

in PCB and IC platforms, which verify PFRS operation are presented in sections 3.6 and 3.7, respectively, followed by the concluding remarks in section 3.8.

3.2 Integrated Antennas on Dielectric Substrates

Design of antennas that are fabricated on dielectric substrates requires a thorough analysis and optimization of the electromagnetic structure. This is mainly due to the fact that dielectric substrates are excellent surface waveguides [47], [48] with a fundamental mode with no cutoff frequency and the integrated antennas act as the source of surface waves in the substrate [22], [23], as shown in Figure 3.1. These surface waves that travel inside the finite substrate form the substrate modes, i.e., the electromagnetic waves that are trapped in the substrate and do not necessarily contribute to the efficient radiation. This phenomenon happens in both printed circuit board (PCB) antennas [24], as well as integrated circuit (IC) antennas [29], where the antenna is implemented on a dielectric substrate and thus requires a careful optimization of the substrate dimensions and permittivity to minimize the power trapped in the substrate modes.

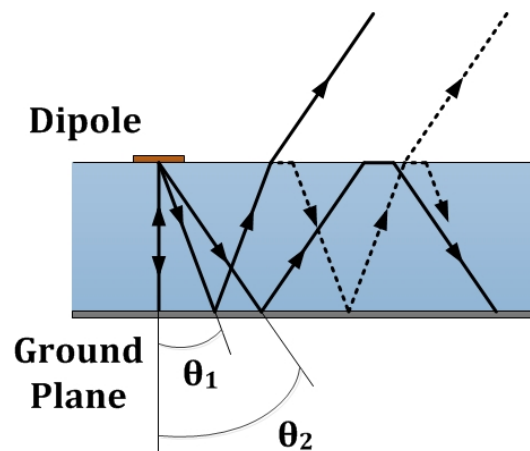


Figure 3.1: Generation of surface waves inside the dielectric substrate of an integrated antenna.

Once the integrated antennas are designed and fabricated, their testing and characterization of far-field radiation properties, as well as monitoring of their performance while in operation present a challenge. This is in part because these tasks often require use of several additional bulky pieces of equipment, which exclude the possibility of in situ correction and calibration. Figure 3.2 shows an example of such a complex measurement setup for a mm-wave integrated radiator operating at 120 GHz.

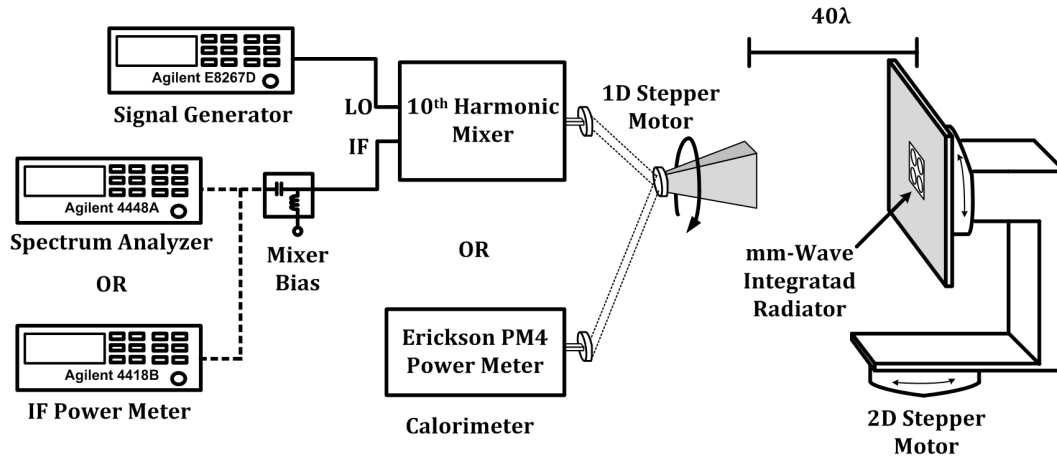


Figure 3.2: Complexity of an exemplary far-field measurement setup for a mm-wave integrated radiator operating at 120 GHz.

Traditionally, a far-field range method has been used for measurement. In this technique, the antenna under test (AUT) is placed a long distance away from an instrumentation antenna with known characteristics. A diagram of the far-field range arrangement is shown Figure 3.3. The large separation between the two antennas ensures that the phase variation across the receiving antenna is low enough for sufficient accuracy. Thus, in addition to the several pieces of equipment required to perform this method, it will also require an extremely large space to permit accurate measurement. At lower frequencies with larger wavelengths, meeting this requirement may not even be possible.

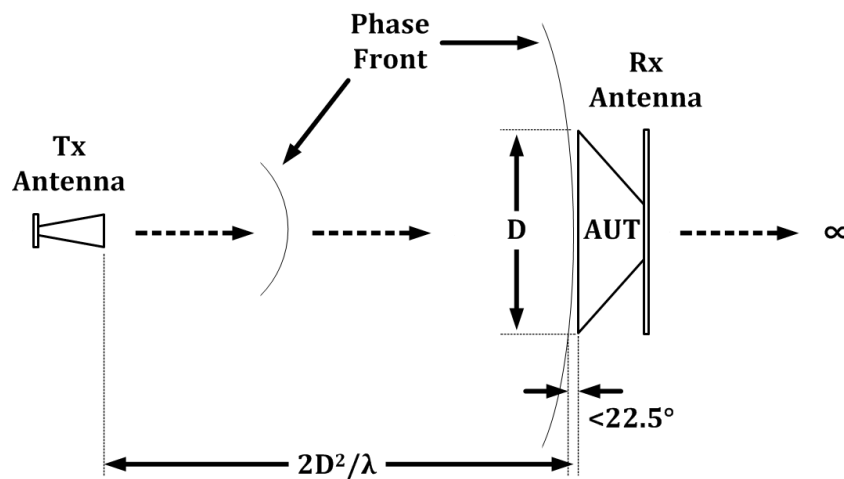


Figure 3.3: A simplified diagram for a far-field measurement range with AUT used as the receiver antenna and a known antenna used as the transmitter antenna.

Another technique is use of a near-field antenna measurement system in a near-field range. This method is conducted by scanning a probe to measure the electric field over a surface in the radiating near-field region of the antenna. This surface might be planar, cylindrical, or spherical. The measured electric field profile is then translated to far field using mathematical transformations such as Fourier transform, cylindrical harmonics, and spherical harmonics. Although the near-field range method reduces the necessary spacing between the probe and the AUT compared to the far-field range, it still requires use of a complex setup for the scanning probe control. Distortion of the field by the probe and associated equipment is a big challenge in such systems. Additionally, at the same time the probe should be small enough to essentially measure the field at a point and large-enough to provide a strong-enough signal for accurate measurement. Figure 3.4 shows the diagram of a planar near-field measurement setup arrangement.

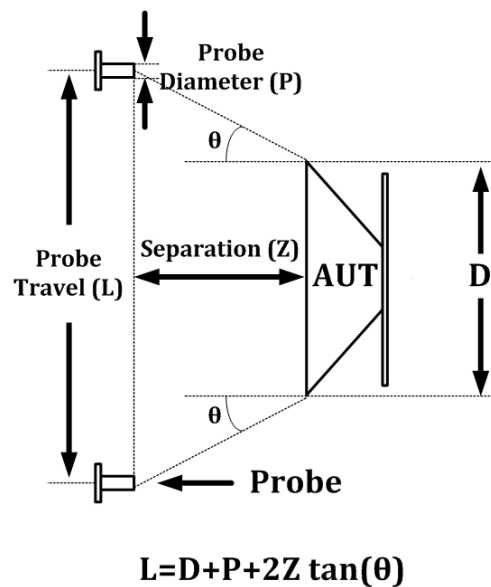


Figure 3.4: A simplified diagram for a palanar near-field measurement setup.

In order to enable characterization of sensitive systems, both far-field and near-field measurement methods may be performed in an anechoic chamber, i.e., a room designed to completely absorb the reflections of the electromagnetic waves and isolate the measurement setup from the exterior noise. Figure 3.5 shows an example of a far-field measurement setup in an anechoic chamber. Clearly, implementation of anechoic chambers and use of electromagnetic absorbers add to the complexity of the required measurement setup for antenna characterization. It may also be impractical to move an antenna from its operating environment to any of these



Figure 3.5: Example of a far-field measurement setup in anechoic chamber.

measurement setups.

Another issue associated with the integrated antennas is that when these antennas are integrated with the driving circuitry, either on a PCB or an IC platform, any variation of circuit components, temperature, mismatch, etc. which changes the drive circuit performance could significantly affect the antenna radiation properties, particularly in antenna arrays and multi-port antennas, where the relative phases and amplitudes of the drives determine the performance [9].

3.3 Proximal-Field Sensing

The surface waves that always exist in the substrate of an integrated antenna indeed contain valuable information, which can be utilized to capture its far-field radiation properties, without any need to use additional test equipment and without removing the antenna from its operating environment or interfering with its operation in a wireless system. Proximal-Field Radiation Sensors (PFRS) are a number of small sensing antennas that are strategically placed and integrated on the same substrate as the transmitting antennas (Figure 3.6) and measure certain properties of the electromagnetic field in immediate proximity of the radiating antennas [49].

Unlike the operational principle of traditional near-field measurement systems [39]–[41] that determine the far-field patterns from measurements in the radiating near-field region of an antenna (scanning the fields outside the plane of antenna structure by an external probe), the proposed proximal-field sensors are integrated with

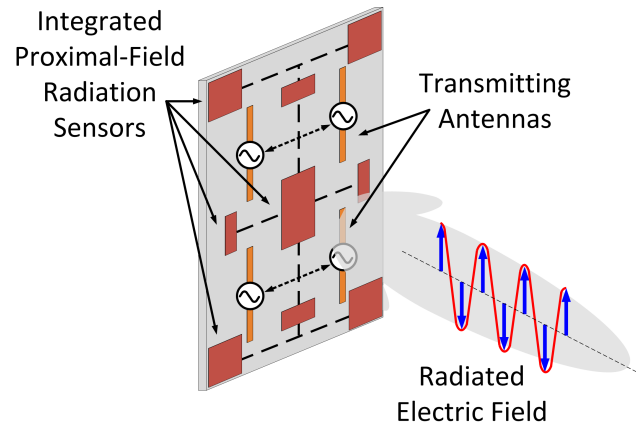


Figure 3.6: Proximal-Field Radiation Sensing (PFRS) concept where small sensing antennas measure certain properties of electromagnetic fields in the immediate proximity of the transmitting antennas.

the transmitting antennas on the same substrate and pick up information from the substrate and close proximity of transmitting antennas, and predict the far-field radiation properties of the transmitting antennas in real time, allowing for self-characterization, self-calibration, and self-monitoring of the radiation properties of the transmitting antennas.

These sensors are not limited to a specific shape in order to be functional and depending on the desired radiation properties and the transmitting antennas' structure, they can be of any antenna type consistent with the rest of the structure to pick up sufficient signal from the substrate. If there exists a large ground plane in the design of the integrated radiator, then various types of slot antennas could be good choices to be implemented on the same ground plane to serve as PFRS since they can be easily implemented by cutting the existing ground plane at various locations on the substrate. A few examples including slot-ring, linear-slot, and folded-slot antennas are shown in Figure 3.7. Other types of antennas such as small dipoles antennas and patch antennas (also shown in Figure 3.7) might be used as PFRS too, as long as their structures are consistent with the rest of the electromagnetic design.

Another advantage of PFRS is that due to their proximity to the radiating source, their received signal is strong enough to enable very small sensors that can be placed anywhere on the substrate, as long as their picked-up signal level satisfies the minimum detectable signal condition for the detector circuitry attached to the sensing antennas. Depending on the desired radiation parameters, affordable circuit complexity, and choice of data processing scheme, either both amplitudes and

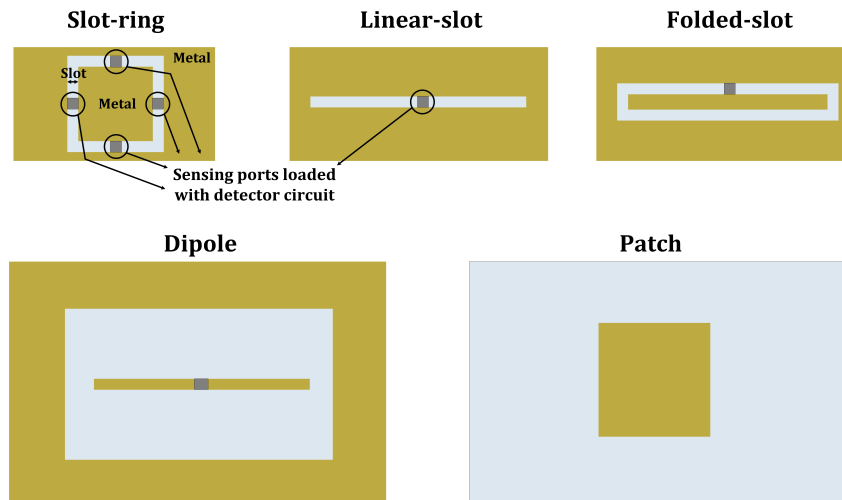


Figure 3.7: Few examples of different antenna types to be used as PFRS.

phases or only the amplitudes of the signals from the sensing antennas may be used to determine the desired far-field radiation properties.

Integration of PFRS units with the radiating elements on the same substrate enables a variety of applications. Similar to any other type of sensors, PFRS can be used in closed-loop systems. The extracted information from PFRS read-outs provides valuable feedback based on system's performance. This allows the data from PFRS to be processed either by a processing unit on the same chip as the integrated radiator IC or through external processing and control units to close the loop off chip. The read-outs may be used once right upon start-up to perform a one-time self-calibration or they might be continuously monitored to keep the loop closed and adjust the control signals in real time to ensure self-correction and minimal deviation from the optimal performance during the operation. Figure 3.8 shows the conceptual block diagram of such a closed loop system where a 2×2 antenna array implemented on a CMOS chip is equipped with integrated PFRS units, and the sensors data is processed on-chip through a digital core which also controls the actuators' values to adjust the performance.

Ideally, sensitivity of PFRS antennas on an integrated radiator to the undesired mechanisms that can potentially affect their performance should be minimal. Consider the 2×1 multi-port driven integrated radiator array shown in Figure 3.9, which operates at 120 GHz and features six slot-ring multi-port PFRS antennas. More details about the design and operation of this radiating antenna and the integrated PFRS antennas will be presented later in section 5.3 and section 3.5, respectively.

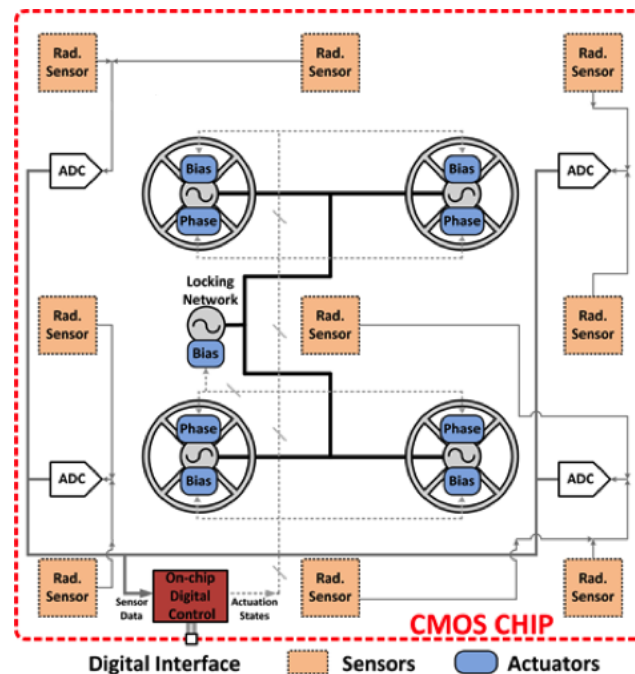


Figure 3.8: Example of a self-correcting integrated radiator as a result of radiator integration with PFRS and digital processing units.

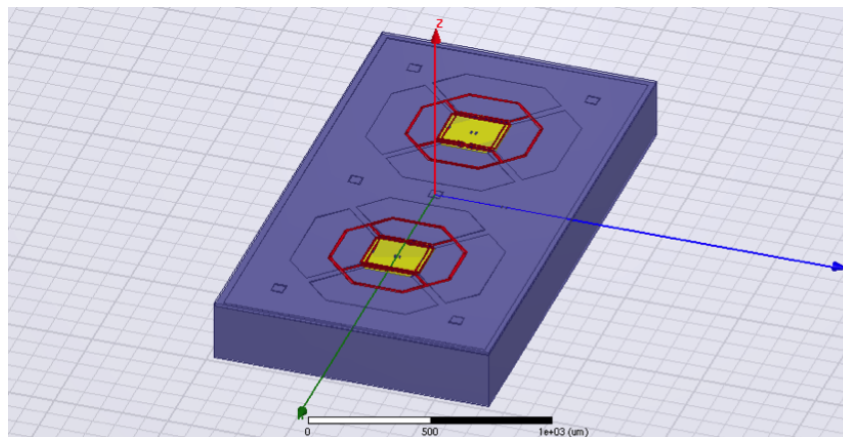


Figure 3.9: A 2×1 multi-port driven integrated radiator array with six slot-ring multi-port PFRS antennas.

Shown in Figure 3.10 are two of such undesired mechanisms that may have destructive impact on the PFRS antennas on this chip: 1) coupling to strongly driven points by the drive circuitry (points *A*, *B*, and *C*) to the sensors through substrate, and 2) incident electromagnetic waves on the integrated radiator from external sources. PFRS design on the integrated radiator should be performed such that the sensors' electromagnetic coupling to the surface waves inside the substrate is much stronger

than their coupling to the driving circuit leakage through the substrate, as well as the incident electromagnetic waves on the chip. Otherwise, the sensor read-outs would be affected by these factors, and inaccurate read-out from PFRS would result in invalid prediction of the radiator's performance.

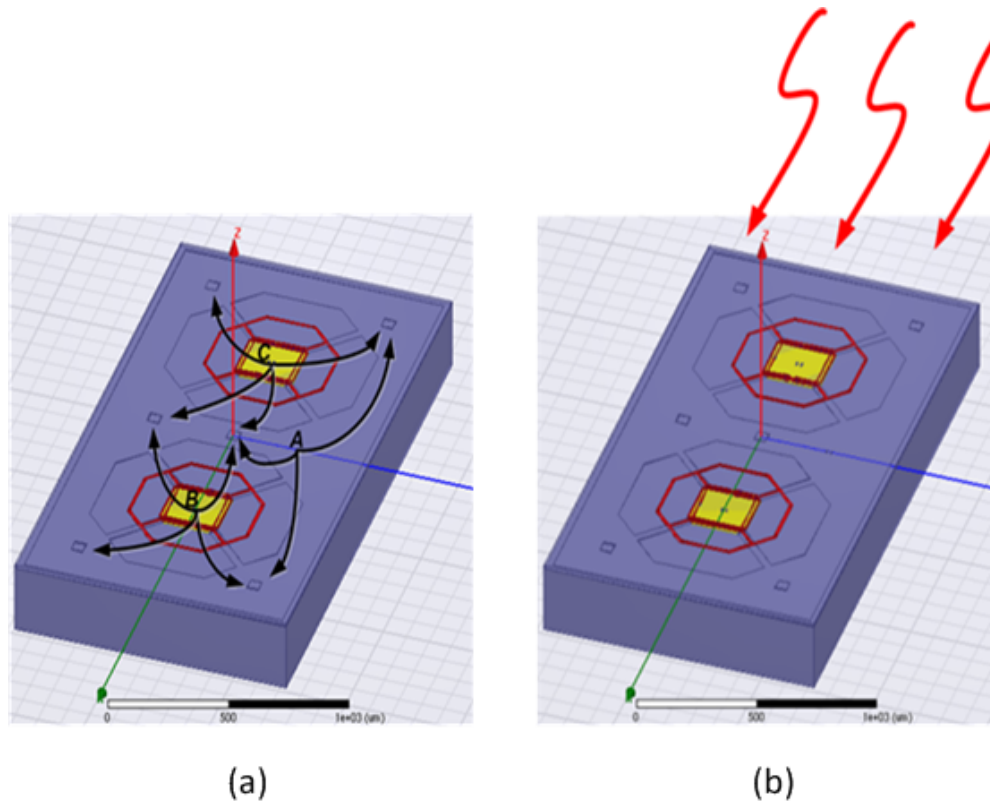


Figure 3.10: Possible undesired mechanisms that could affect PFRS performance: (a) coupling to strongly driven points by the drive circuitry and (b) incident electromagnetic on the system from external sources.

In order to investigate the sensitivity of implemented PFRS on this integrated radiator to the aforementioned undesired mechanisms, first we consider the strength of the signals picked-up by multi-port PFRS antennas through standalone electromagnetic coupling to the substrate modes under nominal operation of the radiator array and in the absence of any electromagnetic waves incident from external sources. Figure 3.11 shows the simulated readouts of the PFRS antenna located at the center of the chip versus the phase difference between the driving signals of the two radiating antennas. It is observed that the voltages at the ports of central PFRS antenna vary in the orders of tens of mV.

To evaluate the circuit leakage to these sensors through the substrate, three pairs of metallic contacts with substrate have been made in the regions with large voltage

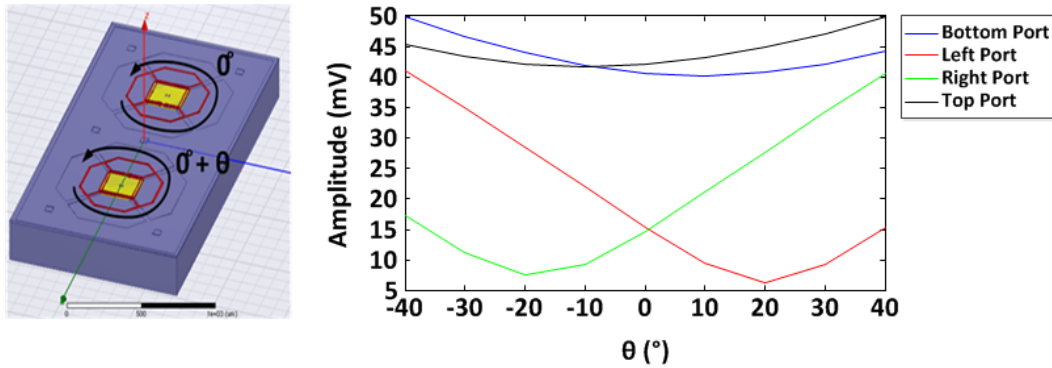


Figure 3.11: Amplitude read-outs of the PFRS antenna located at the center versus the relative phase difference between the two radiating antennas.

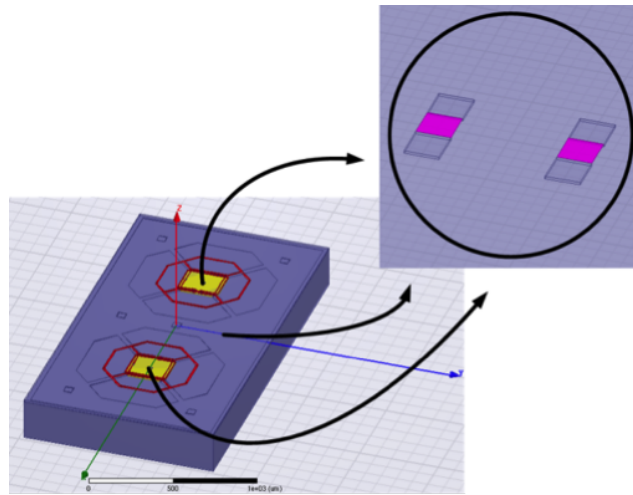


Figure 3.12: Arrange of metallic contacts in the simulation setup to evaluate coupling of PFRS to strongly driven points on the chip.

swing: one pair in each of the two radiator cores and one in the central region which corresponds to the distribution network, as shown in Figure 3.12.

All three pairs of ports are driven with quadrature signals while the radiating antennas are not driven. The simulated voltages picked up by all PFRS antennas are plotted in Figure 3.13. This simulation shows that the maximum sensitivity of the sensors to the driving contacts' amplitude is $\sim 1.8\mu\text{V}/\text{V}$, meaning that the leakage is at least four orders of magnitude smaller than the desired signals whose amplitudes are about tens of mV during the normal operation of radiators.

Figure 3.14 shows the same design under radiation of an external source to evaluate the performance of the sensors in the presence of incident EM waves on the chip.

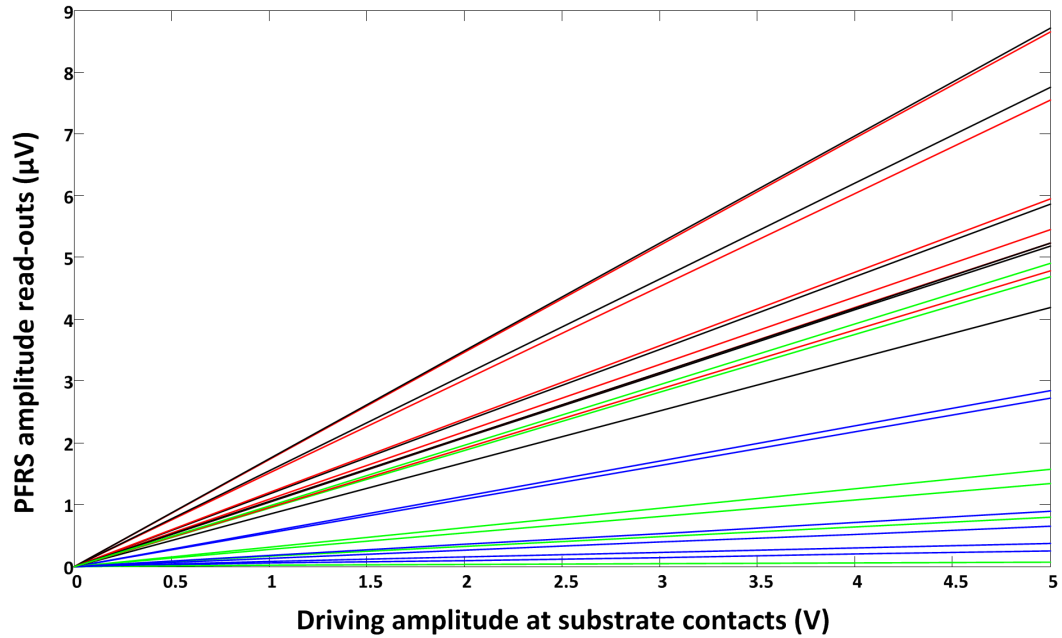


Figure 3.13: Coupling strength of all PFRS antennas to the driving signal amplitude at the strongly driven points through substrate.

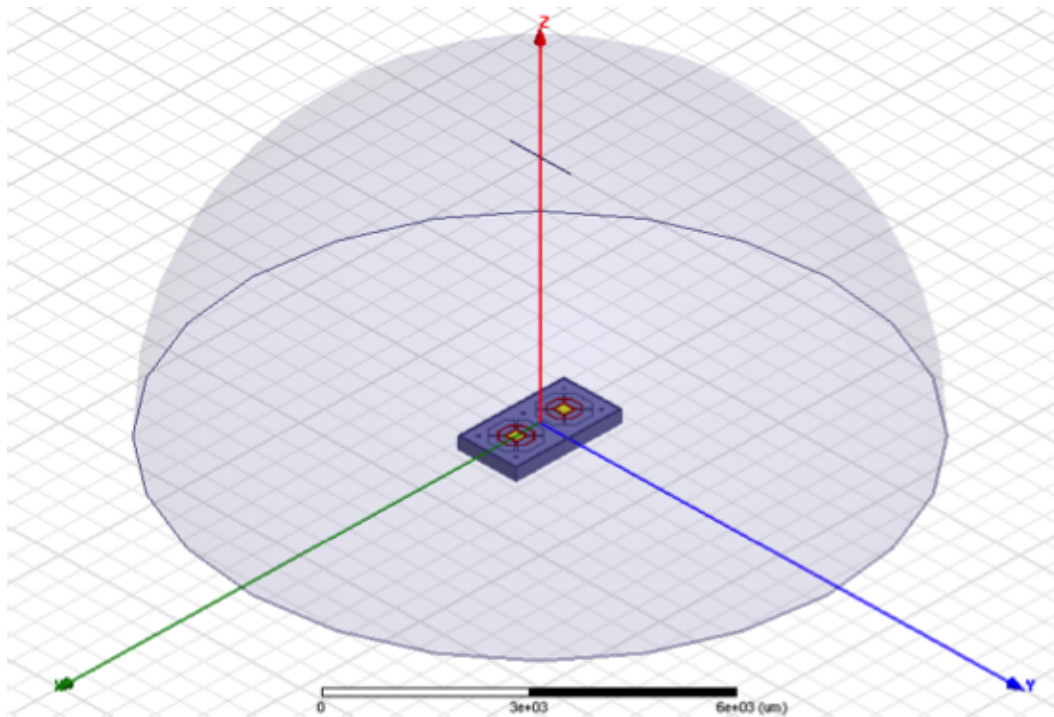


Figure 3.14: Simulation setup for evaluation of PFRS sensitivity to electromagnetic waves incident on the chip from a half-wavelength dipole antenna placed at 2λ distance above the chip.

The radiation source in this simulation is a $\lambda/2$ -dipole placed 5 mm ($= 2\lambda$) above the chip and its total input power is 0 dBm, which is much larger than any expected interference. The magnitude of the Poynting vector on the chip surface is $\sim 15 \text{ W/m}^2$. Shown in Figure 3.15 are the time domain signals picked up by the sensors. This plot shows that the amplitude of the largest signal at the sensors is less than 0.5 mV, which is two orders of magnitude smaller than the desired signal.

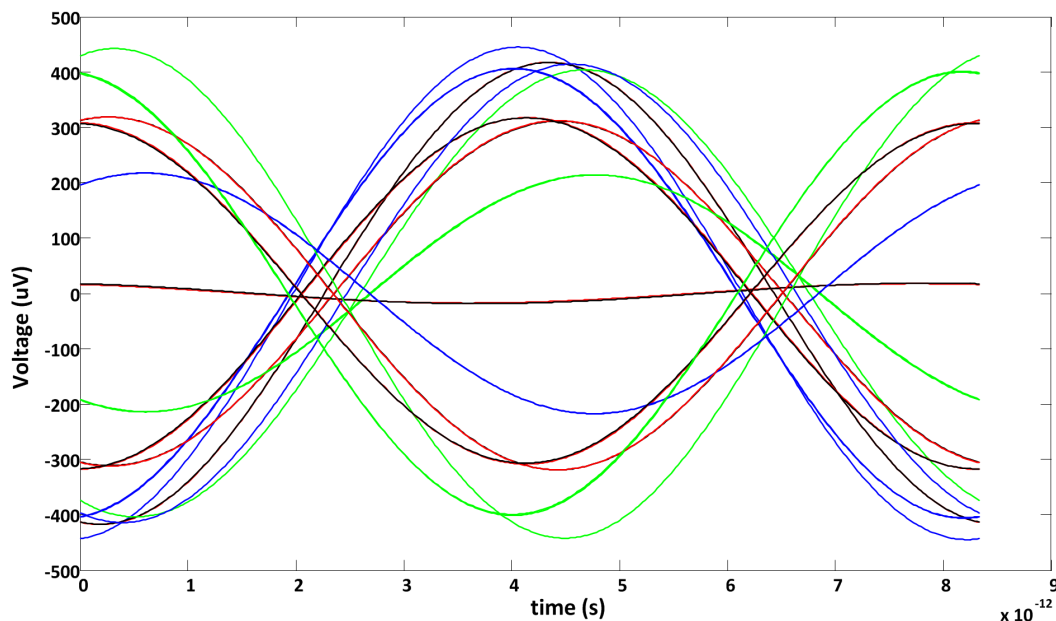


Figure 3.15: Signals picked up by PFRS antennas for 0 dBm input power to the dipole antenna.

The simulations above show that PFRS sensitivity to parasitic coupling through substrate as well as incident waves on the chip due to reflection and scattering and other external sources of electromagnetic waves is minimal. Therefore, the error introduced by these factors to the predicted radiation properties by PFRS is negligible and the sensors would be able to properly predict the undisturbed intrinsic radiation properties of the integrated transmitting antennas, as desired.

3.4 PFRS Data Capture Fundamentals

Various types of antennas can be used as PFRS to collect the valuable information contained in the substrate modes. In this section, some basic examples will be discussed. In order to provide better design intuition for PFRS antennas as well as a better understanding of how these sensors extract information from a dielectric

substrate, a rectangular waveguide with metallic sidewalls, shown in Figure 3.16, is used to demonstrate the operation of a few possible types of PFRS antennas.

The waveguide is excited with different modes with equal power traveling along the y -axis and three equally spaced points, L , C , and R , on the top metallic surface of the waveguide are chosen for the placement of PFRS antennas, with $a = 1000 \mu\text{m}$ and $b = 250 \mu\text{m}$. The dielectric material inside the waveguide is silicon with $\epsilon_r = 11.9$.

With the dimensions selected for the waveguide, the first ten propagating modes and their \mathbf{E} - and \mathbf{H} -field components (normalized to the largest component of each) along the dashed line on the top metal can be easily calculated. These modes and their field components are shown in Figure 3.17.

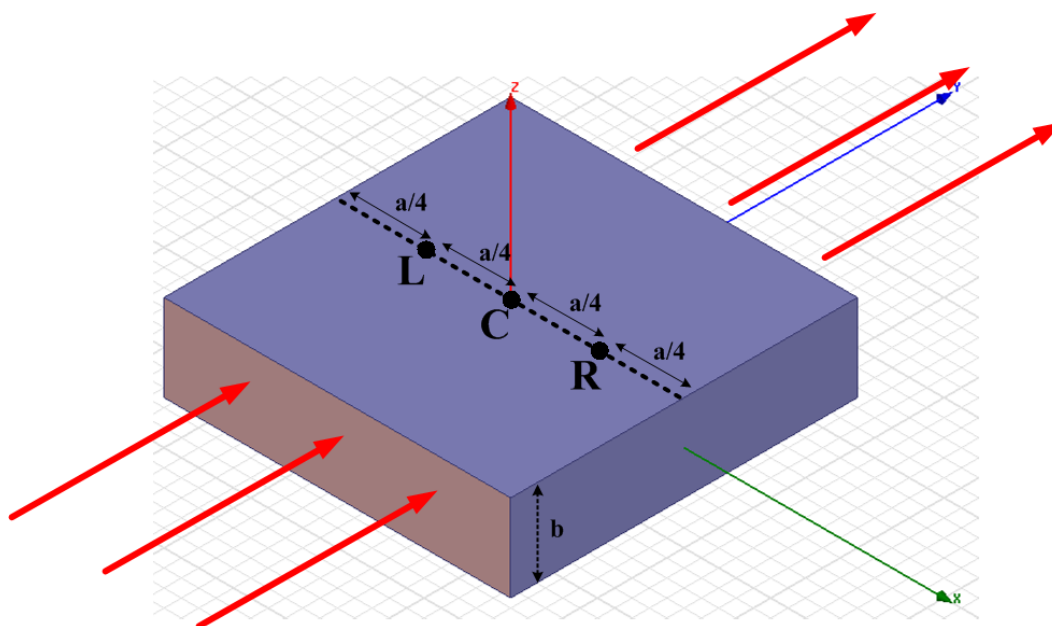


Figure 3.16: Rectangular waveguide configuration to evaluate various types of PFRS antennas when three PFRS units are located at points L , C , and R .

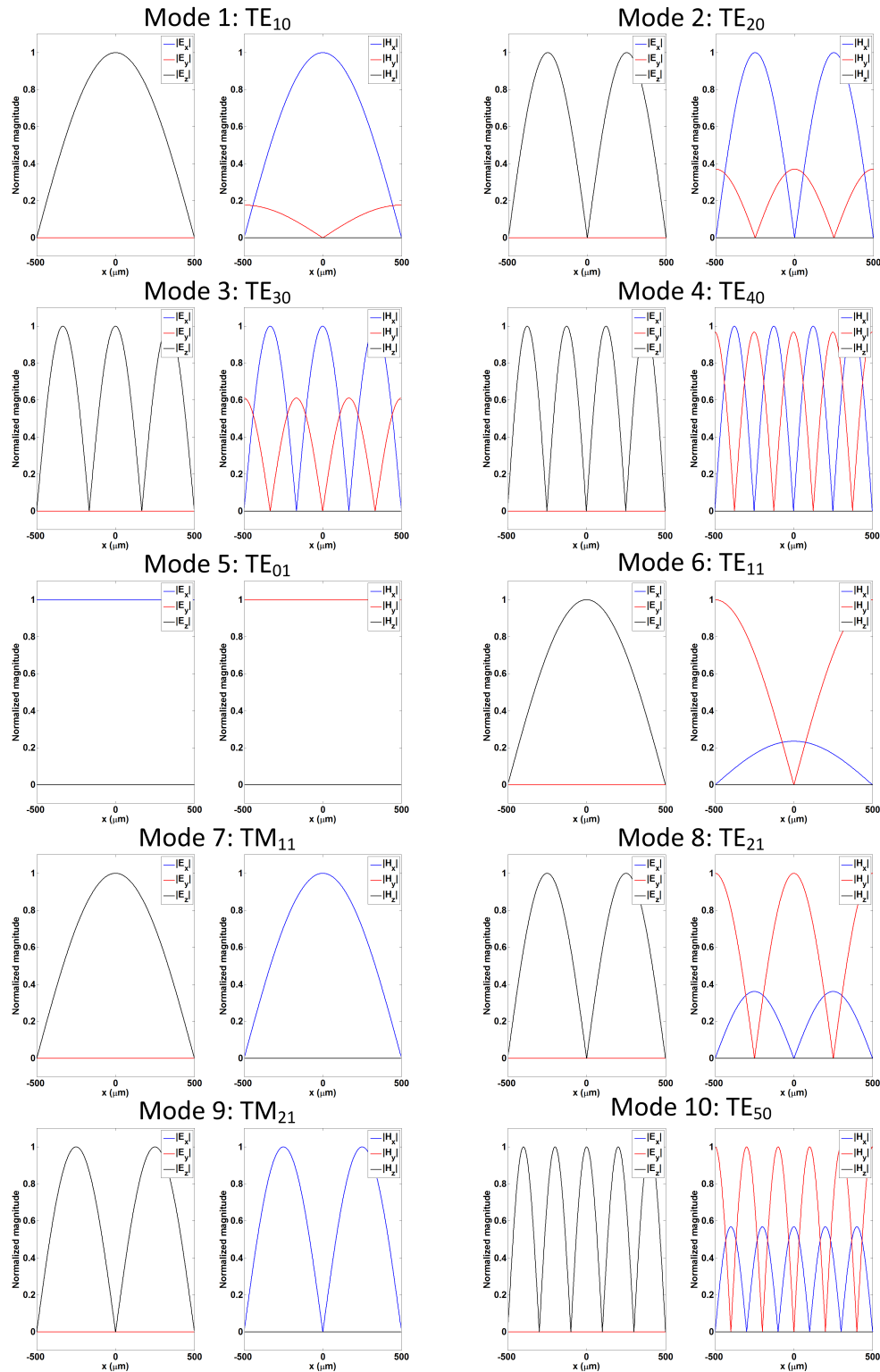


Figure 3.17: Field components of the first ten propagating waveguide modes across the dashed line on top surface.

The first type of PFRS antennas to investigate is a small linear slot antenna oriented along the y -axis, i.e., it is aligned with the direction of propagation. The structure of this type of sensing antenna is shown in Figure 3.18. Each PFRS antenna has one port at the center of the slot, which is terminated with 50Ω load. The voltage picked up by each PFRS antenna is plotted versus the frequency of excitation for each mode of propagation in Figure 3.19. The scales of the axes are kept the same for all the plots to make the comparison easier. For each mode, the sensors do not pick up any signals as long as the frequency of excitation is below the cut-off frequency associated with that mode. As the frequency increases and the excited mode starts to propagate along the waveguide, specific sensors begin to pick up non-zero signals depending on their location and the field distribution of the excited mode.

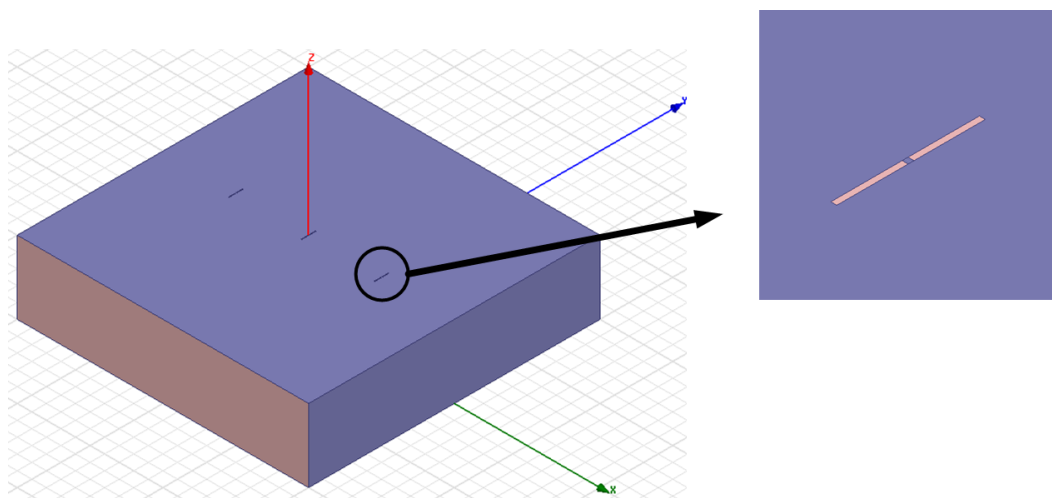


Figure 3.18: Y-oriented linear-slot antenna used as PFRS.

Comparing the amplitude of these signals with the field patterns for each mode shows that the strength of the signals picked up by these sensors is proportional to the magnitude of the H_y component of the electromagnetic waves. For example, for TE_{11} mode, the sensor located at the center does not pick up any signal while the left and right sensors pick up considerably large signals since $|H_y|$ is maximum at those two points. Similarly, for TM_{11} and TM_{21} modes, sensors do not pick up any signal since there is no magnetic field component in the direction of propagation for TM modes, i.e. $H_y = 0$ for TM modes. A similar argument justifies the relative strength of the sensor outputs for all the modes and can be easily verified by comparing the sensor outputs and $|H_y|$ for each mode. The behavior of Y-oriented slot antennas shows that, in this example, they act as TE mode sensors since there is no H_y

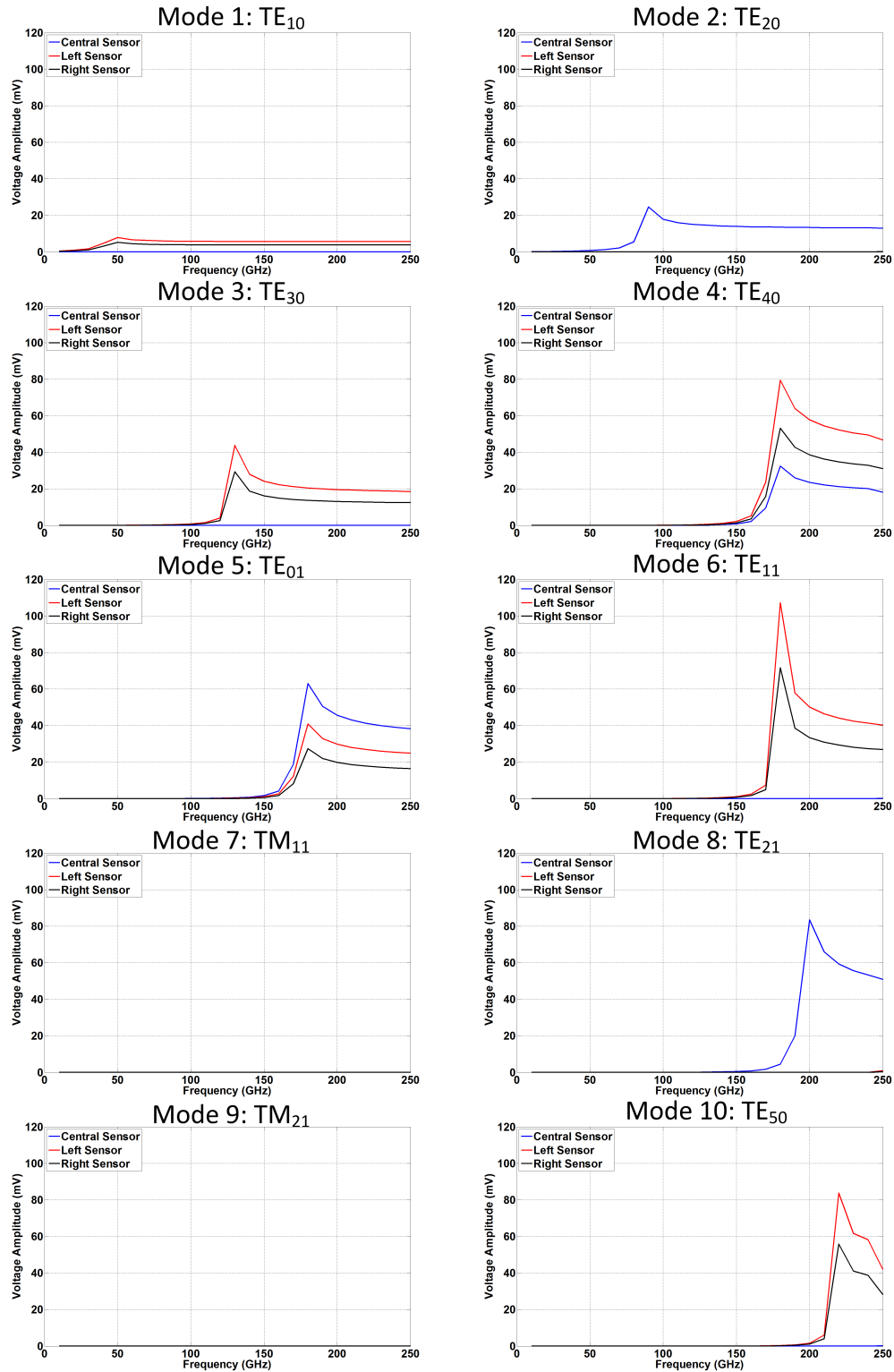


Figure 3.19: Outputs of the Y-oriented slots versus frequency for each excited mode.

component in the TM modes. Therefore, whatever signal is captured by the sensors is only extracted from the excited TE modes.

Another type of PFRS antenna for this example is an X-oriented small linear slot antenna, shown in the Figure 3.20. Again, the magnitude of the voltages picked up by each sensor versus the frequency of excitation for different modes is plotted on the same scale to simplify the comparison and is shown in Figure 3.21. In a similar way to Y-oriented slot antennas, comparison between the outputs of the sensors and the field pattern reveals that X-oriented slot antennas only pick up H_x component of the propagating wave. For example, for TE_{40} mode all three sensors are located exactly where the H_x is zero. So they do not pick up any signal. Also, for TE_{01} mode, $|H_x|$ is equal to zero on x -axis and thus the outputs of all three sensors are zero for this mode. The sensor outputs for other modes can be justified in the same manner as well.

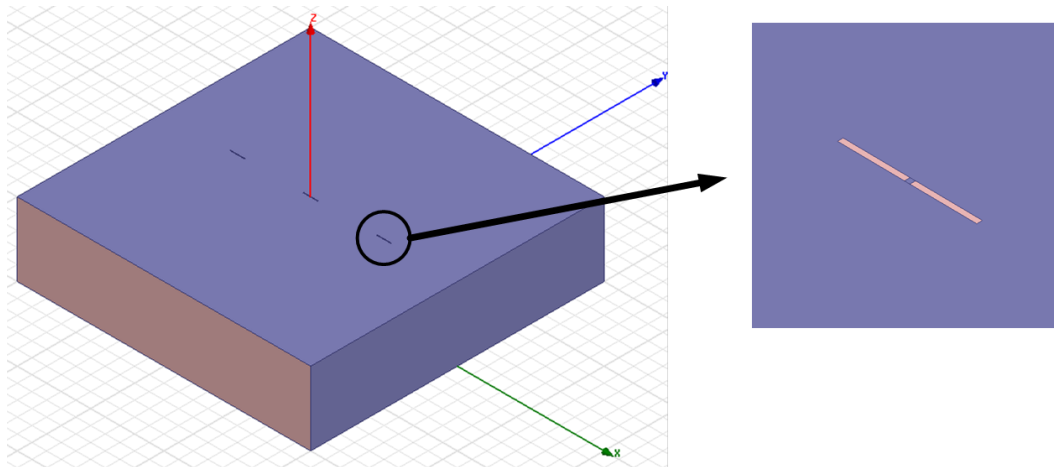


Figure 3.20: X-oriented linear-slot antenna used as PFRS.

A dipole antenna is another type of PFRS antenna that may be used to distinguish between different modes. For the case of our rectangular waveguide, since the tangential components of electric field on the top metallic surface are zero, the dipole is implemented slightly lower than the top surface ($10 \mu\text{m}$ below the top surface), where E_x and E_y can have nonzero values. Profiles of the \mathbf{E} - and \mathbf{H} -field components $10 \mu\text{m}$ below the top metal surface are plotted for each mode and are shown in Figure 3.22.

To implement the sensor, a small section on the top metal close to the dipole is cut

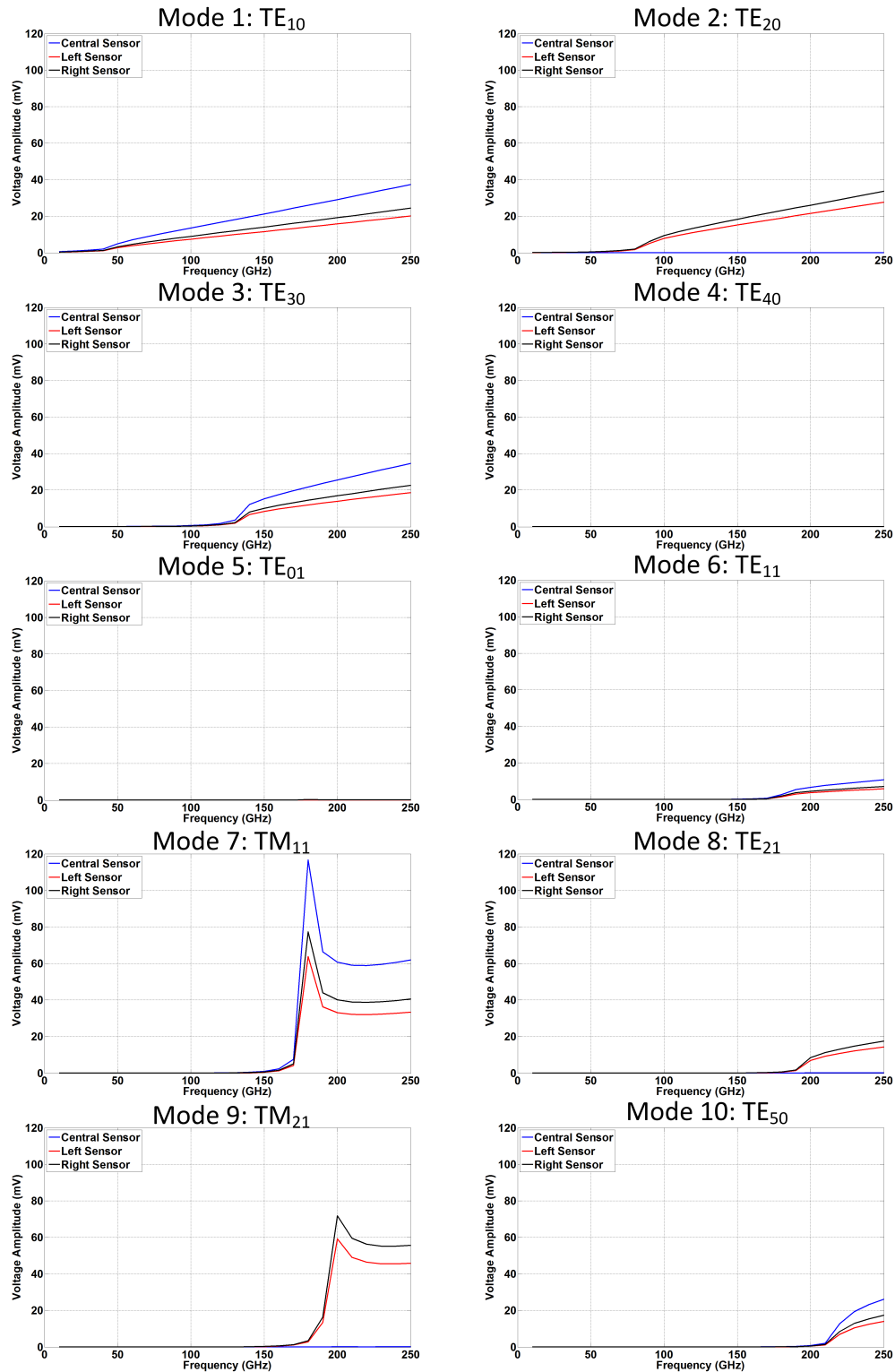


Figure 3.21: Outputs of the X-oriented slots versus frequency for each excited mode.

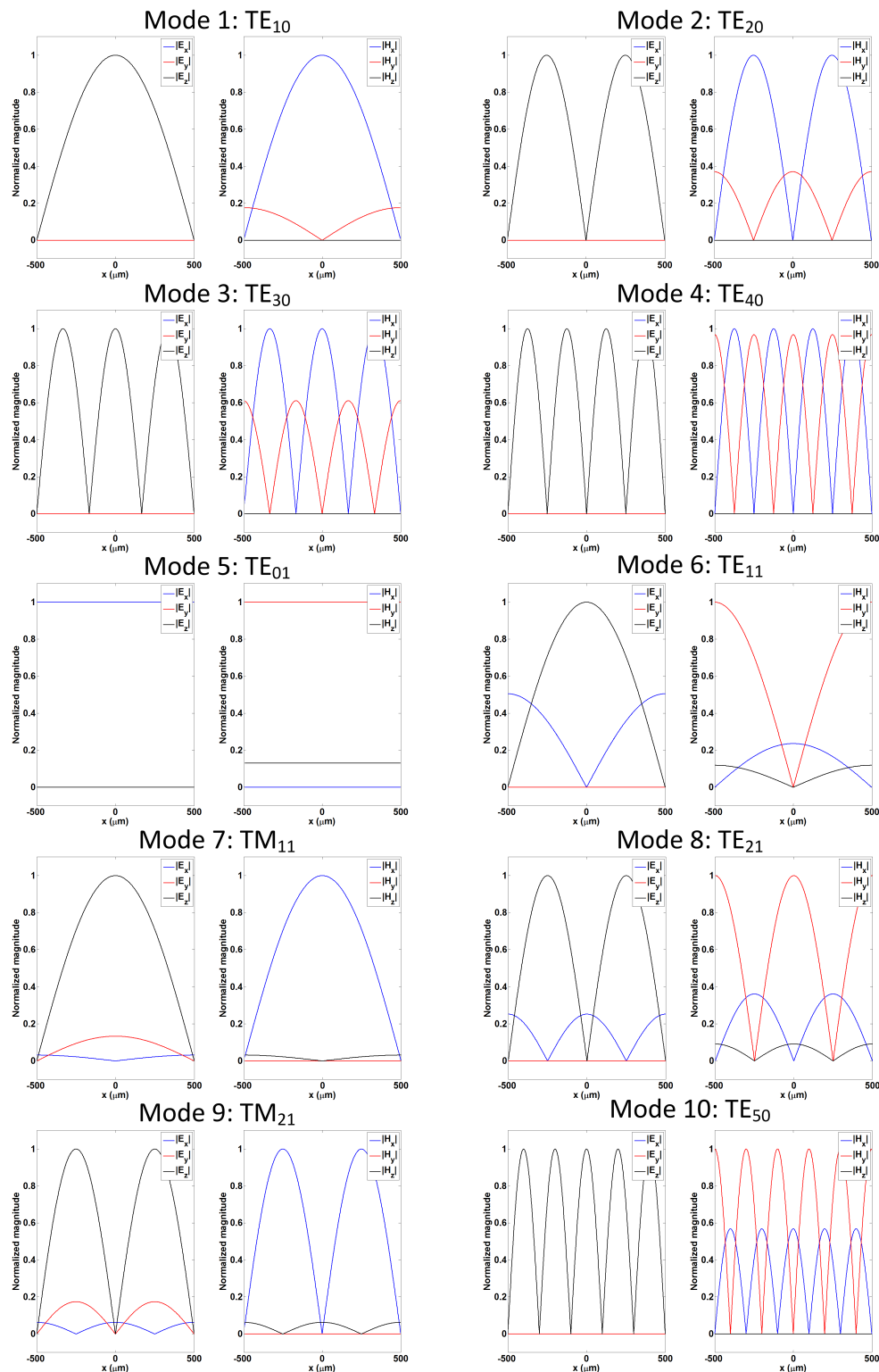


Figure 3.22: Field components of the first ten propagating waveguide modes across a line $10 \mu\text{m}$ below the top metal surface.

to improve the sensor's sensitivity by pushing the mirror current path farther. Figure 3.23 shows the structure of such sensor oriented along y -axis. The signals picked up by each sensor are also plotted in Figure 3.24. The same scale is used for all plots.

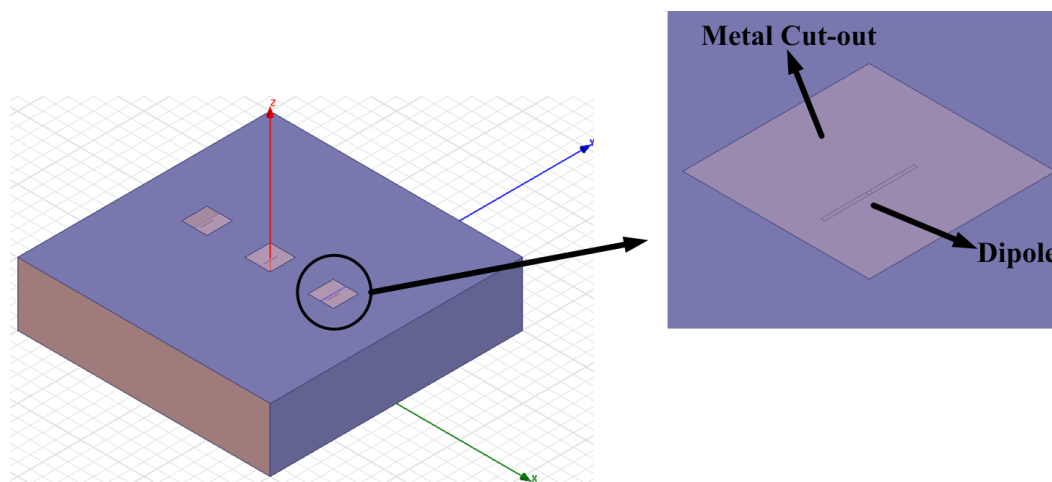


Figure 3.23: Y-oriented dipole antenna used as PFRS.

A comparison between the field patterns and the magnitude of the signals picked up by these sensors in each excitation mode reveals that this type of PFRS antenna picks up the E_y component of the electromagnetic waves. Since E_y is always zero for TE modes and it can be nonzero only for TM modes, this type of sensor acts as a TM mode sensor in this example. As a result we can see that for all the TE modes the strength of the signals is negligible compared to TM modes. For TM_{21} , the central sensor does not pick up any signal since $E_y = 0$ at the center while the left and right sensors pick up almost equally large signals since $|E_y|$ is maximum at these two points. This conclusion can be also verified by looking at the outputs and field patterns for TM_{11} mode. Thus, the information in sensor outputs is only due to the excited TM modes. In a similar way, an X-oriented dipole antenna can be implemented in the same manner to provide information on E_x component. This case is not discussed here since it exactly follows the same procedure and reasoning.

The TE and TM sensors for the rectangular waveguide can be combined into one TE/TM sensor that has two output ports (one for TE modes and one for TM modes) and detects both modes at the same time and the same location. This is made possible by reducing the cutout region of the top metal into a small linear slot located right on top of the dipole. Figure 3.25 shows such a structure. The slot and the dipole are both terminated with 50Ω loads. The Y-oriented slot on top detects the TE modes

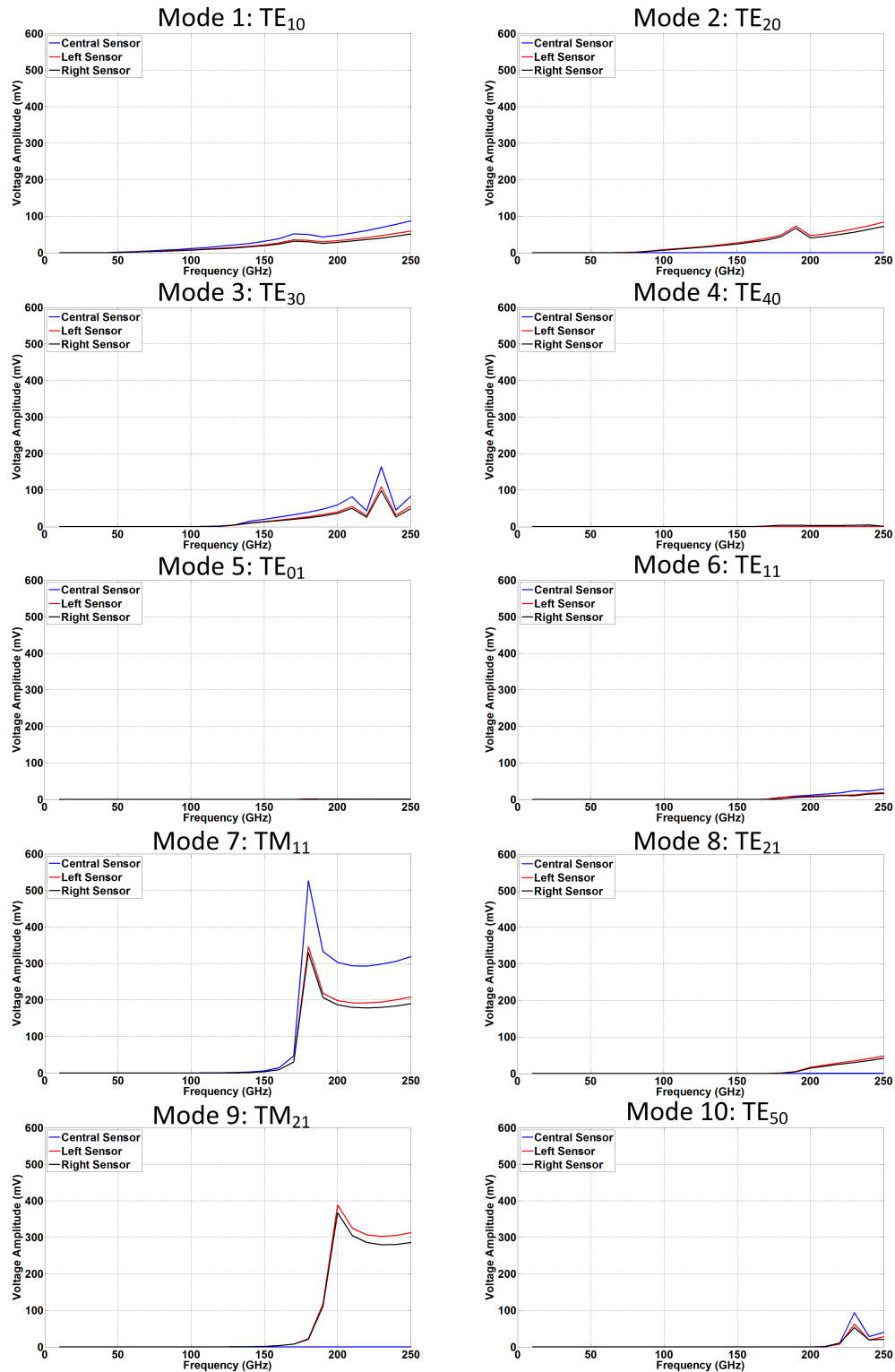


Figure 3.24: Outputs of the Y-oriented dipoles versus frequency for each excited mode.

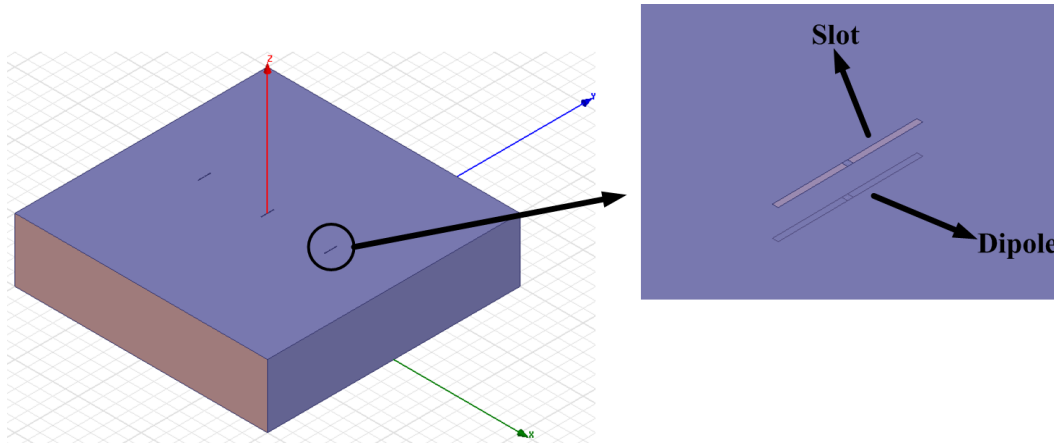


Figure 3.25: Combined TE/TM sensor for the waveguide.

while the Y-oriented dipole, which is placed $10 \mu\text{m}$ lower, detects the TM modes. The magnitude of the voltages picked up by the TE/TM sensors versus excitation frequency is plotted in Figure 3.26 using the same scale for all modes. Solid lines show the outputs of dipoles (TM outputs) while the dashed lines correspond to the slots (TE outputs). The outputs of each sensor unit are plotted with the same color. For each sensor the solid line is the output corresponding to the TM modes and the dashed line is the output corresponding to the TE modes. For example, for TM_{11} and TM_{21} modes all slot outputs (TE outputs - dashed lines) are zero while dipole outputs (TM outputs - solid lines) indicate the strength of the E_y component of these TM modes. Similarly, all the TM outputs are zero when only TE modes are excited and H_y component is picked up by the slot antennas. For both cases the relative magnitude of the outputs follows the magnitude of the corresponding field component (H_y for the slots and E_y for the dipoles).

The TE and TM sensors discussed above, can also be implemented on a chip to identify the excited substrate modes. Figure 3.27(a) shows an ideal Hertzian dipole excitation along the x -axis on a chip where four TE sensors are implemented on the positive and negative sides of X and Y axes, and in Figure 3.27(b), four TM sensors are placed in the same way, also with a Hertzian dipole excitation located at the center along the x -axis. From theory, we know when a Hertzian dipole excitation exists on the interface between air and the substrate material, surface waves start to propagate in different directions. In X_+ and X_- directions only TE modes propagate, while in Y_+ and Y_- directions only TM modes propagate. So in our experiment we expect V_{X_+} and V_{X_-} to be much larger than V_{Y_+} and V_{Y_-} for TE sensors, while V_{Y_+} and V_{Y_-} should be much larger than V_{X_+} and V_{X_-} for TM sensors.

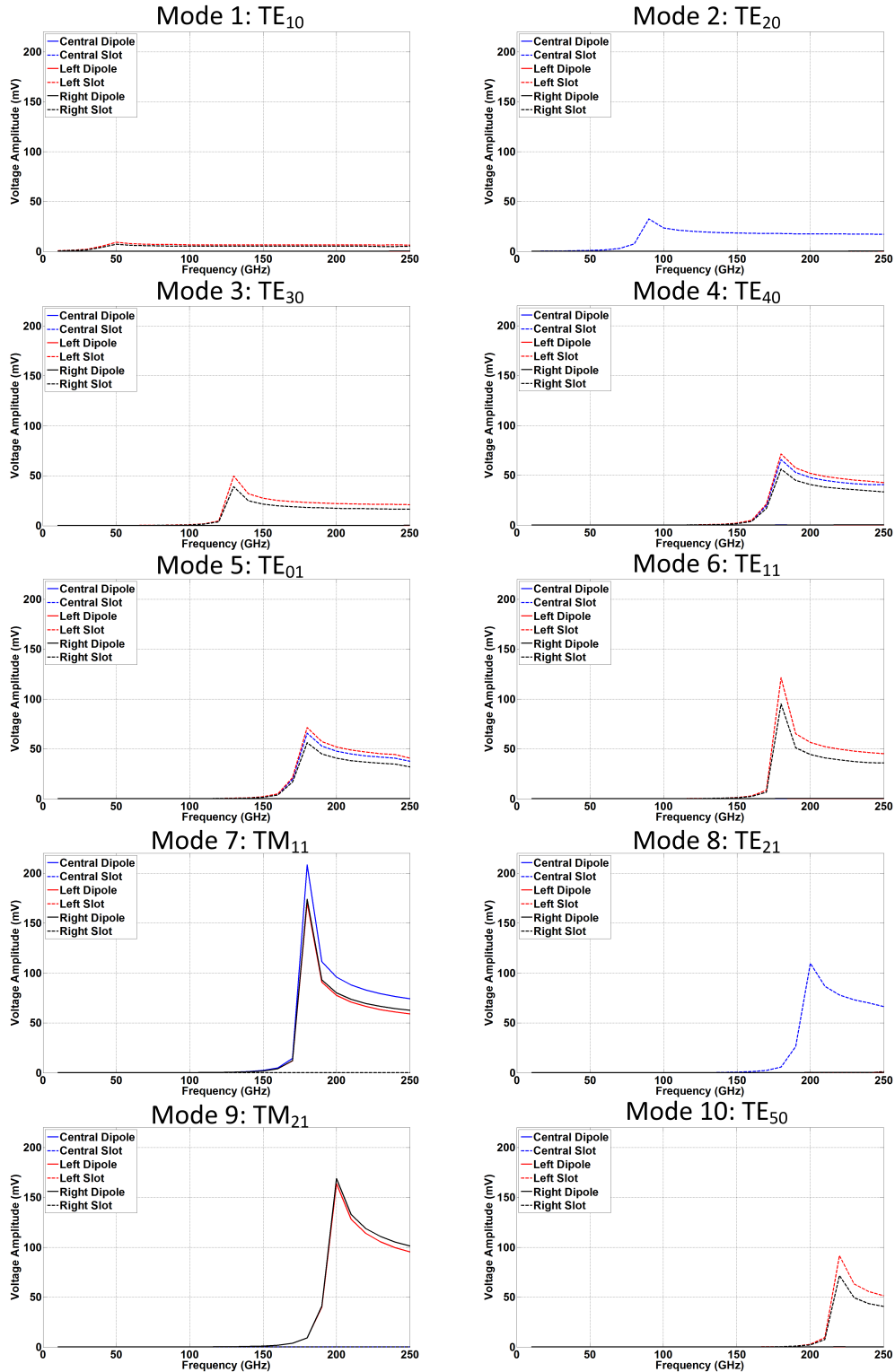


Figure 3.26: Outputs of the TE/TM sensors versus frequency for each excited mode.

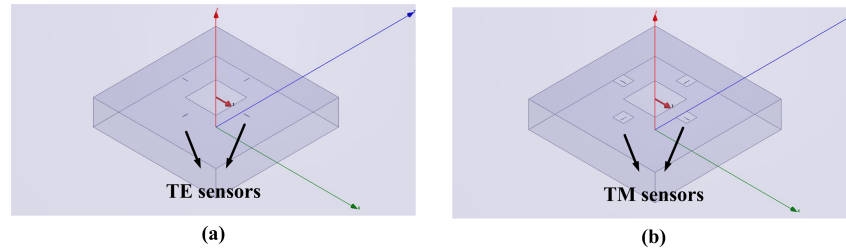


Figure 3.27: Hertzian dipole excitation on a chip with (a) TE sensors and (b) TM sensors.

Figure 3.28 shows the outputs of TE and TM sensors versus the frequency of excitation. We can see that for TE sensors V_{Y+} and V_{Y-} are almost zero while V_{X+} and V_{X-} take almost equal non-zero values. On the other hand, for TM sensors V_{X+} and V_{X-} are almost zero while V_{Y+} and V_{Y-} take almost equal non-zero values. Thus, the outputs of the sensors match the theory. These last simulations also show that depending on the nature of the integrated radiating antennas, a wise choice for PFRS antenna type and strategic placement of them can provide read-outs with valuable information. This information can be analyzed through various methods to provide capabilities such as self-correction, self-calibration, and self-monitoring of the performance of an integrated radiator.

We can make an important observation from the waveguide simulations above. That is, in the extreme hypothetical scenario where the sensing antennas are infinitesimally small, they can serve as probes for specific field components' distributions across the plane they are implemented on. This means, taken to their limit, they can provide us with the excited field distribution over the entire plane, which can directly be used for calculation of far-field radiated electromagnetic waves.

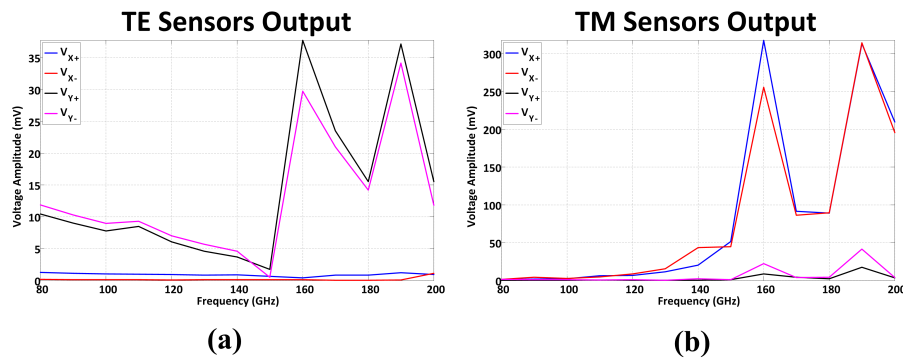


Figure 3.28: (a) Outputs of the TE sensors and (b) outputs of the TM sensors for Hertzian dipole excitation.

3.5 PFRS Data Processing

Once PFRS antennas are properly implemented on a substrate to pick-up meaningful signals from the surface waves, their captured data needs to be analyzed for prediction of radiation properties or monitoring of the radiator performance. The specific radiation or performance properties of the system that are desired to be extracted from PFRS data are the major factors that determine what data processing scheme should be used. Deviation of a drive signal from nominal value, polarization of the far-field radiated electric field, the direction of the radiated beam in an array, or the entire radiation pattern of an integrated radiator, each may need different processing schemes with different complexity. A simple data processing method may be sufficient to capture small deviations from the nominal operation of the system while a more complex scheme should be used if the entire far-field radiation pattern is to be predicted by the PFRS. Another parameter that determines the data processing approach is the affordable complexity of the detecting circuitry or measurement equipment that provide PFRS read-outs for processing. Depending on the frequency of radiation and the operation environment of the radiator, it may be possible to directly hook up sensors outputs to a measurement device to measure the amplitudes and phases of PFRS signals. For some cases, it may be easier to integrate the detector circuits that are capable of both amplitude and phase detection on the same substrate as PFRS antennas. Coherent detection of phase and amplitude of PFRS signals often requires complex circuitry. In such cases, it might be easier to implement detectors that solely detect the amplitudes and use an amplitude-based data processing scheme.

Therefore, considering all these parameters, the data from sensors may be processed at different levels of complexity. One can simply use the structural symmetry of an electromagnetic structure and strategic placement of the sensing antennas to capture any performance deviation from the nominal design, or use simulation-based pre-defined transformations to directly convert sensors' data to the desired far-field radiation pattern. Also, various statistical methods can be used to extract existing correlation between PFRS read-outs and the desired radiation parameters.

In this section, we discuss a variety of methods to interpret the data and capture various far-field radiation and performance properties through different examples. However, it should be noted that the use of PFRS antennas and their data is not limited to the presented designs and methods.

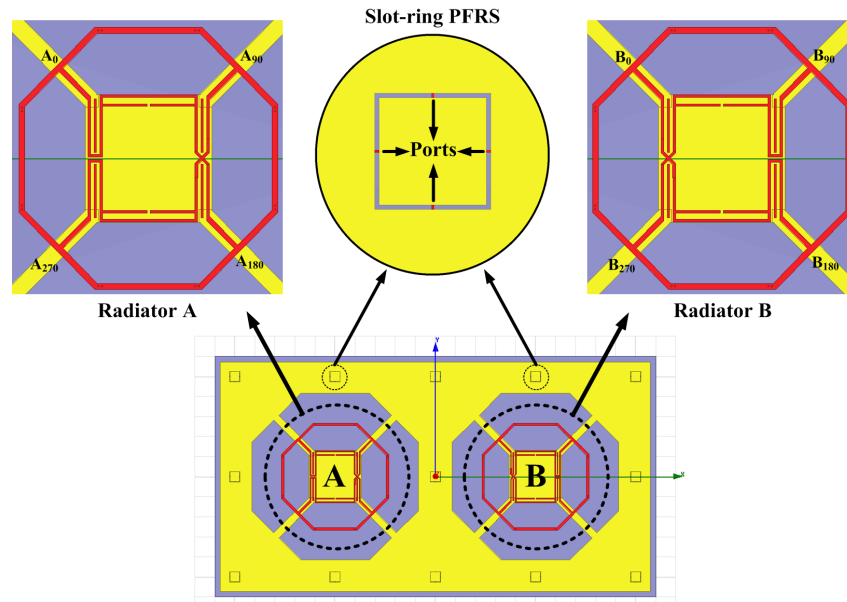


Figure 3.29: A 2×1 multi-port driven radiator array with 13 slot-ring PFRS antennas.

3.5.1 Symmetry-based Methods

The electromagnetic structure of most of integrated radiators, especially integrated antenna arrays, features some sort of geometrical symmetry. This is mainly because, intuitively, a symmetric structure allows the radiation properties of the transmitting antennas to be the same in all directions. Also, symmetrical drive circuitry and balanced feed lines can be easily used to drive such antennas. Depending on the operation principle of the individual antennas and their specific application, the existing symmetry might be of different types, such as reflectional symmetry with respect to a plane, rotational symmetry around an axis, etc. The existence of such structural symmetries in integrated antennas provides a great opportunity for PFRS implementation. The placement of PFRS antennas could be chosen wisely to use the existing symmetries in the electromagnetic structure such that the sensors could easily detect any deviations which disrupt the symmetric operation and nominal performance of the integrated radiator. In this section, we investigate a few different exemplary designs that benefit structural symmetry and strategic placement of PFRS antennas. We explore what type of information the sensors could capture and how this information could be used.

One implementation of proximal-field sensors on a 2×1 multi-port driven radiator array with slot-ring PFRS antennas is shown in Figure 3.29. This design includes a 2×1 array of loop antennas radiating at 120 GHz with a ground plane surrounding

the loops (shown in yellow) to provide the path for the return current. Due to the presence of such ground plane, slot antennas can be easily implemented as PFRS by chopping the ground plane at desired locations. In this example, 13 square-shaped slot-ring antennas are placed symmetrically around the loops and act as PFRS. Each of these sensing antennas is loaded with four detection circuits at the four ports on the four sides of the slot-ring antenna. Each radiator element is driven at four ports ($A_0, A_{90}, A_{180}, A_{270}$ for Radiator A , and $B_0, B_{90}, B_{180}, B_{270}$ for Radiator B on Figure 3.29) using a quadrature oscillator. The antenna elements are designed to radiate circular polarization. The optimal broadside radiation happens when both of them are driven in-phase with the driving signals of adjacent ports being 90° apart, as shown in Figure 3.30. Electromagnetic simulations by Ansoft HFSS show a maximum gain of 3.4 dB and directivity of 10.8 dB when both radiators are driven in-phase. The simulated patterns for gain and directivity are shown in Figure 3.31.

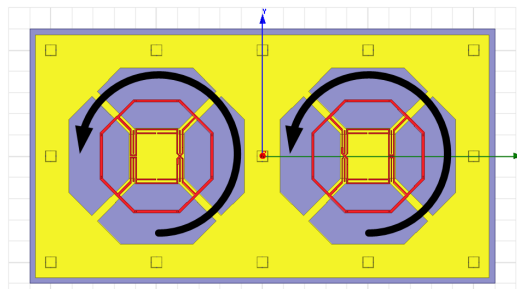


Figure 3.30: In-phase drive of the transmitting antennas for optimum broadside radiation.

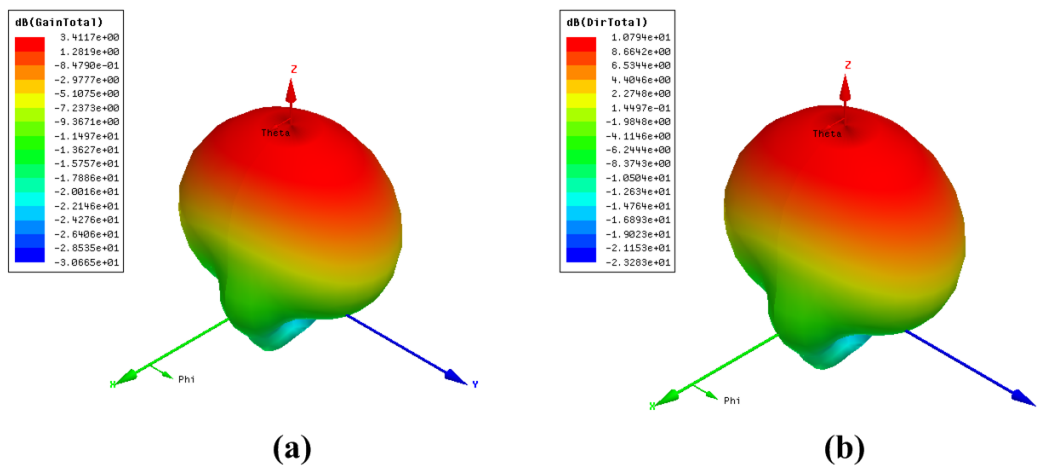


Figure 3.31: Simulated patterns of (a) gain and (b) directivity for optimum broadside radiation.

We will use the following notation for the phase of the signals (ϕ) driving each port to include possible phase errors of the driving signals: $\phi_{A_0} = p_0 + \Phi_{QA}/2$, $\phi_{A_{90}} = p_{90} - \Phi_{QA}/2$, $\phi_{A_{180}} = p_{180} + \Phi_{QA}/2$, and $\phi_{A_{270}} = p_{270} - \Phi_{QA}/2$ for Radiator A, and $\phi_{B_0} = p_0 + \Phi_{QB}/2$, $\phi_{B_{90}} = p_{90} - \Phi_{QB}/2$, $\phi_{B_{180}} = p_{180} + \Phi_{QB}/2$, and $\phi_{B_{270}} = p_{270} - \Phi_{QB}/2$ for Radiator B. In this notation, Φ_{QA} and Φ_{QB} correspond to the quadrature phase error of each radiator's quadrature signals and θ shows the relative phase error between the two radiators. When the operation of system is correct there would be no error and thus $\theta = \Phi_{QA} = \Phi_{QB} = 0^\circ$. Each radiator can be driven either clockwise (CW) or counter-clockwise (CCW). For CCW operation $p_0 = 0^\circ$, $p_{90} = 90^\circ$, $p_{180} = 180^\circ$, $p_{270} = 270^\circ$ and for CW operation $p_0 = 0^\circ$, $p_{90} = -90^\circ$, $p_{180} = -180^\circ$, $p_{270} = -270^\circ$. The optimum broadside radiation happens when both radiators are driven in the same direction and the simulated gain patterns in Figure 3.32 show that if there is a relative phase error between the two radiators while the quadrature errors of both of them are still zero, then the array gain will drop by ~ 0.4 dB.

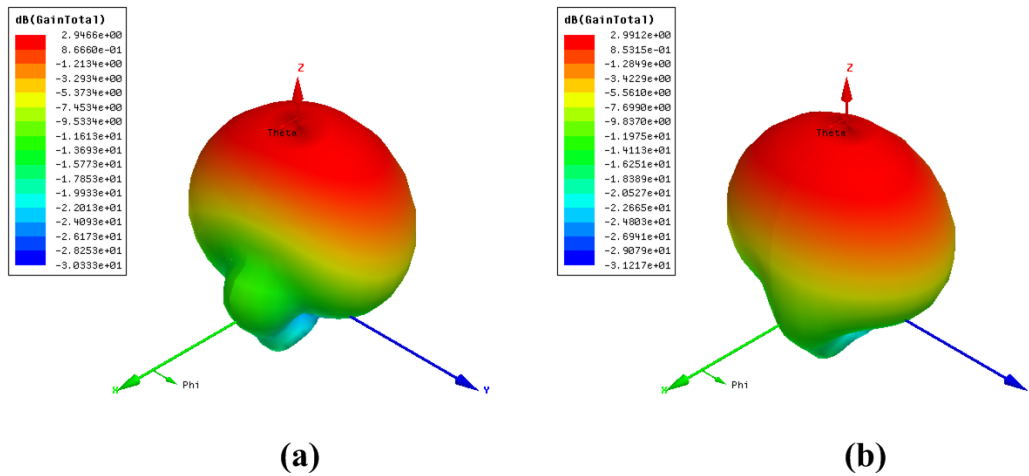


Figure 3.32: Simulated gain of the 2×1 array with relative phase error of (a) $\theta = +40^\circ$ and (b) $\theta = -40^\circ$ while $\Phi_{QA} = \Phi_{QB} = 0^\circ$.

This deviation from the optimal performance of the radiator can be detected from the amplitude of the signals that are picked up by each PFRS antenna and be used to compensate for the errors and set the system back to the optimum configuration for radiation. The plots of Figure 3.33 show the amplitude of the 120 GHz signal which is picked up at each port of each PFRS antenna versus the relative phase difference, θ , between the two radiating antennas when they are both driven counter-clockwise. The locations of the plots correspond to the locations of the sensors on the chip.

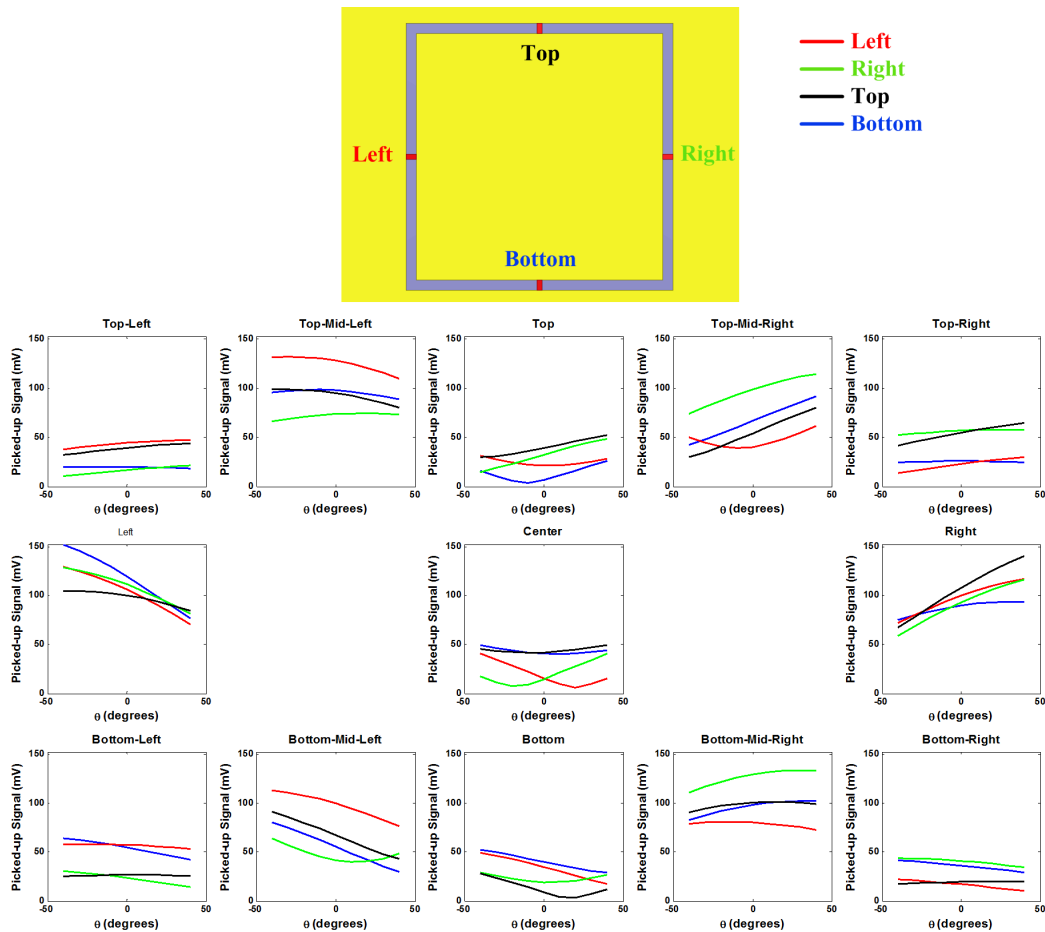


Figure 3.33: Outputs of the PFRS antennas versus the relative phase error, θ , and the color codes for the outputs of each PFRS.

Each plot corresponds to one PFRS and for each sensor's output voltage the red curve shows the signal picked up at the port on the left, the green curve corresponds to the signal across the port on the right, the black curve relates to the port on the top, and the blue curve is that of the port on the bottom.

Looking at these plots one can make several observations. First, there are two pairs of signals picked up by the central PFRS, which follow symmetric patterns as θ varies (Red, Green and Black, Blue). This symmetric behavior can be used to detect the relative phase error, θ , by comparing the signals in each pair. To better demonstrate this, Figure 3.34 shows the difference between the signals at the left and right ports, i.e. Red, Green pair versus θ . The one-to-one nature of this curve shows how it can be used to capture the phase error between the two radiating antennas.

Another observation is the symmetry of all the sensing ports with respect to the

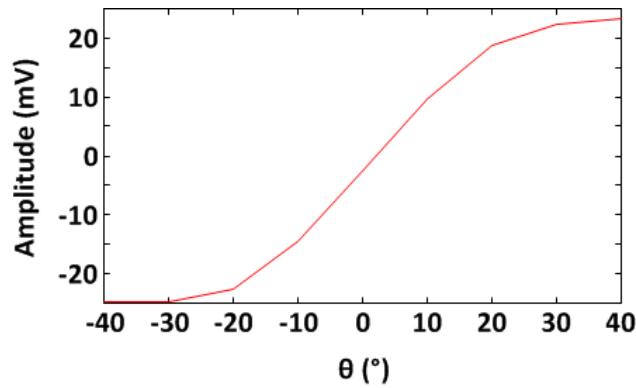


Figure 3.34: Difference between the signals at the left and right ports of the central PFRS antenna.

center of the chip as θ varies in either direction, i.e. for each port of each PFRS there is one other port from another PFRS which is located symmetrically on the other side of the chip with respect to the center and picks up the same signal. One pair of symmetrically located ports is shown in Figure 3.35. For this pair, as θ increases towards positive values the voltage at the top port of the top-right sensor (black curve) is exactly same as the voltage at the bottom port of the bottom-left sensor (blue curve) when θ decreases towards negative values. This happens because of the circular symmetry of the EM structure around the center point and the fact that these two ports are located symmetrically with respect to the center of the chip. This is true for every single port on all the sensors. This symmetric behavior of the signals due to the symmetrically located ports is another tool that can be used to sense the degradation in the performance of the chip.

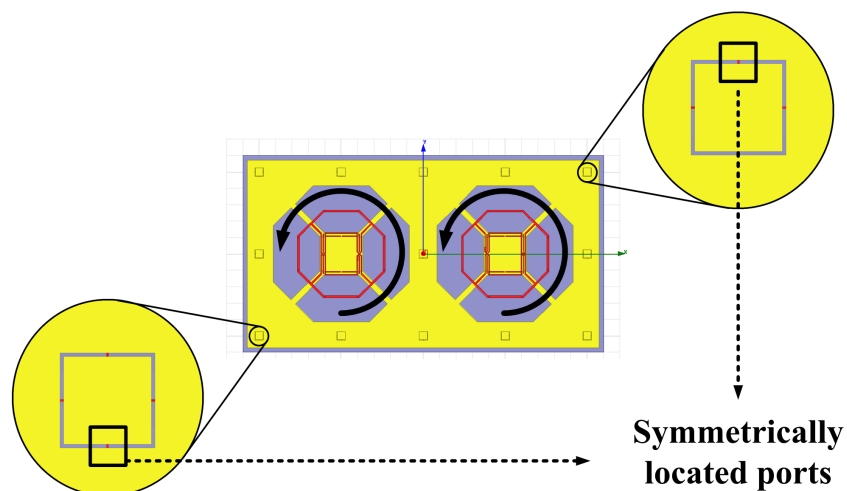


Figure 3.35: Circular symmetry of the electromagnetic structure.

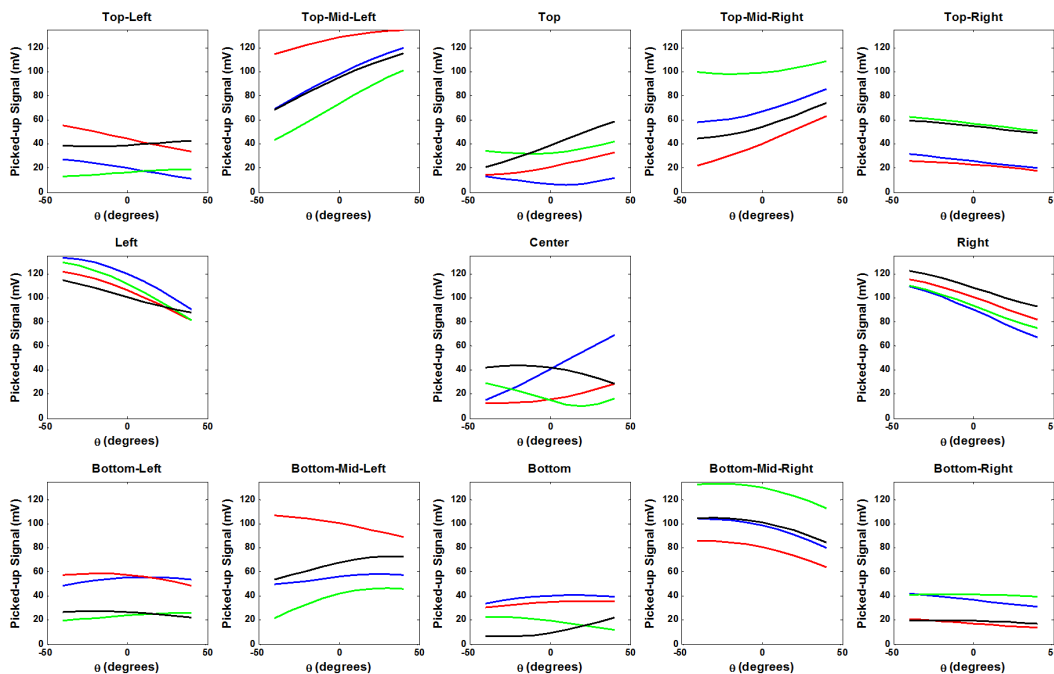


Figure 3.36: Outputs of the PFRS antennas versus quadrature phase error Φ_{QA} in Radiator A and the color codes for the outputs of each PFRS.

Next, we consider the effect of quadrature phase error when the radiators are driven counter-clockwise with an error Φ_{QA} in the quadrature signals driving radiator A. The PFRS amplitude read-outs for this situation are demonstrated in Figure 3.36. This type of deviation from normal operation can also be detected through the PFRS antennas. For instance, if we look at the signals picked up by the left and right sensors in Figure 3.36 and compare them with the same signals for the case of relative phase error from Figure 3.33, we will notice a difference in their trends. When there is a relative phase error, the voltage amplitudes on the ports of the left and right sensors vary in two different directions, i.e. on one sensor the amplitudes of signals increase while they get smaller than the nominal readings on the other sensor. But the trend is different when quadrature phase error exists instead of relative phase error. In this case we can see that all the signals follow the same trend on both sensors.

What we have discussed so far was mostly qualitative, aiming at monitoring the trends of PFRS read-outs as the performance changes over time through variation of certain parameters, and readjusting the control knobs of the drive circuitry in the reverse direction towards the nominal operation. Although these qualitative methods provide valuable insight to design algorithmic control mechanisms for the

integrated radiators, we are more interested in quantitative methods that can quantify the deviations from nominal operation.

Figure 3.37 shows another design example for this purpose. It consists of a 2×2 array of the same four-port radiating antennas as the previous example, integrated with nine similar slot-ring PFRS antennas, each of which has four ports for signal detection on its four sides, resulting in a total number of 36 PFRS outputs. Again, nominal operation of the radiator array requires in phase operation of all four radiating elements and each antenna is driven by quadrature signals such that the overall radiated electromagnetic waves have circular polarization.

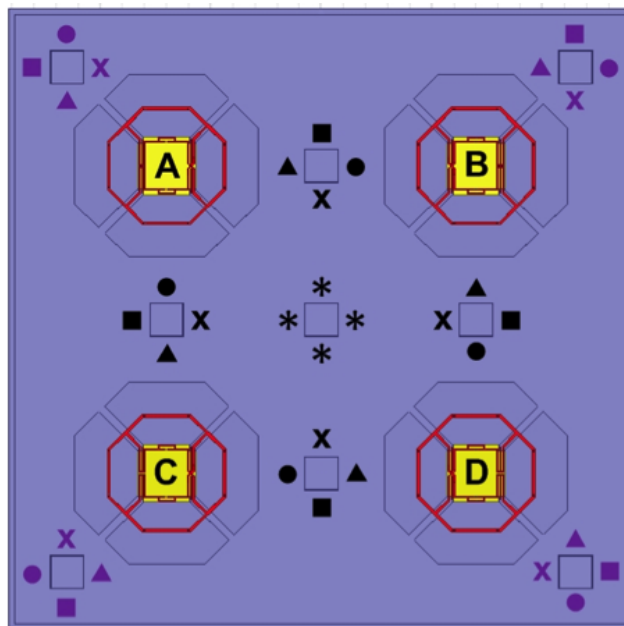


Figure 3.37: A 2×2 multi-port driven integrated radiator array with nine slot-ring multi-port PFRS antennas. Due to circular symmetry, the total 36 PFRS outputs can be divided into nine sets where all four output ports in each set are expected to have the exact same signal.

Due to the circular symmetry of the radiating structure, the 36 outputs of the PFRS antennas can be divided into nine sets. Each set includes four sensor outputs from different antennas that should ideally pick up signals with the exact same strength under correct operation of the radiating array. Output ports of each set are marked by a different symbol and color combination on Figure 3.37.

If there is any deviation from the optimum settings, the sensor outputs in each set would no longer be equal to each other and would deviate from their expected value in different ways. This deviation from the optimal operation setting could be

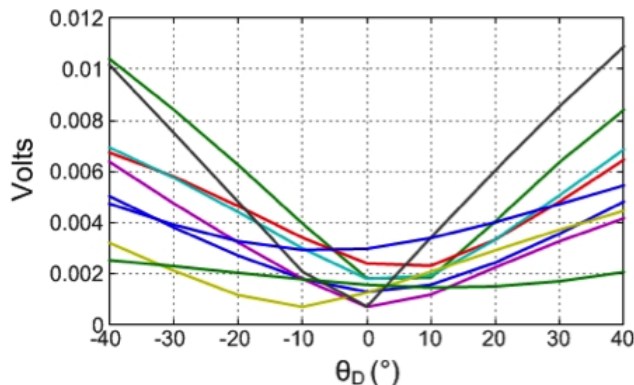


Figure 3.38: Sensitivity of the standard deviations of all nine sets to the relative phase error θ_D .

quantified and used in many different ways. One possible method is to consider the standard deviation in each set of PFRS outputs. When there are any errors and the radiator's performance is not optimal, the increase in the standard deviation of each of the nine sets reveals the non-optimal performance and its value quantifies how off from the nominal setting the system is operating. Figure 3.38 shows how the standard deviations of each set varies when one of the radiating antennas (D) is no longer operating in phase with other three elements and suffers from a phase error, θ_D . One can monitor all nine values of standard deviations for all nine sets individually, to detect different types of errors separately or simply combine all nine values together (e.g. sum of all standard deviations) to monitor the overall performance deviation from the optimal settings based on a single metric. Shown in Figure 3.39, we can see such a combined metric and its relationship with the strength of the radiated signal in broadside direction base on the captured signals by a receiver antenna placed in the same direction on top of the integrated radiator. As a result, the standard deviation of each set reveals the deviation from optimal operation. Using these metrics, the best radiation performance happens when the standard deviations of all nine sets and thus their sum are minimized.

The last example we investigate in this section is to demonstrate how we can use PFRS and structural symmetry to extract information about the polarization of the far-field radiated electric field in a system that is capable of radiating various polarizations. Figure 3.40 shows a 2×2 array of four-port antennas very similar to the previous examples, with minor modifications, accompanied with a variety of PFRS antennas. We will discuss the differences and capabilities of these four-port transmitting antennas in details later in section 5.3.4. A major factor that can make

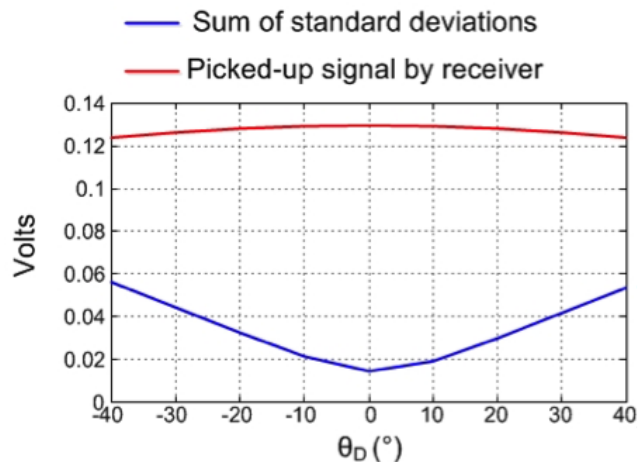


Figure 3.39: Sum of the standard deviations for all nine sets as well as the relative strength of the radiated signal as θ_D varies.

a significant difference in the radiation performance of such antennas is the relative phases of the four signals driving the antenna. As we will see in Chapter 5, if instead of driving the four ports of each antenna with quadrature signals, they are driven with two pairs of differential signals, $V_{diff,X}$ and $V_{diff,Y}$, whose phase difference, $\Delta\psi$, can be adjusted, it would directly control the polarization of the radiated electric field.

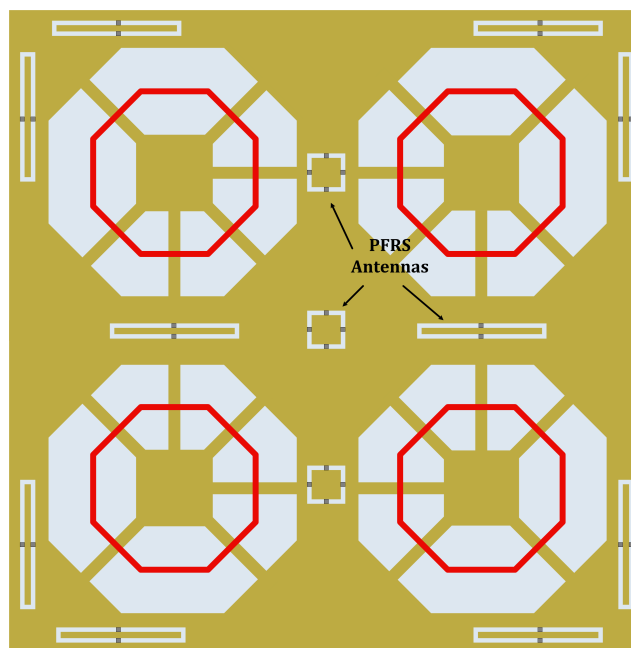


Figure 3.40: A 2×2 multi-port driven integrated radiator array with 13 PFRS antennas.

No matter what value $\Delta\psi$ takes, as long as it is the same for all four transmitting antennas and all antennas are synchronized to operate with the same phase reference, the peak of the radiated beam of the entire radiator is still directed at broadside, with a polarization that is determined by $\Delta\psi$. The resulting linear polarization of the radiated field for the two cases of $\Delta\psi = 0^\circ$ and $\Delta\psi = 180^\circ$ are shown in Figure 3.41. For values between these two limits, elliptical polarizations aligned with one of these two orientations (depending on the exact value of $\Delta\psi$) are created. Similarly, if $\Delta\psi$ is the same for all for antennas but their phase references are varied with respect to each other, the radiated beam could be steered in other directions within the 2-D steering range of the array. However, still the polarization of the radiated electric field is solely determined by $\Delta\psi$ in a similar way.

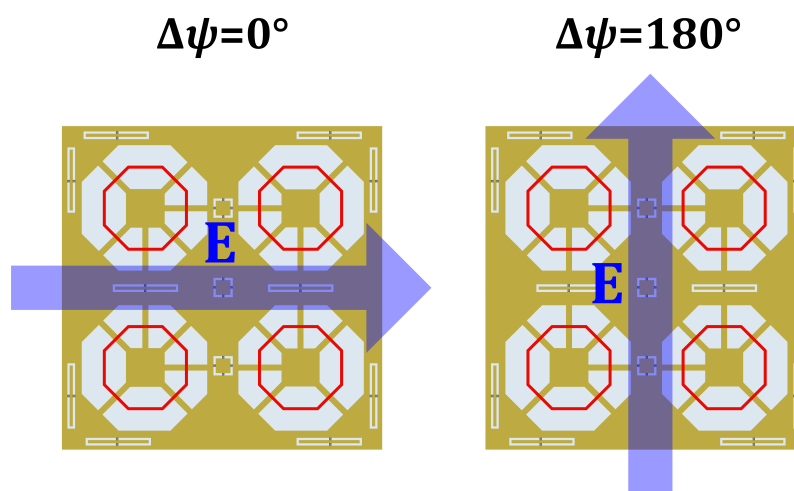


Figure 3.41: Switching between horizontal and vertical polarization of the radiated electric field for $\Delta\psi = 0^\circ$ and $\Delta\psi = 180^\circ$, respectively.

What we are interested in capturing with PFRS read-outs in this example is the polarization of the radiated electric field using the outputs of the four-port PFRS located at the center. Figure 3.42 shows how the amplitude of four outputs of the central PFRS change as $\Delta\psi$ is varied from 0° to 360° to control the polarization, while the phase reference for all four antennas is the same. We can observe that when the radiated polarization is horizontal ($\Delta\psi = 180^\circ$), PFRS outputs are minimized, while they are maximized for vertical polarization ($\Delta\psi = 0^\circ$). Moreover, starting from ideal horizontal polarization, the read-outs monotonically increase when the polarization gets closer to vertical polarization from either direction. This means the amplitude read-outs from this PFRS can be used in an algorithm to monitor the radiated polarization.

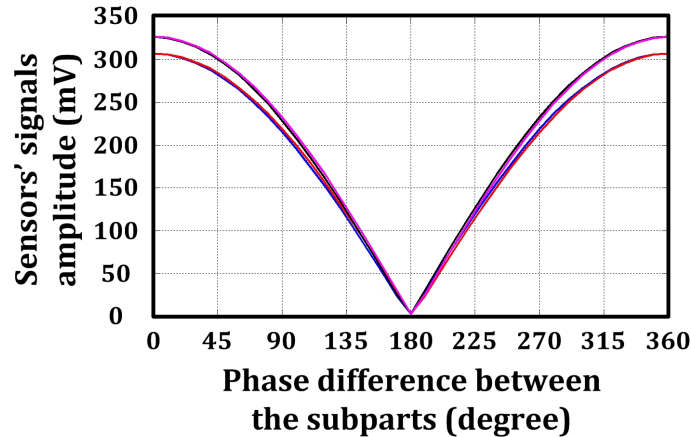


Figure 3.42: Amplitude read-outs of the slot-ring PFRS antenna located at the center versus $\Delta\psi$ for all four radiating antennas. All radiating antennas are driven in phase.

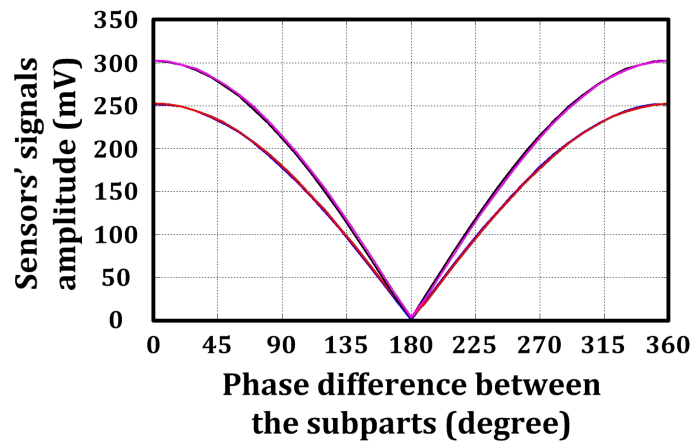


Figure 3.43: Amplitude read-outs of the slot-ring PFRS antenna located at the center versus $\Delta\psi$ for all four radiating antennas, with relative phase difference between the right and left radiating antennas to steer the beam.

This is also true when the antenna elements are phased with respect to each other to steer the beam. Shown in Figure 3.43 are the same PFRS outputs for such a scenario when a phase difference is applied between the phase references of the transmitting antennas on the left with respect to the transmitting antennas on the right. The normalized gain patterns in the two orthogonal planes of $\phi = 0^\circ$ and $\phi = 90^\circ$ for both cases of broadside and off-axis radiation when $\Delta\psi = 180^\circ$ (i.e., horizontal polarization) are shown in Figure 3.44.

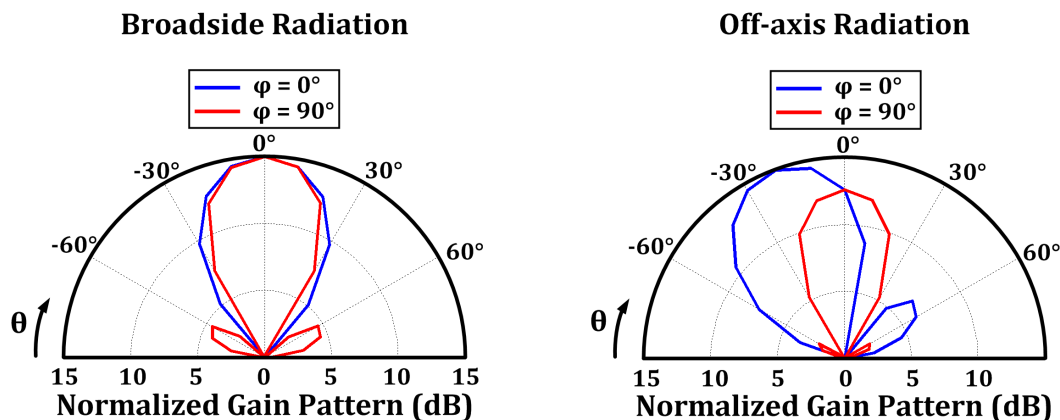


Figure 3.44: Simulated gain patterns of the 2×2 array when $\Delta\psi = 180^\circ$ for the two cases of broadside and off-axis radiation.

3.5.2 Statistical Methods

In the previous section, we saw how it was possible to take advantage of implementing a large number of PFRS antennas on the same substrate as an integrated radiator and compare their read-outs as a tool to monitor the performance of the radiator. The larger the number of sensors gets, the larger data set would be available to analyze, potentially containing significantly more information. This larger data set enables possible detection and decoupling of different factors' impact on the radiator's performance. However, as the number of PFRS outputs increases, it would become more difficult to extract all the meaningful information and trends by solely looking at the data and manually manipulating them. Here is where statistical methods can serve as great tools for data analysis.

One such method that can be used for our application is Principal Component Analysis (PCA) [50], [51]. PCA is a statistical method that performs an orthogonal transformation on a set of data points of possibly correlated variable and converts them into a set of values of linearly uncorrelated variables. This new set of variables are called principal components. PCA is defined such that the first principal component always has the largest possible variance, i.e. it demonstrates the largest variation in the data points. At each step, the variance for the next calculated principal components gets smaller and the calculated principal component is orthogonal to the preceding components. The number of principal components is less than to the number of original variables or number of data points, whichever is smaller. An example of PCA on a set of 2-D observation data points, and the principal components are shown in Figure 3.45.

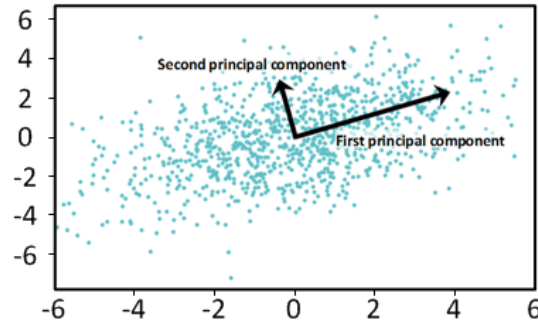


Figure 3.45: Example of Principal Component Analysis (PCA) on a 2-D data set.

Essentially, PCA represents a data set in a way that best demonstrates the variance in it. If we imagine a large dataset of N variables as points in an N -dimensional space, i.e., one variable per axis, PCA provides a projection of the data with fewer dimensions and the most information. This is performed by reducing the dimensionality of the data set to its first few principal components through the transformation.

In order to better understand how we can use PCA in PFRS data processing context, we need to first define the problem in a consistent way to PCA. We know that many different parameters can potentially affect the performance of a radiator. These parameters include the phases and amplitudes of the signals at the driving ports (which in turn depend on various biasing signals that control the drive circuitry), dimensions of the substrate, relative placement of the electromagnetic structure on the substrate, etc. Any changes in one of these parameters or any subset of them directly affects the far-field radiation properties of the system. If, hypothetically, for every single such parameter, there existed a function of PFRS read-outs which could provide a specific mapping between its output and that particular parameter when applied to the sensors outputs, such a function could have been used in determination of the state of that parameter and readjustment of that, if possible, to improve system's performance. This is what we wish to use PCA for.

First, we try to identify as many quantifiable parameters as we can, which could affect the performance. The nominal operation of the radiator happens when all the identified parameters take their nominal values, and as they vary the radiation performance deviates from the nominal operation. Also, let's assume there are N PFRS outputs available on the integrated radiator. This means each set of values for the parameters results in a set of N PFRS read-outs. One way to interpret the read-outs is to assume an N -dimensional space whose N orthogonal axes correspond to the N PFRS outputs. Each set of N read-outs corresponds to a point in this

space. Any combination of these parameters results in a different point in the N -dimensional space.

The parameters that affect the performance do not necessarily change one at a time. Often it is a combination of variations of a number of them, which results in a deviation of performance. However, through simulations and calibration measurements, we can investigate the effect of each parameter on the read-outs, assuming no other parameters have changed compared to their nominal values. A sweep of the parameter of interest (e.g. a biasing voltage, a phase control parameter, a physical length in the structure) over a range of possible values that it might take around the nominal value during the radiator's operation, provides a large set of data points in the N -dimensional space. However, not all sensor outputs are fully uncorrelated, which means that significant redundancy exists in the data set. This is why we can use PCA to analyze the data. PCA maps the data into its essential components in the multi-dimensional space to eliminate redundancy and reduce the dimensions of data set. In fact, for small variations around the nominal value which allow assumption of linearity, since only variation of one parameter is used to generate this data set we expect that the data points mostly vary in one dimension, defined by a linear combination of N PFRS read-outs, i.e. the first principal component calculated by running PCA on the data set. We can do the same for all the identified parameters, which could potentially introduce error to the performance, and use the resulting functions as a tool to monitor the performance and adjust it back to the optimum setting.

As a demonstration, again consider the same 2×2 array of four-port transmitting antennas with nine slot-ring PFRS antennas, where all the transmitting antennas are driven by quadrature signals to radiate circular polarization. If the transmitting antennas are not operating in phase, the relative phase errors, θ_A , θ_B , θ_C , and θ_D would exist between the antennas A , B , C , and D and an arbitrary phase reference, respectively. For simplicity, let's assume these four parameters are the only parameters that affect the radiation performance, and they can be adjusted through phase control units in the drive circuit to allow error correction. For proper operation we must have $\theta_A = \theta_B = \theta_C = \theta_D = 0^\circ$, and any deviation of each of them from the nominal zero value results in deviation of the radiation performance. We can use PCA and simulation to define the first principal component for each of these parameters. The resulting coefficients of this linear combination are then used to define a sensitivity function which shows the largest sensitivity to that particular

parameter among all possible linear combination of PFRS outputs. Figure 3.46(a) shows the sensitivity of the first four principal components to θ_D when both phase and amplitude information from PFRS read-outs is used for PCA, and Figure 3.46(b) shows the first four principal components when only amplitudes are used.

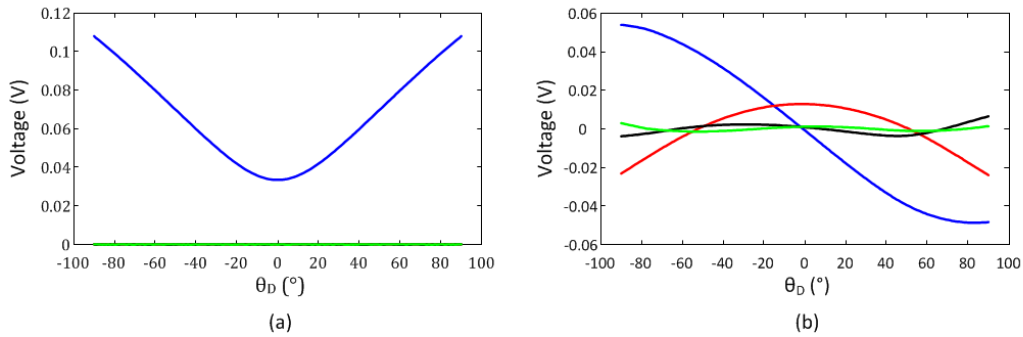


Figure 3.46: Magnitude of the principal components associated with θ_D calculated using (a) both phases and amplitudes and (b) only amplitudes of the PFRS read-outs.

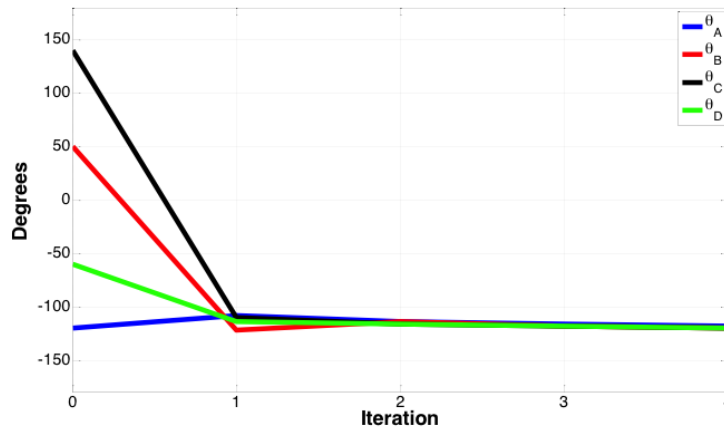


Figure 3.47: Application of an exemplary phase error correction algorithm to a random combination of relative phase errors θ_A , θ_B , θ_C , and θ_D , using the first principal component for each parameter.

These sensitivity functions can be used in a basic algorithm to calibrate the drive circuitry such that the phase errors caused by process variation, temperature variation, unexpected electromagnetic coupling to the adjacent objects, etc., are corrected. Figure 3.47 shows an exemplary application of such an algorithm using the first principal components calculated based on both amplitudes and phases of the sensors' read-outs to an arbitrary initial condition for θ_A , θ_B , θ_C , and θ_D . In each

iteration, the algorithm tries to reduce the calculated value for all four sensitivity functions associated with the phase errors and adjust the control knobs until they are all minimized. We can see that although the initial values for θ_i 's are very far from each other, the algorithm is still able to bring them all close to each other within a few iterations, which is a required condition for maximum broadside.

It should be noted that use of PCA or any other statistical analysis tool is not limited to this specific example. PCA can be used to characterize system's sensitivity to a combination of multiple parameters. A variety of other methods based on different fundamentals can also be used.

3.5.3 Simulation-based Methods

Similar to the design procedure for any system, design of electromagnetic structures such as transmission lines, inductors, antennas, etc., in high frequency systems requires performance validation through analysis and simulation before the structure could be fabricated and tested. The bases for analysis of electromagnetic problems are Maxwell equations. Due to the complex nature of these equations, use of numerical methods is essential to solve them in order to determine field profiles, radiation performance, and electromagnetic coupling between different parts of the structure in most practical cases. Many commercial electromagnetic solvers are available to address this issue. With the recent advancements in computational resources, it has been made possible to characterize extremely complex structures such as very large arrays of antennas with hundreds of ports for verification. However, design validation is not the only area where electromagnetic solvers can be used. They also provide a great opportunity to extract valuable relationships between various design parameters and the far-field radiation properties, which later can be used in self-correcting and self-monitoring systems as a part of a processing unit to enable error correction and performance evaluation. In this section, we describe two exemplary applications of such methods that are based on extracted relationships between performance and design parameters. However, it goes without saying that the use of simulation-based methods is not limited to the presented examples.

3.5.3.1 Pattern Prediction

Use of tiny “sniff” antennas in the same electromagnetic simulation setup that is used for radiation pattern characterization enables extraction of mathematical relationships between various radiation properties and PFRS read-outs. If the sniff

antenna is small enough in terms of wavelength and EM structure dimensions, and is placed at a large-enough distance from the chip, the impact of its presence on the radiation performance is negligible compared to the nominal performance in its absence. Depending on the properties of interest, different types of antennas can serve as sniffers. The sniff antenna can be placed a couple of wavelengths away from the surface of the integrated radiator in broadside direction or at any other off-axis angle. As the design parameters vary, the relative strength of the signal picked up by the sniff antenna changes and enables detection of variations. The required mathematical relationship is extracted through using the S-parameter matrix of the EM structure calculated by the electromagnetic solver.

One possible choice for the sniff antenna is a small dipole antenna shown in Figure 3.48. The polarized nature of this antenna enables performance evaluation for different polarization angles of the radiated electric field. We use this small dipole antenna in an example to explain one possible methodology to estimate the far-field radiation pattern of a radiator based on PFRS read-outs. For simplicity, in this example we only consider the effect of drive signals' amplitudes and phases variations on the performance. However, the use of this method is not limited to these parameters.

Figure 3.49 shows an HFSS simulation setup for the same 2×2 integrated radiator array of four-port transmitting antennas with nine slot-ring PFRS antennas that we used in examples described in sections 3.5.1 and 3.5.2. Two orthogonal small dipole antennas are used as a sniffer unit and are placed 2λ away from the center of integrated radiator in broadside direction. Duplicated sets of the same configuration are repeated at multiple off-axis angles on a spherical surface with radius 2λ with respect to the center of the integrated radiator, across the two orthogonal planes of $\phi = 0^\circ$ and $\phi = 90^\circ$. The sniffer units are spaced 10° apart with respect to the center.

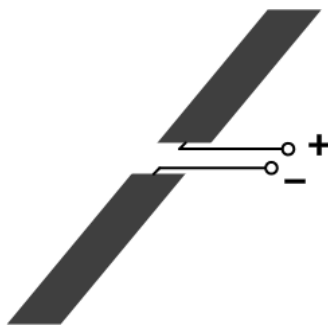


Figure 3.48: Sniff antenna.

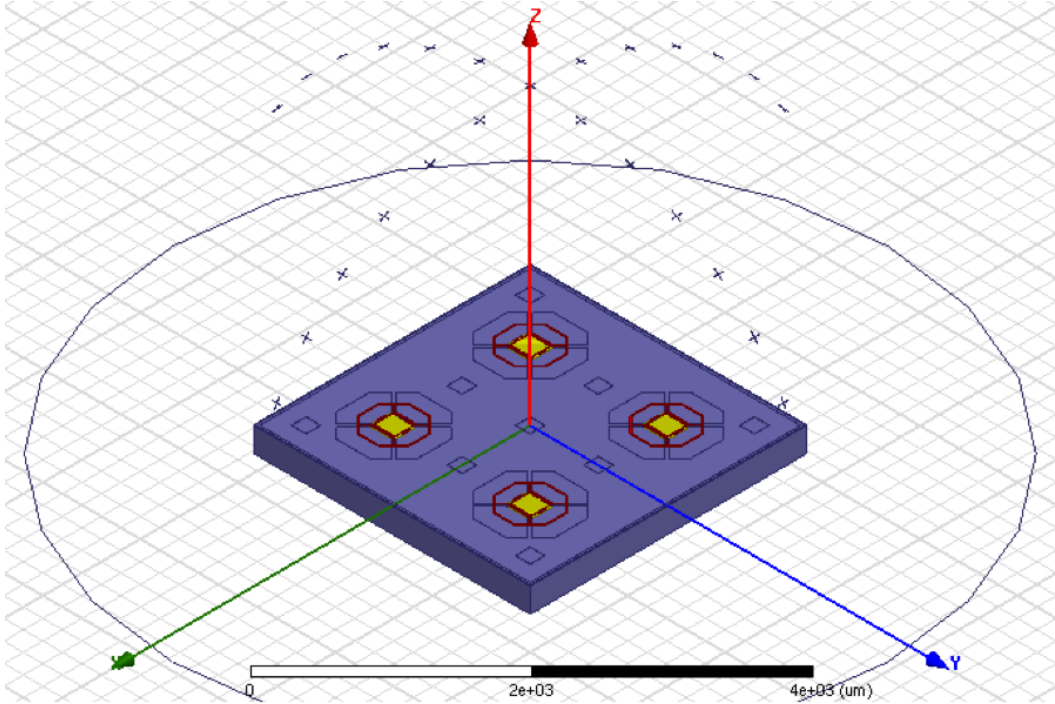


Figure 3.49: Example of an electromagnetic simulation setup using orthogonal dipole sniff antennas with the integrated radiator chip to extract mathematical relationships required for pattern prediction.

Such arrangement of sniff antennas allows detection of two orthogonal polarizations (E_ϕ and E_θ), and thus the overall radiated signal, in each direction specified by ϕ and θ of the polar coordinates across $-60^\circ < \theta < 60^\circ$ for $\phi = 0^\circ$ and $\phi = 90^\circ$ planes. Therefore, the relative strength of the sniffers' captured signals could approximate the overall far-field radiation pattern across $\phi = 0^\circ$ and $\phi = 90^\circ$ cross sections.

The simulation ports in HFSS are defined such that the first n_d ports correspond to the driving ports of the transmitting antennas, the next n_s ports are the PFRS ports, and the last n_r ports are associated with the receiving sniff antennas. Thus, the entire simulation includes an overall number of $N = n_d + n_s + n_r$ ports. In this example, $n_d = 16$, $n_s = 36$, and $n_r = 50$, resulting in $N = 102$.

The simulated S-parameter of this arrangement from HFSS is used for our calculation. Converting the S-parameters to Z-parameters we have

$$\begin{bmatrix} V_d \\ V_s \\ V_r \end{bmatrix}_{N \times 1} = Z_{N \times N} \times \begin{bmatrix} I_d \\ I_s \\ I_r \end{bmatrix}_{N \times 1} \quad (3.1)$$

where $[V_d]_{n_d \times 1}$, $[V_s]_{n_s \times 1}$, and $[V_r]_{n_r \times 1}$ are the phasors' vector for the voltages at the driving ports, sensor ports, and sniffer ports, respectively, and similarly, $[I_d]_{n_d \times 1}$, $[I_s]_{n_s \times 1}$, and $[I_r]_{n_r \times 1}$ are the phasors' vector for the ports' currents. Since the load impedances for the PFRS ports and the sniffer ports (z_s and z_r) are known through design of detector circuitry and simulation of sniff antennas ($V_s = -z_s I_s$, $V_r = -z_r I_r$), they can be used to simplify equation 3.1 such that

$$\begin{bmatrix} V_d \\ 0 \\ 0 \end{bmatrix}_{N \times 1} = A_{N \times N} \times \begin{bmatrix} I_d \\ I_s \\ I_r \end{bmatrix}_{N \times 1} \quad (3.2)$$

where $A_{N \times N}$ is the modified Z -matrix after including the terminations. Once matrix A is inverted, two of the sub-matrices of A^{-1} relate PFRS ports voltages to the driving ports voltages ($[S_1]_{n_s \times n_d}$), and the sniffers' ports voltages to the driving ports voltages ($[S_2]_{n_r \times n_d}$) as follows:

$$A_{N \times N}^{-1} = \begin{matrix} n_d \{ \\ n_s \{ \\ n_r \{ \end{matrix} \begin{bmatrix} \overbrace{\times}^{n_d} & \overbrace{\times}^{n_s} & \overbrace{\times}^{n_r} \\ S_1 & \times & \times \\ S_2 & \times & \times \end{bmatrix}_{N \times N} \quad (3.3)$$

$$V_s = -z_s S_1 V_d \quad (3.4)$$

$$V_r = -z_r S_2 V_d \quad (3.5)$$

If $n_s > n_d$, then the columns of S_1 are linearly independent. Thus, we can use the pseudo-inverse matrix of S_1 (i.e., S_1^+) to write

$$V_r = z_r/z_s [S_2]_{n_r \times n_d} [S_1^+]_{n_d \times n_s} V_s \quad (3.6)$$

which directly expresses the voltages picked up by the sniffers, V_r , in terms of PFRS read-outs, V_s . Knowing V_r , we combine its vector components that correspond to E_ϕ and E_θ at each point in order to calculate the overall radiated signal in that direction. Therefore, this method achieves the far-field radiation pattern obtained by PFRS read-outs over the region of interest.

Figure 3.50 compares the normalized far-field radiation pattern from HFSS simulations to the normalized predicted radiation pattern through our method based on simulated PFRS read-outs, when the transmitting antennas are driven in phase for

optimal broadside radiation. Figure 3.51 demonstrates the same comparison when the transmitting antennas are phased such that the beam is steered in $\phi = 0^\circ$ plane. We see that in both cases the predicted pattern matches the simulated pattern from HFSS within reasonable accuracy.

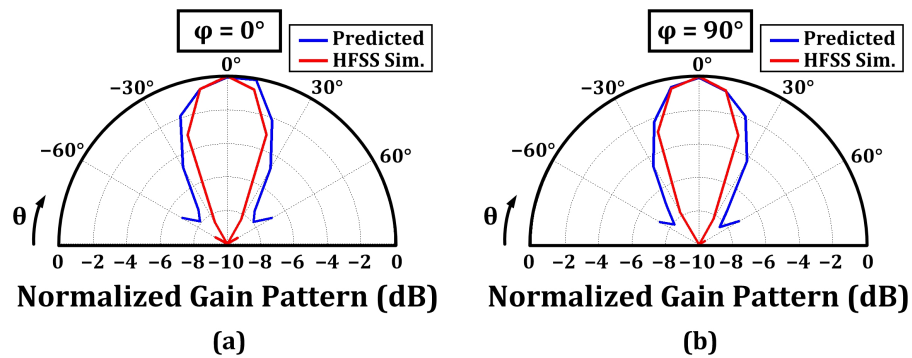


Figure 3.50: Comparison between the normalized predicted pattern using simulated PFRS read-outs and normalized simulated pattern by HFSS in (a) $\phi = 0^\circ$ and (b) $\phi = 90^\circ$ planes for broadside radiation.

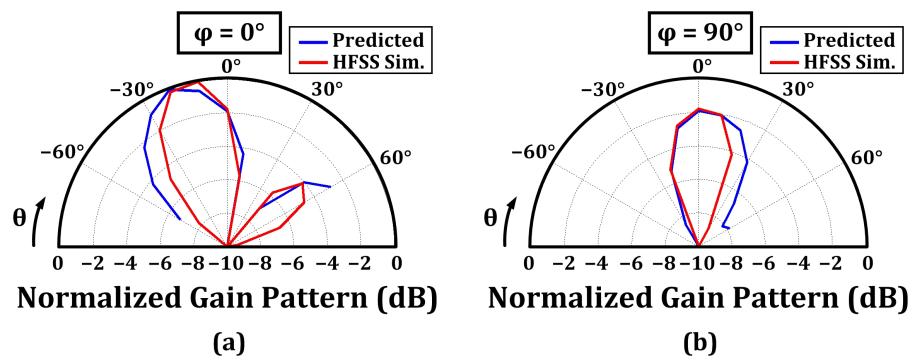


Figure 3.51: Comparison between the normalized predicted pattern using simulated PFRS read-outs and normalized simulated pattern by HFSS in (a) $\phi = 0^\circ$ and (b) $\phi = 90^\circ$ planes for off-axis radiation.

3.5.3.2 Beam Angle Prediction

Knowing the field profile of electromagnetic waves across an entire planar surface provides valuable information regarding how they are propagating in the medium. One way to analyze the field profile is its decomposition into plane waves, traveling in different directions. Using Cartesian coordinates, let's assume we know

the field profile of propagating electromagnetic waves over $z = 0$ plane for all $(x, y, 0)$ points. It has been shown [52] that the two-dimensional Fourier transform of a propagating wave front from (x, y) domain to (f_x, f_y) domain can be interpreted as decomposition of the original wave front into plane waves traveling with direction cosines $(\lambda f_x, \lambda f_y, \sqrt{1 - (\lambda f_x)^2 - (\lambda f_y)^2})$. This means that once the Fourier transform is calculated, its magnitude for each (f_x, f_y) point in the Fourier domain corresponds to the amplitude of a plane wave propagating in $\vec{\mathbf{k}} = 2\pi/\lambda(\lambda f_x, \lambda f_y, \sqrt{1 - (\lambda f_x)^2 - (\lambda f_y)^2})$ direction.

Such decomposition can be interpreted in an antenna array context as well. When the radiating elements in an antenna array are phased to steer the radiated beam in a specific direction, we expect the decomposition of its radiated field into plane waves result in the strongest component propagating in the direction of beam steering. In other words, if the field profile of the radiated electric field of an antenna array is known across a plane parallel to the array plane, the magnitude of its two-dimensional Fourier transform can be used to calculate the direction of beam steering. Although the entire field profile across the infinite plane is required for an accurate analysis, knowing the field profile on a finite (windowed) plane at discrete points close enough to each other could still provide the same information with acceptable accuracy.

This analysis may also be used to interpret PFRS data. The sniff antennas described in the previous section can also be arranged on a planar surface on top of the radiator instead of a spherical surface. Figure 3.52 shows such a simulation setup for the same 2×2 array with the same number of sniff antennas arranged on a plane on top of the integrated radiator array. The same method described in section 3.5.3.1 can be used to express the voltages of sniff antennas in terms of PFRS read-outs. Since these voltages are proportional to the x - and y -components of the radiated electric field, we can perform 2-D Fourier transformation on them for plane-wave decomposition in order to find the propagation direction of the strongest plane wave, and thus the direction of the radiated beam.

Figure 3.53(a) shows the heat map for the magnitude of the reconstructed electric field based on sniff antennas' voltages when the transmitting antennas are operating in phase for optimal broadside radiation. As expected the sniff antennas that are aligned with each radiating element pick up the strongest signal. Figure 3.53(b) illustrates the magnitude of the calculated 2-D Fourier transform, which reveals that the strongest component is propagating for $(f_x, f_y) = (0, 0)$, i.e. broadside direction.

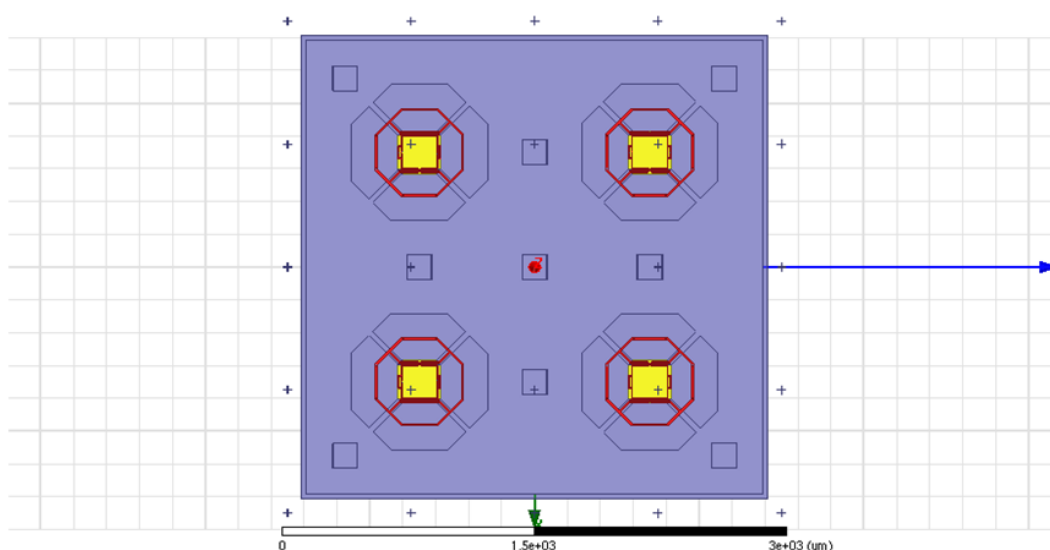


Figure 3.52: Arrangement of sniff antennas on a planar surface on top of the integrated radiator chip in simulation to be used for plane-wave decomposition.

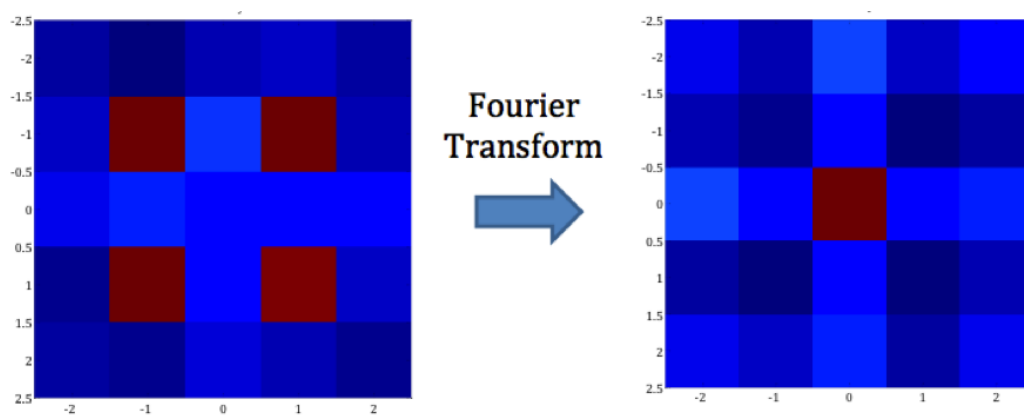


Figure 3.53: (a) Heat map for the relative magnitude of the reconstructed electric field on the planar surface using sniffers' voltages and (b) decomposition of the field into plane waves propagating at different angles, showing a maximum at $f_x = f_y = 0$, i.e. broadside radiation.

3.6 PFRS Implementation on a PCB prototype

In this section, we demonstrate a PCB prototype [53] consisting of two transmitting antennas and four integrated PFRS antennas, which is fabricated and tested to verify the concept and show the implemented sensors' capabilities to capture the radiation properties such as gain pattern, radiated polarization, and the steering angle of the antenna array as a few examples of radiation sensors applications.

3.6.1 Prototype Design

Figure 3.54 shows the proof-of-concept prototype PCB transmitter antenna array. We will use few simple methods to interpret the data to capture various far-field radiation properties. However, it should be noted that the use of PFRS antennas and their data is not limited to the presented design and methods. The example prototype PCB antenna array consists of two transmitter patch antennas, tuned at 5 GHz, and four folded-slot PFRS antennas (followed by their output matching networks) placed symmetrically with respect to the patch antennas on the same substrate. All antennas are matched to 50Ω at 5 GHz. The structure is fully passive and there are no driver or detector circuits attached to the transmitting and sensing antennas. This allows for direct control of transmitter antennas drive and accurate read-out of the sensor antennas.

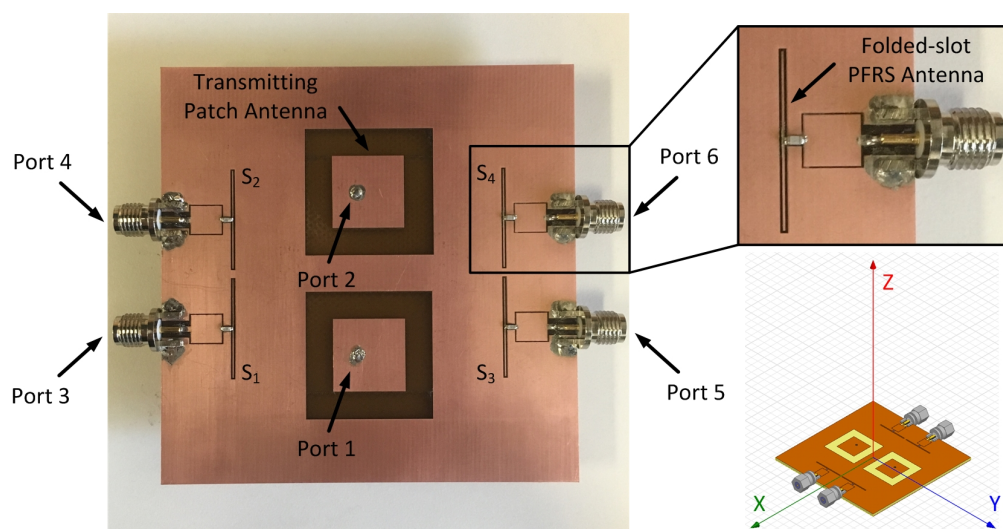


Figure 3.54: The prototype PCB antenna array with two transmitting patch antennas and four folded-slot PFRS antennas.

3.6.2 Data Interpretation

The first parameter that we can investigate in this design is the steering angle of the far-field radiated beam in the yz -plane as a result of the phase difference between the patch antennas' inputs. One easy way to extract this phase difference is to monitor and compare the amplitudes of either of the sensor pairs S_1, S_2 or S_3, S_4 that are placed symmetrically with respect to the x -axis (Figure 3.55). The amplitude difference of these PFRS pairs can be used to monitor the beam steering angle of the array by tracking the drive phase difference due to symmetrical placement of the PFRS antennas.

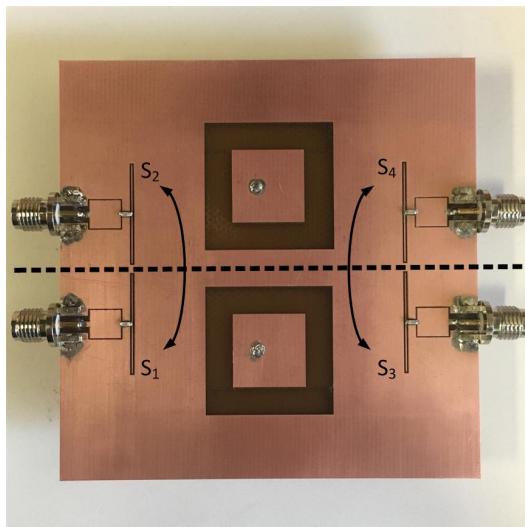


Figure 3.55: Symmetrically-placed sensors to detect the phase difference between the driving signals of the two patch antennas.

We can also extract the mathematical relationship between the read-outs of PFRS antennas and different components of the radiated fields of the transmitting antennas (and thus the polarization of the radiated electric field) in any direction using the method described in section 3.5.3.1. Figure 3.56(a) shows a simulation setup in HFSS electromagnetic solver, where a very small polarized “sniff” antenna is added to the simulation and placed at $\phi = 90^\circ$, $\theta = 30^\circ$ direction to receive the θ -component of the radiated electric field in this direction. Since the number of PFRS outputs is larger than the number of transmitting antennas’ driving ports, the phasor of the voltage picked up by the sniff antenna, V_{sniff} , which is proportional to the magnitude of the θ -component of the radiated electric field at the specified direction, can be directly calculated from the vector of PFRS read-outs’ phasor voltages, V_{sen} , by a simple matrix multiplication, $V_{sniff} = TV_{sen}$, where T is a $1 \times N_s$ matrix (N_s being the number of PFRS outputs) and is formed by using the simulated S-parameters of the structure and the load impedances attached to PFRS antennas and the sniff antenna as described in section 3.5.3.1.

We can even go one step further and use the same method for all θ angles across any $\phi = \phi_0$ plane (shown in Figure 3.56(b) for $\theta = 90^\circ$) to calculate both co- and cross-polarizations across this plane and combine E_ϕ and E_θ components to capture the entire radiation pattern across the $\phi = \phi_0$ plane.

It is important to note that for any type of radiating antennas, the presence of disturbing objects in the radiation path or the close vicinity of the radiator affects the

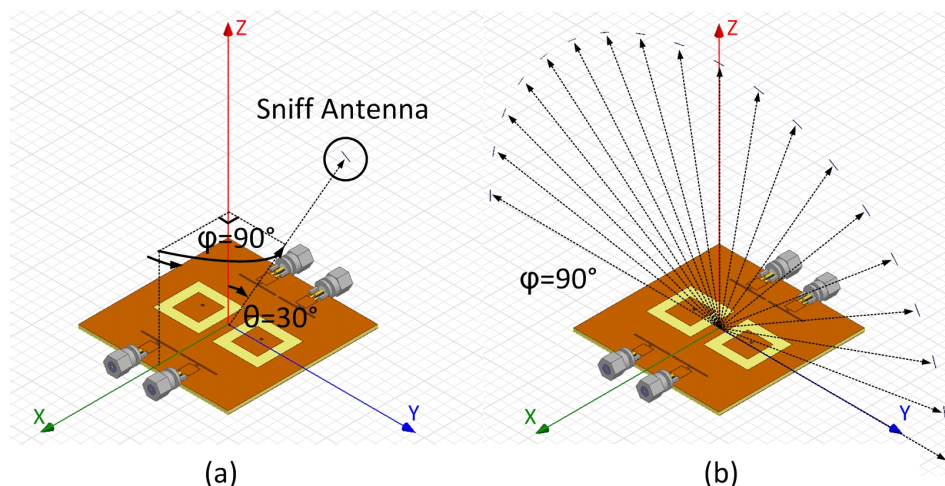


Figure 3.56: Simulation setups to relate PFRS read-outs to the polarization of radiated field (a) in an arbitrary direction, and (b) across an entire plane.

far-field radiation pattern. This is mainly due to reflection and scattering from the surface of the metallic objects and the additional loss and phase shift of electromagnetic waves as they travel through disturbing dielectric materials. Furthermore, the impedance levels and electromagnetic coupling between different parts of the radiating structure could change significantly when the disturbing object is very close to the radiating antenna, which in turn affects the radiation performance. However, PFRS antennas are placed on the same substrate as the radiating antenna and their coupling to the excited surface waves inside the substrate is much stronger than their sensitivity to the external incident waves resulted from reflection, scattering, interference, etc. Therefore, the perturbations to the predicted radiation properties by PFRS antennas caused by disturbing objects in the radiation path and close vicinity of the radiating antennas are minimal. This makes these sensors robust in predicting the unperturbed intrinsic radiation properties of the transmitting antennas as they are not prone to disturbing objects which might have potentially introduced error to the PFRS predictions of intrinsic radiator performance.

The HFSS simulation setup depicted in Figure 3.57(a) investigates an example of such a scenario for our prototype, where a $\lambda/2 \times \lambda/2 (= 3 \text{ cm} \times 3 \text{ cm})$ metallic reflector is placed in the radiation path of the transmitting patch antennas at the vertical distance h from the PCB. Figure 3.57(b) shows the top view of the same setup to clarify the relative placement of the reflector with respect to the transmitting and PFRS antennas. The normalized simulated gain patterns from HFSS across the $\phi = 90^\circ$ plane for the four cases of a) no reflector present, b) reflector at $h = 1 \text{ cm}$, c)

reflector at $h = 6$ cm, and d) reflector at $h = 12$ cm, are shown in Figure 3.58(a). The same normalized gain patterns predicted by the simulated PFRS read-outs for the four aforementioned cases are illustrated in Figure 3.58(b). A comparison between the two sets of plots reveals that although the presence of the metallic reflector affects the radiation pattern of the antenna array significantly, its effect on the PFRS prediction of the intrinsic radiation pattern is minimal.

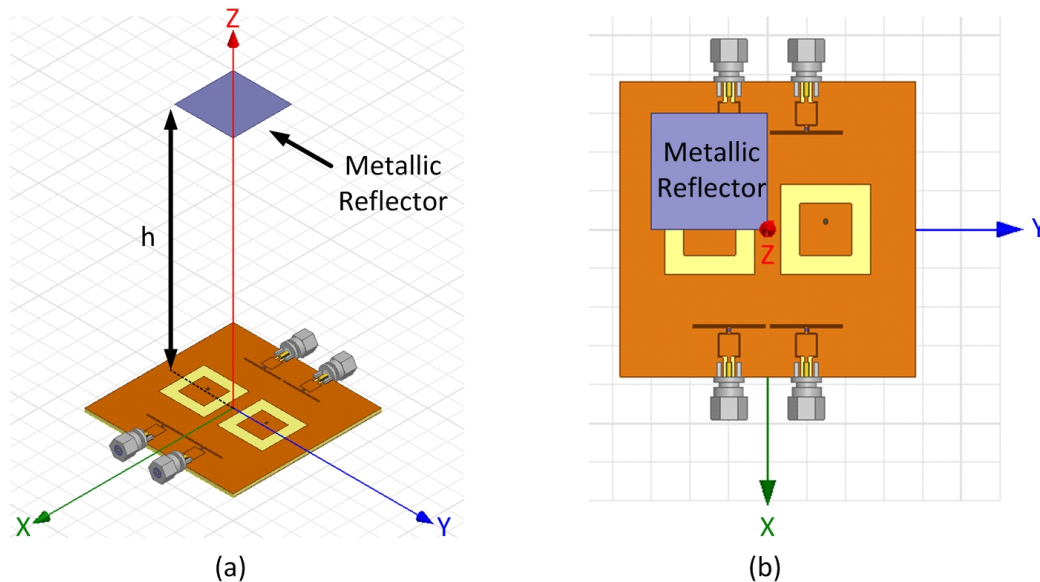


Figure 3.57: Simulation setup to investigate the impact of a disturbing metallic reflector on the performance of PFRS: (a) 3-D view and (b) top view.

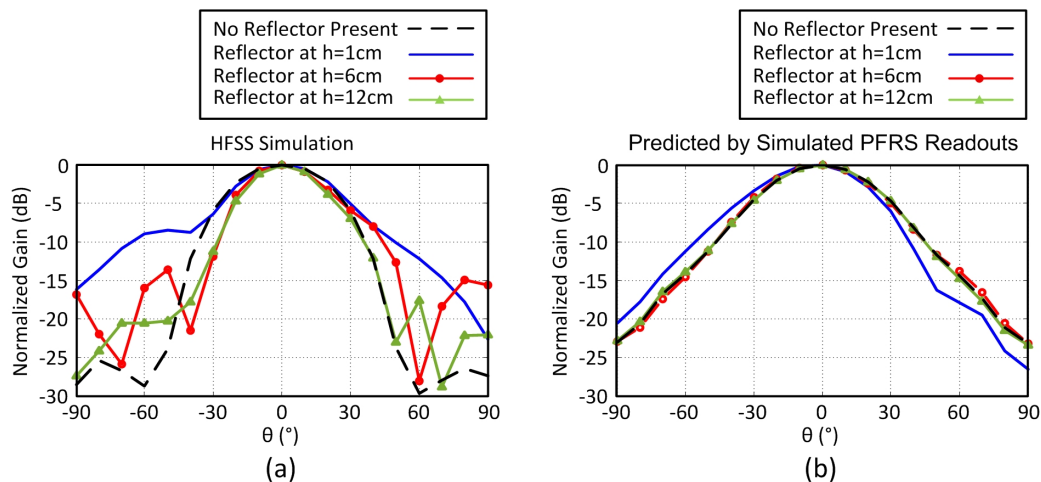


Figure 3.58: Comparison of the reflector impact on the normalized gain patterns for $\phi = 90^{\circ}$ plane based on (a) HFSS simulation and (b) prediction by simulated PFRS read-outs.

3.6.3 Measurements

The PCB prototype shown in Figure 3.54 was fabricated on a 1.6 mm thick FR4 substrate. The measured and simulated input reflection coefficients for both the transmitting and sensing antennas (S_{11} and S_{33}) are presented in Figure 3.59.

In order to evaluate PFRS performance in capturing far-field radiation pattern for a given drive setting, we compare the results of three different methods: 1) simulated radiation pattern using the HFSS simulation setup of Figure 3.60(a), 2) direct measurement of the far-field radiation pattern using an NSI far-field antenna pattern measurement setup, shown in Figure 3.60(b), and 3) predicted far-field radiation pattern by PFRS, based on measured read-outs of sensors, shown in Figure 3.60(c).

Figure 3.61 compares the simulated gain pattern from HFSS to the measured gain pattern by the far-field antenna pattern measurement setup and the predicted gain pattern by the measured PFRS read-outs in two orthogonal planes of $\phi = 0^\circ$ and $\phi = 90^\circ$, when the two patch antennas are driven in phase. The patterns are normalized to allow easier comparison. The predicted pattern is calculated by using the same method introduced in the previous section (using the T matrix and phasor voltages from the sensors). As it can be seen, the three radiation patterns match well, particularly in $\phi = 90^\circ$ plane where the radiated beam is narrower. This is further illustrated in Figure 3.62, where the relative phases of the two patch antennas are switched to 90° , -90° , and 180° , respectively, to significantly change the radiation pattern in $\phi = 90^\circ$ plane, and yet for all three cases the simulated, measured, and sensor-predicted normalized gain patterns match very closely.

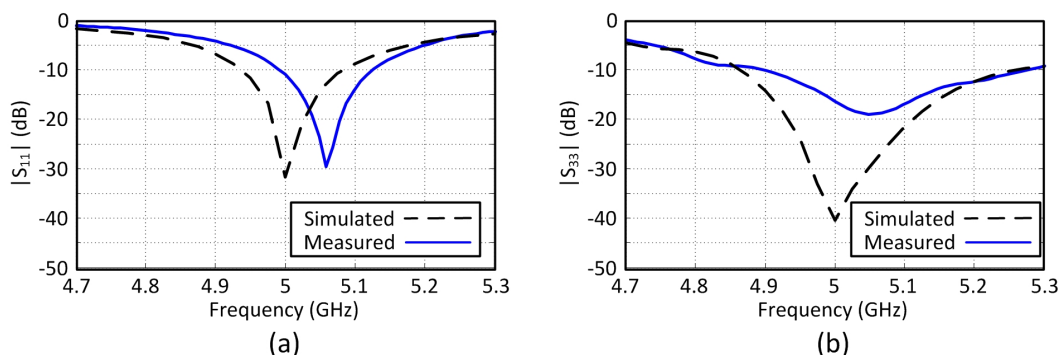
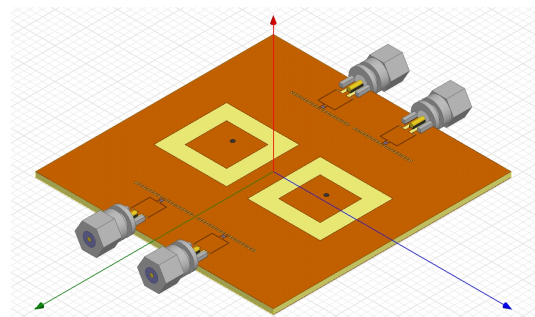
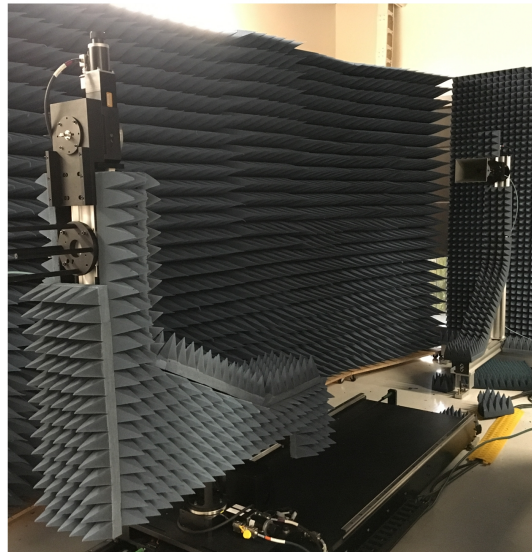


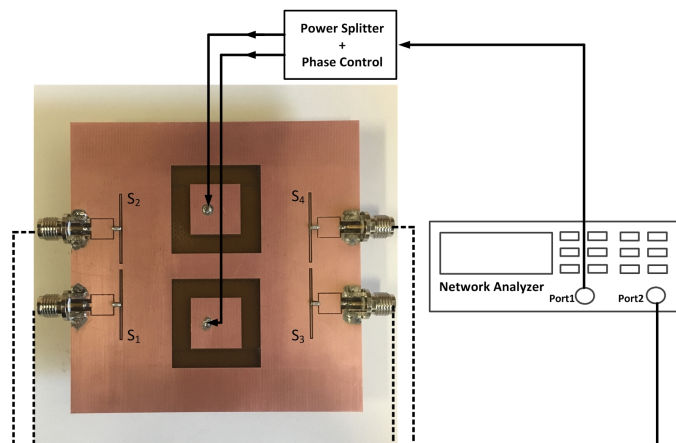
Figure 3.59: Measured and simulated input reflection coefficients of (a) the patch and (b) PFRS antennas.



(a)



(b)



(c)

Figure 3.60: PFRS performance is evaluated through comparison between (a) simulation of radiation pattern through HFSS, (b) direct measurement of radiation pattern in a far-field measurement setup, and (c) prediction of radiation pattern through measured PFRS read-outs.

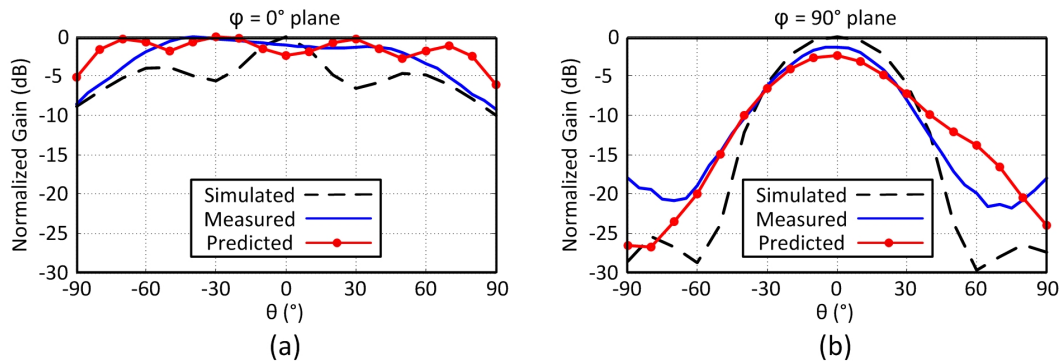


Figure 3.61: Normalized simulated, measured, and predicted gain patterns based on PFRS read-outs in (a) $\phi = 0^{\circ}$ and (b) $\phi = 90^{\circ}$ planes for in-phase drive.

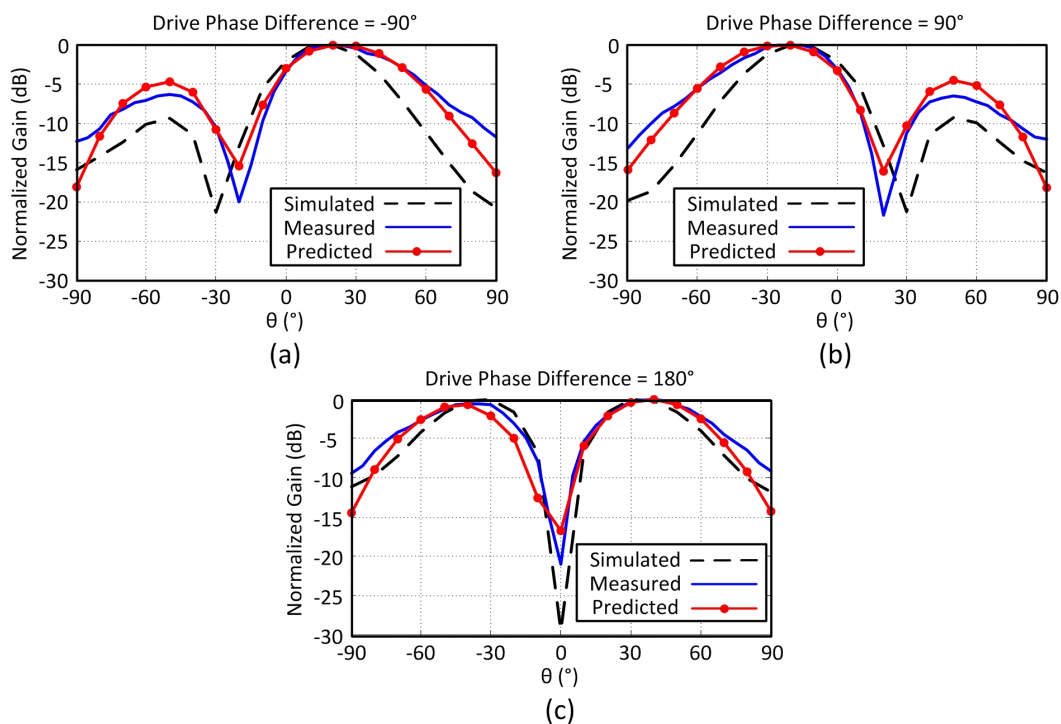


Figure 3.62: Normalized simulated, measured, and predicted gain patterns based on PFRS read-outs in $\phi = 90^{\circ}$ plane for (a) 90° , (b) -90° and (c) 180° of phase difference between the patch antennas.

As mentioned before, more specific far-field radiation properties such as polarization of the radiated electric field can also be predicted by PFRS read-outs. Figure 3.63 shows the normalized simulated, measured, and predicted co- and cross-polarizations of the fabricated antenna array in $\phi = 90^{\circ}$ plane to demonstrate this capability. Again, we can clearly see that PFRS prediction for the radiated polarization is well matched to the simulation and direct polarization measurement. Finally,

the simulated and measured relationship between the amplitudes of signals picked up by S_1 and S_2 PFRS antennas and the phase difference between the transmitting patch antennas as a measure to track the beam steering angle is shown in Figure 3.64.

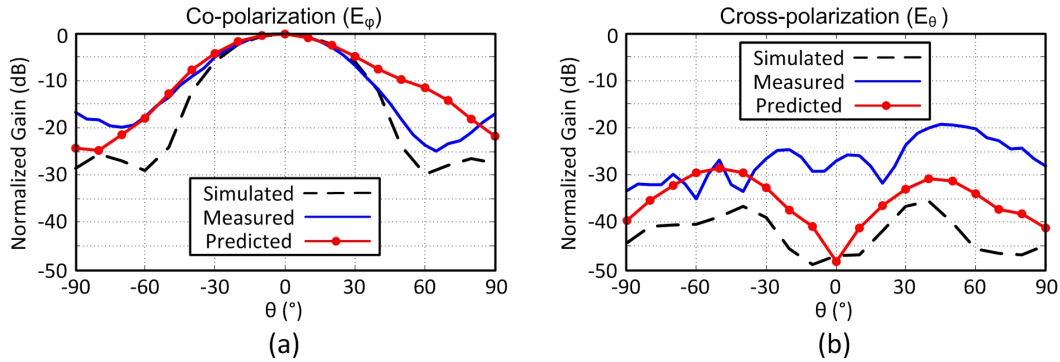


Figure 3.63: Normalized simulated, measured, and predicted (a) co-polarization and (b) cross-polarization gain patterns in $\phi = 90^\circ$ plane for in-phase drive.

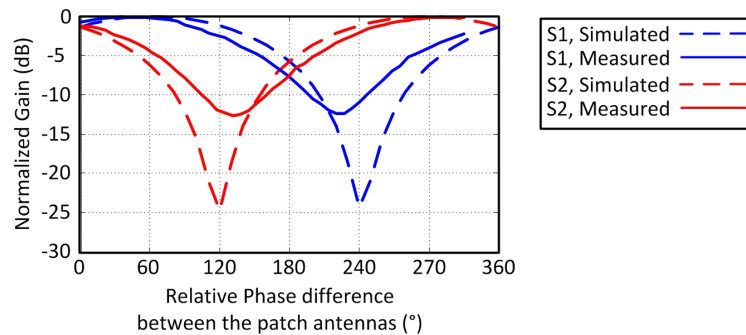


Figure 3.64: Measured and simulated amplitude response of S_1 and S_2 .

3.7 PFRS Implementation on an IC prototype

In this section, we demonstrate an IC prototype of PFRS integration with transmitting antennas. A 72-GHz 2×1 radiator array of linear-slot antennas integrated with their drive circuitry is equipped with four folded-slot PFRS antennas and their detection circuitry. Figure 3.65 shows a simplified block diagram of the system. A central oscillator unit serves as the source for mm-wave signal generation. These signals are then used for both driving the transmitting antennas through the drive circuitry as well as providing the LO signals for sensors detection circuitry. The LO signals allow coherent detection through downconversion of the signals that are picked up by the PFRS antennas and enable capturing both their phases and amplitudes.

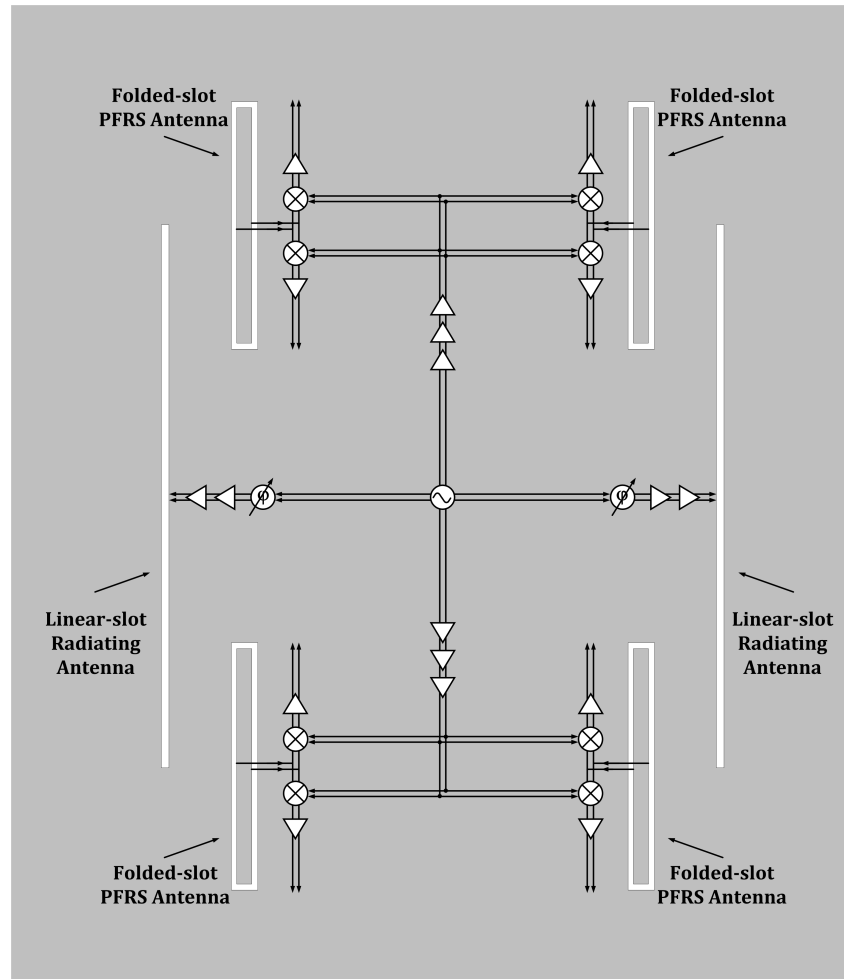


Figure 3.65: Simplified block diagram of the 2×1 integrated linear-slot radiator with four PFRS antennas.

3.7.1 System Architecture

The detailed block diagram of the system is shown in Figure 3.66. The central oscillator unit consists of four quadrature oscillators running at f_{osc} . The outputs of all four oscillators are shorted to each other to ensure synchronized operation and the same phase reference for all of them. Two of the oscillators provide the quadrature signals that allow 360° phase control of the driving signals by proper weighted summation of I and Q components through the phase rotators. These signals then experience two stages of amplification and eventually drive the transmitting antennas. The quadrature outputs of the other two oscillators are routed towards the upper and lower sensors and enable quadrature downconversion of the PFRS picked-up signals to allow extraction of their phases as well as their amplitudes. The sensor LO signals are distributed to the PFRS locations through multiple transmission line

sections and three buffer stages. For noise reduction purposes in the downconversion scheme, a differential off-chip low frequency reference at frequency f_0 is also fed to the chip and mixes with the on-chip LO signals before they get to the sensors. The signals that are picked up by PFRS antennas are then downconverted to f_0 with these LO signals that run at $f_{osc} \pm f_0$. The outputs go through another round of amplification at f_0 before they are downconverted to DC. Finally, the baseband outputs are routed to the pads and provide the PFRS read-outs for off-chip processing.

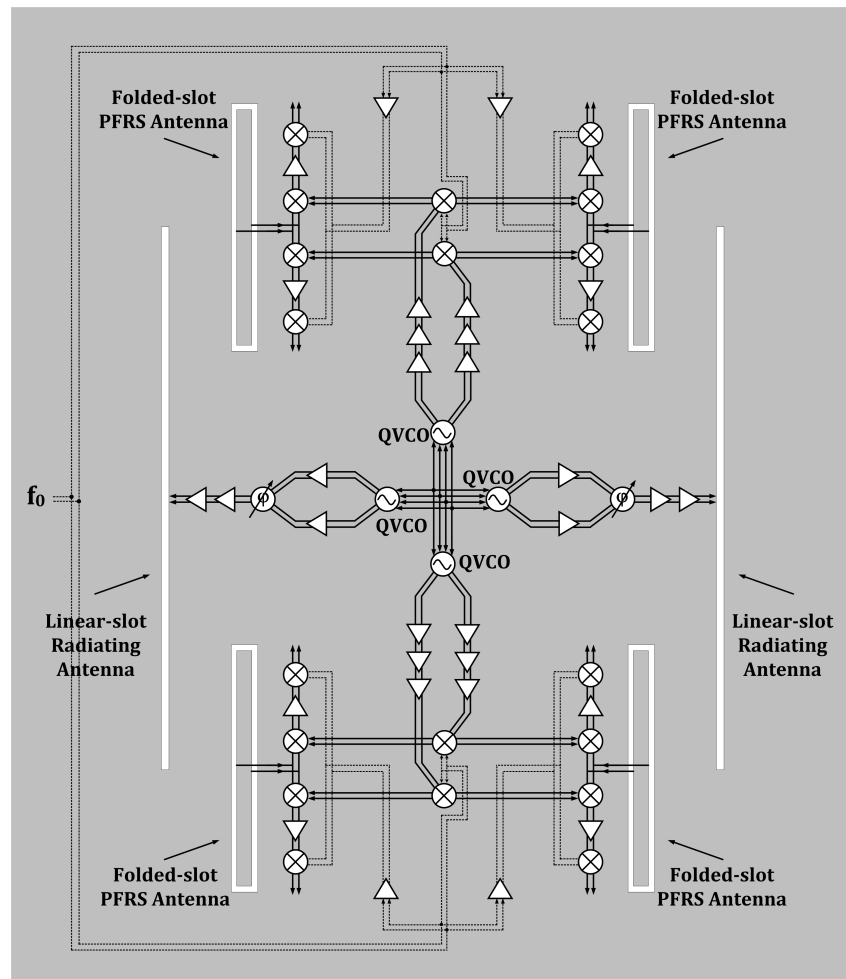
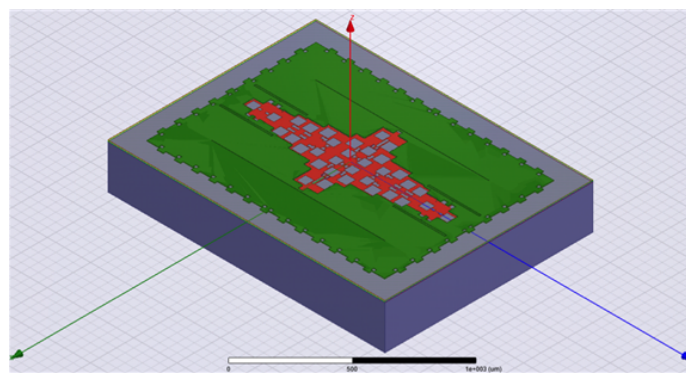


Figure 3.66: Detailed block diagram of the 2x1 integrated linear-slot radiator with four PFRS antennas.

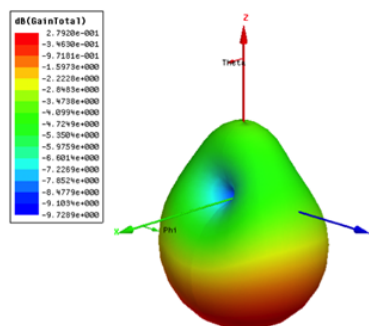
3.7.2 Radiator Design

3.7.2.1 Transmitting Antennas

The integrated radiator chip consists of two linear-slot antennas and is designed to radiate from the backside. Figure 3.67(a) shows the 3-D electromagnetic model of the chip in HFSS whose simulated gain pattern is depicted in Figure 3.67(b). One practical issue for integrated radiators with backside radiation in the absence of flip-chip packaging option is that the radiated signal needs to travel through the lossy substrate of the testing PCB. Also, since the chip cannot be mounted on a ground plane, transferring the heat off the chip creates another challenge. To solve these issues, we have made a plated circular cutout in the PCB substrate and attached a piece of diamond to its backside. This way the integrated radiator chip sits inside the cutout region and on top of the diamond piece, which serves as a good heat conductor as well as a good dielectric matching layer between IC's silicon substrate and free space. Figure 3.68(a) illustrates the 3-D electromagnetic model of this configuration and the resulting simulated gain pattern is shown in Figure 3.68(b).



(a)



(b)

Figure 3.67: (a) Electromagnetic structure of the 2×1 integrated linear-slot radiator and (b) simulated gain pattern.

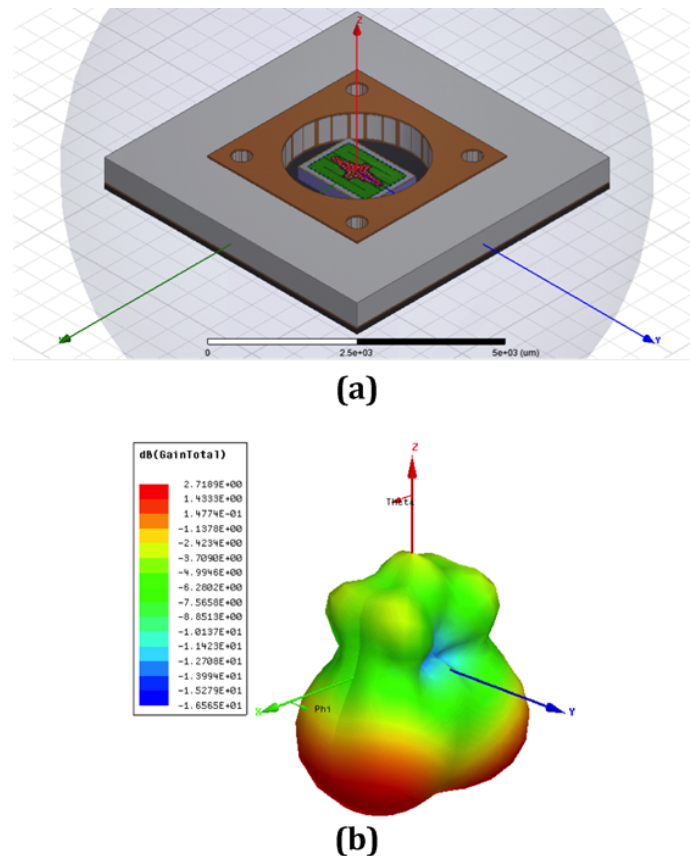


Figure 3.68: (a) Electromagnetic structure of the integrated radiator's packaging and (b) simulated gain pattern.

3.7.2.2 Oscillators

The same oscillator design is used for all quadrature oscillators to ensure identical operation. Figure 3.69(a) shows the schematic of the quadrature oscillators. Each oscillator consists of two cross-coupled VCOs with additional quadrature coupling through parallel transistors [54]. Proper radiation through the two transmitting antennas requires the two QVCOs to have the exact same frequency. Also the beam steering feature requires the drive circuit of both antennas to share the same phase reference. Furthermore, proper downconversion PFRS outputs only happens if the QVCO's that provide the LO signals operate at the exact same frequency as the radiating signal with a known phased reference. To address all these constraints at the same time, the quadrature outputs of all four QVCOs are shorted to each other through microstrip transmission lines. This way the QVCOs are enforced to operate in phase and at the exact same frequency. The simulated output waveforms of all oscillators are depicted in Figure 3.69(b).

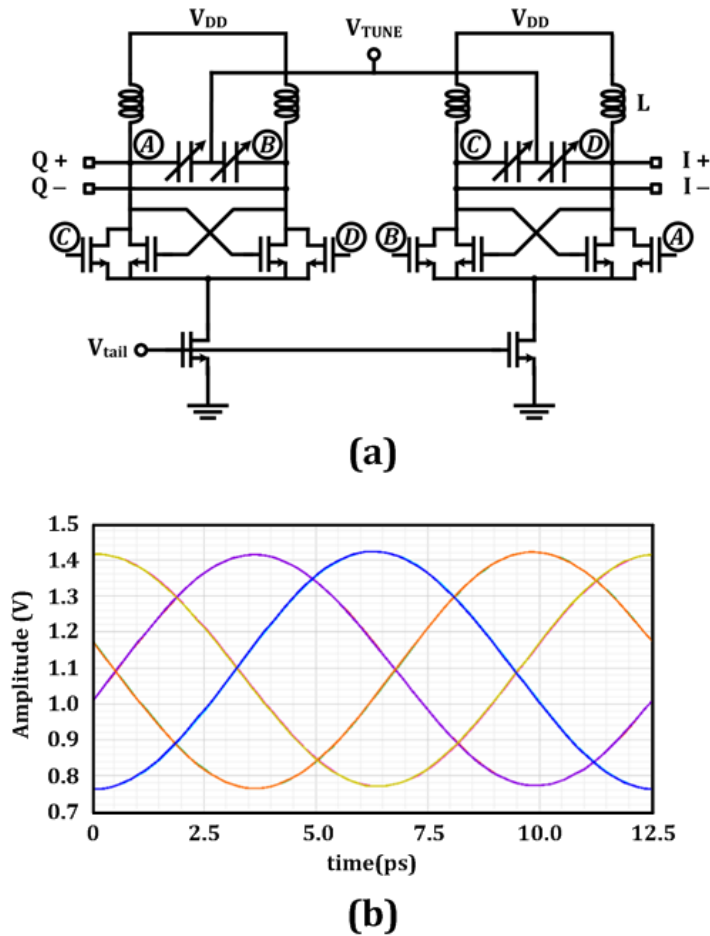


Figure 3.69: (a) Schematic of the quadrature oscillators and (b) the simulated quadrature outputs of all four oscillators.

3.7.2.3 Drive Circuit

The quadrature oscillator associated with each transmitting antenna is loaded by a buffer stage to increase the isolation between the oscillator and the rest of the circuit blocks. After the first buffer stage, the differential output I and Q signals feed the phase rotator unit which consists of two Gilbert cells whose outputs are added to produce the desired phase. Arbitrary weights for I and Q signals for summation are set through direct access to individual control voltages for the biasing current of I_{\pm} and Q_{\pm} subparts. Once the desired phase is set, the driving signal goes through two additional buffer stages and is finally fed to the transmitting antennas. All the buffer stages have the same cascode topology but different device size. The schematics for the buffers and the phase rotator are shown in Figure 3.70 and Figure 3.71, respectively.

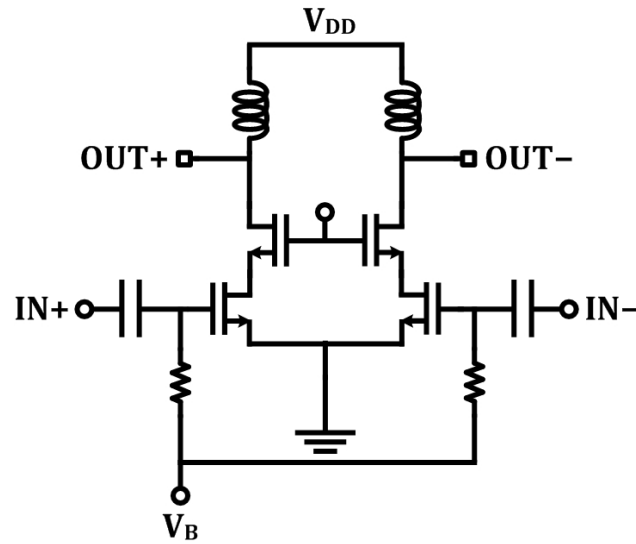


Figure 3.70: Schematic of the buffers. All buffers use the same cascode topology but the devices widths are scaled up as the power increases in the buffer chain.

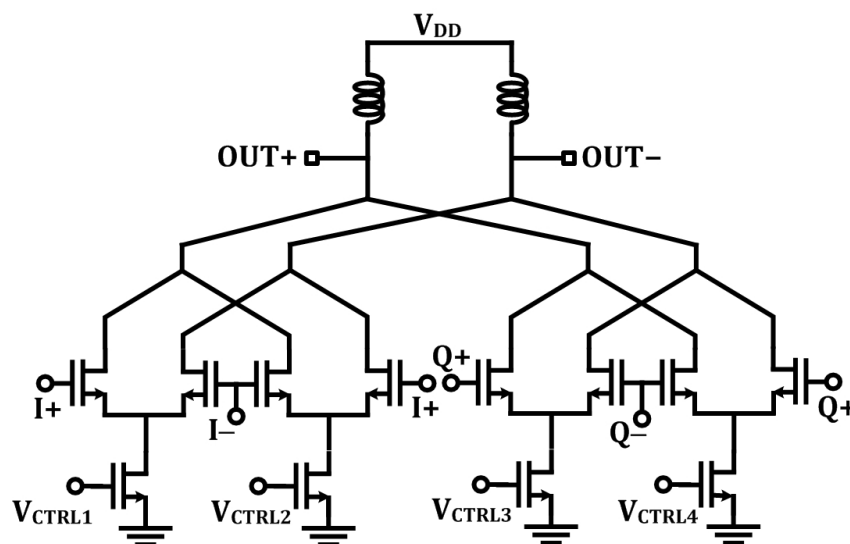


Figure 3.71: Schematic of the phase rotator consisting of two Gilbert cells to allow arbitrary weighted summation of I and Q signals.

Figure 3.72 shows the simulated output signals that feed the transmitting antennas when the phase settings for the path on the left are kept constant while the phase rotator weights for the other path on the right are adjusted to vary the phase from 0° to 360° with almost equal steps of 22.5° .

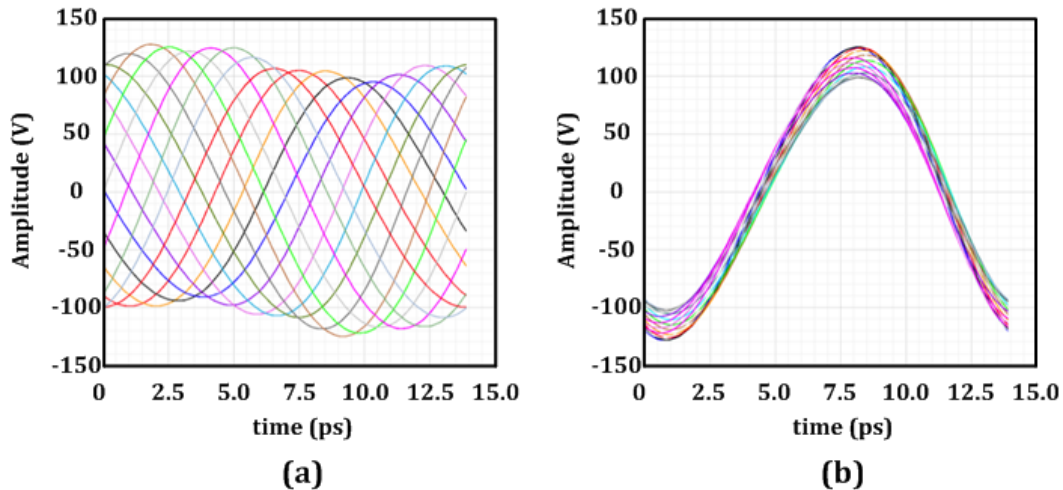


Figure 3.72: Simulated waveforms of the driving signals for (a) linear-slot antenna on the left and (b) linear-slot antenna on the right when their phase difference is controlled from 0° to 360° .

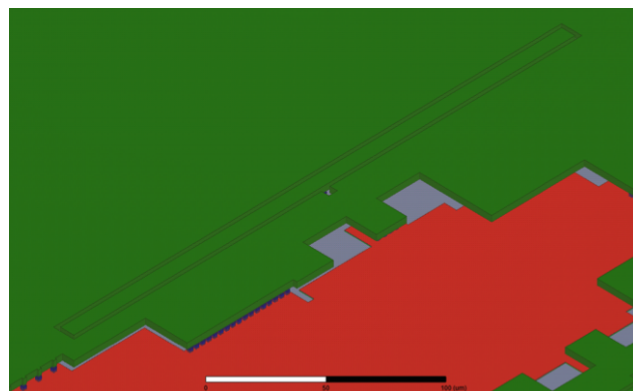


Figure 3.73: 3-D structure of the folded-slot PFRS antenna.

3.7.3 PFRS Design

3.7.3.1 PFRS Antenna

Due to the presence of a large ground plane, slot antenna is an intuitive choice for PFRS. This is both because of ease of implementation and consistency with the transmitting antennas. For this design, we used folded-slot structures as PFRS antennas because of providing larger electrical length and thus better sensitivity within a compact area. Figure 3.73 shows the electromagnetic design of one of the PFRS antennas. The simulated strengths of the signals picked-up by each PFRS antenna for the same phase rotator settings as previous section are depicted in Figure 3.74.

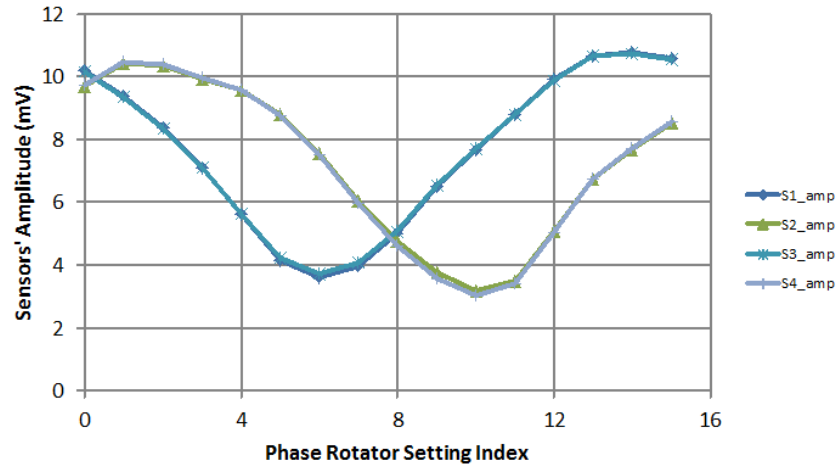


Figure 3.74: Simulated magnitude of the signals picked up by PFRS antennas when the phase difference between the two antennas is swept from 0° (setting index = 0) to 360° . (setting index = 16)

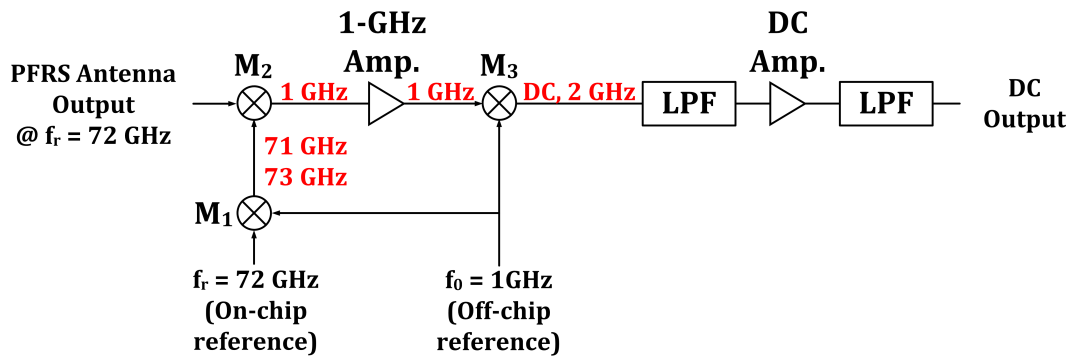


Figure 3.75: Downconversion scheme for coherent detection of PFRS signals.

3.7.3.2 Detection Circuit

A conceptual block diagram of the downconversion scheme used for coherent PFRS signal detection is given in Figure 3.75. Since the picked-up signal levels are small, they are vulnerable to noise and thus noise considerations need to be taken into account in the design of detection circuitry. In this design, to avoid the destructive effect of transistors flicker noise in a zero-IF receiver, we have used a different scheme in which a low frequency off-chip reference at $f_0 = 1$ GHz is fed to the chip to generate LO signals at $f_{osc} \pm f_0$ through the first mixer M_1 for downconversion. This way the signal from PFRS is first downconverted to f_0 by mixer M_2 and is amplified at this frequency. Once this low frequency signal is large enough, it is

downconverted to DC using the mixer M_3 .

The full circuit block diagrams of the LO distribution network (from QVCO to the sensors' locations) and the local detection circuitry (located next to each PFRS antenna) with more details are shown in Figure 3.76.

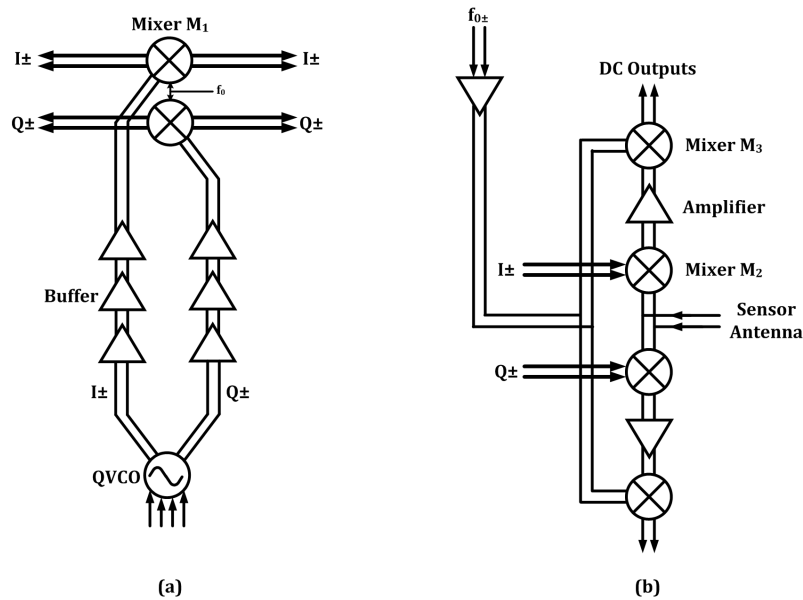


Figure 3.76: (a) LO distribution network to PFRS locations for downconversion and (b) detection circuitry located next to PFRS antenna.

The buffer stages in the LO distribution network are the same cascode buffer stages used in the drive circuit of the transmitting antennas. The schematics of the rest of the circuit blocks are shown in Figure 3.77.

3.7.4 Measurements

The radiator is fabricated in UMC 55 nm CMOS process and it radiates from the backside. The chip is placed inside a circular cutout region in the 20-mil-thick Rogers RO4003 PCB substrate used for testing. A 25 mm \times 25 mm piece of diamond is also attached to the backside of the PCB and covers the cutout region and is glued to the PCB ground plane on the backside by thermal paste to enable heat transfer from the chip to the ground plane. The chip is attached to the diamond piece through thermal paste as well and is wirebonded to the traces on PCB. The radiated signal is first received by a linearly polarized horn antenna facing backside of the chip and is downconverted using a 7th harmonic mixer, and is eventually fed

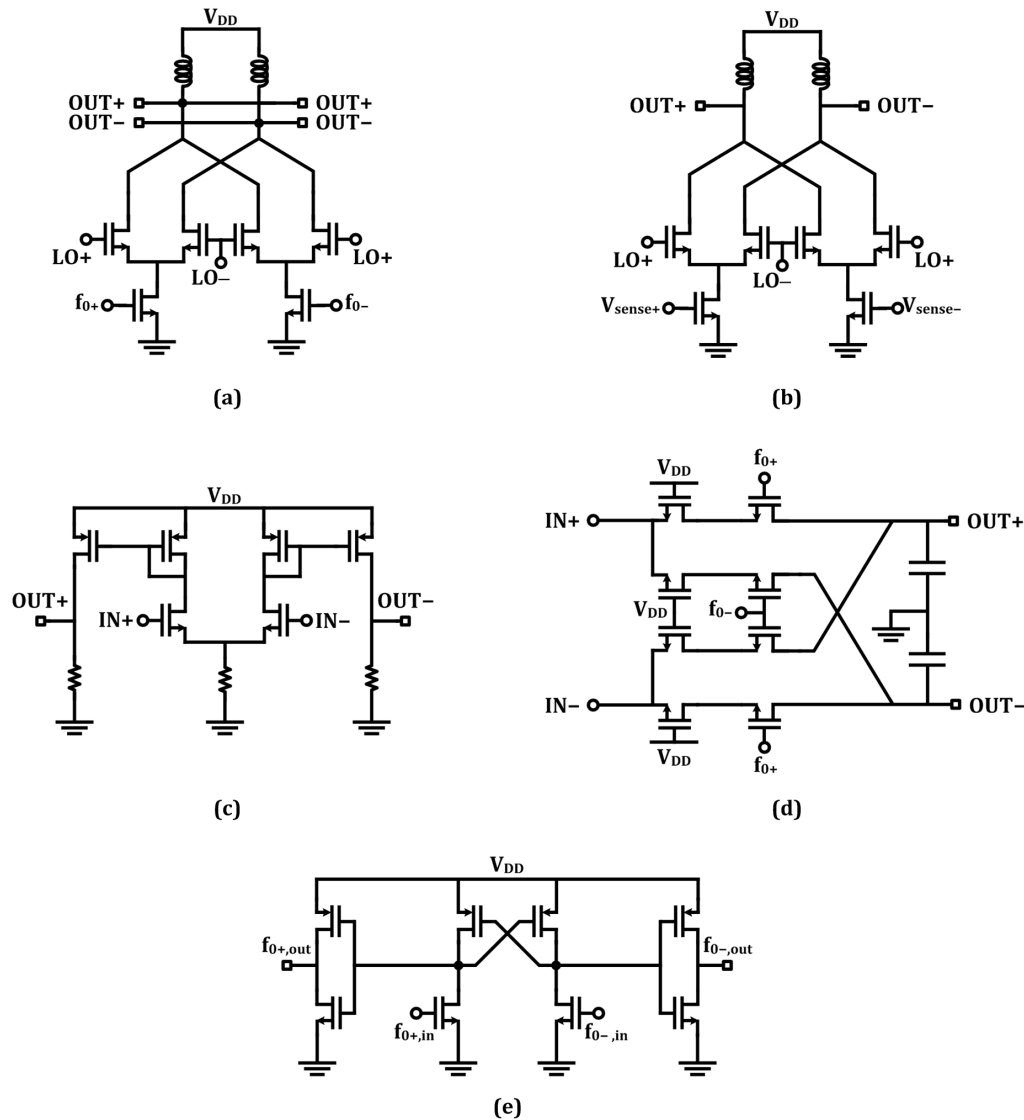


Figure 3.77: Circuit schematics for (a) mixer $M1$, (b) mixer $M2$, (c) amplifier at f_0 , (d) mixer $M3$, and (e) buffer for distribution of off-chip low-frequency reference at f_0 .

to a spectrum analyzer. Figure 3.78 shows the measured radiation frequency of the chip versus the tuning voltage of the oscillators.

The same phase rotator control voltages that were used to achieve 0° to 360° phase control between the two transmitting antennas drives in simulation (Figure 3.72) are applied to the drive circuit to measure detection circuit outputs. Calibrated measured downconverted PFRS read-outs for both I and Q components of all sensors versus the phase rotator settings are shown in Figure 3.79.

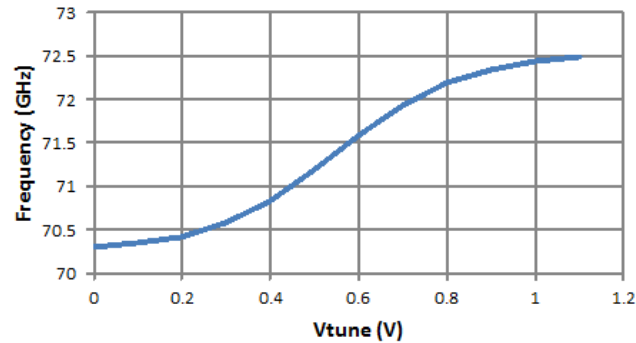


Figure 3.78: Measurement of the radiation frequency of the 2×1 integrated linear-slot radiator array versus the tuning voltage of the quadrature oscillators.

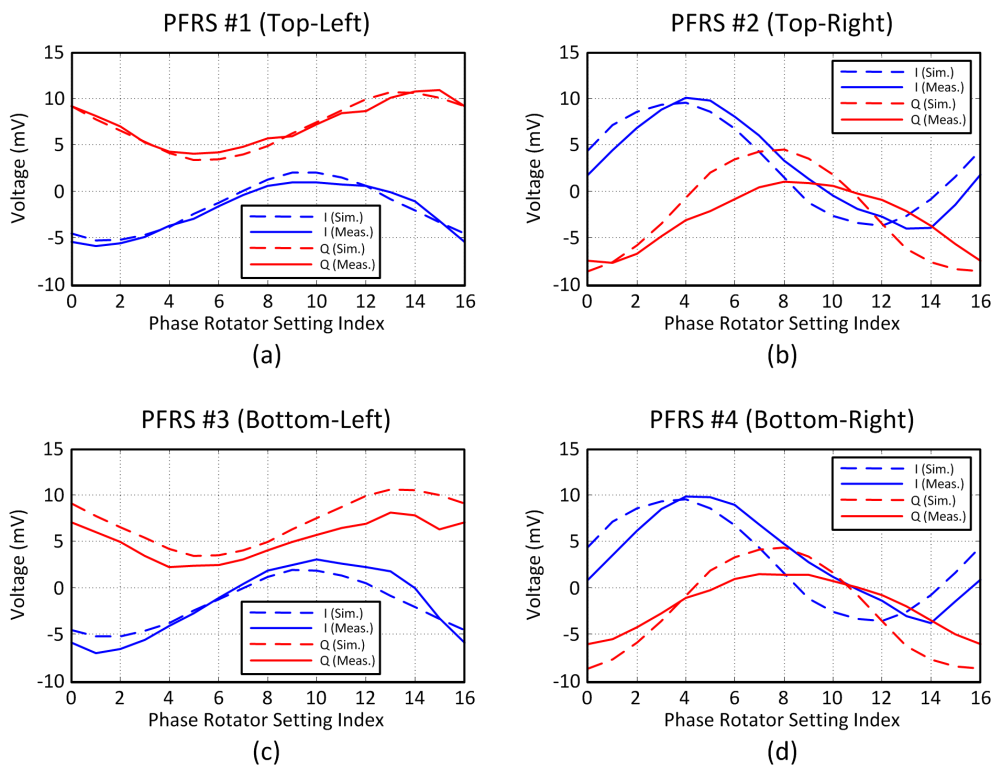


Figure 3.79: Comparison between calibrated measured read-outs of PFRS for both I and Q channels of each sensor and simulated downconverted signals versus the phase difference between the two radiating antennas. The difference between two consequent phase rotator settings is roughly equal to 22.5° .

A similar method to the one explained in section 3.5.3.1 is used to predict the far-field radiation pattern based on the measured PFRS read-outs. The relationships between PFRS read-outs and the E_ϕ and E_θ patterns for $\phi = 0^\circ$ and $\phi = 90^\circ$ planes are extracted from four individual simulations. Figure 3.80 shows one of these simulation setups in HFSS associated with E_θ pattern in $\phi = 0^\circ$ plane. Using the measured PFRS read-outs, radiation patterns for each polarization in each plane are calculated separately and are then combined together to form the overall radiation pattern.

The predicted normalized radiation gain patterns through this method based on measured PFRS read-outs for three cases of in-phase, -90° out of phase, and $+90^\circ$ out of phase operation of the two transmitting antennas are compared to the normalized simulated gain patterns from HFSS and are shown in Figures 3.81, 3.82, and 3.83, respectively. The results indicate a close match between PFRS prediction and the simulated radiation pattern.

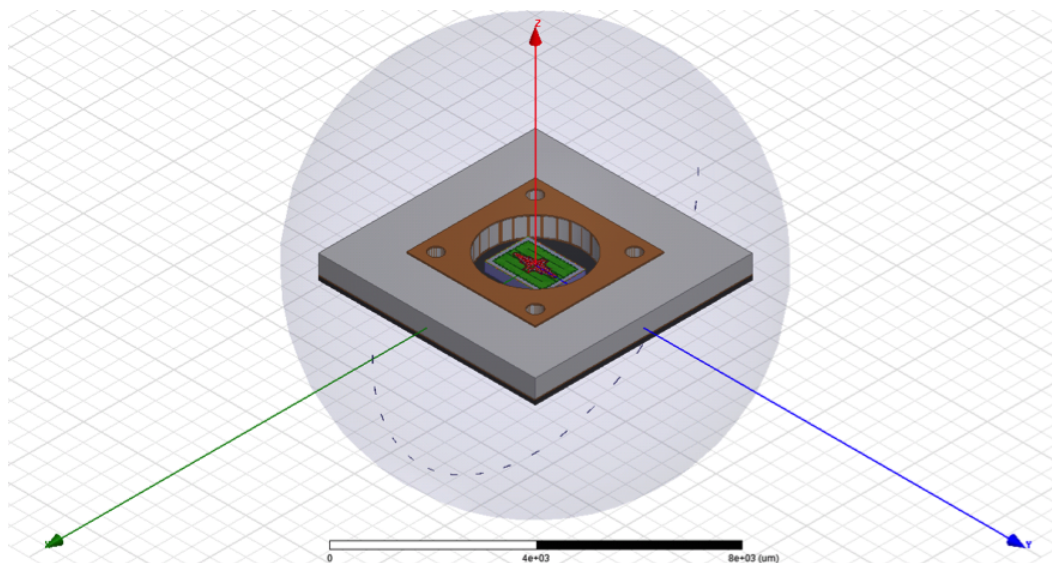


Figure 3.80: Electromagnetic simulation setup to extract relationship between PFRS antennas and far-field radiation pattern of E_θ in $\phi = 0^\circ$ plane.

3.8 Conclusions

Proximal-Field Radiation Sensors (PFRS) are introduced as a new set of tools to enable extraction of far-field radiation properties of integrated antennas from the surface waves inside their dielectric substrates. These sensors allow self-characterization, self-calibration, and self-monitoring of the radiation performance for both printed circuit board (PCB) antennas and integrated circuit (IC) antennas

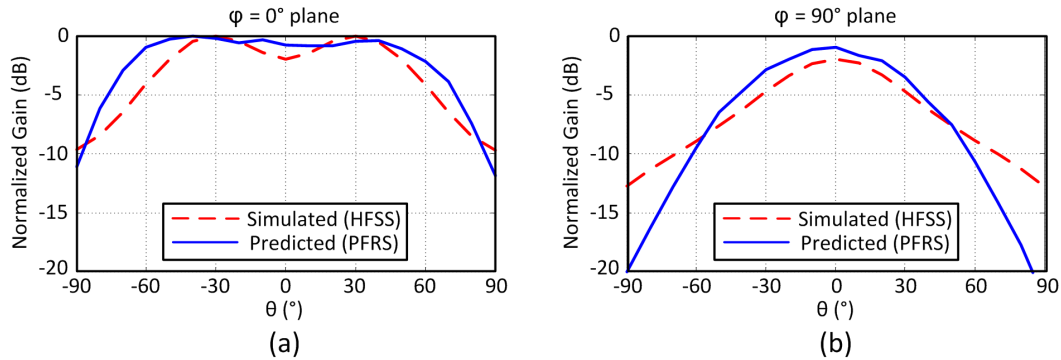


Figure 3.81: Normalized simulated gain pattern from HFSS and predicted gain pattern based on measured PFRS read-outs in (a) $\phi = 0^{\circ}$ and (b) $\phi = 90^{\circ}$ planes for 0° phase difference between the two linear-slot antennas.

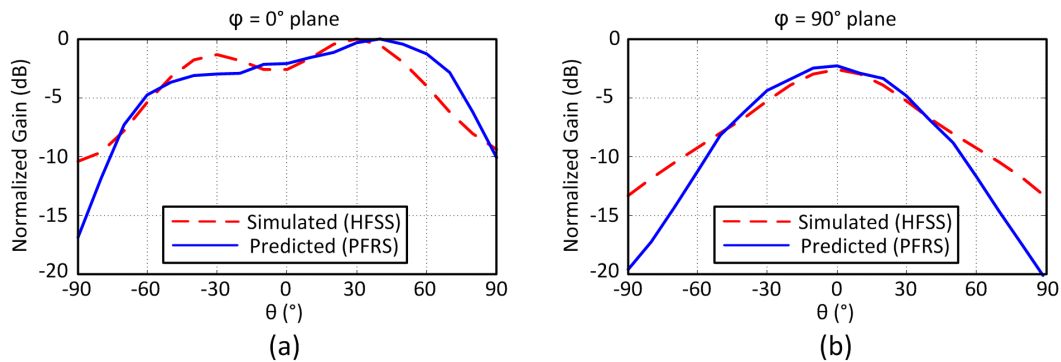


Figure 3.82: Normalized simulated gain pattern from HFSS and predicted gain pattern based on measured PFRS read-outs in (a) $\phi = 0^{\circ}$ and (b) $\phi = 90^{\circ}$ planes for $+90^{\circ}$ phase difference between the two linear-slot antennas.

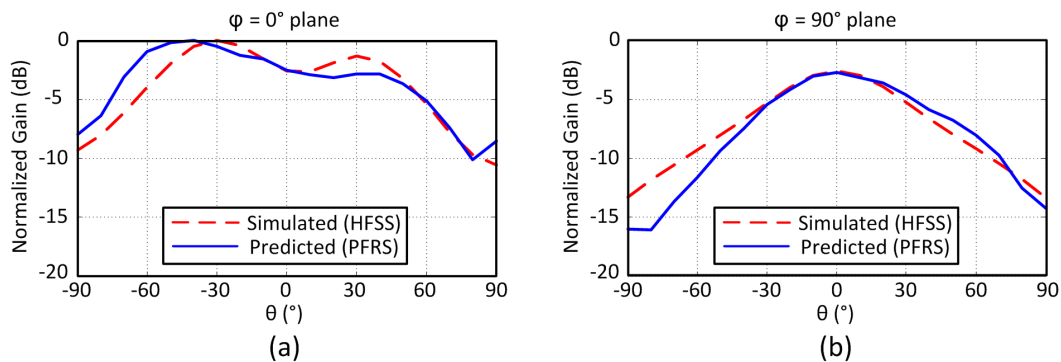


Figure 3.83: Normalized simulated gain pattern from HFSS and predicted gain pattern based on measured PFRS read-outs in (a) $\phi = 0^{\circ}$ and (b) $\phi = 90^{\circ}$ planes for -90° phase difference between the two linear-slot antennas.

without any need to additional test equipment. We discussed how these sensors can be implemented and demonstrated how the far-field radiation properties can be determined from the data they capture through a variety of examples and methods. A PCB prototype consisting of two transmitting patch antennas and four integrated PFRS antennas as well as an IC prototype design of a 2×1 integrated radiator array of linear-slot antennas with four PFRS antennas was fabricated and tested to verify the concept and demonstrate the implemented sensors' capabilities to capture the radiation properties such as gain pattern, radiated polarization, and the steering angle of the antenna array as a few examples of radiation sensors applications.

MULTI-PORT DRIVEN ANTENNAS

4.1 Introduction

Transistor performance increases in silicon CMOS processes have enabled reliable and cost effective millimeter-wave systems, which open up new applications that can take advantage of the high integration level of CMOS to incorporate digital, baseband, mixed-signal, RF, electromagnetic (EM), and radiating designs on a single die [55]–[62]. At high millimeter-wave frequencies, traditional methods of power transfer off chip such as wire bonding and flip chip become increasingly lossy as their self-resonant frequencies are reached, significantly degrading the performance [63], [64]. However, at these frequencies, the dimension of a wavelength becomes comparable to the dimensions of the chip, allowing for efficient power transfer using antennas to radiate directly from the chip using standard planar CMOS metal layers [4]–[6], [65]–[68].

Integration of the radiating antenna with the driving circuitry of a transmitter on the same substrate enforces a new set of trade-offs between the cost of the system and the design parameters, which is different from those of discrete domain. This means the same design approach that was used for discrete circuit blocks and antennas is not necessarily the optimum approach for integrated radiators. Traditional design methodology of transmitters in discrete domain often enforces use of single-port antennas, which adds several unnecessary limitations to the design and performance. However, integration of antennas and driving circuitry on the same substrate opens up an opportunity to explore new design approaches such as co-design of the antenna and circuit blocks. In an integrated radiator, it is easy to drive antennas from multiple points. These Multi-Port Driven (MPD) antennas present many advantages such as elimination of many lossy blocks and enable several additional degrees of freedom that can be used for engineering their current distribution for various purposes such as dynamic control of the performance of the integrated radiator.

This chapter is organized as follows. Section 4.2 compares the advantages of MPD antennas to the limitations of single-port antennas. Design and fabrication of an exemplary integrated MPD antenna is presented in section 4.3, which includes the details of the electromagnetic design of the antenna and the driving circuit imple-

mentation, as well as the measurement results. In section 4.4, we will explain how MPD radiators can be used as a tool for dynamic control of radiation performance, followed by concluding remarks in section 4.5.

4.2 Multi-Port vs. Single-Port Antennas

Transmitter architectures for wireless communications systems are traditionally implemented through connecting separately designed blocks to perform specific tasks. Circuit blocks such as oscillators, mixers, amplifiers, matching networks, power combiners, etc., are independently designed and optimized for power generation, frequency conversion, power amplification, impedance matching, power combining, etc., and are connected to each other in a specific way to provide the output signal to be transferred. This signal is then fed to a single-port antenna to be radiated as electromagnetic (EM) waves at RF or mm-wave frequencies (Figure 4.1). This block-by-block design approach is the result of cost optimization for implementation of transmitters using discrete circuit blocks and antennas. In discrete domain, individual transistors are expensive. Moreover, making more than one physical connection through multiple ports between the blocks would also significantly add to the cost. However, as integrated circuits (IC) technologies have advanced to enable integration of the antenna and the circuit blocks onto the same substrate at mm-wave frequencies, the primary factors that determine the overall cost of the system have also changed. Yet, the traditional block-by-block design methodology has continued to be used even in integrated domain, preventing us from exploring new methods and opportunities, which could potentially provide new advantages.

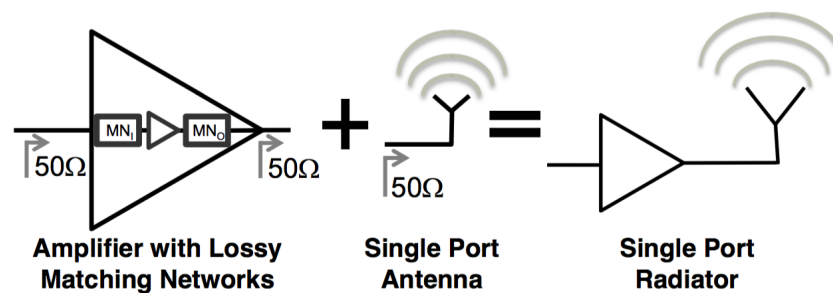


Figure 4.1: Example of traditional single-port radiator with lossy matching networks and independent design of individual blocks [6].

In integrated domain, unlike discrete designs, it is the area of an IC that primarily determines the cost. At high mm-wave frequencies, the size of the antennas is small enough to justify the cost of its integration on the same substrate as the

transistors. However, they are still very large compared to individual transistors and the supporting circuitry. Therefore, the size and consequently the cost of the transmitter IC are mainly determined by the frequency and number of the antennas implemented on the substrate, not by the number of individual transistors which are essentially free of cost. Additionally, as long as the design rules for the metal layers and their density requirements are met, connections between the transistors and antennas are also free. One way to take advantage from this different cost trade-offs in integrated radiators is to perform co-design of circuit blocks and antennas. Also, now the antenna can be driven from any point as long as it is useful from a radiation standpoint (Figure 4.2). This opens up the new design space of Multi-Port Driven (MPD) antennas [6] that has been often ignored in conventional single-port design methods.

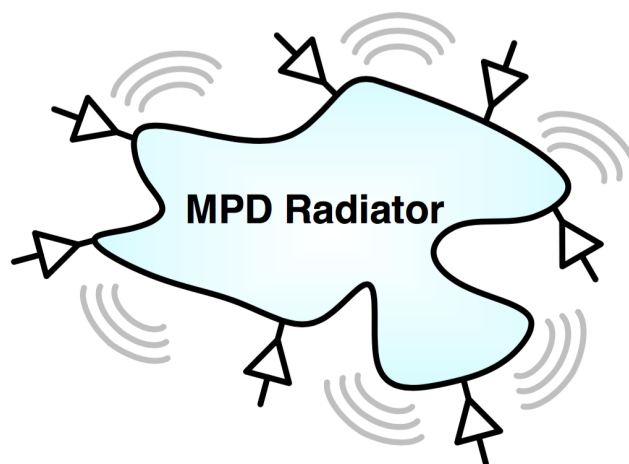


Figure 4.2: Multi-port driven radiator design methodology for integrated radiation where drivers directly feed multiple ports of the antenna [6]

4.2.1 Limitations of Single-Port Antennas

In the design of traditional transmitters with single-port antennas, often the fact that the transistors and the connections between them and the antenna are free is ignored. Such antennas enforce separate design and independent optimization of circuit blocks and antennas and prevent us from using the advantages of additional degrees of freedom, which could be achieved through the co-design of antenna and circuit blocks. Also, it is usually difficult to design a single-port antenna with high radiation efficiency and low input impedance. This is mainly because the radiation resistance, and thus the input impedance of the single-port antenna needs to be high so that it is much larger than the loss resistance. In a transmitter with a single-port

antenna, usually the signal is first divided and amplified by parallel stages and is then combined at the output to increase the output power level before feeding the antenna. Since the power combining stage happens after the final output transistor any loss in that stage would directly degrade the output power and significantly reduce the efficiency.

4.2.2 Advantages of Multi-Port Antennas

Use of an MPD antenna in an integrated transmitter allows hybrid design of the antenna and the drive circuitry that is also implemented on the same substrate. This, in turn, allows taking advantage of the additional design space provided through the co-design. They could eliminate use of many independent elements and blocks for power combining, output impedance matching network, and power transfer, etc., and consequently reduce the losses associated with them. As a result of elimination of these blocks, the driver circuitry can now be placed much closer to the driving ports of the antenna. The additional degrees of freedom provided by the additional driving ports on the antenna enable engineering of the current pattern on the antenna structure based on the desired far-field radiation properties.

In an MPD antenna, the location of the driving ports can be selected such that virtual short circuits are created on the antenna. In such an arrangement, the currents from different driving ports can add up without increasing the voltages seen at the ports and thus allow implementation of low impedance designs with high efficiencies. For high power applications, the breakdown voltage of the output transistors limits the peak voltage at the driving points. Therefore, the output stage needs to provide high output current to meet the high output power level requirement, which in turn results in low output impedance. In such scenarios, again the MPD antenna can be engineered to present low input impedance through the superposition of multiple drive ports to match the low optimal load impedance of the output stage.

The MPD antenna performs the power combining as well, since the currents produced by the various driver stages begin to radiate immediately after being produced by the transistors. Furthermore, an analysis of an MPD antenna [6] shows that they are also capable of supporting a wide bandwidth.

4.3 Integrated Multi-Port Driven Slot Ring Traveling-Wave Radiator

Two types of antennas commonly used on-chip include patch and wire antennas such as dipoles, loops, and the multi-port driven (MPD) wire antennas [6]. Patch antennas have the benefit of being able to shield the antenna from the lossy doped substrate

by putting a ground plane on the lowest metal without a significant loss in radiation efficiency. However, their resonant nature means that they become narrowband, and occupy a large exclusive use area for the antenna unless the ground plane is raised to a higher metal layer, reducing the efficiency of the antenna. Wire antennas, on the other hand, are often exposed to the substrate, though work has been done to minimize the amount of power lost through coupling to substrate modes. They also usually require all metals to be pulled back from the antenna to prevent mirror currents that would cancel out their radiation. This both increases their exclusive use area, as well as requires the use of metal fill exclude or a low fill marker similar to that of an inductor to prevent eddy currents in the fill that can cause a significant degradation to radiation efficiency.

One way to reduce the exclusive use area of the antenna and the low fill requirement is to use EM duality [69] to create a slot dual of a wire antenna, such as a slot dipole or folded slot dipole [70], as shown in Figure 4.3. The MPD antennas can also have slot duals, which allow for a low exclusive use area, as well as the power-combining, impedance-matching, and power-transfer benefits [68].

In this section we present a slot-based multi-port driven radiator operating at 134.5 GHz that creates a traveling wave around the multi-port slot ring antenna by driving it at four different points in quadrature to create circularly polarized radiation directly from the chip.¹

4.3.1 Slot Antenna Design

4.3.1.1 Electromagnetic Duality for Slot Antennas

Electromagnetic duality as it relates to slot antennas comes from Babinet's principal, which states that if the fields behind a conducting screen with an opening are added to the fields of its complementary structure, the resulting summation is equal to the field produced when there is no screen [1]. This observation of screens in the presence of EM fields can be applied in the case where the screens themselves are being excited and producing their own radiating fields. The fields produced by the complement of the known antenna are the same as if a fictional magnetic current replaced the electric currents of the known wire antenna, which has the effect of replacing the external fields \mathbf{H}_w with \mathbf{E}_s/η and \mathbf{E}_w with $-\eta\mathbf{H}_s$, where \mathbf{E} and \mathbf{H} are the electric and magnetic fields, the subscripts w and s denote the wire and slot

¹This project was a joint effort with my colleague Steven Bowers. I was responsible for the circuit design including the oscillator and amplifiers as well as electromagnetic design of the inductors and matching networks, and Steven was in charge of the antenna design.

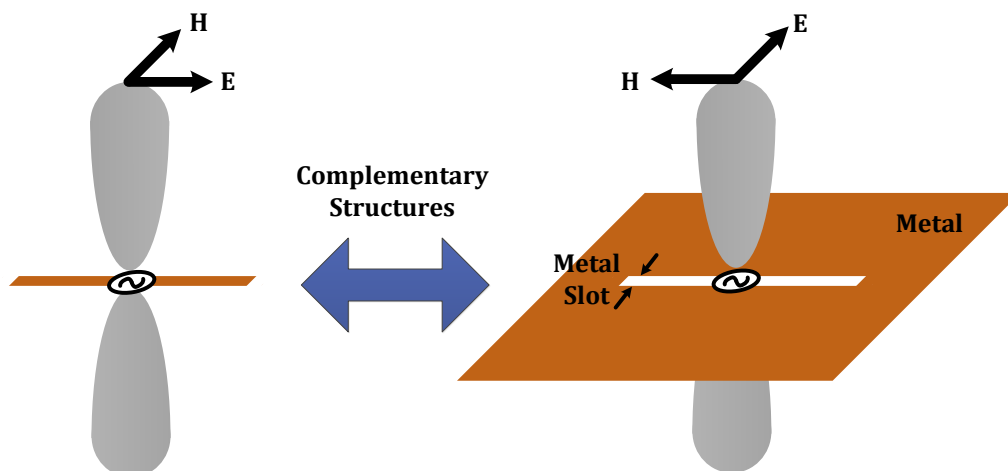


Figure 4.3: Example of EM duality for a dipole antenna, with the cross-section of the beam, and \mathbf{E} and \mathbf{H} fields shown. The dual complement of this is the slot dipole, where the series source of the dipole has been replaced with an orthogonal source across the slot, and the \mathbf{E} and \mathbf{H} fields have been normalized and swapped.

antennas, respectively, and η is the characteristic impedance of the medium. Also, the series sources of the wire antenna are replaced with parallel sources across the slot antenna, as depicted in Figure 4.3. This result means that a wire antenna that radiates effectively will also have a slot dual that radiates effectively, with a similar radiation pattern, but possibly with different polarizations, as the directions of the far field \mathbf{E} and \mathbf{H} vectors have changed. An example shown in the figure is that of a dipole, with a series source located at the origin, along with its complement slot dipole, and the resulting change in \mathbf{E} and \mathbf{H} fields.

4.3.1.2 Traveling-Wave Slot Antenna

The multi-port traveling-wave slot antenna is created by taking the complement of a multi-port ring antenna whose ports are driven in series along the ring, as shown in Figure 4.4 [68]. The ring is about one wavelength in circumference. The series ports along the ring of the wire version of antenna contrast to [6], where current was injected into the ring at ports around the ring. These series ports still create a traveling wave, which can be better understood by using symmetry and source substitution. The symmetry of the antenna means that when driven in quadrature these four power sources will have the same voltage and current running through them, each phased 90° apart. For this specific drive setup, source substitution can be used to replace the power sources with their equivalent current sources.

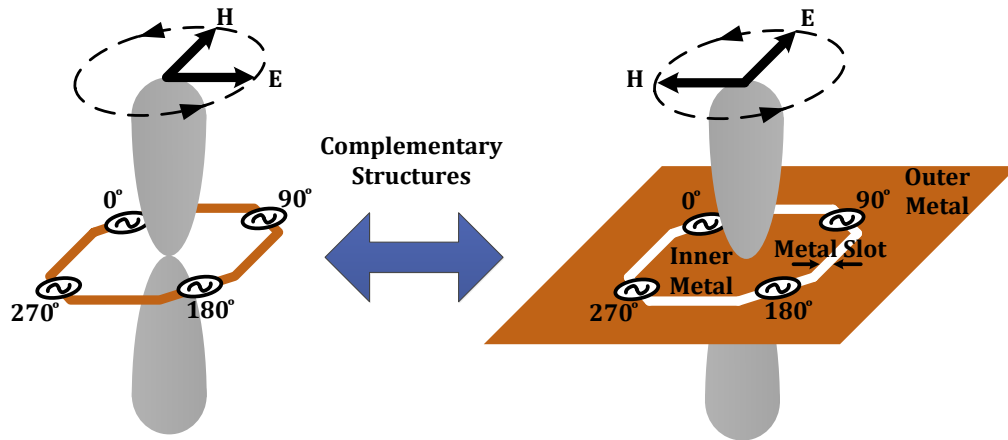


Figure 4.4: Electromagnetic Duality for the MPD slot ring antenna converts a four-series port wire ring antenna into a four-port slot ring driven in quadrature, producing a traveling wave around the ring and circular polarization in the far field.

Looking at the antenna with current sources, each source is located about a quarter-wavelength around the ring and driven 90° out-of-phase compared with the source that follows it. This means that when one of the sources is at a maximum, the source opposite from it on the ring is also at a maximum, with a 180° phase shift, and a 180° change in direction due to the curvature of the ring, which makes its current pointed in the same direction in space. At the same instant, both of the other two sources 90° out-of-phase will have zero amplitude, with the current creating a sinusoidal wave in a similar manner to a current wave on a transmission line, as shown in Figure 4.5, which then rotates around the ring as a traveling wave over one period of oscillation. The far-field electric field \mathbf{E} in the broadside direction due to a set of currents on a plane can be expressed as

$$\mathbf{E} = \frac{j\omega\mu}{4\pi} \int_C \mathbf{I} \frac{e^{-jkR}}{R} dl \quad (4.1)$$

The two current maximums on the ring are always pointed in the same direction at any given instant, which means that the integration of that current around both sides of the ring will add constructively, and thus radiates effectively. This circularly traveling current wave creates a circular polarization in the far field.

The complement of this wire antenna is a slot ring driven across the slot at four ports in quadrature. This will create a radiated field equivalent to having a fictitious magnetic current traveling wave identical to the electrical current traveling wave of Figure 4.5, and since the wire antenna radiates effectively, so will its slot dual.

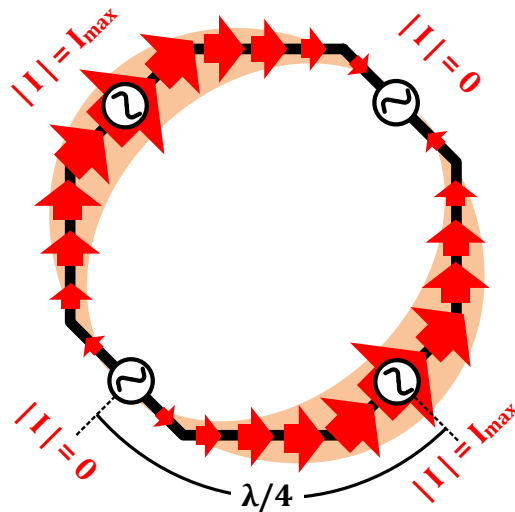


Figure 4.5: Current distribution on the four-series port ring antenna when two of the ports are at their maximum amplitude, while the other two have zero amplitude. This current distribution then rotates around the ring in a traveling-wave fashion over one oscillation period.

When the E and H fields are swapped, the polarization is also rotated 90° in space, but because the polarization is still circular, a 90° shift in space is identical to a 90° shift in phase.

The antenna is divided into two pieces of metal by the slot ring, an inner ground plane, and an outer ac ground plane. In order to drive the four antenna ports across the slot, microstrip transmission line feeds are used where the ground plane of the transmission line is the inner ground of the antenna, and the signal line crosses the slot and connects to the outer ground plane to drive the port, as shown in Figure 4.6. The drive circuitry is located at the center of the antenna and consists of a quadrature oscillator followed by amplification stages and is discussed in Section 4.3.2. The output of the driver circuitry is routed using these microstrip transmission lines to the antenna's ports, maintaining similar line lengths to preserve amplitude and phase matching. The physical size of the inner ground is on the same order of magnitude as the wavelength, meaning that it must be considered as a distributed element, rather than a lumped element. This means that the local, rather than a global, ground reference must be considered at the input to the feed microstrip transmission lines, as well as at the ports of the antenna that the feed lines drive.

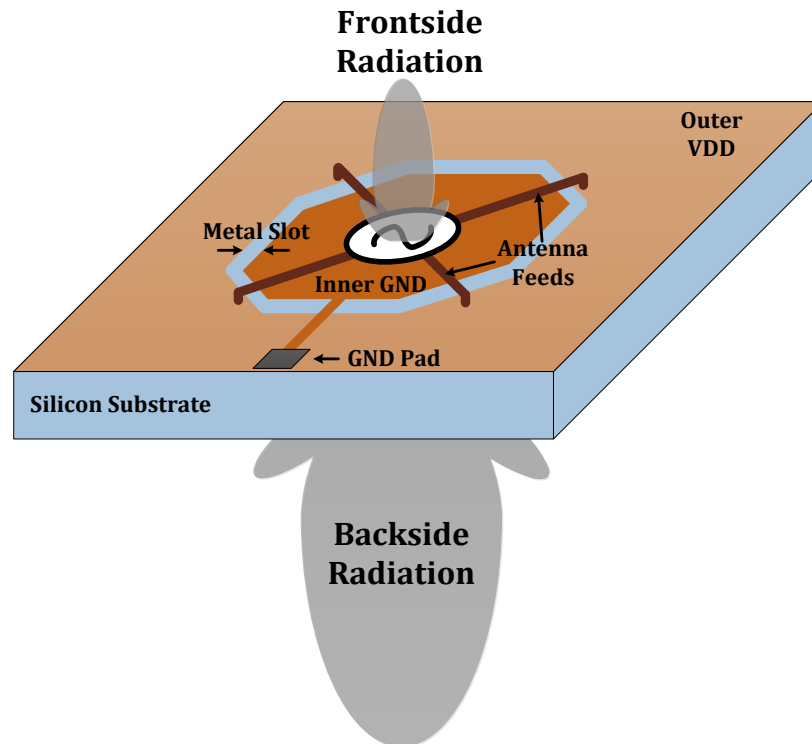


Figure 4.6: 3-D depiction of the traveling-wave slot radiator, with quadrature driver circuitry at the center of the chip that drives across the metal slot at four ports. The inner ground plane extends orthogonally across the slot out to the edge of the chip to provide a bond pad to sink the dc current, and the outer ac ground plane is biased at VDD to provide dc power to the driver circuitry through the antenna feeds.

The outer ac ground plane is biased at VDD and the supply is fed through the transmission lines to the driver circuitry. The slot ring is a complete ring, isolating the inner ground plane from the outer ground plane, so a secondary line is fed orthogonal to the slot from the inner ground plane out to a bond pad at the edge of the chip to provide a dc ground current path, as seen in Figure 4.6. Routing this line orthogonal to the slot minimizes its interaction with the radiation, but does create an asymmetry that shifts this angle of the radiated beam off of the broadside axis and detuned the polarization away from the ideal circular polarization axial ratio of 0 dB. Additional taps can be added to increase the symmetry of the radiator, and thus the radiation pattern and polarization, but come at a cost of additional on-chip loss, due to the finite quality factor of the EM structures.

The substrate also creates challenges for antennas integrated onto lossy silicon substrates. Most of the power will be radiated down into the substrate due to the

higher dielectric constant of silicon. This radiator is designed for direct backside radiation without a lens. The entire four-port traveling-wave slot antenna with the silicon substrate was simulated using Ansoft HFSS, and exhibits a simulated maximum gain of 3.0 dBi, a 3-dB bandwidth of the gain of the antenna of 48 GHz, and radiation efficiency of 39%, with a single lobe radiation pattern (shown along with the measured pattern in Figure 4.20). The simulated polarization axial ratio is 3.1 dB, which corresponds to a cross polarization of right-handed circularly polarized radiated field compared with the desired left-handed circularly polarized radiated field of -14.9 dB. The tolerance of the antenna to significant phase mismatch of $\pm 15^\circ$ of the quadrature signals is also simulated to affect the antenna gain by less than 0.2 dB and polarization axial ratio by 1.2 dB.

4.3.2 Circuit Implementation

Efficient radiation of circularly polarized slot antennas relies on generation of correct phases through driving circuitry. Quadrature signals must be generated to drive the antenna at the desired ports. In this work, we have designed a quadrature oscillator to meet this requirement. Figure 4.7 shows the block diagram of the driving circuitry. The quadrature oscillator generates two differential sets of signals whose phases are 90° apart, i.e., (OSC_0 , OSC_{180}) and (OSC_{90} , OSC_{270}). Each differential set is amplified through three buffer stages, which provide additional power, as well as isolation between antenna and oscillator inductors. The four final output lines of the last buffers (P_0 , P_{180} , P_{90} , and P_{270}) are then routed to the corresponding ports on the slot antenna through microstrip transmission lines. This requires crossing two of the lines (P_{90} and P_{180}) such that the correct sequence of the phases appears on the antenna.

4.3.2.1 Oscillator and Inductor Design

The quadrature oscillator provides the four required phases to drive the slot antenna for circularly polarized radiation. Quadrature signal generation is achieved by coupling two differential cross-coupled pair oscillators to each other. Previously, it has been shown that coupling two cross-coupled oscillators through parallel transistors is sufficient to achieve quadrature oscillation [54]. However, generation of accurate quadrature signals through such a coupling mechanism requires strong coupling (large parallel transistors) between the two oscillators, which, in turn, degrades the phase noise of the generated outputs [71], [72]. To avoid strong quadrature coupling through large parallel transistors, we have used two simultaneous coupling

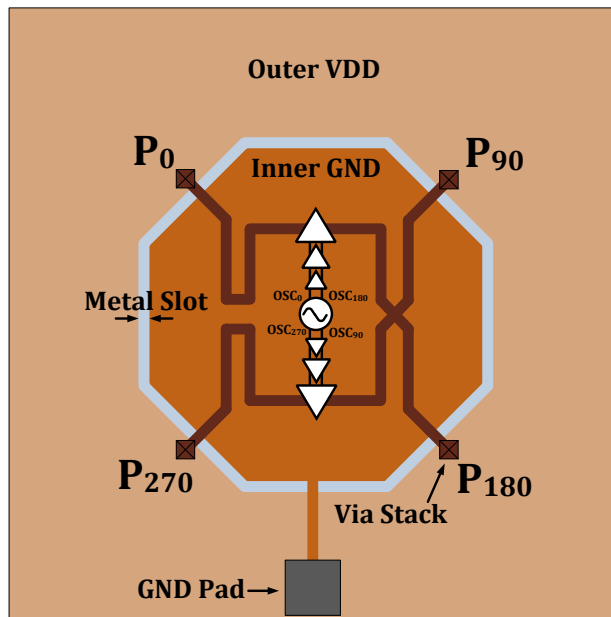


Figure 4.7: Block diagram showing the driver circuitry and the slot ring antenna. A quadrature oscillator sits at the center of the chip and is amplified through three buffer amplifier stages before being routed out to the antenna ports across the slot.

mechanisms between the two oscillators.

The first coupling mechanism happens through the resistive network (R_C), which couples the two oscillators at the tails by second harmonic injection between them, as seen in Figure 4.8. Assuming this symmetric two-port network as the only coupling mechanism between the two oscillators for the moment, the overall coupled system can be considered as a four-port network whose voltage–current relationship is described by $[V] = [Z].[I]$, where $[V]$ and $[I]$ are vectors of voltage and current phasors of the four output ports, respectively, and $[Z]$ is the impedance matrix. The existing symmetries in the network enforce that $Z_{11} = Z_{22} = Z_{33} = Z_{44}$, $Z_{12} = Z_{14} = Z_{23} = Z_{34}$, and $Z_{13} = Z_{24}$. Thus, the analysis done in [73] predicts that such system can support four modes of operation corresponding to the four eigenvectors of the system, which are 1) common-mode oscillation (where all four outputs oscillate with the same phase, $I_1 = I_2 = I_3 = I_4$), 2) differential-mode oscillation (where each oscillator's output is differential, but the two differential sets have the same phase, $I_1 = I_2 = -I_3 = -I_4$), 3) leading quadrature-mode oscillation ($I_1 = e^{+j\pi/2}I_2 = e^{+j\pi}I_3 = e^{+j3\pi/2}I_4$), and 4) Lagging quadrature-mode oscillation ($I_1 = e^{-j\pi/2}I_2 = e^{-j\pi}I_3 = e^{-j3\pi/2}I_4$). According to the antenna structure, the first two modes would not result in effective circularly polarized radiation since

Another important parameter in the design of quadrature oscillators at 135 GHz is the tank inductor design. In order to have enough margin for reliable oscillator startup, large transistors have been used to provide sufficient gm, which, in turn, reduces the required inductance value for oscillation at 135 GHz. Lower inductance value increases the sensitivity of the oscillation frequency to any inductance deviation from the nominal value due to possible simulation inaccuracy or process variation in the metal stack. In this work, we have used a custom EM structure, as well as extensive EM simulations and modeling to design the tank inductors as a parallel combination of larger and more reliable inductors to overcome this issue.

Figure 4.9 shows the 3-D structure of the two tank inductors that was used in Ansoft HFSS for EM simulation. Microstrip transmission lines have been used to implement the inductors. Each of the upper and lower structures correspond to one differential inductor for one of the cross-coupled pair oscillators and the open area in the middle of the ground plane corresponds to the location of oscillator active devices, which were excluded from EM simulation. Each differential inductor consists of four single-ended inductors that are formed by shorting four transmission lines to VDD at two of the corners through two via stacks. In other words, the drain of each transistor of the cross-coupled pair is connected to VDD through two parallel inductors, which are twice the size of the required inductance for oscillation at 135 GHz. Such a structure reduces the sensitivity of oscillation frequency to inductance variation since the reliability in the design and simulation of larger inductors is much higher compared to small inductors.

The simulation setup includes six ports on each of the two inductors: two input ports (the drains of cross-coupled transistors), two output ports (the gates of first buffer stage), and two VDD ports (at the two VDD taps for each differential inductor). The first step to verify that such a structure is practical for our quadrature oscillator is to make sure that the EM coupling between the upper and lower inductors is negligible. Otherwise, such interaction between the two inductors would affect the other two coupling mechanisms that are implemented with circuit components and could significantly affect quadrature operation. To evaluate this concern, magnitudes of all the S-parameters between one of the input ports of the upper inductor and all six ports of the lower inductor are plotted in Figure 4.10. As can be seen on the plot, the isolation between all the ports is more than 42 dB over a wide frequency range from 120 to 140 GHz, which means that EM coupling between the two inductors would not be an issue.

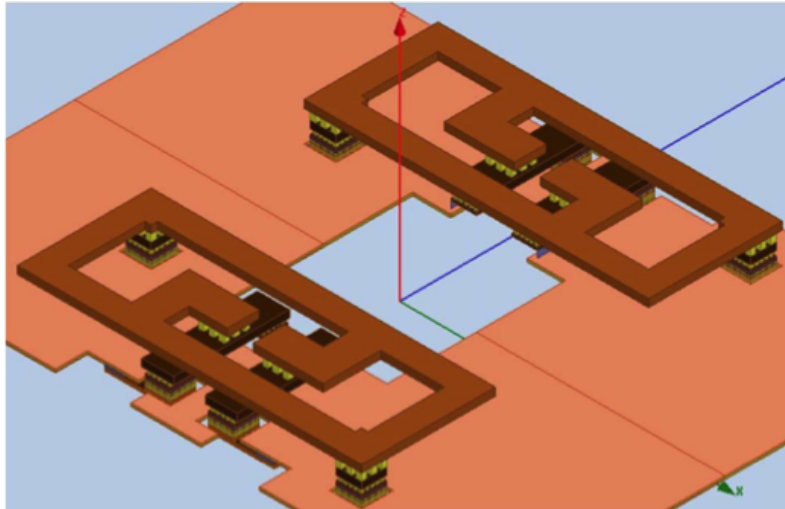


Figure 4.9: 3-D structure of the custom microstrip-line-based tank inductors. Each of the two structures corresponds to one differential inductor with two VDD taps, which is attached to one of the two cross-coupled VCOs.

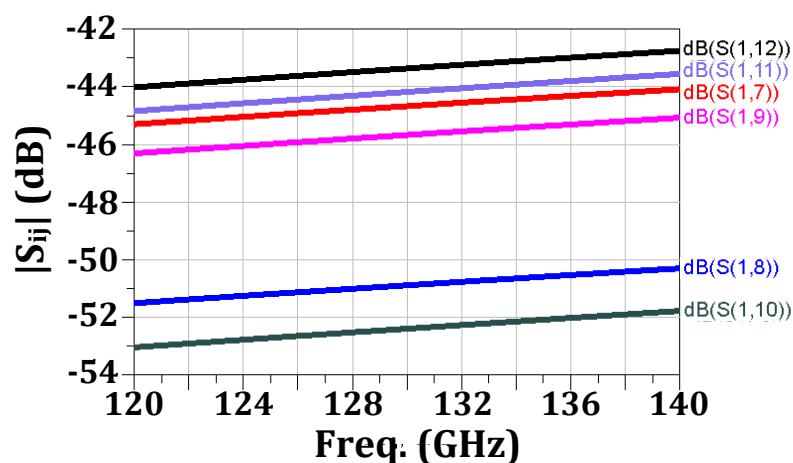


Figure 4.10: Isolation between one of the input ports of the upper inductor (port 1) and all six ports of the lower inductor (ports 7–12). Isolation is more than 42 dB over a wide frequency range.

The next step in the design of tank inductors is to use a circuit simulator to simulate the oscillation frequency of the whole quadrature oscillator including both circuit elements and EM structures. Running such a simulation through periodic steady state (PSS) or transient analysis in Cadence by using the simulated S-parameter matrix directly from HFSS requires EM simulation of the structure down to very low frequencies. Furthermore, convergence time for such circuit simulations is very

large even if the structure is EM simulated at very low frequencies. To overcome this issue, we used an equivalent-circuit model for the inductors based on the physics of their EM structure, as shown in Figure 4.11. The values of the circuit elements in this model are optimized by Agilent ADS so that the corresponding S-parameters of the equivalent-circuit model and the EM simulated structure in HFSS are matched over a wide frequency range of 120–140 GHz. It should be noted that due to large isolation between the upper and lower inductors, we are able to neglect the EM coupling between them and use the same circuit model for both of the two inductors. Figure 4.12 demonstrates the accuracy of the model by comparing two of the S-parameters (S_{11} and S_{13}) of the equivalent-circuit model and HFSS simulation as an example. As can be seen from these plots, the model is well matched to the EM simulated structure over the desired frequency range.

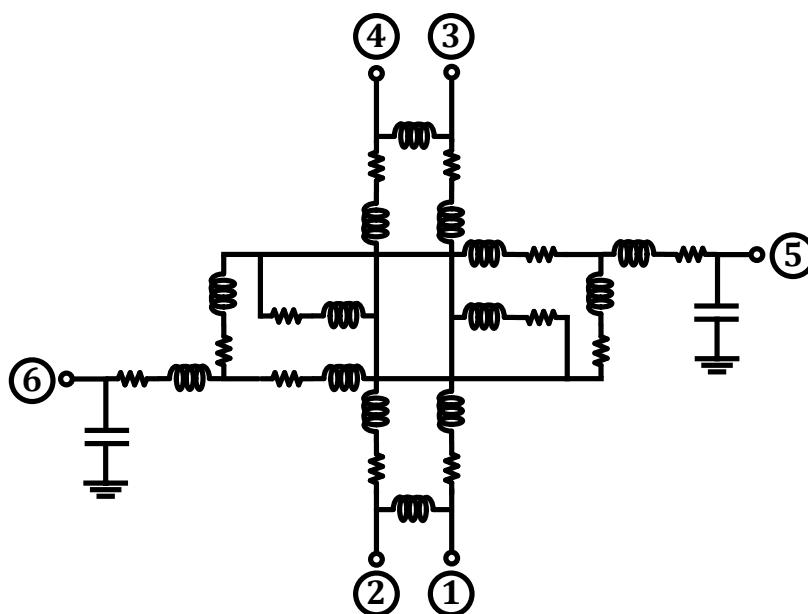


Figure 4.11: Equivalent-circuit model for each differential tank inductor. The topology of the model is chosen based on physical structure and nature of the coupling between different segments of the inductor. Component values are optimized by Agilent ADS to minimize modeling error.

Using the equivalent-circuit model together with the extracted layout of the rest of the quadrature oscillator circuit, shown in Figure 4.13, we can simulate the oscillation frequency. Figure 4.14 shows the simulated waveforms of the quadrature oscillator with such simulation. The simulated frequency of oscillation is 131 GHz and the waveforms verify quadrature oscillation as expected.

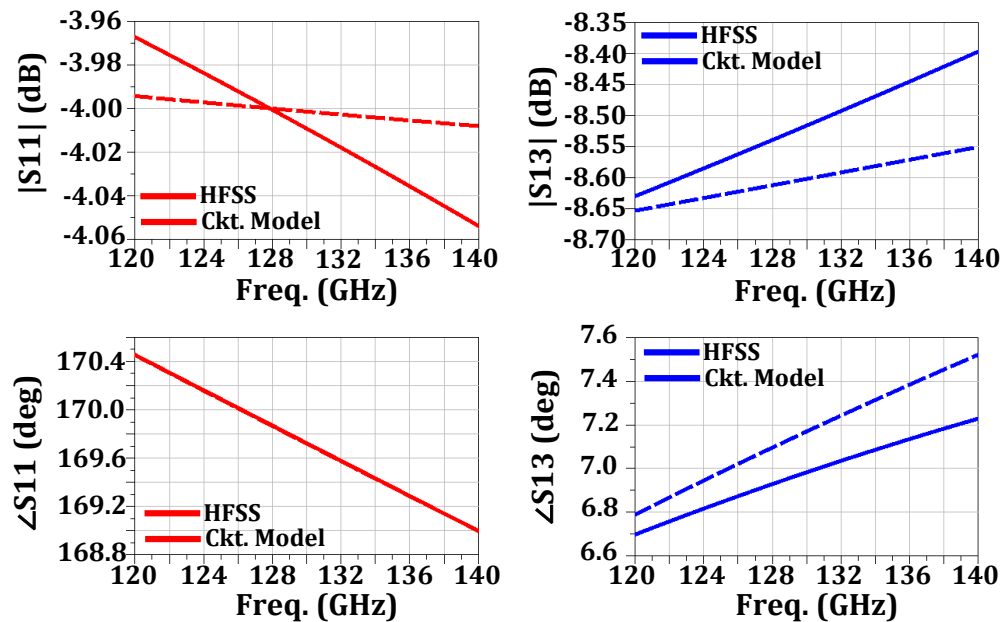


Figure 4.12: Comparison between S-parameters of the EM simulation of the inductor and S-parameters of the optimized equivalent-circuit model of the inductor. The circuit model is well matched to EM simulation over a wide frequency range.

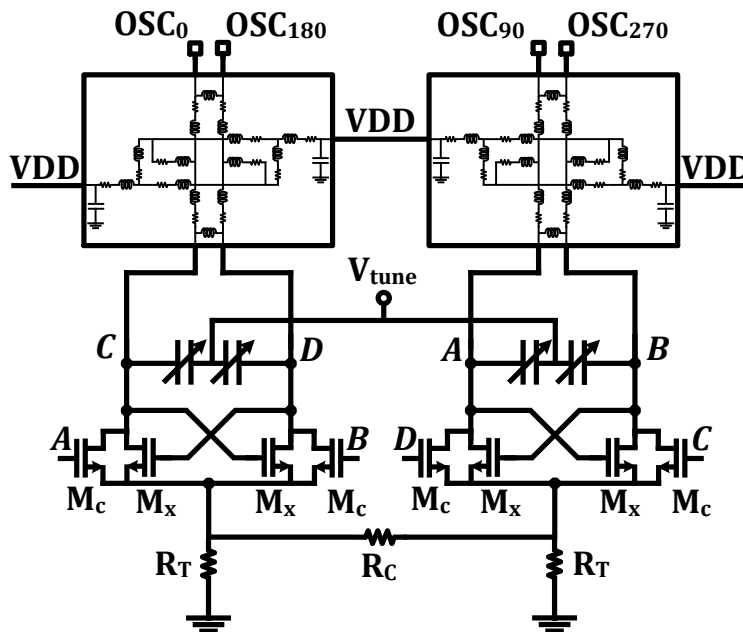


Figure 4.13: Equivalent-circuit model is used with extracted layout of quadrature oscillator's transistors and resistors to simulate oscillation frequency.

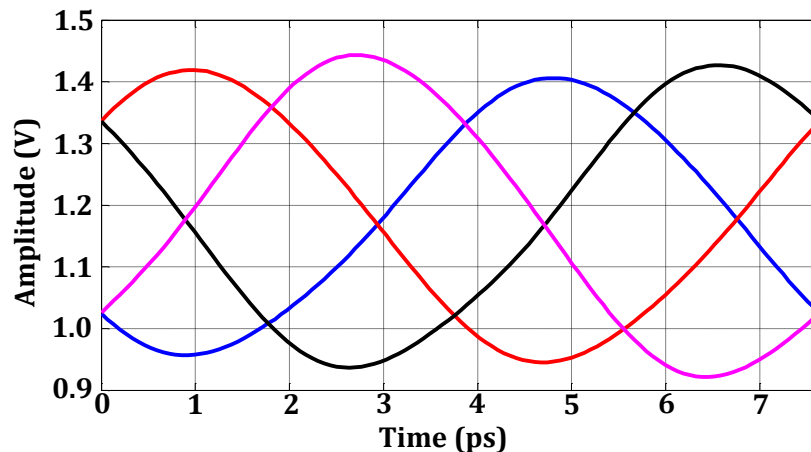


Figure 4.14: Simulated output waveforms of the quadrature oscillator. Quadrature waveforms verify correct operation of the two coupling mechanisms.

4.3.2.2 Amplifier Design

Each of the two differential outputs of the quadrature oscillator is fed to a chain of differential buffer stages after which they drive the antenna ports. This allows for considerable isolation between the antenna and quadrature oscillator and minimizes the effect of the antenna on oscillation frequency. The buffer stages are implemented as differential amplifiers to enable using differential inductors to take advantage of the virtual grounds and reduce the amount of required bypass capacitance for proper differential performance. The schematic of the buffer chain is shown in Figure 4.15. All three buffers are cascode stages and are accordingly sized to maintain sufficient power levels. The first buffer is $20\text{-}\mu\text{m}$ wide, the second one is $40\text{-}\mu\text{m}$ wide, and the last stage consists of $60\text{-}\mu\text{m}$ -wide transistors. Impedance matching between the buffer stages is performed by shunt inductors and series capacitors, which also serve as ac coupling capacitors to allow using different bias voltages for the input gates of each stage and the output drains of the previous buffer. The matching inductors are implemented by microstrip lines and were designed and simulated in Ansoft HFSS to achieve $L_1 = 40\text{ pH}$ and $L_2 = 24\text{ pH}$ and the matching capacitors values are $C_1 = 45\text{ fF}$ and $C_2 = 75\text{ fF}$. The total simulated output power going into the four ports of the antenna is 3.6 dBm . The main design variable for impedance matching of the output stage of the amplifier to the antenna is the size of the output stage's shunt inductor (L_3). The widths of the feed lines can also be modified to affect the match, but are more limited by layout constraints.

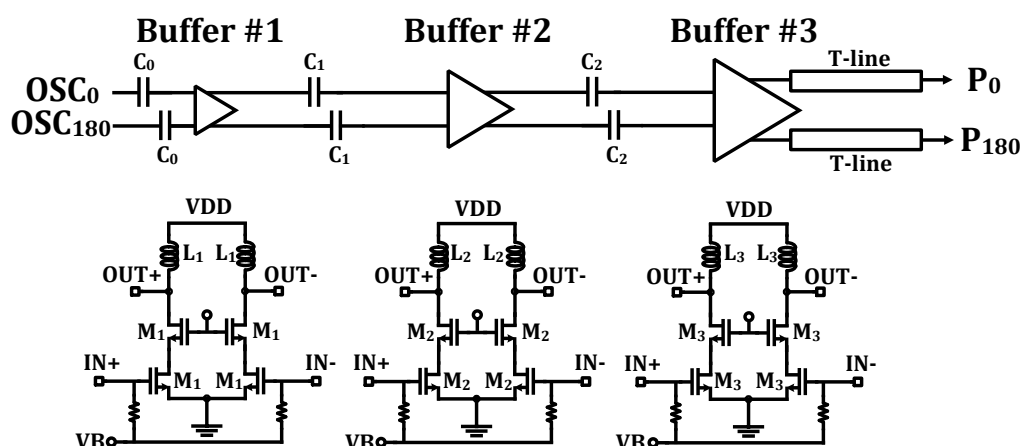


Figure 4.15: Schematic of the amplifier chain consisting of three cascode stages with 20-, 40-, and 60- μm widths, respectively.

4.3.3 Measurements

The radiator was fabricated using IBM's 32-nm CMOS silicon-on-insulator (SOI) process with 11 copper metal layers, as well as a top aluminum redistribution layer. The VDD plane was implemented using the eighth and ninth metal layers, the inner ground used the fifth and sixth metal layers, and the microstrip transmission lines and inductors were implemented on the eleventh metal layer. A 6- μm -wide strip of metal fill exclude is implemented directly around the slot itself (3 μm on each side of the slot) to prevent loss caused by the fill in the regions of highest electric field. Due to the narrowness of this fill exclude, it does not violate any standard design rules of the process. Foundry approved fill exclude is also implemented for the top six metal layers under the transmission lines and inductors. A die photograph of the radiator with a breakout photograph showing the antenna, amplifier inductors, and fill exclude is given in Figure 4.16.

The chip is mounted on a piece of transparent tape to enable backside radiation. To provide dc supply and a bias adjustment, the tape is attached to the back of a printed circuit board (PCB) with a cutout for the chip, enabling wire bonds to connect from the top of the chip to the top of the PCB, as shown in Figure 4.17.

The PCB is then mounted to a 2-D stepper motor that allows for antenna pattern measurements oriented so that the radiating backside of the chip is facing outward, as shown in Figure 4.18. The radiated signal is received using a 23-dB gain (provided by the manufacturer) linearly polarized horn antenna. The antenna is placed 9 cm

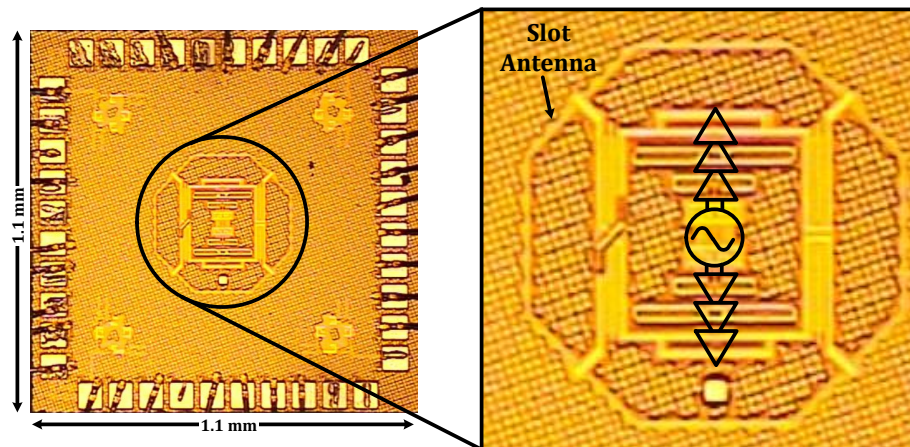


Figure 4.16: Die photograph of the traveling-wave slot ring radiator with a breakout view of the antenna, driver circuitry, and areas of fill exclude.

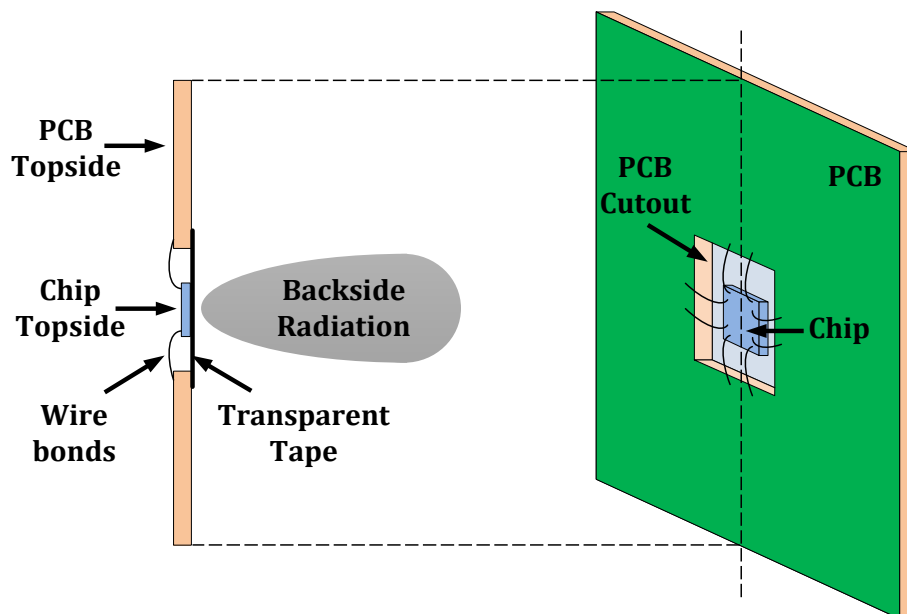


Figure 4.17: Device packaging to enable wire-bond connection of dc supply while radiating out from the backside of the chip.

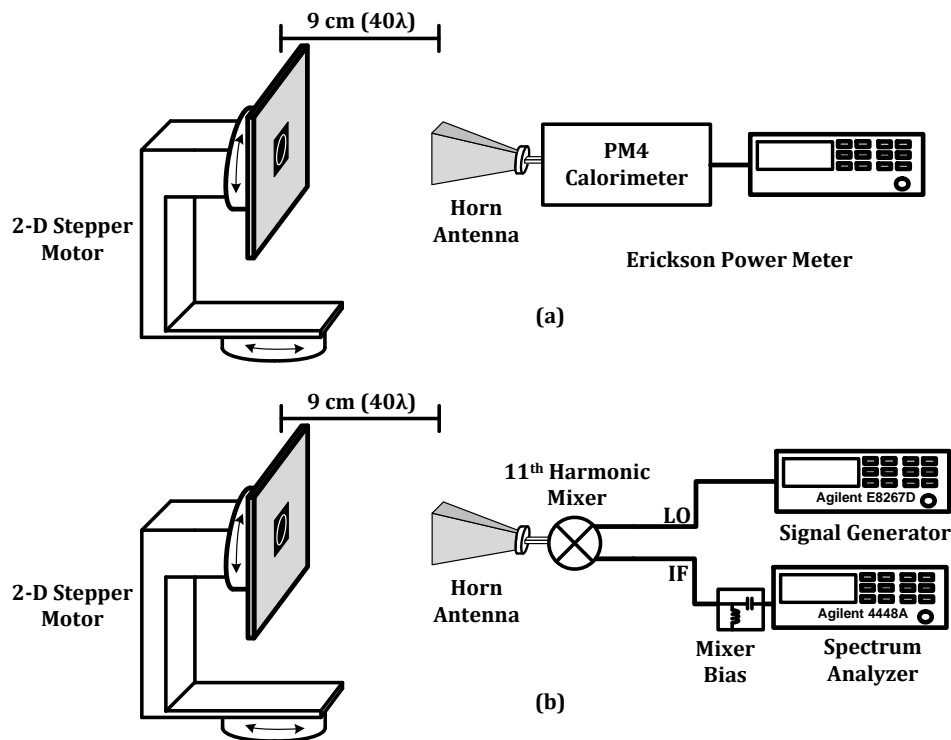


Figure 4.18: Measurement setup for the traveling-wave slot radiator for: (a) absolute power calibration and (b) spectral measurement.

away from the chip. After the antenna, the signal is fed either into an Erickson Power Meter PM4 calorimeter for absolute power measurements or into a Pacific millimeter-wave model DM eleventh harmonic mixer. After that the baseband signal is amplified and the spectrum is read by a spectrum analyzer.

The horn antenna captures the projection of the radiated electric field onto the axis of the horn's polarization. By rotating the antenna 180° , and measuring this projection at many points in between, the major and minor axes of the polarization ellipse can be identified, and the polarization ratio of those two axes gives a measure of how close the measured radiation is to circular polarization.

The radiated signal is first captured by the PM4 power meter, capturing 1.55 mW of power summed from two measurements taken with orthogonal antenna polarizations. Given the 23-dB gain of the antenna and 9-cm distance to the chip, the Friis equation can be used [1] to calculate the effective isotropic radiated power (EIRP) to be 6.0 dBm, similar to the simulated EIRP of 6.6 dBm. This data is then used

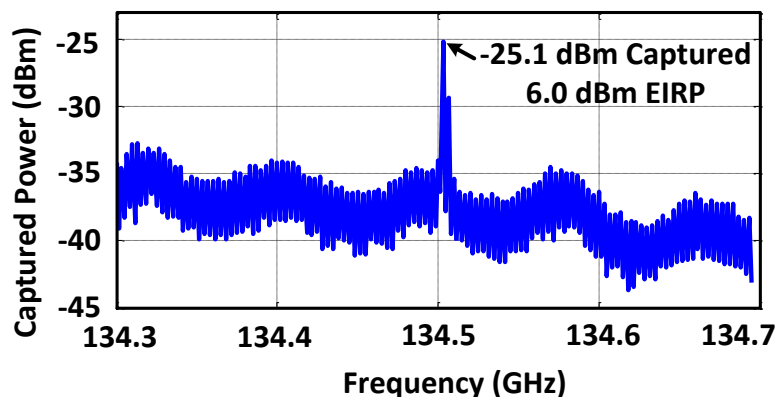


Figure 4.19: Measured calibrated spectrum of the received signal shows -25.1 -dBm captured power, which corresponds to an EIRP of 6.0 dBm at 134.5 GHz when considering the distance and gain of the receive antenna.

to calibrate the harmonic mixer and spectrum analyzer. This calibrated spectrum is shown in Figure 4.19. The spectrum shows a tone at 134.5 GHz compared with the simulated oscillator frequency of 131 GHz.

The axial ratio of the radiator is measured to be 3.3 dB. This corresponds to a cross polarization of right-handed circularly polarized radiated field -14.8 dB compared with the desired left-handed circularly polarized radiated field. Small cracks due to chip dicing were also observed and may have contributed to further asymmetry.

Next, the chip was rotated in two dimensions to measure the radiation pattern. The full radiation pattern measurement was taken twice with the linearly polarized receiver antenna oriented in two orthogonal polarizations whose summation gave the total power flux in any given direction regardless of the radiated polarization. Two elevation radiation planes of this total radiated power are plotted in Figure 4.20 along with the simulated pattern for orthogonal cases when $\phi = 0^\circ$ and $\phi = 90^\circ$ and from $\theta = -70^\circ$ to $\theta = 70^\circ$, limited by the measurement setup. Integrating the power flux over the entire cone angle from $\theta = -70^\circ$ to $\theta = 70^\circ$ yields a total measured radiated power of -1.3 dBm, compared with the simulated total power of -0.5 dBm.

The radiator draws 140 mA from a single 1.2 -V source and occupies an area of 1.2 mm². A comparison to other state-of-the-art integrated radiators in silicon that do not use external dielectrics or lenses is given in Table 4.1.

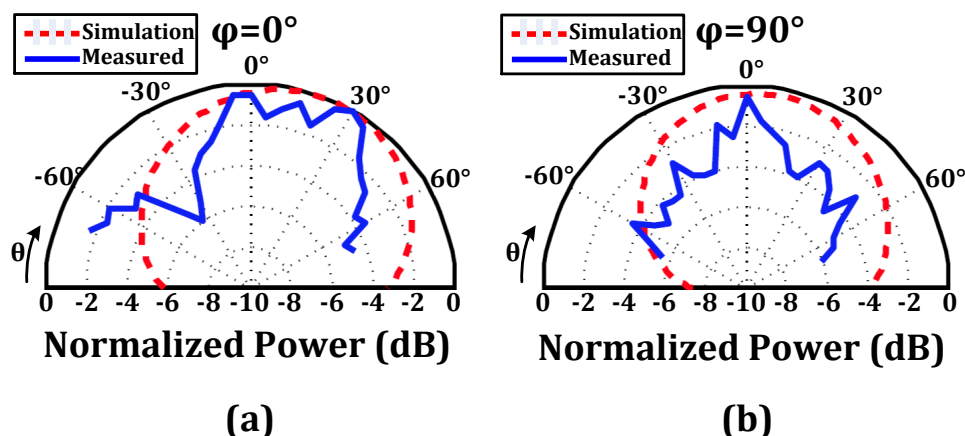


Figure 4.20: Orthogonal elevation planes of the simulated and measured radiation pattern when: (a) $\phi = 0^\circ$ and (b) $\phi = 90^\circ$.

Metric	This Work	[65]	[66]	[67]	[4]	[5]	[6]
Frequency (GHz)	134.5	105.5	338	210	280	191	161
Rad. Power (dBm)	-1.3	-0.5	-0.9	N/A	-7.2	-12.4	-2.0
Max EIRP (dBm)	6.0	7.8	17.1	5.1	9.4	-1.9	4.6
Process	32nm SOI CMOS	32nm SOI CMOS	65nm CMOS	32nm SOI CMOS	45nm SOI CMOS	65nm CMOS	130nm SiGe
Num. of Elements	1	2	16	4	16	4	1
EIRP per Element* (dBm)	6.0	1.8	-6.9	-6.9	-14.6	-13.9	4.6
Polarization	Circular	Dynamic	Linear	Linear	Circular	Circular	Circular
DC Power (mW)	168	476	1540	240	817	77	388
Area (mm ²)	1.2	2.64	3.9	3.5	7.3	1.1	1

*EIRP per element estimated as $EIRP/Num. \text{ of Elements}^2$ to account for array gain.

Table 4.1: Comparison with integrated radiating sources in silicon without external dielectrics

4.4 MPD Antennas for Dynamic Control

As we discussed in previous sections, MPD radiators present a new design space for integrated radiators. Ideally, MPD antennas can be used to create any physically realizable current pattern on the plane by injecting currents wherever they are needed around the antenna, something that is often not feasible or even possible with a single port design. In this MPD inverse design approach, the current pattern is first determined by the desired far field radiated pattern. The MPD antenna and its driver circuitry are then designed to produce the desired current. From a more practical standpoint, intelligent choice for the arrangement of driving ports across an MPD antenna structure could satisfy different design constraints such as a specific far-field polarization, a desired input impedance level for certain ports, a desired

coupling strength or maximum isolation between specific ports, etc. However, not all the driving ports may need to be driven simultaneously to perform a certain task. Different subsets of the driving ports could be designated to enable different features. This means that if the driving circuitry of the integrated radiator incorporates switching capability to allow connecting the driving signals to different subsets of available antenna ports, the same MPD antenna could be reconfigured through the switches into various modes of operation, each of which achieves a certain goal. Moreover, the relative phases and amplitudes of the signals at different driving ports provide additional degrees of freedom, which can also be used to achieve a certain behavior for the radiator or perform a certain task. If the drive circuitry is capable of setting these phases and amplitudes to different values, various combinations for relative phases and amplitudes corresponding to various performance features can be provided to also enable different modes of operation.

In addition to the capability of MPD antennas to be reconfigured into various modes of operation from time to time through the supporting circuitry, they can also be used for continuous control and adjustment of the radiation properties. Dynamic control over relative phases and amplitudes and switches through the driving circuitry of an MPD radiator enables dynamic control over the radiation performance. Furthermore, once these dynamically controllable MPD antennas are used in 1-D or 2-D phased arrays to enable beam steering of the radiated electromagnetic waves, the resulting array would also be capable of maintaining the same radiation property (e.g. polarization) and dynamically controlling it across the entire steering range. In the next chapter, we discuss dynamic controllability of the MPD radiators in more details.

4.5 Conclusions

The advantages of MPD antenna design methodology of using multiple input ports on an integrated antenna compared to a single-port antenna have been described. Electromagnetic duality was used to take an MPD wire antenna design and create an integrated MPD traveling-wave slot antenna. This slot antenna still has effective radiation while occupying much less exclusive use area. This can allow for other circuitry to be added without increasing the area, and does not require large areas of fill-exclude or low density fill with just a $6\text{-}\mu\text{m}$ fill exclude across the slot and under the oscillator inductors, and full density fill everywhere else. The multi-port slot ring antenna is driven at four ports in quadrature to create a traveling wave around the ring that produces circular polarization in the far field. These ports

are driven by an amplified quadrature oscillator that employs an inductor layout designed to minimize degradation due to process variation and parasitic inductance and capacitance. The measured radiation achieves a 6.0-dBm EIRP with a single element and radiates a total of -1.3 dBm at 134.5 GHz. Finally, various capabilities of MPD antennas to act as a tool for dynamic control of radiator performance and radiation properties were discussed.

DYNAMIC POLARIZATION CONTROL AND MODULATION

5.1 Introduction

Advancements in silicon CMOS integrated circuit (IC) technologies have provided devices capable of operating at mm-wave frequencies where the wavelengths are on the same order of magnitude as the IC dimensions. This has opened new design and application spaces for integrated mm-wave systems engineering while also providing new challenges as low frequency lumped models of devices and metals begin to fail [55]–[62]. One challenge associated with this mm-wave system engineering is generating RF power and coupling it to the outside world [74]–[76]. Traditional methods of power transfer such as wirebonding and flip-chip become increasingly lossy at mm-wave frequencies above 100 GHz, necessitating other power transfer methods [63], [64]. Integrating antennas on-chip and radiating directly from the IC becomes feasible when the carrier electromagnetic wavelengths are similar to the dimensions of the IC [4]–[6], [65]–[68]. This increased level of integration can improve efficiencies and lower costs compared to solutions requiring external power transfer components.

One challenge in mobile wireless communication links is coupling loss due to polarization mismatch. Polarization mismatch is a phenomenon where additional coupling losses between the transmit and receive antennas occur in addition to the free-space propagation loss if the antennas are not of the same polarization and aligned in space. Three examples of various transmit antennas and their associated far-field electric fields are depicted in Figure 5.1. If the signal is being received by a horizontally polarized receive antenna, it will be polarization matched to the transmit antenna with horizontal linearly polarized and the power received at the port of the antenna will simply be the input power to the transmitter multiplied by the free space propagation loss. If the transmit antenna is rotated in space, the received signal will continue to degrade due to polarization mismatch to the point where very little signal is received when the antennas are completely mismatched with orthogonal polarizations. Theoretical 3-dB degradation in coupling due to polarization mismatch will also occur when one of the antennas is circularly polarized while the other is linearly polarized.

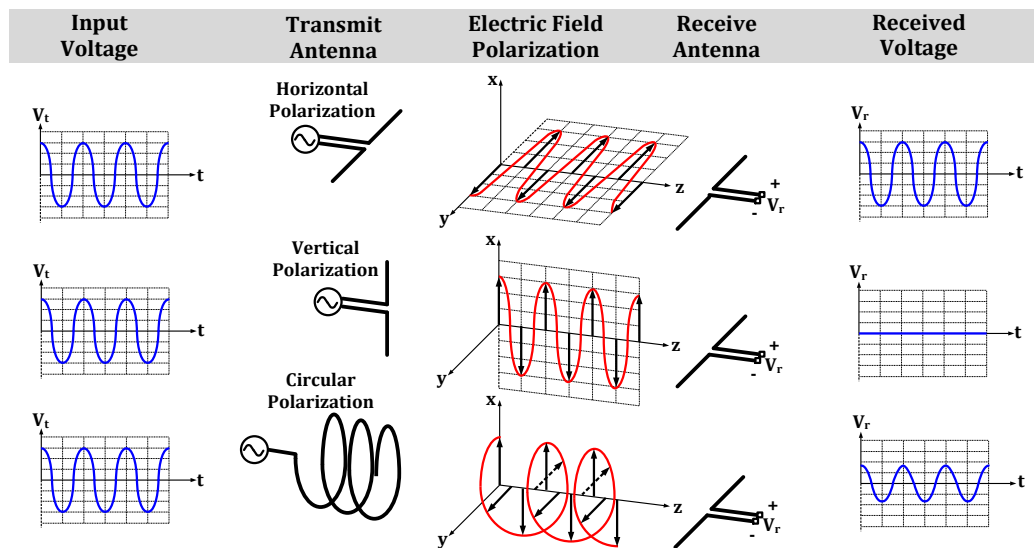


Figure 5.1: Effects of polarization mismatch on coupling transmit/receive antenna pairs. Maximum coupling occurs for polarization matched antenna pairs (top), no coupling for completely mismatched pairs (middle) and partial coupling for partially mismatched pairs (bottom).

Dynamic Polarization Control (DPC) serves as a solution to overcome polarization mismatch. A unit element DPC antenna is capable of transmitting all polarizations based on the receiver's need. Furthermore, DPC antennas can be phased properly in an array to form a more directive beam with higher power and to steer it towards a target while maintaining polarization matching. Thus, a two-dimensional (2-D) phased array of DPC antennas ensures polarization matching to the receiver within the 2-D steering range of the DPC phased array regardless of the polarization of the receiver, its orientation in space, or its location. If dynamic control and switching of the transmitted polarization is performed at very high rates, it can be used to encode information into the polarization itself, enabling Polarization Modulation (Pol-M) as a new modulation scheme, which can also augment existing phase and amplitude modulation schemes to add one additional degree of freedom and create 4-D data constellations.

Section 5.2 will briefly discuss polarization and its application in wireless systems, and then review polarization mismatch issue as a major challenge. The concept of DPC and a proposed DPC antenna using multi-port driven (MPD) antenna design approach are described in details in section 5.3, including the design, implementation, and measurement results for 2×1 and 2×2 proof-of-concept integrated DPC radiator arrays. In section 5.4, Pol-M and its advantages are introduced and exem-

plary architectures using DPC feature for Pol-M are presented, and finally, section 5.5 includes the concluding remarks.

5.2 Electromagnetic Polarization

Polarization of electromagnetic (EM) waves is a significant property in wave propagation, which can be utilized in many wireless applications such as communications, radar, sensing, and imaging [77]–[82]. In communication systems, this parameter can be used to transmit and receive information with different polarizations to increase the channel capacity over the same frequency band by adjusting the transmitting and/or receiving antennas for one or the other polarization(s). Polarization is also important in the transmission of radar pulses and reception of radar reflections due to the partially polarized nature of reflections from different objects. This additional information, which is carried by the polarization of the EM waves, can also be used in sensing and imaging applications.

With recent advancements in silicon processes and scaling of transistors that enable designers to implement very high-frequency millimeter-wave (mm-wave) systems in silicon-based integrated circuits, a wide range of opportunities has opened up to integrate transmitting/receiving antennas on the same substrate as the wavelength becomes comparable to the dimensions of the chip at these frequencies. In addition to serving as an alternative to the traditional power transfer methods such as wirebond and flip chip that become increasingly lossy at high mm-wave frequencies [63], [64], this opportunity allows us to implement integrated transmitters and receivers at these frequencies [6], [83]–[91] even beyond the frequency limit (f_{max}) of the integrated circuit technology [92]–[97], which, in turn, allows implementation of such wireless systems that utilize polarization information on an integrated platform.

Electromagnetic polarization describes the parametric trajectory of the electric and magnetic field vectors of an electromagnetic plane wave as it propagates through space. The polarization of the far-field electric field can be defined by its polarization axial ratio and polarization angle. The electric field, when plotted on a 2-D plane normal to the direction of propagation, produces an ellipse over one period, as shown in Figure 5.2. The polarization axial ratio is the ratio of the major to minor axes of the ellipse and determines how circular (low axial ratio) or how linear (high axial ratio) the polarization is. In order to orient the ellipse in space, the polarization angle can be defined as the angle between the major axis of the ellipse and a reference vector, which for the purposes of this chapter will be taken as the horizontal x -axis.

Elliptical Polarization

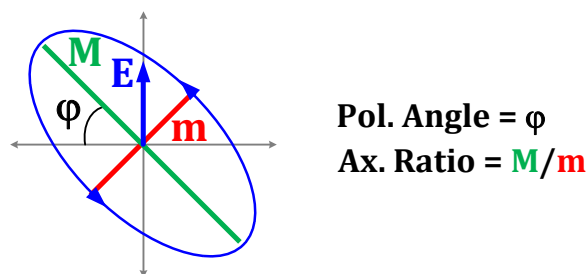


Figure 5.2: Definitions of the polarization parameters for the general elliptical polarization.

This means that the full range of axial ratios is from unity through infinity, and the full range of polarization angles is from 0° through 180° . Finally, the direction that the electric field travels around the ellipse will determine if the polarization is left-handed (clockwise when propagation is toward the observer) or right-handed (counter-clockwise when propagation is toward the observer).

Polarization of the EM waves is usually enforced by the transmitting and receiving antennas in the system since they are often intrinsically polarized based on their specific physical shape and particular orientation in space. On the other hand, the significance of polarization in the proper operation of wireless systems emphasizes both the importance of polarization control over the transmitted EM waves and the polarization matching between the transmitter and receiver antennas in the system.

In a wireless link, any mismatch between the polarizations of the transmitter and receiver antennas results in additional power loss on top of propagation path loss of the radiated EM waves. One possible scenario where polarization mismatch could happen is when the transmitter and receiver antennas have inherently different polarizations. For example, the transmitted signal of a vertical linearly polarized antenna is only polarization matched to a vertical linearly polarized receiver antenna and if the receiver antenna has horizontal linear polarization or circular polarization, full polarization mismatch or partial polarization mismatch would happen, respectively. This scenario is shown in Figure 5.3. Additionally, even if the transmitter and receiver antennas are polarization matched, the receiver could still move with respect to the transmitter or change orientation and cause polarization mismatch. An

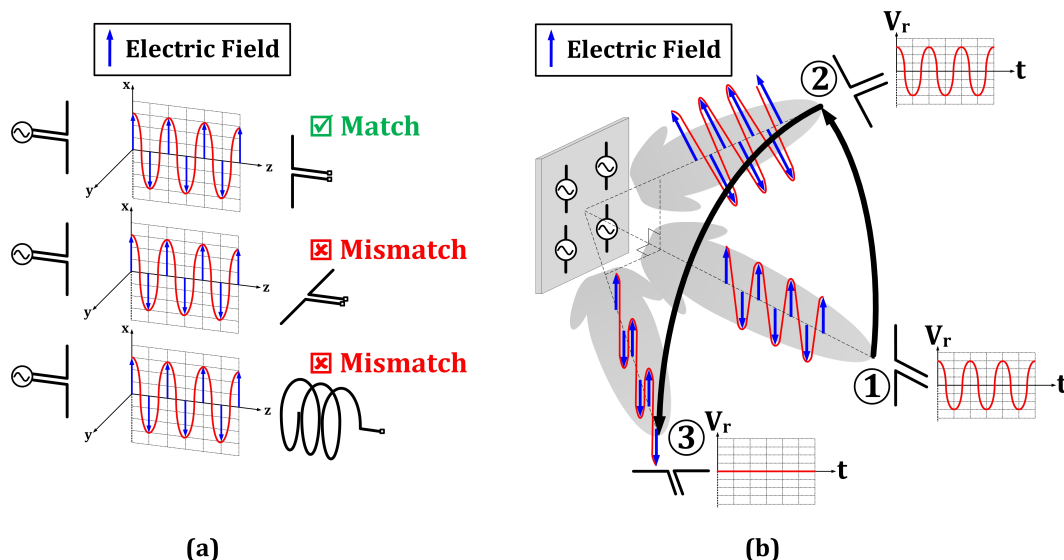


Figure 5.3: Examples of polarization mismatch in wireless communication links: (a) due to antenna mismatch, (b) due to orientation change between the transmitter and receiver in mobile systems.

example of this second scenario is a 2-D phased array of the same vertical linearly polarized transmitter antennas that can track a vertical linearly polarized receiver with the correct polarization only if the receiver antenna remains aligned with the transmitting antennas. When the linearly polarized receiver changes its orientation as it moves around, the transmitter would no longer be able to match the polarization due to orientation mismatch. In this chapter we will see how a 2-D phased array of DPC antennas [98] can solve both of these issues at the same time.

5.3 Dynamic Polarization Control

5.3.1 Concept

Dynamic polarization control (DPC) is the method of setting the polarization of the far-field electric field generated by a radiating antenna entirely electronically in order to maintain polarization matching with the receiving antenna regardless of its polarization or orientation in space. If an electromagnetic radiator is capable of controlling the polarization angle and axial ratio over their full tuning range for right- and left-handed polarization in the far field, then it can produce any possible far-field polarization, and can produce a polarization match with a receiver regardless of its polarization or orientation in space as shown in Figure 5.4 [65].

It is important to note that as the receive antenna rotates, both its polarization and

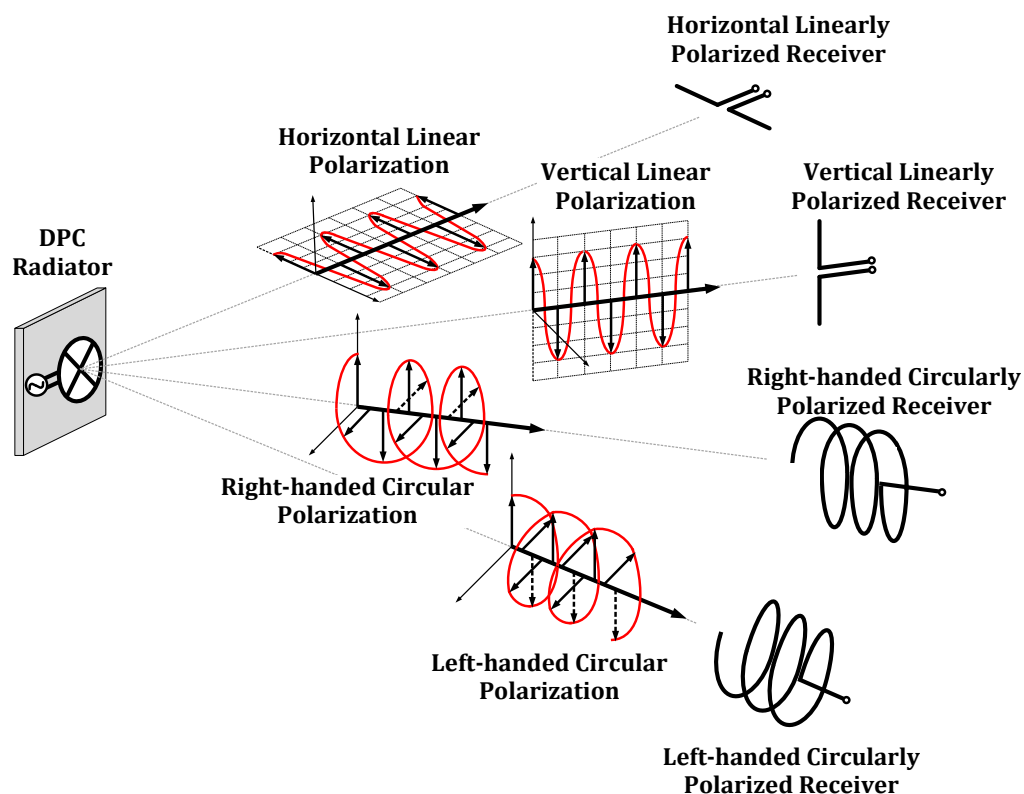


Figure 5.4: A radiator with Dynamic Polarization Control (DPC) can transmit any polarization angle and polarization axial ratio in order to maintain polarization matching with a receive antenna of any polarization or orientation in space.

directivity in the direction of the transmit antenna may change. While a transmit antenna with DPC will be able to maintain polarization matching by changing its polarization, the coupling between the two antennas may change due to changes in the free space propagation loss due to the changes in directivity. In order to know what polarization to transmit to a mobile receive antenna, some information feedback from the receiver to the transmitter would be required for this implementation. While some work has been done on switchable polarization on printed circuit board (PCB) antennas [99], [100] where polarization can be switched between different modes, truly dynamic control of the polarization is desired where the polarization can be set to match any receiver polarization. This is particularly important in the case of portable communication systems based on integrated electronics due to the unpredictability of the orientation during usage.

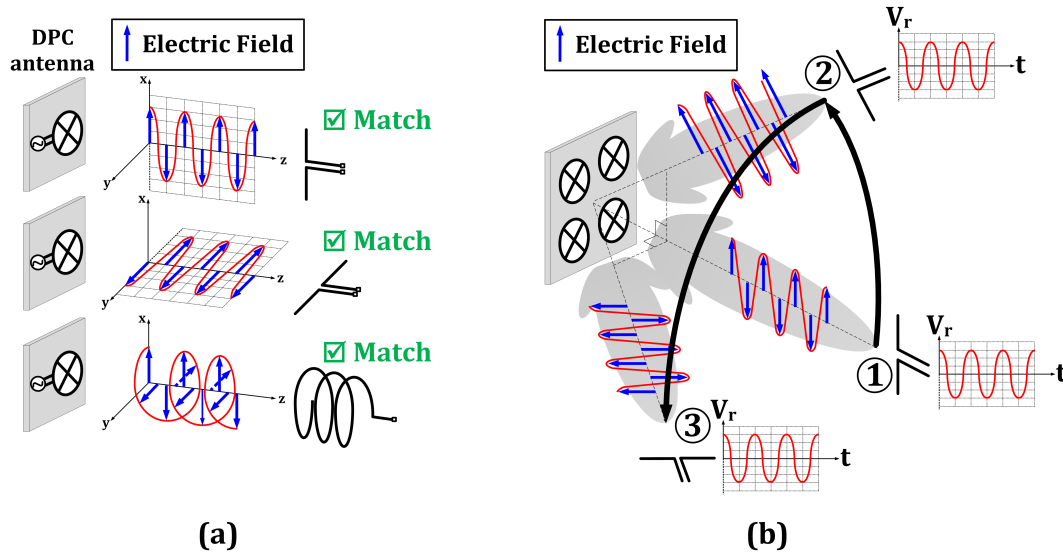


Figure 5.5: (a) DPC antenna ensures polarization matching between the transmitter and receiver regardless of receiver antenna type and (b) solves polarization mismatch in mobile systems when used in 2-D phased arrays.

5.3.2 DPC Antenna

A unit DPC antenna can radiate any polarization to match the receiver's need and avoid additional power loss due to polarization mismatch. For instance, a DPC antenna can be used in the first scenario of the previous example in section 5.2 to transmit vertical polarization, horizontal polarization, and circular polarization to ensure polarization matching for all three receiver antennas, as depicted in Figure 5.5(a). Moreover, a 2-D phased array of DPC antennas, such as the one in Figure 5.5(b), can steer the radiated beam in either dimension while simultaneously adjusting the transmitted polarization to follow both the location and the orientation of the receiver in space to maintain polarization match.

For a DPC antenna, in order to have full control of both dimensions of polarization, as well as the amplitude and phase of far-field electric field, a minimum of four degrees of freedom are required from the input ports. This is why a stationary single-port antenna in a linear, isotropic medium cannot perform DPC, and rather has a fixed polarization at a given frequency (for example, a dipole antenna is linearly polarized along the axis of the dipole, and a helical antenna is circularly polarized). For these single port antennas at a given frequency, there are only two degrees of freedom at the input, namely its amplitude and phase, and adjusting these values will

in turn adjust the amplitude and phase of the far-field electric field without changing its polarization.¹

Additional degrees of freedom can be obtained by driving a single antenna from multiple ports. By independently controlling the amplitude and phase of the various ports, it is possible to generate the four degrees of freedom required to have full control of polarization as well as amplitude and phase of the signal in the far field. One type of antenna that is particularly well suited for integrated radiators with DPC is the four-spoke multi-port driven (MPD) antenna [6] shown in Figure 5.6. It consists of a signal ring that is driven at four points against a set of ground spokes that extend radially from the center of the antenna out to the signal ring. While the previous implementation of the MPD antenna involved equally spaced drive phases to create a circular polarization, modifying the amplitudes and phases of the various drive ports can create any polarization.

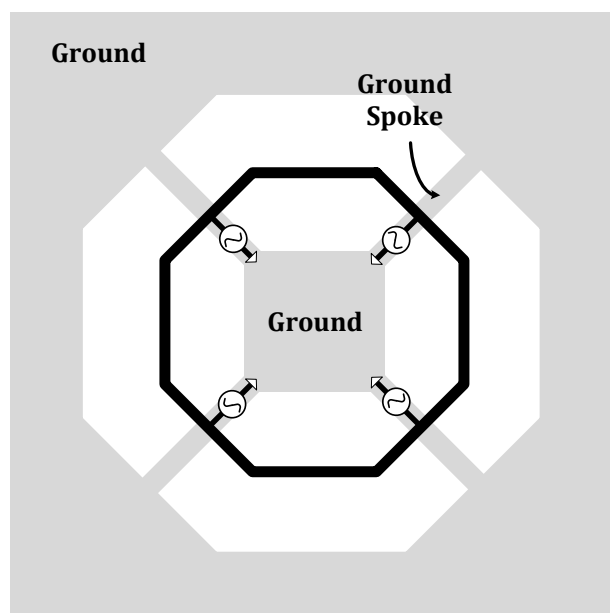


Figure 5.6: Four-spoke Multi-Port Driven (MPD) antenna for dynamic polarization control.

¹Multiple single port antennas with different polarizations can control the polarizations in the far field through the superposition of the individual antennas. However, in an integrated setting, it is difficult to create the feeds for these antennas while maintaining their isolation, and the additional area adds significantly to the cost of the IC.

5.3.2.1 Operation Principle

A DPC antenna is a multi-port driven (MPD) [6] ring antenna with four ports that are driven against a set of orthogonal ground spokes (Figure 5.7). The drive circuitry that generates the four required excitation signals to drive the ring at the four ports is located in the center ground plane of the antenna. Each pair of opposing ports in the antenna is driven differentially as a subpart against their corresponding ground spokes, with adjustable amplitude and phase, which are independent of those of the other subpart pair of ports. This allows each DPC antenna to radiate two linear polarizations, aligned with the ground spokes and orthogonal in space, in the far field. The amplitudes and the relative phase difference of these two polarizations can be arbitrarily adjusted by the phase and gain control units of the antenna. Thus, the overall polarization of each DPC antenna is set by the superposition of these two orthogonal linear polarizations.

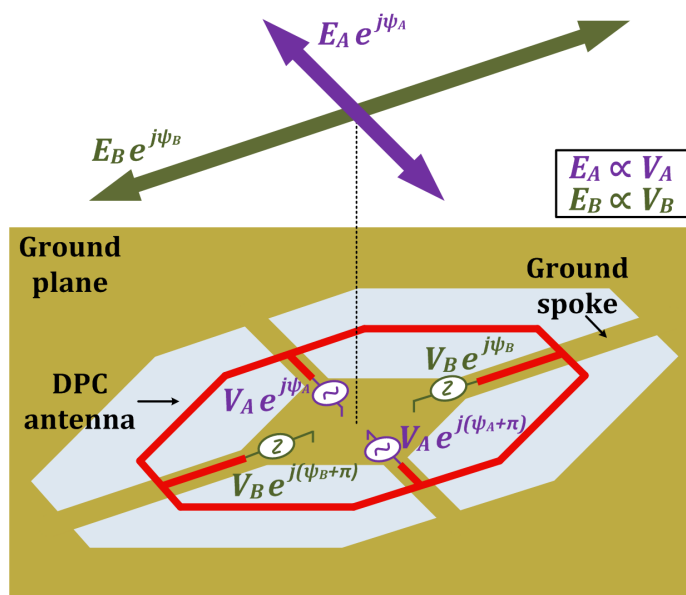


Figure 5.7: Operation principle of the original DPC antenna based on superposition of two orthogonal linear polarizations.

The general form for this polarization is elliptical polarization, as depicted in Figure 5.8(a), where the electric field travels in an elliptical trajectory. Any arbitrary choice of amplitudes and phases for the two subparts (V_A , V_B , ψ_A , and ψ_B) would result in a specific set of values for the polarization angle and axial ratio and determines the net polarization of each DPC antenna, which could range from linear polarization (Axial Ratio = ∞) at any desired polarization angle, illustrated in Figure 5.8(b), to

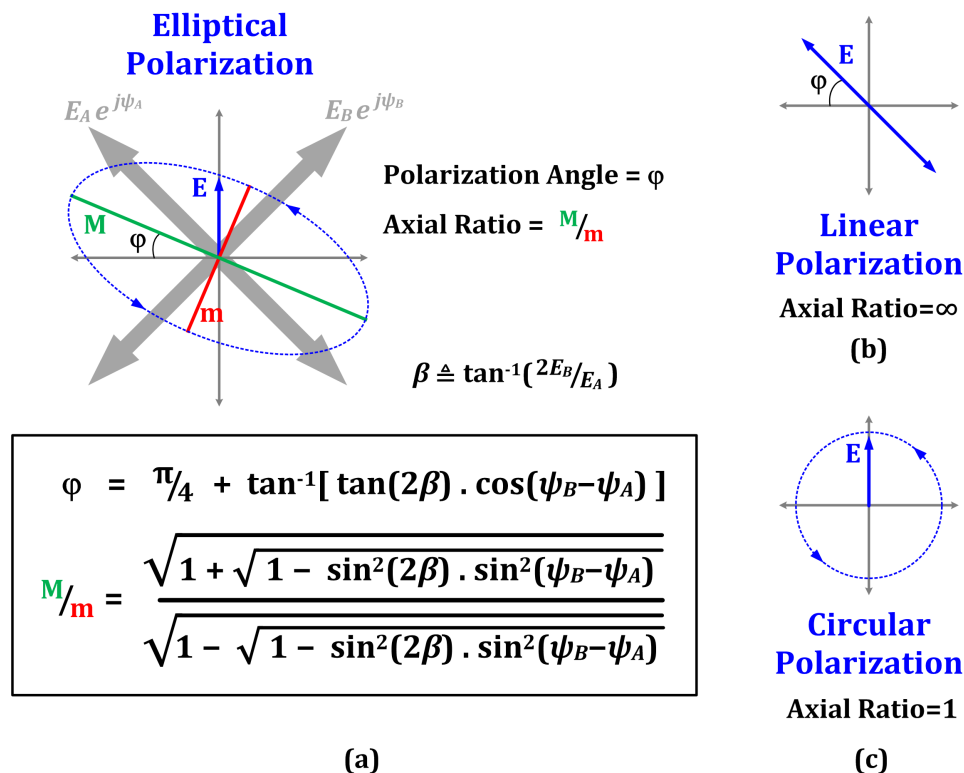


Figure 5.8: Realization of any arbitrary elliptical polarization with two orthogonal linear polarizations, as well as (b) graphical representation of the extreme cases of linear and (c) circular polarizations.

circular polarization (Axial Ratio = 1), shown in Figure 5.8(c), based on the relative phases and amplitudes of the two drive sets.

5.3.2.2 Analysis

A simplified analysis¹ similar to that in [6], but generalizing for the ports' phases and amplitudes provides insight into how this polarization control is obtained. The DPC is achieved by separating the antenna into two isolated superposition subparts that independently produce two orthogonal polarizations. By controlling the amplitude and phase of each of these polarization subparts independently, the polarization of the overall electric field can be controlled. In order to gain design insights a couple of simplifying assumptions must be made: the antenna will have a circumference of $g\lambda$ (Figure 5.9) and it will be analyzed in free-space with the substrate neglected for the moment. The first assumption is that there is low coupling between the

¹This analysis is due to my colleague Steven Bowers, which was published in our joint paper [89], and is included in this dissertation for completeness.

ring and various spokes, and this assumption has been verified through full 3-D electromagnetic simulation [6]. This will allow for superposition where the signal ring and ground spokes will be analyzed separately, two ports at a time. The second assumption is that currents on a line that are terminated with a virtual short will form sinusoidal standing current waves similar to a lossless transmission line. The broadside electric field, \mathbf{E} , due to a set of time harmonic currents, \mathbf{I} , on a plane can be given by [1]:

$$\mathbf{E} = \frac{j\omega\mu}{4\pi} \int_C \mathbf{I} \frac{e^{-jkR}}{R} dl \quad (5.1)$$

where μ is the permeability of the medium, ω is the angular frequency of the signal, $k = \omega\sqrt{\mu\epsilon}$, ϵ is the permittivity of the medium, and R is the distance between the current plane and the observer. Thus, the direction of the electric field vector will be the same as that of the integration of the currents, and its polarization will be determined by that same integration. Thus, once the currents on the ring and spokes are defined, they can be integrated to generate expressions for the far-field electric field. For this Four-spoke MPD antenna, pairs of ports on opposite spokes (ports 1 and 3, and 2 and 4) will be analyzed separately using superposition, and will be referred to as superposition subpart A (ports 1 and 3) and superposition subpart B (ports 2 and 4). These pairs of ports are driven with the same amplitude but 180° out of phase.

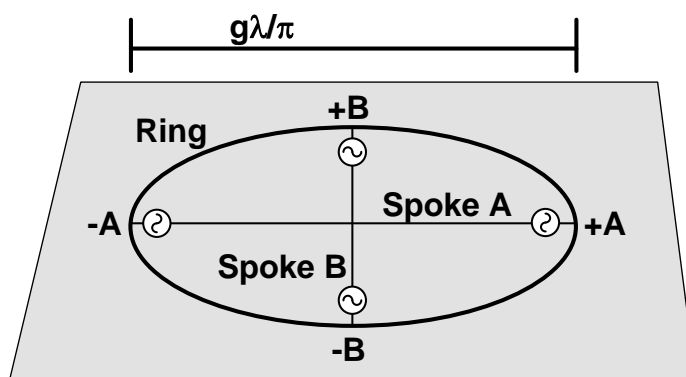


Figure 5.9: Modified MPD antenna of circumference $g\lambda$ used for polarization control. The phases and amplitudes of the drives of spokes A and B are controlled independently from each other, while ports on opposite ends of each spoke are driven differentially with the same amplitude.

Due to the symmetry of the ring, the portion of the currents orthogonal to spoke A on the top half of the ring will cancel those from the bottom half, while the currents parallel to the spoke will add constructively. Thus, a single quadrant of the ring can be analyzed and the electromagnetic field produced by the currents parallel to the spoke will be quadrupled to take all four quadrants into account. Once only superposition subpart A is being considered, there will be three virtual shorts along the differential axis of symmetry. The port impedances of ports 2 and 4 can thus be neglected in the calculations for subpart A as they are in parallel with the virtual short. In practice, this means that as the phase and amplitude of subpart B are changed, the current densities being contributed by subpart A will not be changed, and there is isolation between the two subparts in this simplified model. The current densities can then be defined on the ring and spoke structures shown in Figure 5.10.

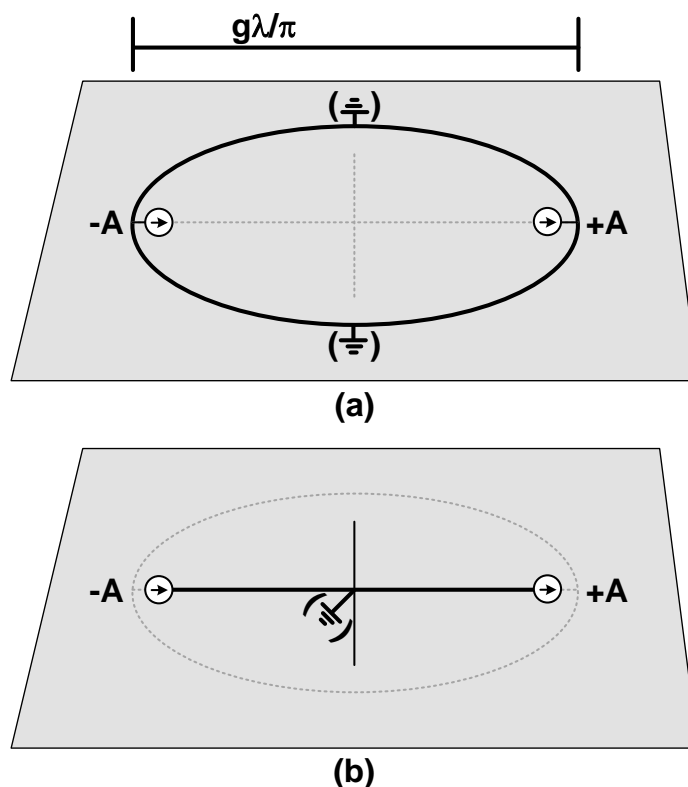


Figure 5.10: Analysis setup for superposition subpart A when broken up to consider just (a) the signal ring or (b) just the spokes. The port impedances from subpart B are in parallel to the virtual shorts and thus do not affect the current distribution due to subpart A.

This allows the current densities to be expressed as

$$|I_{ring,AQ1}| = I_{max,r} \cos(\beta l) = I_{maxr} \cos[g(\frac{\pi}{2} - \phi)] \quad (5.2)$$

for the current on the ring in the first quadrant, and

$$\mathbf{I}_{sp,A} = I_{max,sp} \cos(\beta l) = I_{max,sp} \cos(\frac{2\pi}{\lambda}) \hat{\mathbf{u}}_x \quad (5.3)$$

for the current on spoke A. Integrating this current for the far-field electric field given in Equation 5.1 yields

$$\mathbf{E}_{ring,A} = -I_A \frac{j\mu c}{2\pi} \frac{e^{-jkR}}{R} \frac{g}{g^2 - 1} \hat{\mathbf{u}}_x \quad (5.4)$$

$$\mathbf{E}_{sp,A} = -I_A \frac{j\mu c}{2\pi} \frac{e^{-jkR_0}}{R_0} \tan(g) \hat{\mathbf{u}}_x \quad (5.5)$$

for the electric fields due to currents on the ring and spoke respectively from subpart A, and that sum to the far-field electric field for the entirety subpart A of

$$\mathbf{E}_A = -I_A \frac{j\mu c}{2\pi} \frac{e^{-jkR_0}}{R_0} \left[\frac{g}{g^2 - 1} + \tan(g) \right] \hat{\mathbf{u}}_x \quad (5.6)$$

The analysis for subpart B is identical to subpart A, but rotated 90° , and yields a far-field electric field for the entirety subpart B of

$$\mathbf{E}_B = -I_B \frac{j\mu c}{2\pi} \frac{e^{-jkR_0}}{R_0} \left[\frac{g}{g^2 - 1} + \tan(g) \right] \hat{\mathbf{u}}_y \quad (5.7)$$

There are two interesting observations to note from equations 5.6 and 5.7. The first is that the ring should be sized such that $1 < g < \pi/2$ in order to have

the currents on the spoke and ring add up constructively. The resulting current distributions for each subpart for a design within this range are shown in Figure 5.11 and provide both a general design guideline, and also a frequency range over which a given implementation of the design will maintain the desired current patterns [6]. The second observation is that regardless of any of the design parameters being considered, the far-field electric field will always be linearly polarized along the axis of the subpart's spoke.

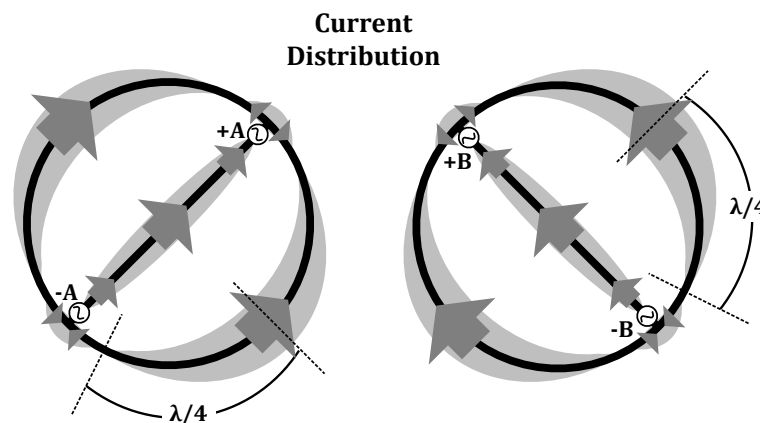


Figure 5.11: Standing current wave distribution when $1 < g < \pi/2$ for subparts A and B.

5.3.3 A 2×1 Integrated DPC Radiator Array

In this section, we show a fully integrated 105.5 GHz 2×1 phased array radiator implemented in a 32 nm CMOS SOI process with dynamic polarization control capable of tuning polarization angle and axial ratio with effective isotropically radiated power of 7.8 dBm and 0.9 mW total radiated power.¹

5.3.3.1 System Architecture

We implemented the 2×1 DPC radiator array in 32 nm CMOS SOI process using two polarization-controlling MPD antennas locked to each other in a 1-D phased array, shown in Figure 5.12. Each DPC radiator element is designed to perform local power generation using its own driver circuitry within the element's core. The drive phases and amplitudes of the generated waveforms are controlled through

¹This design was a joint project with my colleague Steven Bowers. I designed the entire circuitry including the oscillators, amplifiers, phase rotators, locking network, as well as the electromagnetic structures such as passives and matching networks. Steven was responsible for the electromagnetic design of the array and the measurements.

phase rotators and multiple buffer stages, respectively. Although such a drive circuit is sufficient for dynamic polarization control of a single element DPC radiator, the proper operation of the entire DPC phased array requires a central locking network to ensure phase locking of the individual elements. It should be kept in mind that these array-dependent blocks introduce additional power overhead for small phased arrays such as this, but they become less significant as they become shared among more elements in a larger array, and are a requirement of the radiator being a phased array. This overhead should not be associated primarily with the ability to control polarization.

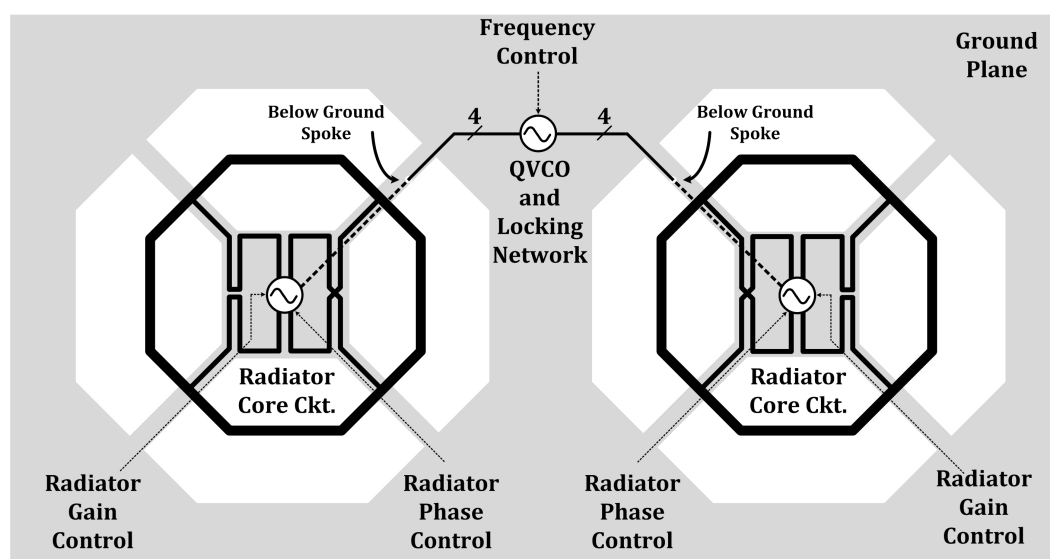


Figure 5.12: Block layout of the 2×1 radiator array. A central QVCO and locking network located between the two antennas locks the core circuitry located at the center of each antenna, with polarization control of the far field electric field achieved through amplitude and phase control of each individual antenna.

The block diagram of the driver circuitry of the DPC phased array is shown in Figure 5.13. The DPC phased array is designed to locally generate power within each element of the array and also lock the phases of the two individual radiating elements to a central reference. This allows us to synchronize the frequencies of the two elements as well as locally adjusting the phase of the reference signal within each element to enable independent control over its phase based on the reference phase [65].

A central quadrature oscillator provides the reference quadrature signals at the

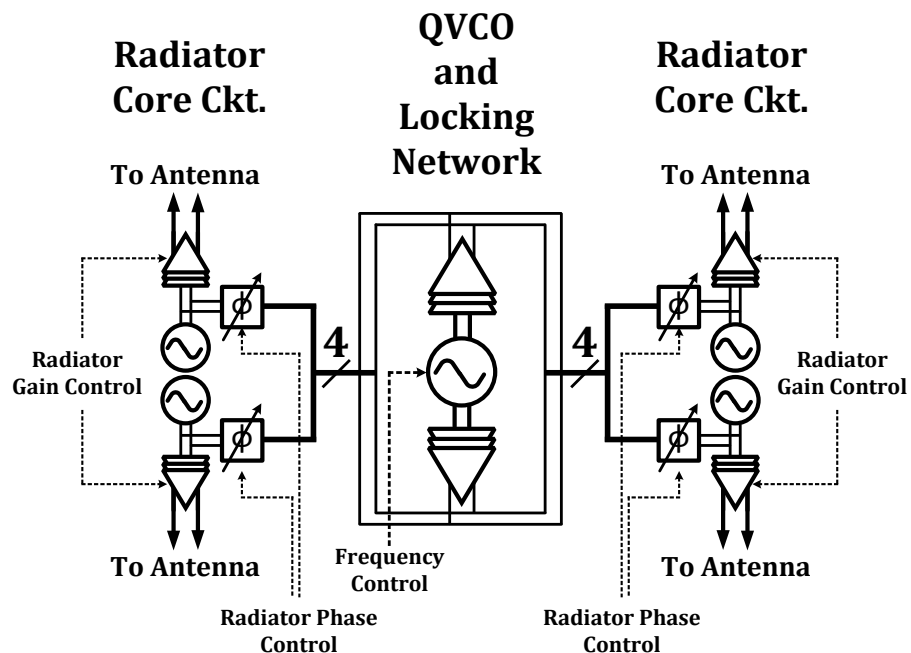


Figure 5.13: Block Diagram of the driver circuitry of the 2×1 radiator phased array with DPC. The central QVCO is amplified before distribution to phase rotators within each radiator core, which are then injected into the radiator core oscillators before being amplified and sent to the antennas.

desired frequency for radiation. The quadrature signals are then distributed across the chip through a locking network consisting of three buffer stages and additional feed lines that route the quadrature signals into the cores of the two radiating elements. In each core, these quadrature signals drive two phase rotators whose phases can be arbitrarily set through independent control lines. Output of each of these phase rotators is then injected into one of the two oscillators of the core, as seen in Figure 5.13. These oscillators are implemented to locally generate power inside the core, which allows the locking network to distribute lower power levels. Injection of phase rotators' outputs into the oscillators results in locking each oscillator's phase and frequency to the phase and frequency of the injected signal from the corresponding phase rotator, thus achieving both frequency synchronization and full phase control over core's driving circuit. Oscillators' outputs are then amplified by another set of three buffer stages and drive the antenna of the radiating element and radiate with the desired polarization that corresponds to the phase rotator's specific settings.

5.3.3.2 Circuit Implementation

The driver circuitry used in this design contains blocks including the oscillators, locking network phase rotators and amplifying stages (Figure 5.13). These blocks allow for power generation, signal distribution, frequency synchronization of the radiating elements, and phase and amplitude control of the driving signals.

Oscillator Design: The central quadrature oscillator generates quadrature signals at the fundamental frequency of operation to synchronize the frequencies of individual radiators and to overcome possible frequency drifting or mismatch of individual elements' oscillators. An inaccuracy in the modeling of the tank inductors and parasitic capacitors that manifested differently in the central oscillator than the radiator oscillators due to their loading differences resulted in a slight frequency deviation to 105.5 GHz and diminished frequency overlap of the locking range. The quadrature signals, when routed to each element, provide the possibility of arbitrary phase generation through proper weighted summation of in-phase and quadrature components.

The quadrature oscillator's schematic is shown in Figure 5.14. It consists of two cross-coupled differential oscillators that are also coupled to each other to provide quadrature signals. Although strong coupling through quadrature coupling transistors would have been sufficient to ensure quadrature oscillation [54], such strong coupling degrades the phase noise of the oscillator [71], [72]. Thus, in our design, the coupling between the two oscillators happens through two different mechanisms whose simultaneous operation ensures quadrature oscillation while avoiding strong quadrature coupling to minimize phase noise degradation.

The first coupling mechanism is a resistive network at the tails of the two cross-coupled oscillators that couples them through second harmonic injection. Such resistive coupling on its own allows four different oscillatory modes: leading quadrature, lagging quadrature, differential, and common-mode oscillation [73]. In order to prevent differential and common-mode oscillations and enforce quadrature oscillation, a second coupling mechanism through small quadrature coupling transistors is added to the circuit. Although the resistive network does not guarantee quadrature oscillation on its own, its presence reduces the effective strength of quadrature coupling transistors and thus improves the phase noise.

Simultaneous operation of the two mechanisms can be better understood by replacing the “Y” resistive network (R_c and R_t) with its equivalent “ Δ ” network (R'_c and R'_t)

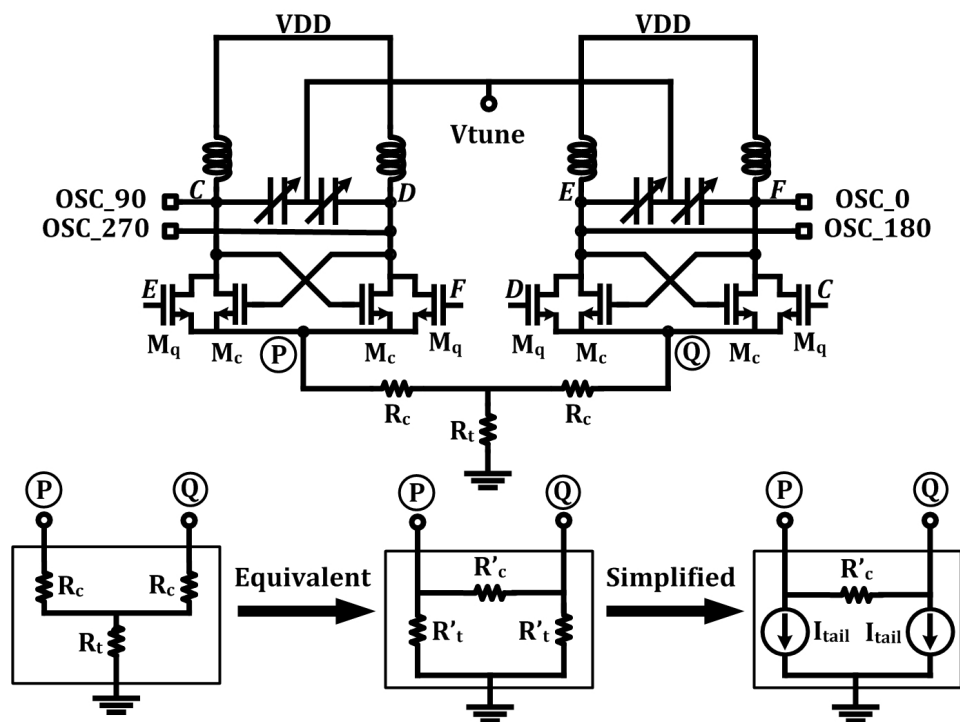


Figure 5.14: Schematic of the central QVCO with two coupling mechanisms: Resistive network at the tail ($R_c = R_t = 15\Omega$) and quadrature coupling through transistors ($W_{M_q} = 0.5\mu\text{m}$, $W_{M_c} = 20\mu\text{m}$). The “Y” resistive network can be simplified through its “ Δ ” equivalent for analysis.

and then simplifying it by introducing ideal current sources (I_{tail}) instead of tail resistors, R'_t , as demonstrated in Figure 5.14. In the simplified circuit, the value of coupling resistor, R'_c , can be adjusted to apply any arbitrary second harmonic coupling strength between the two oscillators without affecting their DC currents which are set to I_{tail} by ideal current sources. In the absence of any second harmonic coupling at the tails, i.e. large values of R'_c , phase noise of the quadrature oscillator at 1 MHz offset degrades as the width of the coupling transistors increases, as shown in Figure 5.15, motivating use of very small transistors for improved phase noise performance. However, in practice, using very small coupling transistors may result in insufficient coupling strength for the two oscillators to lock to each other in the presence of layout parasitics and undesired coupling through substrate to other signals. In order to overcome this issue, we add second harmonic coupling between the two oscillators by reducing R'_c . In quadrature mode of operation, each oscillator tries to push the other oscillator out of phase through the coupling transistors and the equal strength of the two oscillators results in quadrature operation. In this mode, the

common nodes of the two oscillators (P and Q in Figure 5.14) contain significant 180° out of phase second harmonic voltages due to transistors nonlinearity. In the presence of R'_c , we can use the Y-parameters of the two-port network to see that the magnitude of second harmonic current at the tail of each oscillator is equal to $|V_{P,h2}/R'_c - V_{Q,h2}/R'_c|$, which means that due to differential operation of $V_{P,h2}$ and $V_{Q,h2}$, each oscillator injects additional in-phase second harmonic current into the other oscillator and helps it to maintain its existing phase as opposed to quadrature coupling transistors. Reducing the value of R'_c , increases the strength of this coupling, which in turn reduces the overall effective quadrature coupling strength but improves phase noise. This is also shown in Figure 5.15, where simulated phase noise at 1 MHz offset is plotted versus R'_c for different coupling transistors widths.

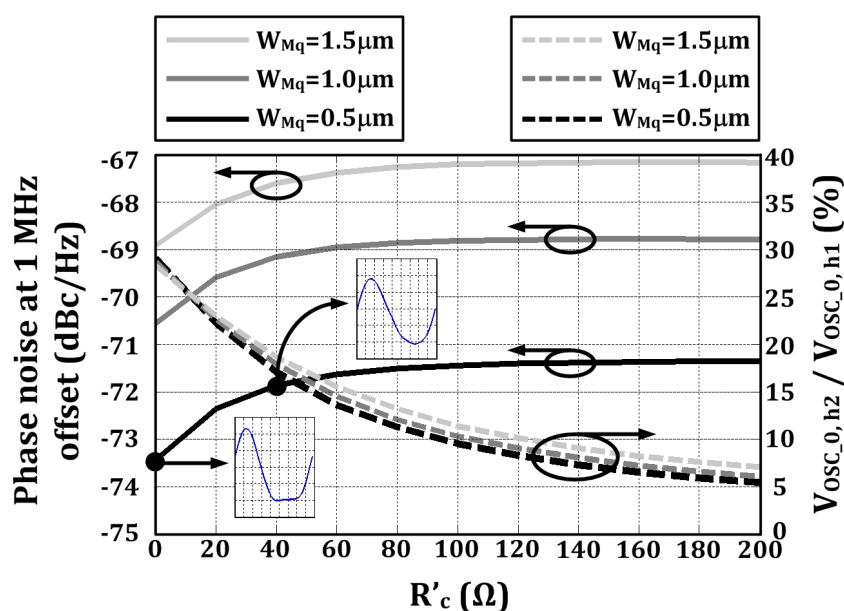


Figure 5.15: Simulated phase noise at 1 MHz offset and the ratio of second harmonic to fundamental of the QVCO vs. coupling resistance (R'_c) for three different widths ($0.5 \mu m$, $1 \mu m$, $1.5 \mu m$) of coupling transistors along with the time-domain waveforms for $R'_c = 0 \Omega$ and $R'_c = 40 \Omega$ when $W_{Mq} = 0.5 \mu m$.

The equivalent “ Δ ” network at the tail also reveals that there is no additional voltage headroom loss due to the resistive coupling network since the coupling resistor, R'_c , appears in parallel to the tail current sources or the tail resistors and does not draw any DC current. The value of R'_c determines the DC current of the oscillators and R'_c sets the desired second harmonic coupling strength. It should also be noted that stronger second harmonic coupling increases the output amplitude of the oscillators

since the two oscillators help each other constructively through the tail network. However, very strong second harmonic coupling (very small values of R'_c) increases the second harmonic content of individual outputs of the oscillators and corrupts the output waveform compared to a clean sine wave, as shown in Figure 5.15. Thus the tolerable amount of harmonics in the output waveform sets a lower limit on R'_c .

Once the values of R'_t and R'_c are set, either of equivalent “ Δ ” or “Y” networks can be used based on layout constraints. In this work, we have used “Y” network due to better layout compatibility with $R_c = R_t = 15 \Omega$, $W_{M_q} = 0.5 \mu\text{m}$, and $W_{M_c} = 20 \mu\text{m}$. The post-extraction simulated phase noise of the quadrature oscillator is 73.5 dBc/Hz at 1 MHz offset from the carrier frequency and it provides -14 dBm of output power per quadrature line that feeds the locking network buffer chain.

Locking Network: Quadrature oscillator outputs are distributed to the radiating elements through the locking network. Two chains of three differential amplifier stages follow both in-phase and quadrature outputs of the oscillator. Each chain consists of a $5\text{-}\mu\text{m}$ -wide differential common source and two differential cascode stages ($15 \mu\text{m}$ and $30 \mu\text{m}$). The gain of the buffer set can be adjusted through the biasing network to allow additional control over the signal strength. After the third stage, the outputs split and form two sets of quadrature signals. Each set is then routed into the core of one of the radiating elements. The feeding lines from the locking network are routed above the ground plane to the vicinity of the antennas. Beyond that point they are pushed below the ground plane and are routed to the core under one of the ground spokes to minimize electromagnetic interaction between the antenna and the reference quadrature signals. Inside the core, these quadrature lines are connected to the phase rotators. Quadrature outputs of the locking network provide 26.5 dBm of input power per quadrature line to the phase rotation unit of each radiating element.

Phase Rotators: The phase rotation unit of each element consists of two phase rotator circuits. Figure 5.16 shows the schematic of each phase rotator circuit consisting of two Gilbert cells that are fed by the four quadrature input voltages (from the locking network) and produce in-phase and quadrature currents as outputs [101]. The outputs of the Gilbert cells are connected together to add up the output currents. All four tail currents of the two Gilbert cells can be independently controlled by adjusting the control voltages at the gates of tail transistors. Independent control over the tail currents allows setting arbitrary weights for I/I and Q/Q components, thus

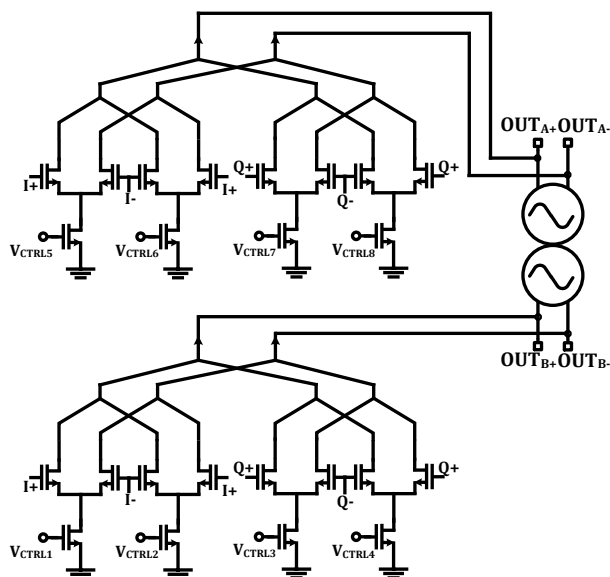


Figure 5.16: Schematic of Gilbert cell based phased rotator. In-phase and quadrature signals from the locking network are weighted arbitrarily and added in current domain to generate the desired output phase to lock cores' oscillator ($W = 2 \mu\text{m}$ for tail transistors, $W = 1 \mu\text{m}$ for upper transistors).

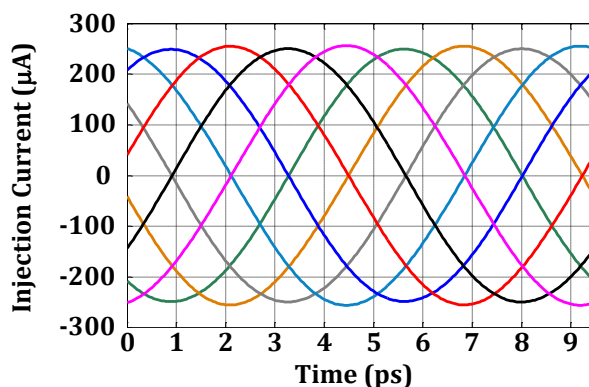


Figure 5.17: Simulated output current of phase rotator for eight different settings. Control voltages are set to generate 45° separated phases while keeping the amplitudes constant.

enabling full 360° phase control as well as amplitude control over the differential output current. Simulated output current of one of the phase rotators for eight different settings results in eight different phases while maintaining constant amplitude as illustrated in Figure 5.17. The differential output current of each phase rotator is then directly injected into the output nodes of one of the two cross-coupled oscillators of the radiator core and locks the oscillator's outputs at the phase and frequency of

the injected current, producing two sets of differential signals whose phases can be arbitrarily adjusted. To maintain polarization matching, only relatively slow control of the phase and amplitude are required, and thus low frequency control lines were routed to the radiator core, though if faster switching of polarization was desired, higher speed lines could be implemented in future versions.

Amplifiers: Each of the two differential outputs of the oscillators in each core drive a differential buffer chain. The chain consists of three stages of amplification (Figure 5.18). The first stage is a $5\text{-}\mu\text{m}$ -wide differential common source stage which is DC coupled to the oscillator. The next two stages are differential cascode amplifiers, $15\ \mu\text{m}$ and $30\ \mu\text{m}$ wide, respectively, and are AC coupled to the previous stage to allow for different DC voltages at the drains and gates of the cascode and common source transistors. The AC coupling capacitors are set at $22.6\ \text{fF}$ to maximize the power transfer to the next stage based on impedance matching requirements. Differential amplification of oscillator outputs allows using differential inductors as load impedances that in turn reduces the amount of required bypass capacitance for proper performance by advantaging virtual grounds.

The DC currents of the amplifiers are set through the biasing network. Thus, by adjusting the DC currents of the amplifiers, we can control the gain of the entire chain. Simulation results show that the gain can be adjusted from $0\ \text{dB}$ to $12.5\ \text{dB}$, while providing a maximum output power of $-3.1\ \text{dBm}$ per quadrature line.

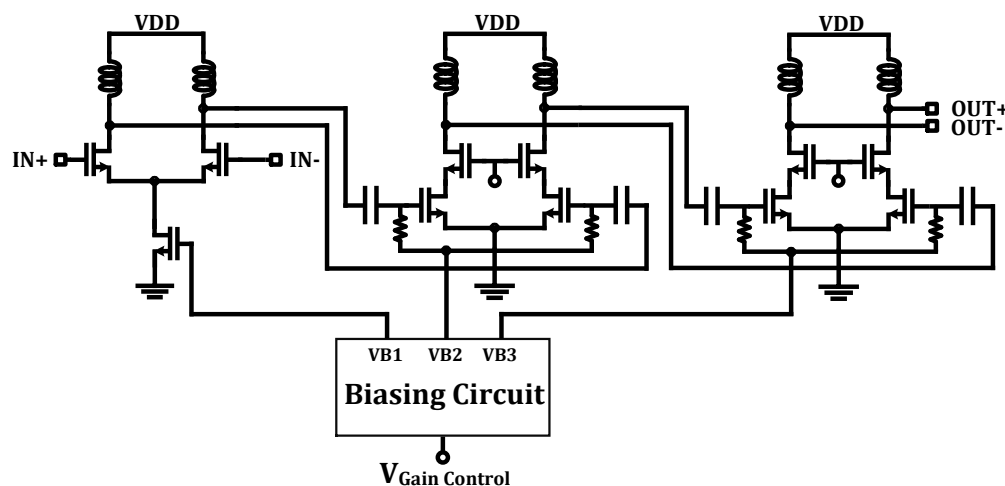


Figure 5.18: Schematic of the amplifier chain consisting of a differential common-source stage ($W = 5\ \mu\text{m}$) and two differential cascode stages ($W = 15\ \mu\text{m}$ and $W = 30\ \mu\text{m}$). Gain of the chain is controlled through the biasing circuit.

5.3.3.3 Electromagnetic Simulation

The simplified analysis of the DPC antenna provides intuition to the operation of the radiator, but some of the non-idealities associated with the physical implementation of the antenna also must be considered to ensure proper functionality of the radiator, including the effect of the surrounding metals on the surface of the chip as well as the effect of the silicon substrate on the radiator. The antenna cannot operate in isolation and proper consideration must be given to providing DC and locking signals to the driver circuitry without being detrimental to the antenna's radiation pattern.

The circuitry will be located within a driver core at the center of the antenna and be shielded by a local ground plane as depicted in the block diagram in Figure 5.13. This ground plane will both help to shield the transistors and inductors from the antenna's electromagnetic radiation as well as to provide a ground to the microstrip transmission lines that route the signals from the output amplifier stages to the ports of the antenna. The size of this local ground plane should be kept to a minimum to ensure that the mm-wave currents traveling through the spoke and ground plane stay as close to the desired operation as possible. This will limit the space to layout the core circuitry and create a trade-off between core size and isolation between the various inductors within the core. The DC ground will be fed through the ground spokes that are extended out to a global ground plane that has been pulled back from the antenna by around $\lambda/4$, as shown in Figure 5.19. The impedance looking outward down the spokes from the antenna's ports should be high as it is $\lambda/4$ from the ground plane, and thus most of the return ground current will flow back down the spoke toward the center of the antenna as assumed in the previous analysis. DC supply and locking signal lines are run underneath the spokes to minimize interference with the radiated signals.

The silicon substrate will also significantly affect the radiation pattern. Because the dielectric constant of silicon is much higher than that of air, most of the radiated power will initially go down into the substrate. The standard 250- μm -thick chip is mounted onto a ground plane to reflect that signal back up and out of the chip (Figure 5.19). The thickness of the chip is close enough to a quarter of a wavelength that the reflected wave will add constructively with the signal that is initially radiated upward. Another way of thinking about it is to look at impedances, where the top of the chip is around a quarter wavelength from the ground plane, which creates a high impedance looking downward and thus directs most of the power upward. In

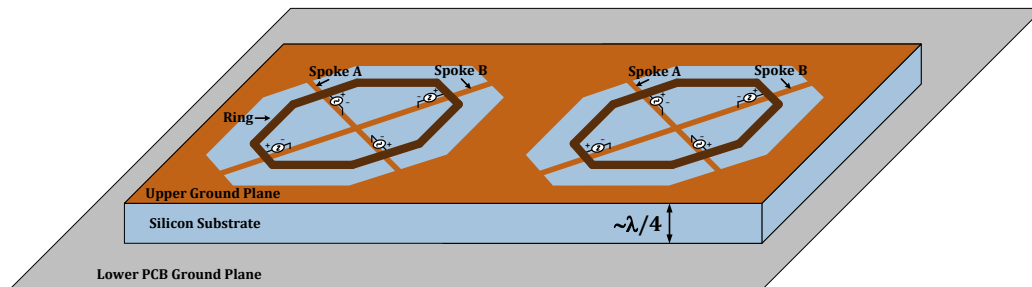


Figure 5.19: Additional non-idealities including the effects of extending the spokes out to an upper ground plane pulled back $\lambda/4$ from the antenna as well as a standard substrate around $\lambda/4$ thick mounted on a PCB with a lower ground plane.

simulation there is a 1 dB variation in gain from the $250\ \mu\text{m}$ substrate thickness for any substrate thickness from $220\ \mu\text{m}$ to $270\ \mu\text{m}$, well within the tolerance of standard thinning processes.

The 2×1 radiator array design was simulated using 3-D finite element method electromagnetic solver HFSS with a lossy substrate and chip conductors, but an ideally conductive reflection off of the PCB ground plane as it is estimated that the losses associated with the doped substrate will dominate. The ground plane of the inner radiator core is included in the simulation, but does not affect the radiation significantly (<1 dB change in gain). The diameter of the antenna ring is $520\ \mu\text{m}$, with an array spacing of 1 mm. It is important that the gain of the antenna be similar regardless of the desired polarization so that the power flux in a given direction will not change significantly as the polarization is controlled. Due to the isolation between the two superposition subparts, the gain of the simplified antenna does not depend on the desired polarization, but verification is required to insure that none of the non-idealities captured by the electromagnetic simulation cause significant deterioration to this isolation. When compared to the equations of the simplified analysis, the polarization achieved for various drives is similar to what is predicted, with full tuning range of polarization angle and a maximum deviation of less than 7° compared with the analysis, and axial ratios from 1.8 dB (compared to 0 dB for circular polarization) through 25 dB (compared with infinity for linear polarization). The antenna gain patterns in linear and circular polarization modes are shown in Figure 5.20 for two planes: $\phi = 0^\circ$ and $\phi = 90^\circ$. The efficiency from the output of the transistors (including impedance transformation, signal routing and antenna) to the far field radiation is 12%. The maximum gain of the antenna (again from the output of the transistors to the far field radiation) in linear polarization mode

is 0.8 dBi, which is within 0.3 dB of the maximum gain in circular polarization of 0.5 dBi, with similar single lobe patterns, which allows the polarization to be controlled while maintaining reasonably similar levels of power flux.

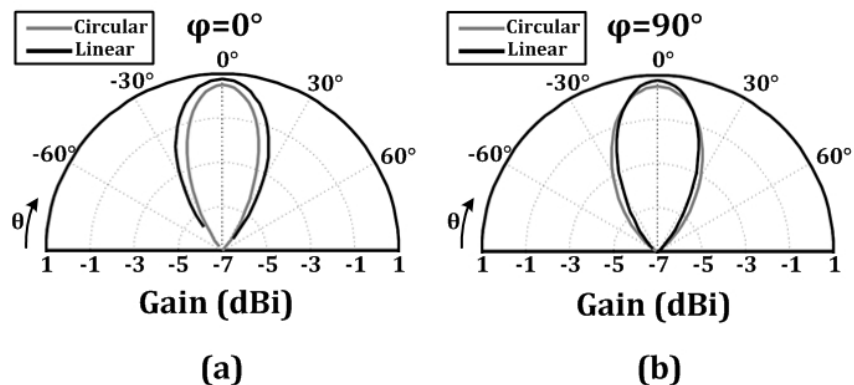


Figure 5.20: Simulated radiation gain pattern of the 2×1 array in circularly polarized mode and linearly polarized mode for planes $\phi = 0^\circ$ (a) and $\phi = 90^\circ$ (b) show similar patterns and maximum gains within 0.3 dBi of each other.

5.3.3.4 Measurements

The chip was fabricated in a 32 nm CMOS SOI process with two $1.2\text{-}\mu\text{m}$ -thick top copper layers and a $2.275\ \mu\text{m}$ aluminum layer. The measurement setup is shown in Figure 5.21. The chip was mounted using silver epoxy onto a ground plane on an FR4 PCB. DC supply and control voltages were wire bonded to traces on the PCB. The PCB was then mounted to a two-dimensional rotational stepper motor to enable radiation pattern measurements. The radiated signal was captured with a 22 dBi gain linearly polarized horn antenna that is fed to an 8th harmonic mixer whose IF output is amplified and fed to a spectrum analyzer. The distance between the radiator and receive antenna is 120 mm, or 42 wavelengths, a distance at which the received power shows a $1/R^2$ dependence, indicating far-field operation. The entire setup is calibrated using an Erikson PM4 calorimeter-based power meter that measures absolute broadband power by converting the electromagnetic power to heat. The antenna is rotated to capture the projection of the polarization onto the linear axis at every angle between 0° and 180° in a similar manner to the approach explained in the appendix of [6]. By capturing the linear projection at all angles, the angles of the maximum and minimum power can be obtained, which correspond to the major and minor axis of the polarization ellipse. The angle of the major axis corresponds to the polarization angle, while the ratio of powers between the major and minor

elliptical axes corresponds to the polarization axial ratio. For the antenna pattern measurements, the entire pattern was swept for receive antenna angles stepped every 5° from 0° to 180° . The radiator consumes 476 mW of DC power from a 1.3 V supply and occupies a physical chip area of 2.64 mm^2 .

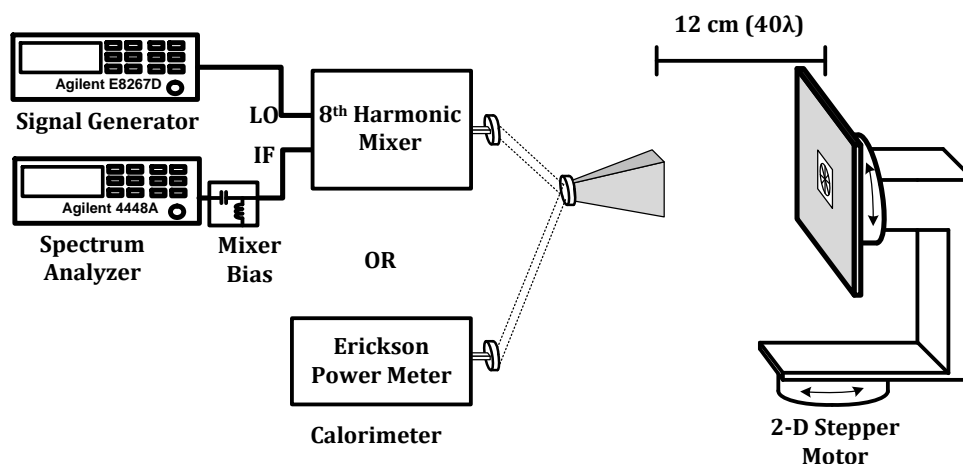


Figure 5.21: Measurement setup for the 2×1 radiator with DPC.

The measured calibrated received spectrum when the radiator array is in linear polarization mode is given in Figure 5.22. An effective isotropic radiated power (EIRP) of +7.8 dBm was measured at 105.5 GHz. Next the radiator was rotated across the entire half-space to produce the antenna patterns. Two measured elevation plane patterns are plotted in Figure 5.23 for $\phi = 0^\circ$, along the axis of the array and $\phi = 90^\circ$, perpendicular to the array. To show the beam steering capabilities of the one-dimensional phased array, the phases of all ports in one of the antennas were shifted to steer the beam along the axis of the array ($\phi = 0^\circ$), and beam steering of up to 15° along that axis is observed and plotted. The steering range is limited to the small size of the two-element array and to substrate mode coupling at more extreme angles and thus also increases coupling between the two antennas through the substrate. A side lobe is observed in the $\phi = 0^\circ$ plane. The beam is narrower in the $\phi = 0^\circ$ plane because it is the plane of the array and thus experiences array gain. The total radiated power integrated over the entire half space was measured to be 0.9 mW which is higher than the expected simulated power of 0.5 mW, which may be due to an overestimation of the loss of the substrate at these frequencies.

It is important to consider polarization in many radiation directions when discussing

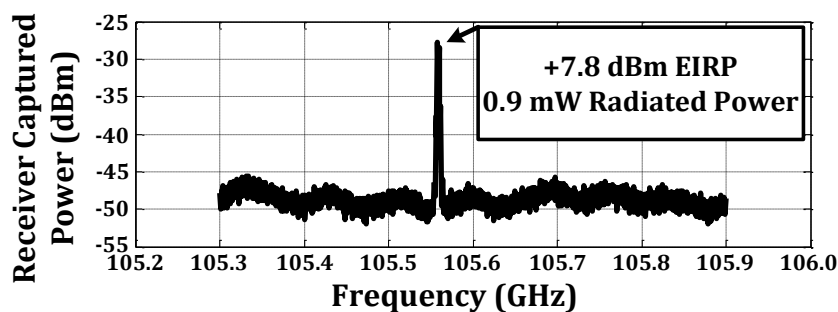


Figure 5.22: Calibrated measured spectrum of the DPC radiator array in linearly polarized mode has a maximum EIRP of +7.8 dBm at 105.5 GHz.

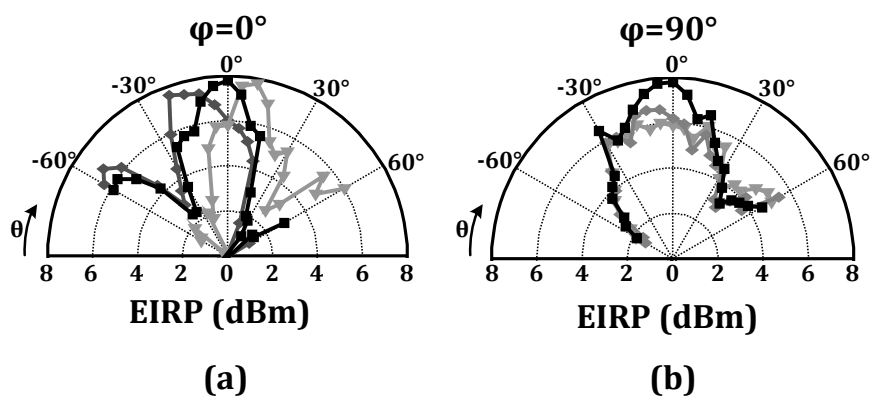


Figure 5.23: Measured radiation pattern for two elevation planes when $\phi = 0^\circ$ (a) and $\phi = 90^\circ$ (b) for broadside radiation as well as beam steering in both directions in the $\phi = 0^\circ$ dimension.

the polarization of antennas, and especially integrated antennas where the substrate can affect the polarization in non-broadside radiation directions. One benefit of this implementation of DPC is that the polarization can be controlled not just in the broadside dimension, but off axis as well. To showcase this, all of the DPC measurements have been performed at three separate directions of Figure 5.24. One is in the broadside direction, one is 20° off axis when $\phi = 0^\circ$ and one is 30° off axis when $\phi = 90^\circ$. When the polarization is being controlled along the axis of the array, beam steering is also implemented to steer the beam toward the target as well as controlling its polarization.

Predictable and deterministic polarization control of the radiator is shown through two measurements: controlling the polarization angle while maintaining linear

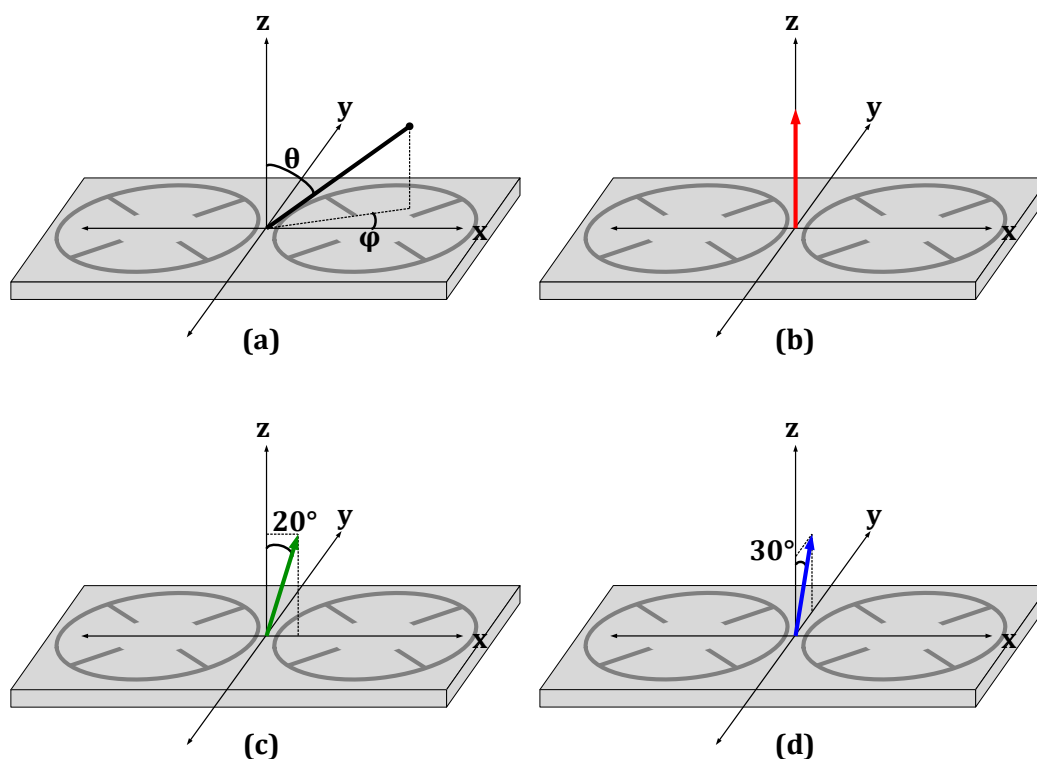


Figure 5.24: Orientation of coordinate system (a) as well as three directions used in demonstration of DPC: $\theta = 0^\circ$ (b), $\theta = 20^\circ$, $\phi = 0^\circ$ (c), and $\theta = 30^\circ$, $\phi = 90^\circ$ (d).

polarization, and controlling the axial ratio while maintaining a constant polarization angle, depicted in Figure 5.25. Due to variation between the various circuit blocks, a calibration was done by measuring the output polarization at various settings and creating a lookup table to ensure that the proper phases were being fed to the antennas. The first measurement shows the viability of using this radiator to maintain polarization matching to a linearly polarized receive antenna whose orientation is rotating in space. The measurements in Figure 5.26 show complete tuning range of the polarization angle from 0° to 180° while maintaining near linear polarization with axial ratios above 10 dB in all three of the demonstrated directions.

The second DPC measurement is to tune the polarization axial ratio while maintaining a constant polarization angle, as shown in Figure 5.27. These measurements show tunability of polarization ratio from 2.4 dB through 14 dB in all three radiation directions, with the high end of 14 dB being limited by the SNR of the measurement test setup. The low end of 2.4 dB, while being typical of circularly polarized systems, means that radiator was not able to produce completely circular polarization,

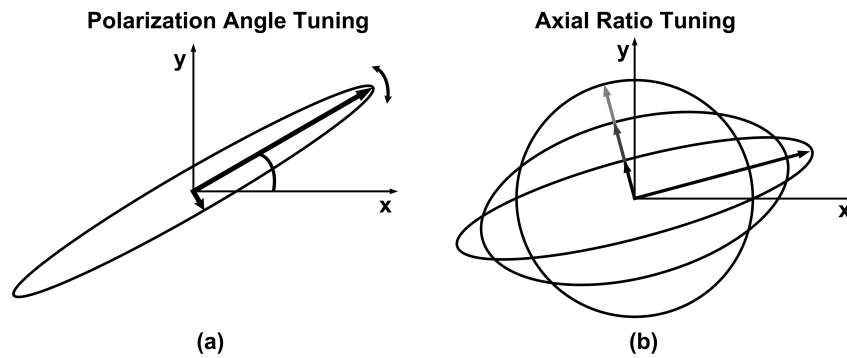


Figure 5.25: Two demonstrations of DPC: tuning of the polarization angle while maintaining linear polarization (a), and tuning of the axial ratio while maintaining constant polarization angle (b).

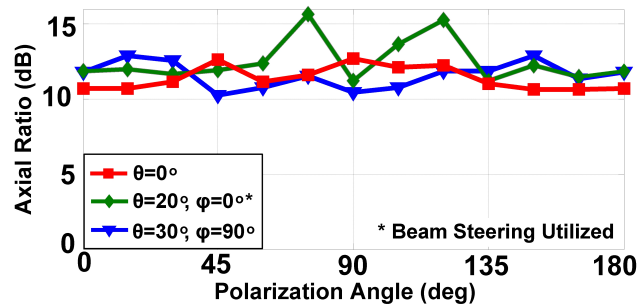


Figure 5.26: Measured tuning of polarization angle while maintaining linear polarization (axial ratios above 10 dB) show full tuning range from 0° to 180° in three different directions.

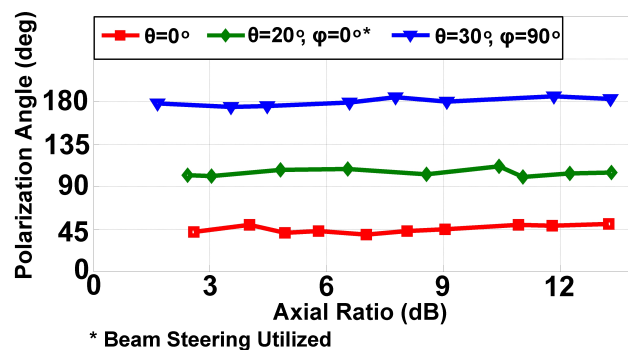


Figure 5.27: Measured tuning of polarization axial ratio while maintain near constant polarization angles in three directions show tuning range from 2.4 dB through 14 dB.

which is likely due to the fact that the array is not square and thus the coupling to substrate modes in the directions parallel and perpendicular to the array were not the same. If lower axial ratios were necessary for the application, a perfectly square phased array can be utilized to achieve a larger tuning range on the axial ratio.

To the best of the authors' knowledge this work presents the first integrated radiator with dynamically controllable polarization. Table 5.1 gives comparisons with other integrated radiators with static polarizations without external dielectrics. A die photo of the radiator is shown in Figure 5.28.

Metric	This Work	[66]	[67]	[68]	[4]	[5]	[6]
Polarization Control	Dynamic	N/A	N/A	N/A	N/A	N/A	N/A
Polarization	Linear Circular Elliptical	Linear	Linear	Circular	Circular	Circular	Circular
Frequency (GHz)	105.5	338	210	134.5	280	191	161
Rad. Power (dBm)	-0.5	-0.9	N/A	-1.3	-7.2	-12.4	-2.0
Max EIRP (dBm)	7.8	17.1	5.1	6.0	9.4	-1.9	4.6
Process	32nm SOI CMOS	65nm CMOS	32nm SOI CMOS	32nm SOI CMOS	45nm SOI CMOS	65nm CMOS	130nm SiGe
Num. of Elements	2	16	4	1	16	4	1
DC Power (mW)	476	1540	240	168	817	77	388
Area (mm ²)	2.64	3.9	3.5	1.2	7.3	1.1	1

Table 5.1: Comparison with integrated radiating sources in silicon without external dielectrics

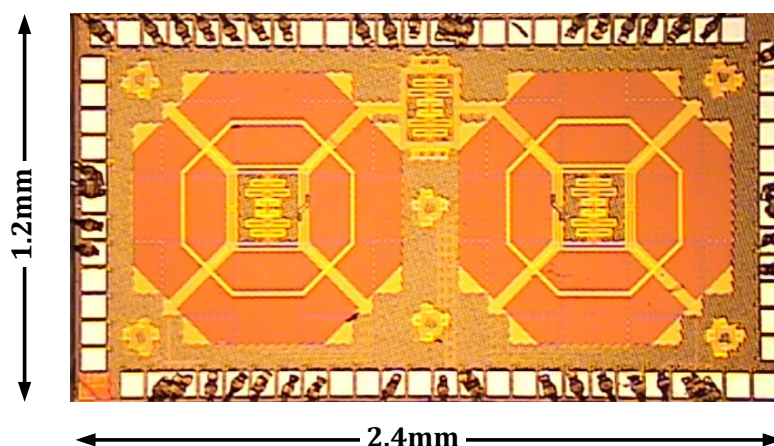


Figure 5.28: Die photo of 2×1 radiator array with DPC.

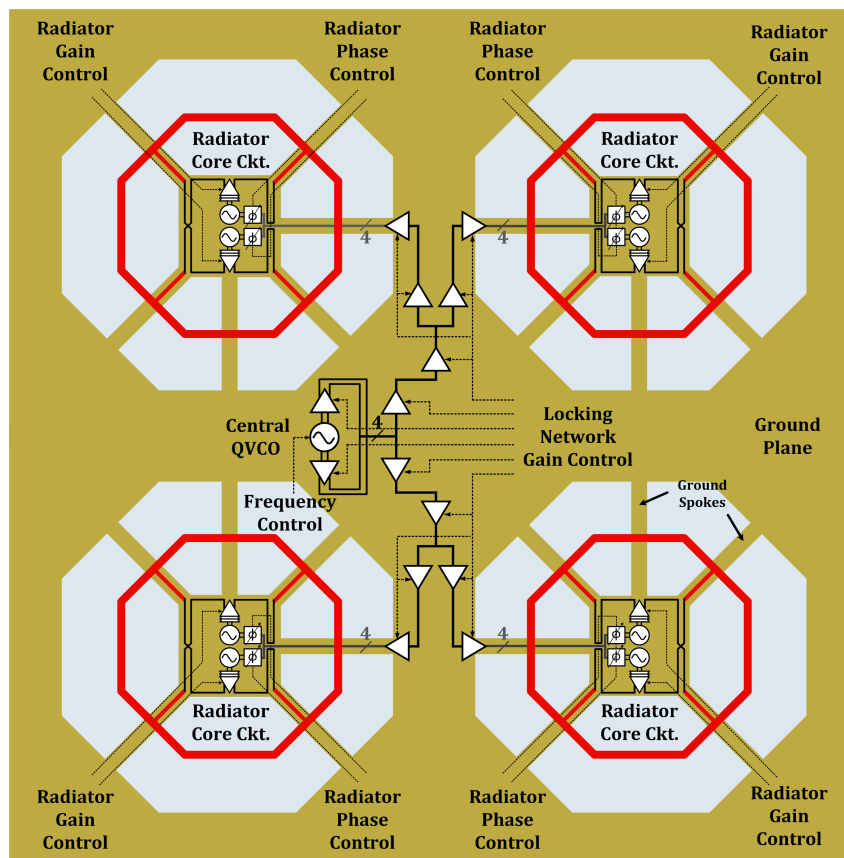


Figure 5.29: Block diagram of the 2×2 DPC integrated phased array.

5.3.4 A 2×2 Integrated DPC Radiator Array

In this section, we present a fully integrated 2×2 DPC phased array radiating at 123 GHz fabricated in IBM's 32-nm CMOS silicon-on-insulator (SOI) process.¹ The 2×2 DPC array enables full control over the polarization of the radiated signal and 2-D beam steering at the same time.

5.3.4.1 System Architecture

The simplified block diagram of the 2×2 DPC integrated phased array is shown in Figure 5.29. It consists of four independent DPC antennas, meaning that each antenna element on its own is capable of DPC of its radiated EM waves, independent of the rest of the antennas in the array. Each individual DPC antenna uses its own

¹This design was a joint project with my colleagues Steven Bowers and Kaushik Dasgupta. I was responsible for the electromagnetic design of the modified DPC antenna and the antenna array, as well as the core and locking network oscillators, the amplifiers, phase rotators, and the electromagnetic design of the passives and matching networks inside each core. Steven was responsible for the design of the distribution network and Kaushik designed the digital to analog converters.

drive circuitry, running at 123 GHz, and incorporates two independent sets of phase and gain control units to set the desired phases and amplitudes for the antenna drives. Frequency synchronization of the four radiating antennas is performed by a central quadrature voltage-controlled oscillator (QVCO) that provides the reference quadrature signals which are also used for phase control units in each core. These quadrature signals are distributed from the central QVCO to the four radiator cores by a locking network consisting of multiple buffer stages and transmission-line sections.

5.3.4.2 Modified DPC Antenna

In a DPC array, in order to synchronize the frequency of operation and also to provide a phase reference for each element, central locking signals must be routed to the inside of each core. In [65], one of the four ground spokes was assigned to route the locking signals underneath the ground since the topside was already used for antenna feed lines. This requires use of thin low-metal layer lossy transmission lines for the locking signals. To alleviate this issue in this work, a 5th ground spoke dedicated to the distribution of the locking signals is added to allow routing thicker transmission lines above the ground spoke with less loss, as shown in Figure 5.30.

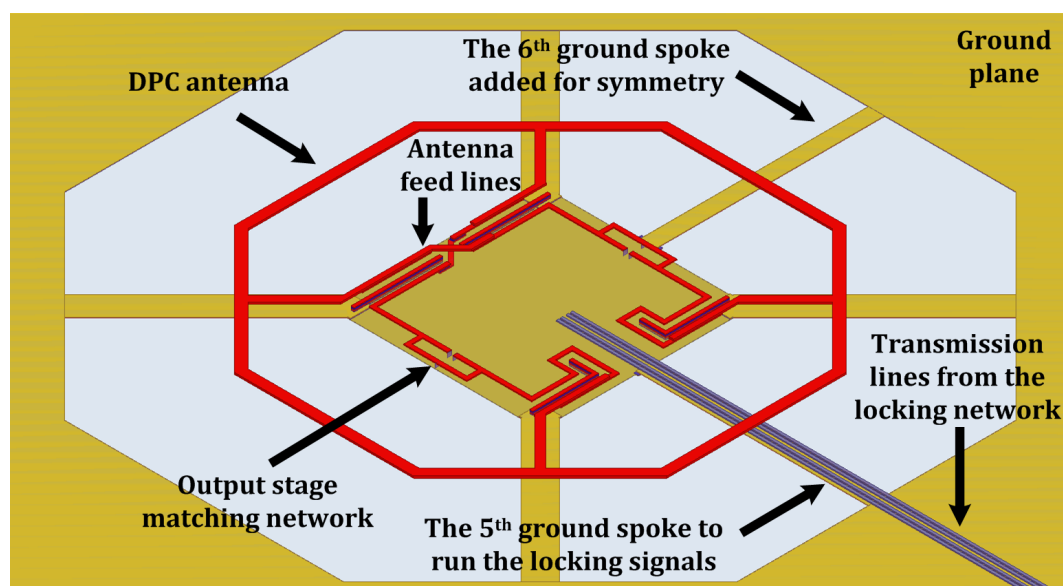


Figure 5.30: Modifications of the DPC antenna by adding two additional ground spokes to allow low-loss transmission lines for the locking signals while maintaining the symmetry of the structure.

This spoke is still orthogonal to the antenna ring to minimize the mirror currents and the effects on the radiation pattern. However, the 5th spoke introduces some undesired asymmetry into the antenna structure. Thus, a 6th spoke is also added orthogonal to the 5th one and the ring to preserve the symmetry of the structure such that one polarization would not be favored over the other one.

The DPC antennas are realized on the top $2.275\text{-}\mu\text{m}$ -thick aluminum layer with $12\text{-}\mu\text{m}$ -wide lines. The periphery of each antenna is $1730\ \mu\text{m}$ with $1400\text{-}\mu\text{m}$ center-to-center separation between two adjacent antennas. The delay-matched feed lines within each antenna that connect the output stages to the four antenna ports extend an overall length of $420\ \mu\text{m}$ and are implemented with multiple transmission-line sections on the top three metal layers due to layout considerations. The four original ground spokes are $30\ \mu\text{m}$ wide while the 5th and the 6th spokes are $24\ \mu\text{m}$ wide and the ground plane is spaced $150\ \mu\text{m}$ away from each antenna.

The radiator chip is designed to radiate from the topside. For this purpose, it is mounted on a printed circuit board (PCB) ground plane. Due to higher dielectric constant of the substrate, most of the power initially radiates down towards the lower ground plane and gets reflected back. However, the substrate is about a quarter-wavelength thick, which allows the reflected signal to add constructively with the initial topside radiated waves to form the overall topside radiation.

The entire 2×2 radiator array is simulated with the ANSYS HFSS 3-D EM solver. Figures 5.31 and 5.32 demonstrate the effects of the two additional ground spokes on the performance of the array in the broadside direction by comparing the simulated results for five- and six-spoke DPC antenna arrays against the theoretical superposition of two ideally expected orthogonal linear polarizations for different drive settings. It should be noted that these simulations solely evaluate the performance of the stand-alone EM design under ideal drive settings in the absence of drive circuit non-idealities. They investigate how close to ideal the summation of two orthogonal linear polarizations is performed and how uniform the antenna array gain behaves for different settings. Figure 5.31(a) shows a scenario where the relative amplitudes of V_A and V_B and the phase difference $\psi_B - \psi_A$ are set based on the theoretical summation for all four antennas to ideally achieve uniform polarization angle tuning from 0° to 180° with steps of 15° . In Figure 5.31(b), the simulated polarization angles corresponding to these settings for the DPC arrays with five spokes and six spokes are plotted and compared with the ideal goal that is mathematically expected from these settings, which reveals the advantage of adding

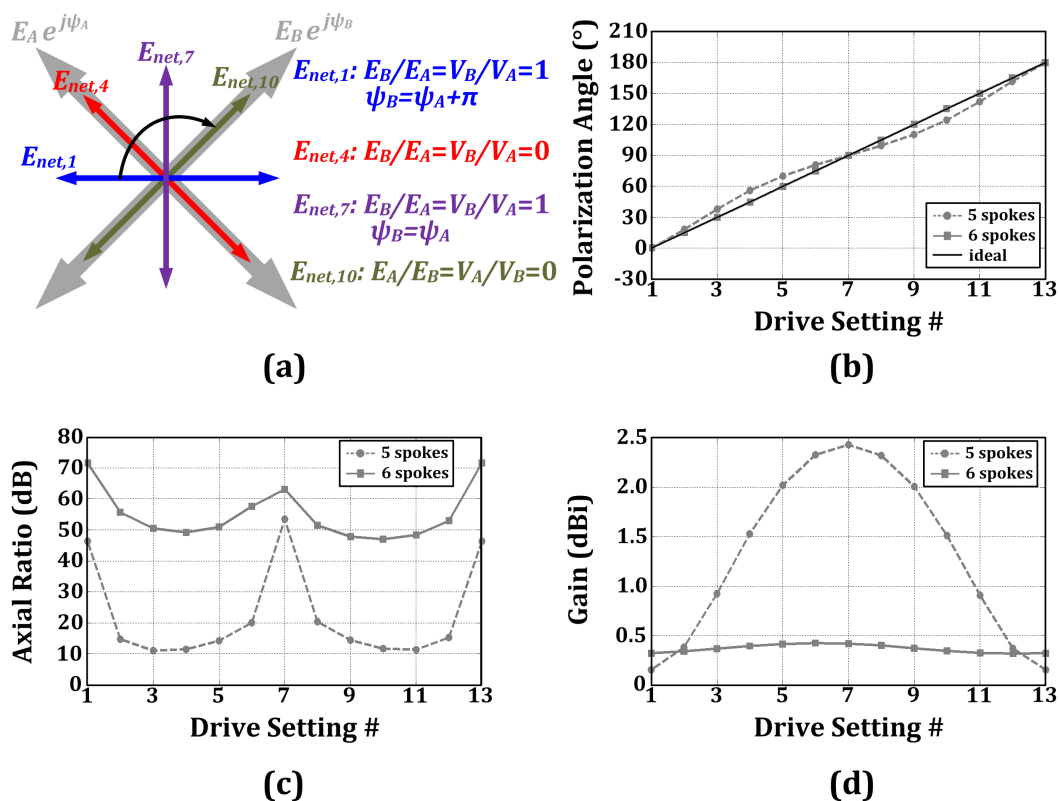


Figure 5.31: Effect of the 5th and 6th spokes on polarization angle tuning. (a) Polarization angle is set by the drive settings and the (b) simulated polarization angle, (c) axial ratio, and (d) antenna array gain show more accuracy and symmetry for six-spoke DPC antennas.

the 6th spoke to achieve more accuracy in polarization angle tuning due to more symmetry in the structure. Furthermore, the achieved axial ratios for the linear polarizations are much higher in the presence of the 6th spoke, as shown in Figure 5.31(c), resulting in closer-to-ideal linear polarizations where infinitely large axial ratios are expected. Also, the antenna gain variation for the entire 2×2 array is much smaller for the six-spoke antennas, as ideally uniform antenna gain is expected for all settings (i.e., all polarization angles). This can be seen in Figure 5.31(d) where the simulated gain of the array for both cases of five- and six-spoke antennas is shown. A similar set of simulation results are shown in Figure 5.32 where the phase difference $\Delta\psi = \psi_B - \psi_A$ is swept from 0° to 360° while the amplitudes V_A and V_B are kept equal. This would ideally result in tuning the axial ratio by changing the radiated polarization from linear polarization to circular polarization while keeping the polarization angle constant at 90° (for $\Delta\psi = 0^\circ$ to $\Delta\psi = 90^\circ$) and then from circular polarization back to linear polarization with a constant polarization angle

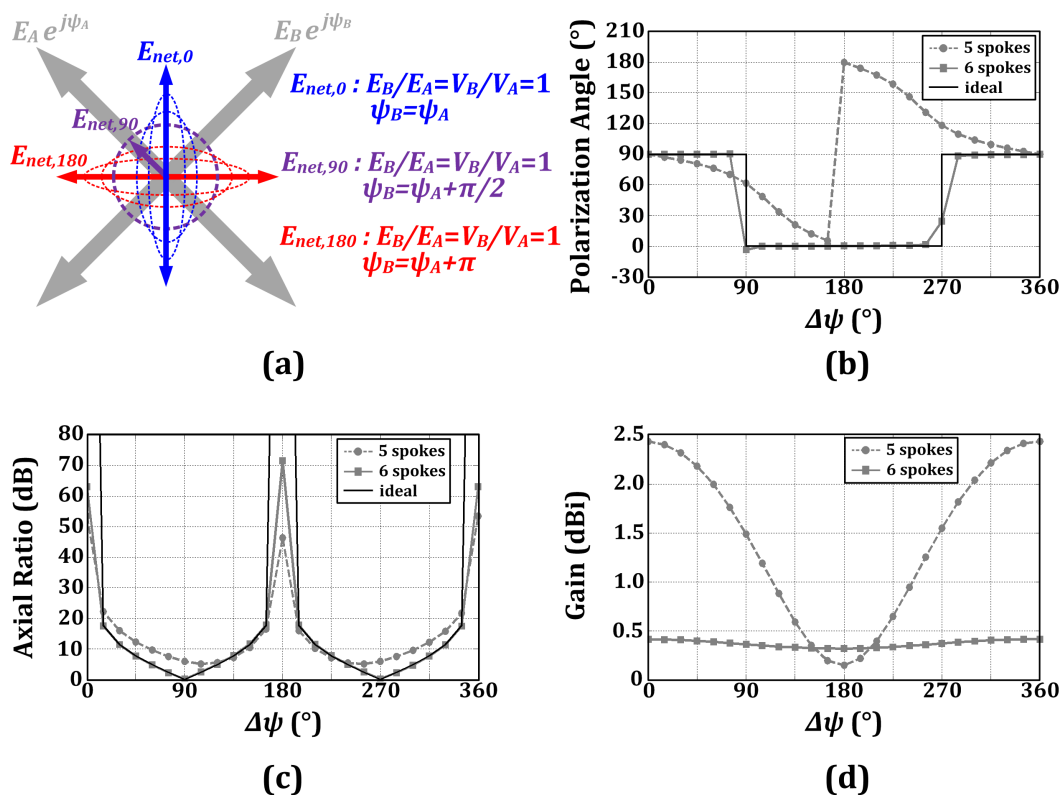


Figure 5.32: Effect of the 5th and 6th spokes on axial ratio tuning. (a) Axial ratio is set by the phase difference of the drive sets, and the (b) simulated polarization angle, (c) axial ratio, and (d) antenna array gain show more accuracy and symmetry for six-spoke DPC antennas.

of 0° (for $\Delta\psi = 90^\circ$ to $\Delta\psi = 180^\circ$). The reverse scenario with reverse handedness happens for $\Delta\psi = 180^\circ$ to $\Delta\psi = 360^\circ$, as depicted in Figure 5.32(a). Similar to the previous set of simulations, a comparison of the simulated polarization angle, axial ratio, and antenna gain for the five- and six-spoke DPC antenna arrays against the theoretically expected values, as shown in Figure 5.32(b)–(d), proves that the 6th ground spoke improves the performance by achieving very accurate polarization angles and axial ratios and a uniform antenna gain for different values of $\Delta\psi$ with less than 0.1 dB variation.

The maximum simulated gain of the 2×2 DPC array in the broadside direction for both linear and circular polarizations is 0.4 dBi with 7% radiation efficiency. However, it should be noted that all antenna feed lines, their crosses, and meandering for delay matching, as well as the matching networks for the output stages, are all included in these EM simulations. The simulated gain patterns of the array for both linear and circular polarization modes are shown in Figure 5.33.

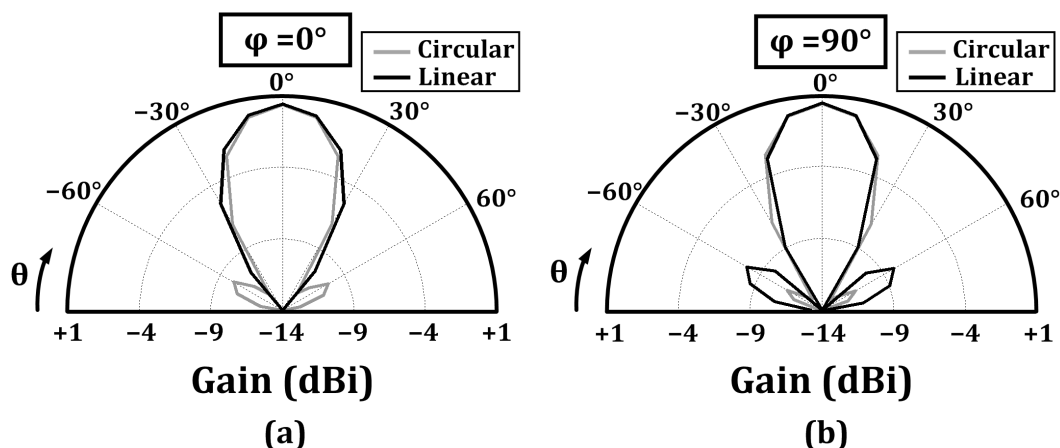


Figure 5.33: Simulated antenna gain patterns for the 2×2 DPC radiator array in circularly polarized mode and linearly polarized mode for planes: (a) $\phi = 0^\circ$ and (b) $\phi = 90^\circ$ show maximum gain of 0.4 dBi in the broadside direction.

5.3.4.3 Circuit Implementation

Antenna Drive Circuitry: Figure 5.34 demonstrates the details of the drive circuitry for each antenna element. The power is generated locally by two differential oscillators. The quadrature lines from the locking network drive two phase rotators and each phase rotator generates a differential current with the desired phase through proper weighted summation of in-phase (I) and quadrature (Q) components. This differential current is then injected into the corresponding oscillator to lock its frequency and control the phase. The differential output of each oscillator goes through a buffer chain with gain control before feeding the antenna at the corresponding ports. The supply voltage for each core's analog drive circuitry is 1.25 V.

1) *Phase Control:* Each phase rotator consists of two Gilbert cells whose outputs are added in the current domain to generate a differential current with the desired phase [101]. The differential current is directly injected into the output nodes of the differential cross-coupled oscillator and locks its output at the desired phase and frequency. The schematic of one phase rotator-oscillator pair is shown in Figure 5.35. The plot in Figure 5.36 shows the simulated output power of the two oscillators as the phase difference between them is controlled from 0° to 360° by the phase rotators. Time-domain waveforms for the two cases of 90° and 180° are also shown on the same plot. Each differential oscillator and its corresponding phase rotator draw 43 and 12 mA of dc current, respectively, in simulation.

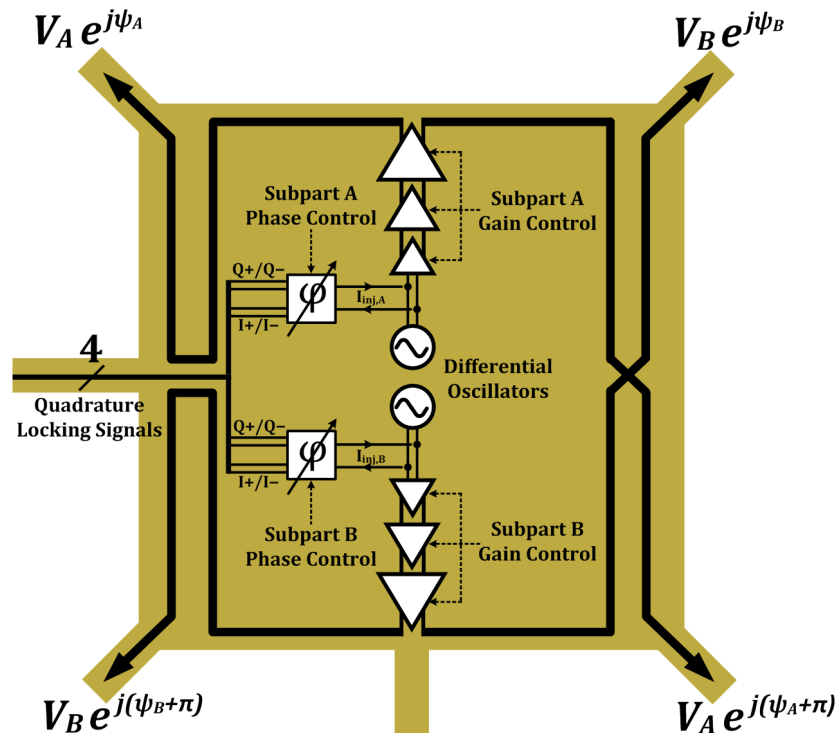


Figure 5.34: Detailed block diagram of the drive circuitry for each DPC antenna with independent phase and gain control units for the two subparts, as well as independent control for each antenna with respect to the other antennas in the array.

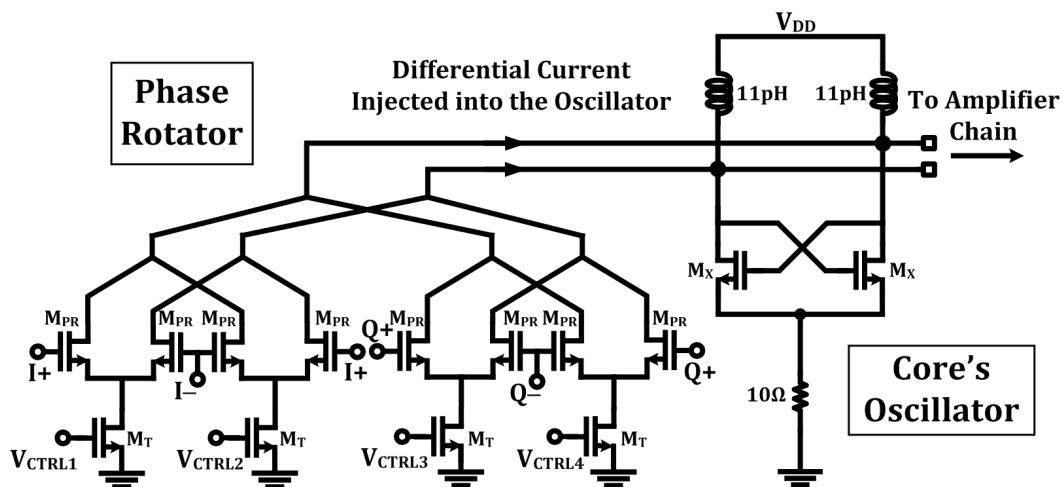


Figure 5.35: Detailed block diagram of the drive circuitry for each DPC antenna with independent phase and gain control units for the two subparts, as well as independent control for each antenna with respect to the other antennas in the array.

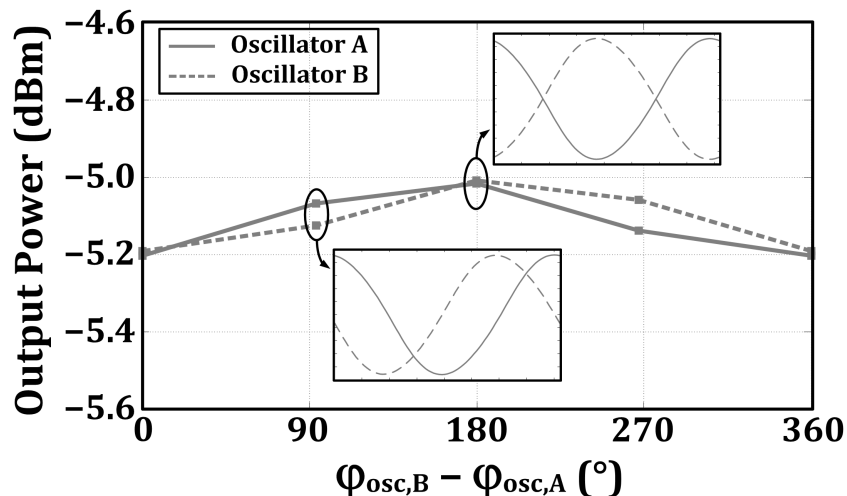


Figure 5.36: Detailed block diagram of the drive circuitry for each DPC antenna with independent phase and gain control units for the two subparts, as well as independent control for each antenna with respect to the other antennas in the array.

2) *Gain Control*: Each oscillator of the core drive circuitry is followed by one buffer chain. This allows independent gain control for each subpart. It also provides isolation between the oscillators and the antenna, minimizing the effects of antenna input impedance variation due to different drive settings on the frequency and the output power of the oscillators. The schematic of one buffer chain and its simulated gain are shown in Figure 5.37. The buffer chain consists of three cascode stages with $W_{M_1} = 20 \mu\text{m}$, $W_{M_2} = 40 \mu\text{m}$, and $W_{M_3} = 60 \mu\text{m}$. The matching network inductors between the stages are realized with shorted transmission lines with lengths/widths of $80 \mu\text{m}/4 \mu\text{m}$, $65 \mu\text{m}/5 \mu\text{m}$, and $85 \mu\text{m}/5 \mu\text{m}$ for L_1 , L_2 , and L_3 , respectively, and the values for ac coupling capacitors, which also contribute to impedance matching, are $C_1 = 50 \text{ fF}$, $C_2 = 60 \text{ fF}$, and $C_3 = 105 \text{ fF}$. The overall gain of the chain is controlled by the bias adjustments of the input gates of the three stages through biasing resistors $R_B = 3 \text{ k}\Omega$. Simulations of different settings show a maximum gain of 10.2 dB for each chain when loaded with the nominal antenna impedance with the three buffers drawing 17-, 34-, and 51-mA dc currents, respectively, for the maximum gain case.

Although the two subparts should ideally be completely isolated from each other to allow independent control over each subpart's polarization, in practice their undesired interaction through the DPC antenna can cause imbalance both in their own circuitry and relative to each other, which, in turn, could introduce error to

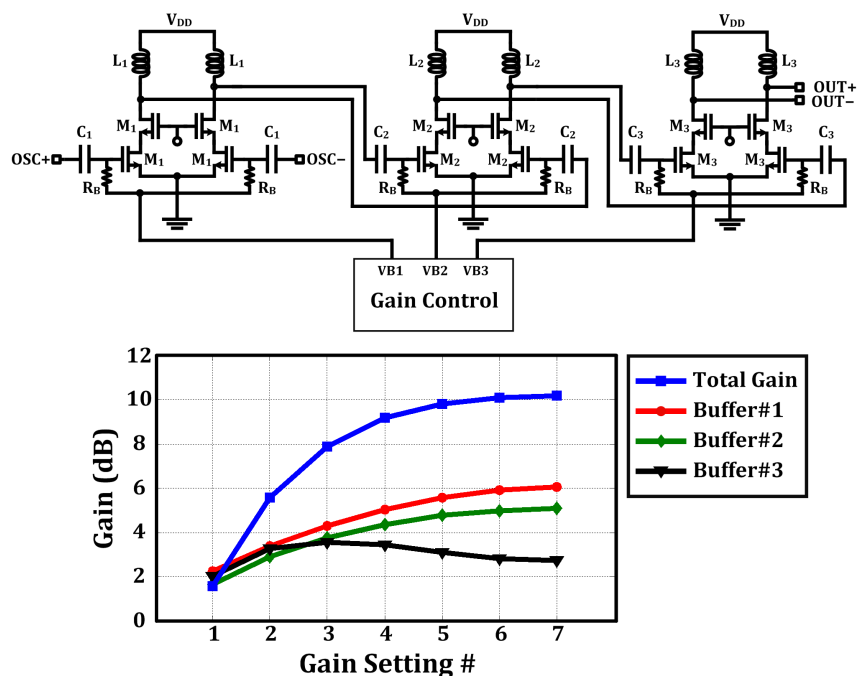


Figure 5.37: Schematic of the buffer chain that controls the gain of each subpart in the antenna drive circuitry with a maximum simulated gain of 10.2 dB.

the overall polarization. To better demonstrate this phenomenon, we investigate the effects of such an interaction on the single-ended antenna input impedances for each subpart ($Z_{in,A+}$, $Z_{in,A-}$, $Z_{in,B+}$, and $Z_{in,B-}$) in one of the antennas. Since the feed lines for these four driving ports are routed in different ways (two of them cross each other while the other two do not), the input impedances behave slightly differently as the drive settings change. Figure 5.38(a) shows how the simulated input impedances for each antenna port of one of the DPC antennas change on the Smith chart as the relative phase difference between the two subparts, $\Delta\psi$, is swept from 0° to 360° by the phase rotators for all four antennas. In Figure 5.38(b), the single-ended input impedances for the same DPC antenna are simulated when the two subparts are driven in phase, but their amplitude ratio, V_B/V_A , is changed from 0.2 to 5 for all antennas. As can be seen in these figures, the variations in the drive settings would cause the antenna input impedances that load each subpart's output stage to deviate from the optimal impedance, which, in turn, reduces the gain and the output power that is delivered to the antenna by each subpart. It should be noted that these two scenarios are not the only possible cases and, in practice, both the relative phases and the relative amplitudes could change while switching to a certain polarization and cause deviations from nominal impedances.

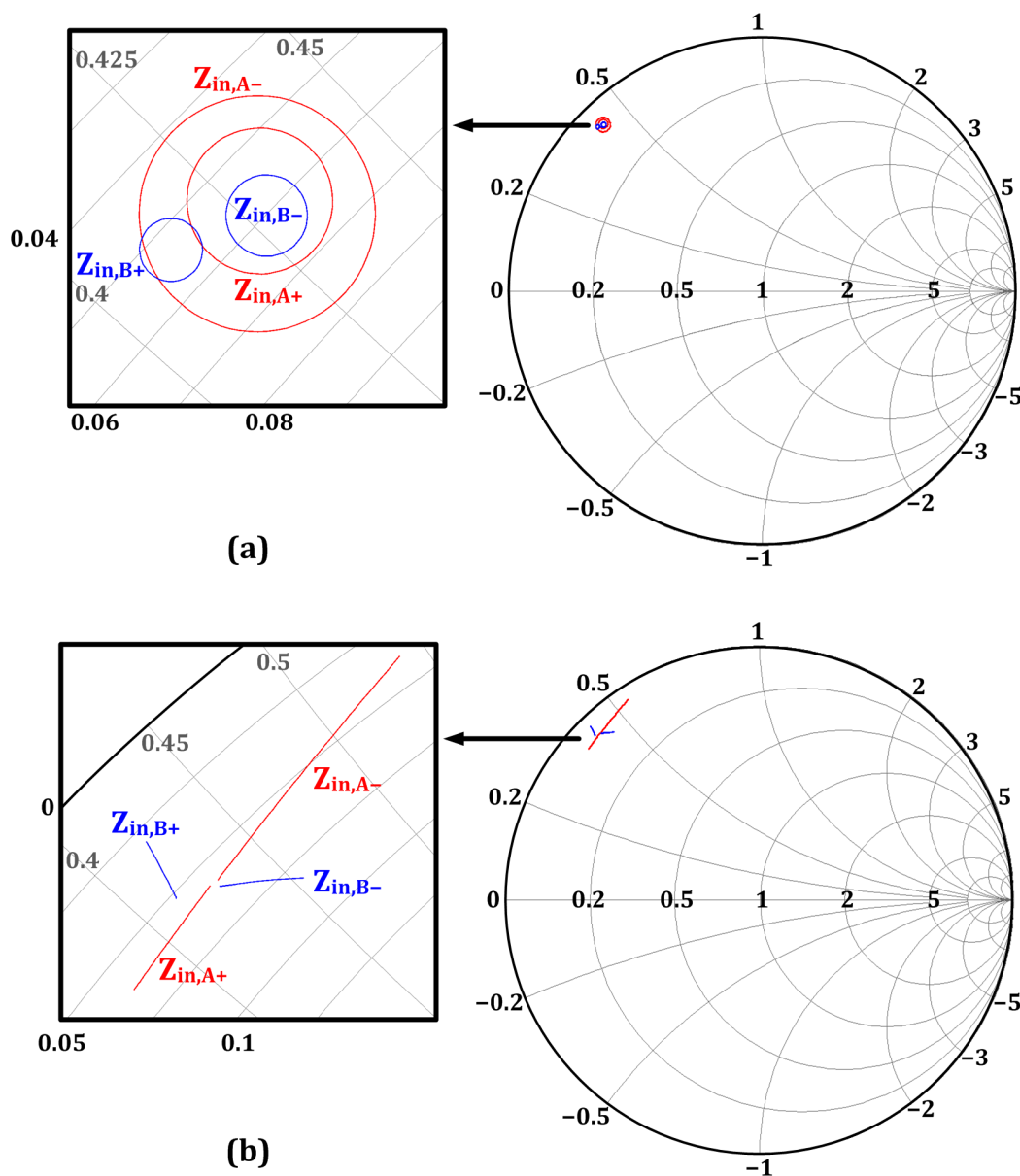


Figure 5.38: Variations of the single-ended input impedances of the DPC antenna for: (a) $0^\circ < \Delta\psi < 360^\circ$ when $V_A = V_B$ and (b) $0.2 < V_B/V_A < 5$ when $\Delta\psi = 0^\circ$.

In addition to the subparts' interaction through the antenna, they could also affect each other through parasitic and EM coupling that happen in the drive circuitry and could potentially cause both gain and phase errors. Based on the implemented layout, the most likely location for the strongest coupling is the center of each DPC antenna where the phase rotators and sub- parts' oscillator are located close to each other. However, simulations show that the parasitic coupling between the two subparts ($|S_{A\pm,B\pm}|$) at the output of the phase rotators is below -36 dB and

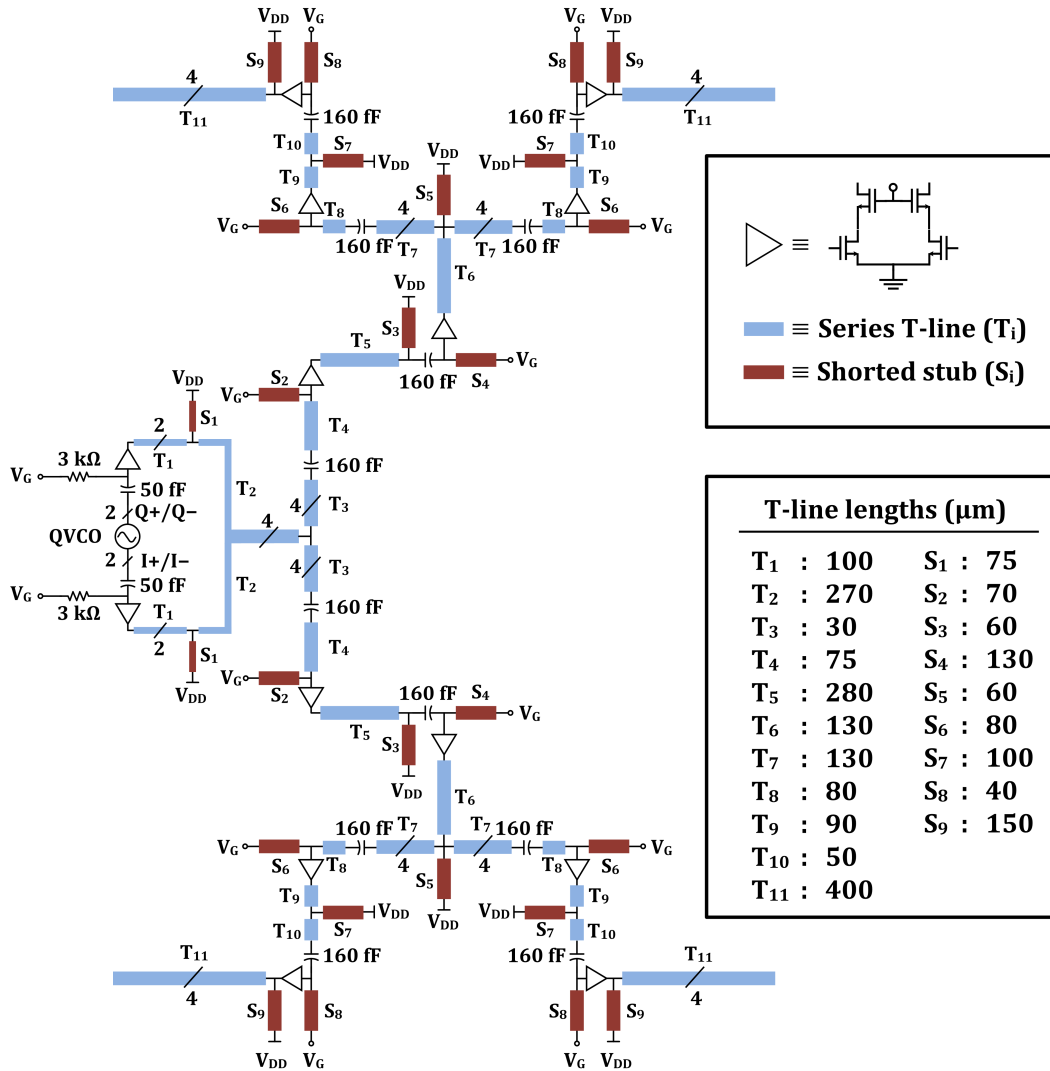


Figure 5.39: Block diagram of the locking network.

the EM coupling between the oscillators' inductors is also less than -51 dB for all combinations of $|S_{A\pm, B\pm}|$, which are both negligible compared to the strength of the injected signal into the oscillator.

Locking Network: Generation and distribution of the reference quadrature signals to the radiator cores are performed by the locking network. It takes the quadrature signals from the central QVCO, and distributes and splits them to feed the drive circuits of the four antennas. The amplification, distribution, and splitting are done in a distributed fashion through five stages of amplification, with two "T" splits after the first and third stages, as shown in Figure 5.39. The buffer stages in this network are the same cascode stages as the ones used in each core's buffer chain, and all

transmission-line sections are realized on the top aluminum layer with 5- μm -wide lines. Each transmission-line section between the amplifiers stages is used both for physical distribution to the fixed locations of the four radiator cores, as well as for impedance matching, with transmission-line stubs used at both the input and output of the amplifiers for matching and biasing, and metal ac coupling capacitors that allow independent dc voltages for the drains of the output transistors of each cascode stage and the gates of the input transistors of the following cascode stage. To minimize the dc power consumption of the initial amplifying stages while allowing for higher RF power on the later stages, the amplifying transistors scale up from the 1st to 5th amplifying stage, with 20- μm -wide, 16- μm -wide ($\times 2$), 20- μm -wide ($\times 2$), 20- μm -wide ($\times 4$), and 40- μm -wide ($\times 4$) transistors used in the 1st through 5th amplifying stages, respectively, for each differential output of the QVCO, with $2\times$ of the 2nd and 3rd stages, and $4\times$ of the 4th and 5th stages due to the power-splitting “T” sections after the 1st and 3rd amplifying stages. The simulated dc current consumption for each of the 16-, 20-, and 40- μm -wide buffers are 14, 17, and 34 mA, respectively. The input gate bias of the cascode stages can be controlled to adjust the gain such that enough power is delivered to saturate the inputs of the phase rotators within the radiating cores with some margin for additional losses due to variations or modeling inaccuracies that might cause slight impedance mismatches between stages.

The quadrature signals that feed the distribution network are generated by the central QVCO. The schematic of the QVCO is shown in Figure 5.40. It uses simultaneous coupling through the tail resistive network ($R_C = R_T = 10 \Omega$) in addition to the basic quadrature coupling transistors (M_q with $W_{M_q} = W_{M_C}/10 = 3 \mu\text{m}$), which are used in conventional QVCOs [54]. More details about the operation principle and advantages of this architecture are discussed in section 5.3.3.2. The QVCO inductors are designed and modeled based on the technique described in section 4.3.2.1 resulting in an equivalent tank inductance of $L = 12 \text{ pH}$, and the varactors are realized by 10- μm -wide thick-oxide NMOS transistors. Simulated tuning range for oscillation frequency of the QVCO, which synchronizes all the elements in the array, is from 120.1 to 121.8 GHz (from 122.9 to 124.7 GHz in measurement) and it generates -7.4 dBm of output power per quadrature line while drawing 90 mA from the power supply. The simulated time-domain waveforms of the QVCO quadrature outputs are also shown in Figure 5.40. The supply voltage for the QVCO and all the buffers in the locking network is 1.4 V.

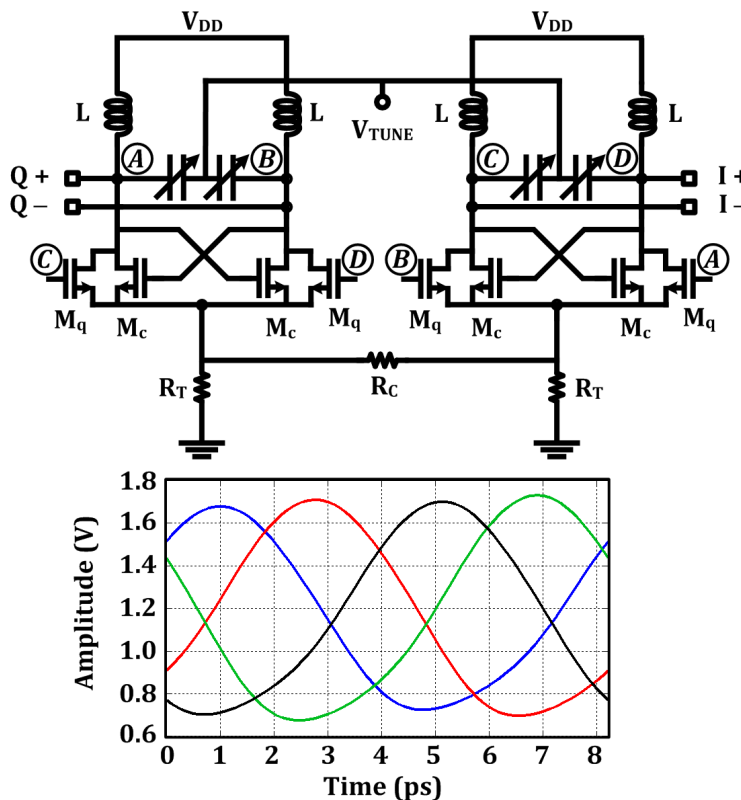


Figure 5.40: Schematic of the central QVCO and its simulated time-domain output waveforms.

Actuators: Digital-to-analog converters (DACs) are used as actuators to set the control voltages for the gain and phase control units in the antenna drive circuitry, as well as for the biasing control in the locking network. 5-bit weighted current mirror based DACs were implemented for the gate voltage controls. Figure 5.41(a) shows the circuit schematic of the single-ended DAC, where cascode current mirrors are utilized for higher output resistance and to ensure monotonicity. The same architecture followed by a current-mode single-ended to differential converter is implemented to form DACs with differential outputs, as depicted in Figure 5.41(b). The single-ended DACs were designed to be able to cover voltage ranges for both common-source, as well as any cascode devices that need bias control. Simulation results, shown in Figure 5.41(c), reveal good linearity over a full range from 0 to 1.5 V and an average least significant bit (LSB) of 50 mV. Differential DACs were designed to be used for differential control of the Gilbert cell tail currents in the phase control units. The simulated output of the differential DACs is shown in Figure 5.41(d). Both DACs use 1.8 V supplies. The differential DAC also uses 1.2 V supply for the single-ended to differential conversion.

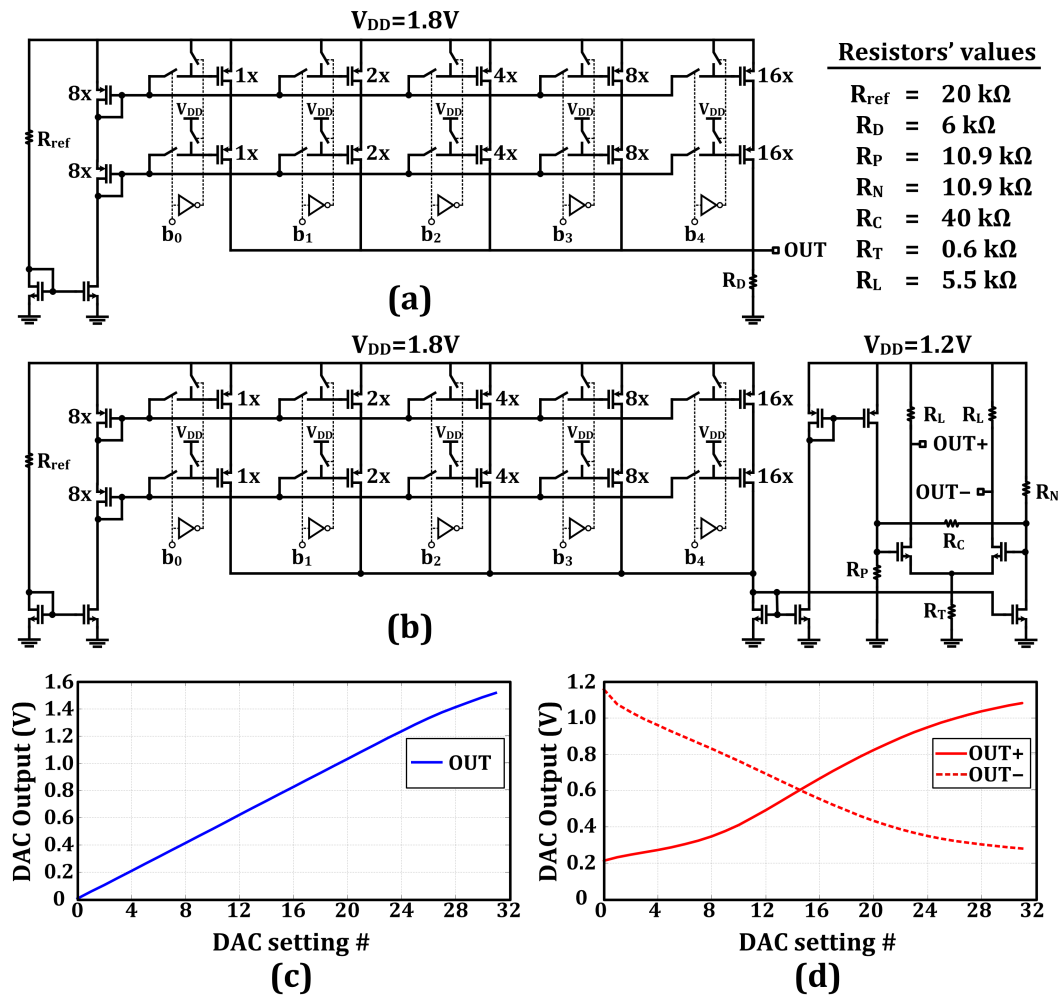


Figure 5.41: Schematics of the 5-bit DACs with (a) single-ended and (b) differential outputs, as well as the (c) simulated output voltage for the single-ended DAC and (d) differential DAC.

5.3.4.4 Measurements

Measurement Setup: The 2×2 DPC radiator array is fabricated in IBM's 32-nm CMOS SOI process and occupies an area of 2.852.85 mm². It is mounted on a PCB and is attached to a 2-D stepper motor to allow antenna pattern measurements, as shown in Figure 5.42. The radiated signal is received by a 22.7-dBi gain horn antenna which is mounted on another stepper motor to allow polarization measurement of the radiated signal by the linearly-polarized horn antenna in any arbitrary direction that is set by the 2-D stepper motor on the transmitter side. The simplified diagram in Figure 5.43 shows the definitions of the angles θ , ϕ , and α that are controlled by these two stepper motors and are frequently used in the measurement results section.

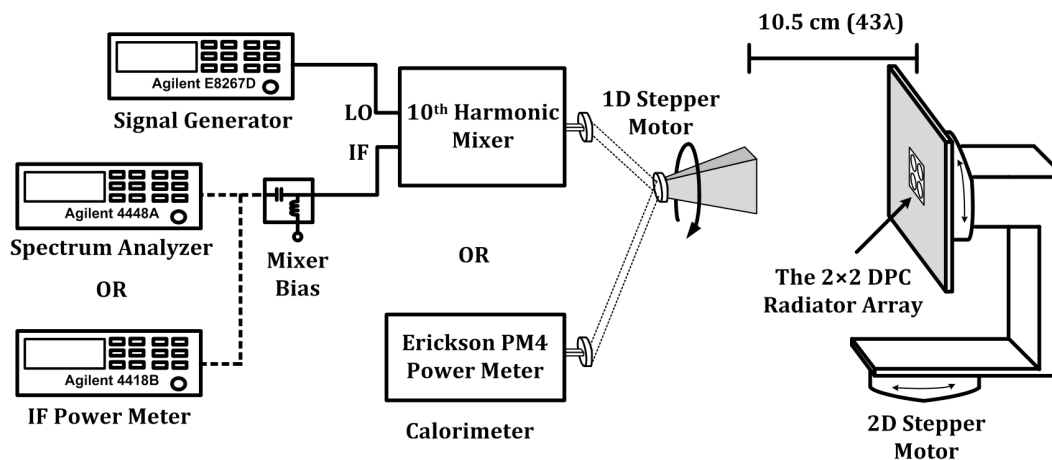


Figure 5.42: Measurement setup for the 2x2 DPC radiator array. A 2-D stepper motor on the transmitter side and a 1-D stepper motor on the receiver side allow independent polarization measurement of the radiated signal at any desired direction.

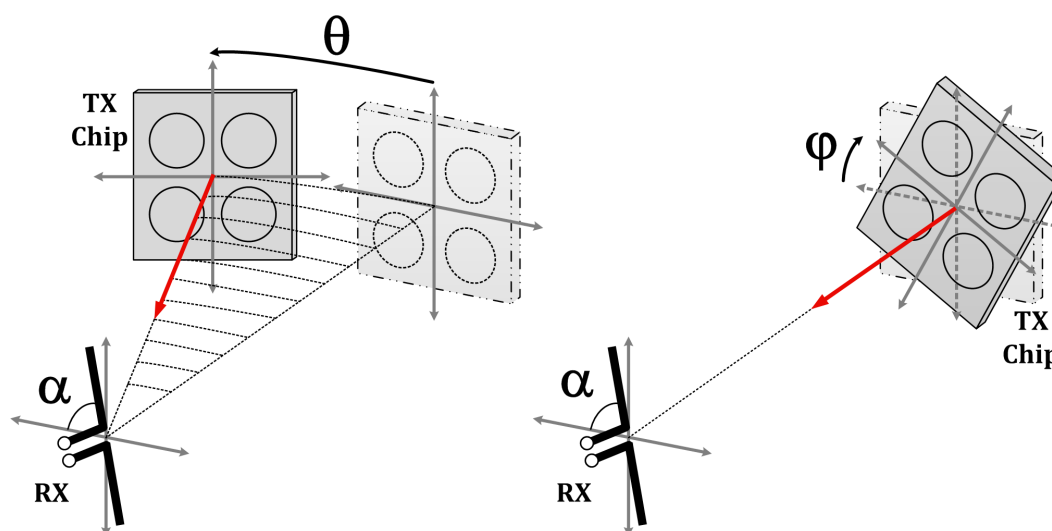


Figure 5.43: Definitions of the angles θ , ϕ , and α that are controlled by the stepper motors. θ and ϕ are controlled by the 2-D stepper motor on the transmitter side and α is controlled by the 1-D stepper motor on the receiver side.

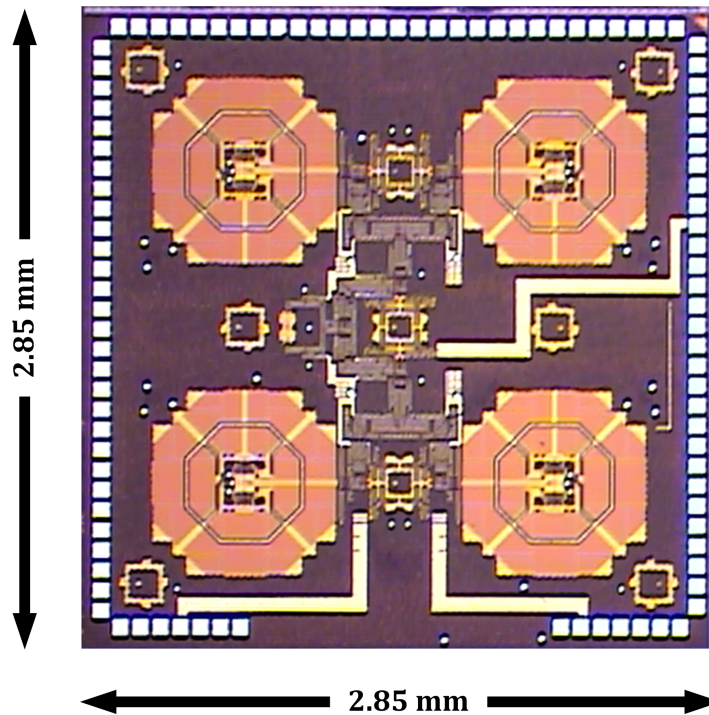


Figure 5.44: Die photograph of the 2×2 DPC radiator array.

Angles θ and ϕ are set by the 2-D stepper motor and determine the direction at which the receiver antenna picks up the radiated signal and the angle α is swept by the 1-D stepper motor on the receiver side to measure the polarization parameters of the transmitted EM waves by the linearly-polarized receiver. The received signal is downconverted by a 10th harmonic mixer, and then amplified by IF amplifiers. The downconverted IF signal is then fed either to a spectrum analyzer or an IF power sensor for spectrum or power measurements, respectively. The entire setup is calibrated with a PM4 Erikson Calorimeter. The overall power consumption of the chip is 1.885 W with 1.726 W for the radiator analog circuitry from 1.25 and 1.4 V supplies and 159 mW for the DACs and the digital interface. The die photograph of the radiator is given in Figure 5.44.

Optimization Process: In order to find the proper settings for the actuators of each antenna's drive circuitry to radiate the desired polarization in the target direction, an off-chip gradient-descent-based optimization algorithm is used. With such an algorithm, possible deviations in the actuators' values from the required theoretical settings that could happen due to process variations, delay mismatch between transmission lines, and modeling inaccuracy can be compensated for. The goal of

the optimization process is to radiate the desired polarization in a specific direction. The target direction is set by the given θ_0 and ϕ_0 , which could be broadside ($\theta_0 = \phi_0 = 0^\circ$) or any off-axis direction within the 2-D steering range of the radiator array. Once the direction is set, two orthogonal planes of $\phi = \phi_0$ and $\phi = \phi_0 + 90^\circ$ are picked for antenna pattern measurement during the optimization process. Starting from an initial setting, each iteration includes measuring the polarization parameters (i.e., axial ratio and polarization angle), as well as the radiation patterns across these two orthogonal planes by sweeping α from 0° to 180° and θ from -90° to 90° for $\phi = \phi_0$ and $\phi = \phi_0 + 90^\circ$. In order to find the setting for the next iteration, all the actuators of the drive circuits of the four antennas are both increased and decreased one at a time by a pre-defined step size, the polarization parameters and radiation patterns are measured again, and the setting which results in the largest improvement in the goal function (depending on the desired polarization type and the target direction) is picked as the next state. The same procedure is done until no further improvements can be made by changing any of the DACs' values. The step size of the actuators should be sufficiently large so that the change they introduce into the radiated polarization and radiation pattern can be reliably captured by the measurement setup so that the algorithm does not lose the optimization path due to the noise.

For linear polarization as the target, the optimization goal is to maximize the axial ratio at the desired polarization angle and the radiated power in the desired direction. In this procedure, the goal function is defined as a combination of the axial ratio, the radiated power in the desired direction, the difference of the measured polarization angle from the desired angle, and the deviation of the radiated beam from the target direction based on the pattern measurements in the two chosen orthogonal planes. With such a goal function, even if during an iteration no setting results in the desired polarization angle and/or beam direction, still the closest angle and/or direction with the highest axial ratio and radiated power is picked as the next state, as long as it provides improvement over the current setting.

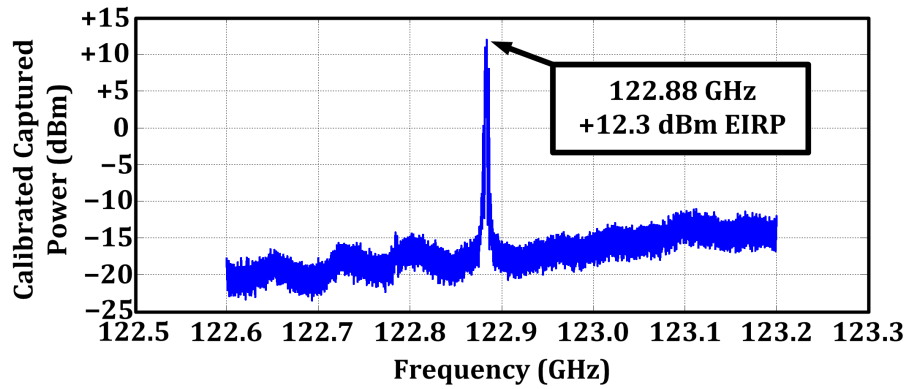
For an elliptical polarization with a desired axial ratio, polarization angle, and direction, we start the optimization process with an already optimized linear polarization with the same polarization angle and beam direction as the initial point (to ensure not only the polarization angle and beam direction are correct, but also the radiated power is maximized initially) and define the optimization goal to minimize the difference between the measured and desired axial ratios during the iterations

while maintaining the polarization angle and beam direction at their initial value by combining their deviation from the target values in the goal function, similar to the optimization for linear polarization. Finally, a circular polarization can also be achieved by starting with an already optimized linear polarization at any polarization angle and minimizing the axial ratio while keeping the beam in the correct direction in a similar way.

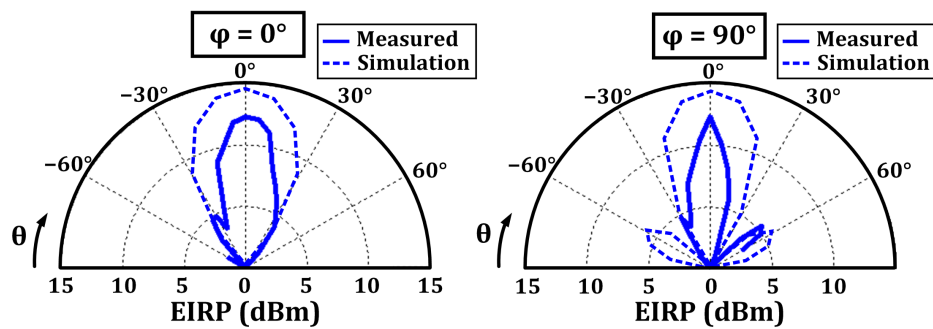
Measurement Results: Figure 5.45(a) shows the measured spectrum of the radiated signal, which reveals a tone at 122.9 GHz with a maximum effective isotropic radiated power (EIRP) of +12.3 dBm in the broadside direction. The corresponding radiation patterns in the two orthogonal planes for this setting were also measured and are given in Figure 5.45(b).

The DPC radiator array is capable of transmitting linear polarizations at any polarization angle. The ideal scenario for tuning the polarization angle is demonstrated in Figure 5.46(a) where three examples of linear polarization are shown as the polarization angle is controlled from 0° to 180° . This figure illustrates the normalized plots of the projected power for the ideal transmitted linear polarizations, measured by the linearly polarized receiver at different polarization angles as the angle α is swept by the stepper motor on the receiver side. Measurement results for broadside radiation, shown in Figure 5.46(b), confirm that linear polarizations with the full 0° to 180° range of polarization angle can be achieved with this design. In these measurements, the goals are set to achieve linear polarizations at different polarization angles and the optimization process is stopped when an axial ratio better than 14 dB is achieved. As can be seen, this design is even able to reach higher axial ratios if we continue the optimization process.

The DPC radiator is also capable of controlling the axial ratio of the transmitted polarization to transmit elliptical polarization with a desired axial ratio and circular polarization. To demonstrate this capability, three arbitrary axial ratios of 4, 7, and 10 dB were selected as targets to achieve elliptical polarizations at two arbitrary polarization angles of 30° and 90° in broadside. In Figure 5.47(a), the ideal expected elliptical polarizations as well as an ideal circular polarization are shown and the measured polarizations that correspond to the desired goals are plotted in Figure 5.47(b). The results show that the axial ratios for the measured elliptical polarizations are within 0.5 dB of the target values and a circular polarization with an axial ratio as low as 1.2 dB is achieved.

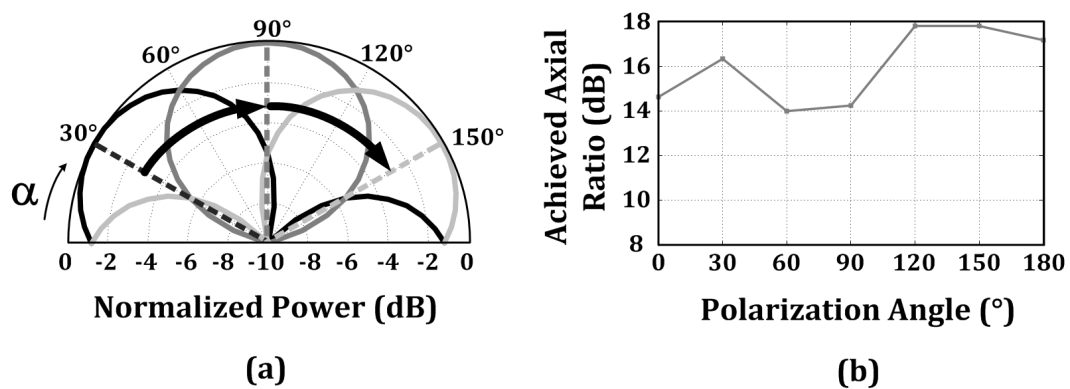


(a)



(b)

Figure 5.45: (a) Measured calibrated spectrum of the radiated signal and (b) measured radiation patterns in two orthogonal planes show a tone at 122.88 GHz with a maximum EIRP of +12.3 dBm in the broadside direction.



(a)

(b)

Figure 5.46: (a) Ideal scenario for polarization angle tuning of the linear polarization across the full 0° to 180° range and (b) measured axial ratio for the optimized linear polarizations at different polarization angles.

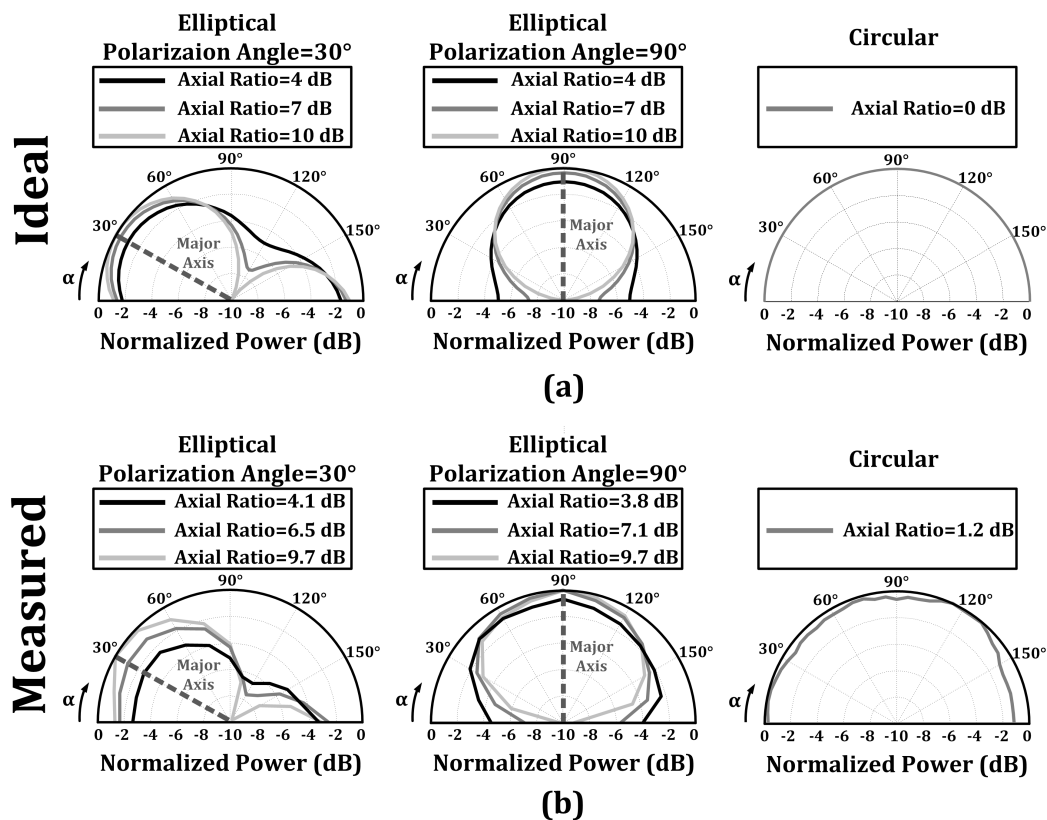


Figure 5.47: Axial ratio tuning of the transmitted polarization to obtain elliptical and circular polarization. Normalized plots of projected power at (a) different polarization angles in broadside for expected target polarizations and (b) measured polarizations after optimization.

The 2-D array of DPC antennas can steer the beam in both of the two orthogonal planes ($\phi = 0^\circ$ and $\phi = 90^\circ$) while controlling the polarization. Figure 5.48(a) shows this scenario for the linear polarization that corresponds to the setting for maximum EIRP. In this figure, the solid black curves in the radiation pattern plots are the same data for maximum EIRP in broadside radiation whose measured polarization together with the ideal target polarization are shown in Figure 5.49(a). The dashed gray curves are the radiation patterns for the same polarization steered in $\phi = 0^\circ$ plane by 15° and the dashed black curves are also the same polarization steered in the other orthogonal plane ($\phi = 90^\circ$), again by 15° . The next set of radiation patterns, shown in Figure 5.48(b), corresponds to steering a linear polarization at a different polarization angle (60°) in one of the orthogonal planes by 10° , demonstrating simultaneous polarization angle tuning and beam steering, and Figure 5.48(c) shows the steered beam of an elliptical polarization with the same polarization angle

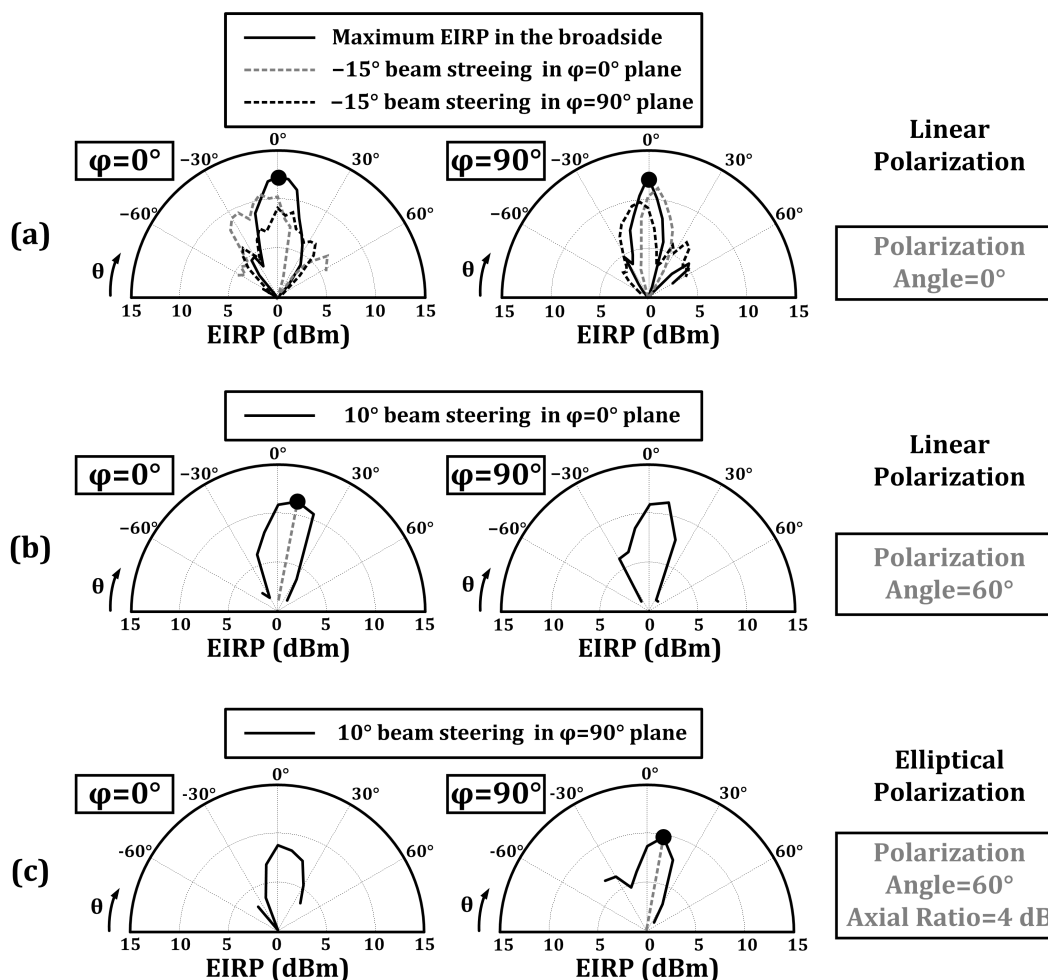


Figure 5.48: Radiation patterns corresponding to 2-D beam steering: (a) for the linear polarization mode, (b) simultaneous beam steering and polarization angle control, and (c) simultaneous beam steering and axial ratio control.

as the previous case, but with a lower axial ratio of 4 dB, steered in the other orthogonal plane, to demonstrate axial ratio control while beam steering. The measured polarizations and the ideal target polarizations for these two cases are plotted in Figure 5.49(b) and (c).

Table 5.2 shows the comparison of the 2×2 DPC radiator with the state-of-the-art, which includes integrated radiators without external lenses or superstrates. To the best of the authors' knowledge, this DPC radiator and its previous version in [89] are the only integrated radiators with DPC capability while the other radiators transmit a fixed polarization.

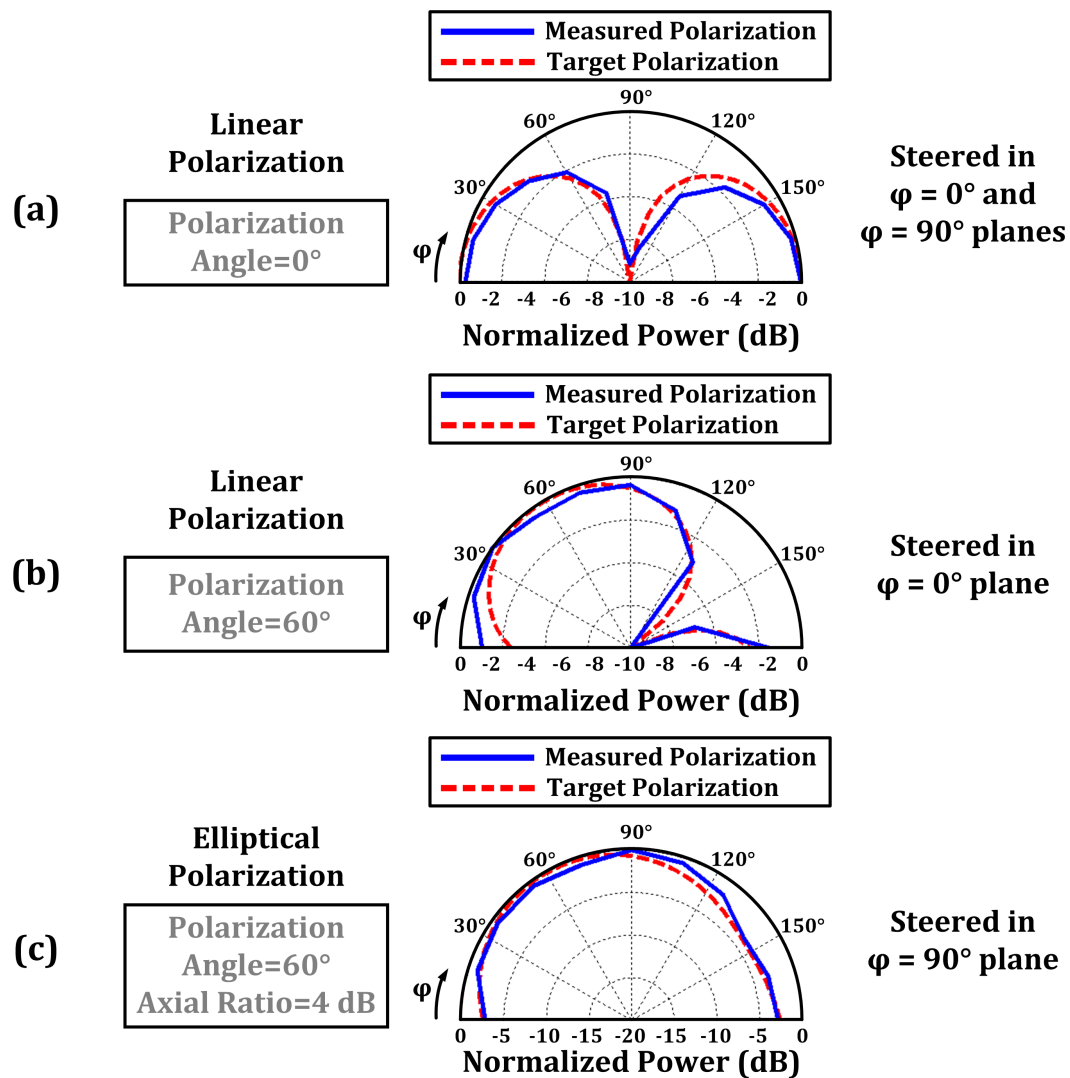


Figure 5.49: Measured and target polarizations corresponding to 2-D beam steering for the: (a) linear polarization mode, (b) simultaneous beam steering and polarization angle control, and (c) simultaneous beam steering and axial ratio control.

Metric	This Work	[89]	[90]	[91]	[92]	[5]	[6]
Polarization Control	Dynamic	Dynamic	N/A	N/A	N/A	N/A	N/A
Polarization	Linear Circular Elliptical	Linear Circular Elliptical	Linear	Circular	Linear	Circular	Circular
Max EIRP (dBm)	12.3	7.8	5.1	6.0	17.1	-1.9	4.6
Number of Elements	4	2	4	1	16	4	1
EIRP per Element* (dBm)	0.3	1.8	-6.9	6.0	-6.9	-13.9	4.6
Beam Steering	2-D	1-D	No	No	2-D	2-D	No
Frequency (GHz)	122.9	105.5	210	134.5	338	191	161
Process	32nm SOI CMOS	32nm SOI CMOS	32nm SOI CMOS	32nm SOI CMOS	65nm CMOS	65nm CMOS	130nm SiGe
DC Power (mW)	1885	476	240	168	1540	77	388
Area (mm ²)	8.12	2.64	3.5	1.2	3.9	1.1	1

*EIRP per element estimated as $EIRP / (\text{Number of Elements})^2$ to account for array gain.

Table 5.2: Comparison of integrated radiating sources in silicon without external dielectrics.

5.3.5 A 2×2 Integrated Slot-Based DPC Radiator Array

As we discussed in the previous chapter, electromagnetic duality can be used to design efficient MPD slot antennas based on their wire antenna dual. In this section, we present a 2×2 integrated slot-ring based DPC radiator¹ array operating at 120 GHz as the dual of the 2×2 integrated DPC radiator of section 5.3.4. Figure 5.50 shows the block diagram of the DPC slot radiator array. As it can be seen on the block diagram, the supporting circuitry and control mechanism of the DPC slot radiator array is identical to that of the 2×2 phased array of DPC wire antennas presented before. Again, power is generated locally within each of the four antenna elements with phase and gain control units incorporated in the drive circuitry inside each antenna. A central QVCO generates the reference signals that are used for phase control and frequency synchronization of the antennas and a locking network distributes these quadrature signals to the inside of each core. However, obviously the electromagnetic structure design and implementation of the slot-ring based DPC antennas should be performed differently.

The DPC slot antenna element shown in Figure 5.51 is designed based on the MPD slot-ring radiator of section 4.3, which is the electromagnetic dual of the original DPC antenna of section 5.3.2. In order to implement each slot antenna, the ground plane of the chip needs to be cut to form two separate reference metal planes: inner

¹This design was a joint project with my colleagues Steven Bowers and Kaushik Dasgupta. I was responsible for the core and locking network oscillators, the amplifiers, phase rotators, and the electromagnetic design of the passives and matching networks inside each core. Steven was responsible for the antenna design as well as the the distribution network, and Kaushik designed the digital to analog converters.

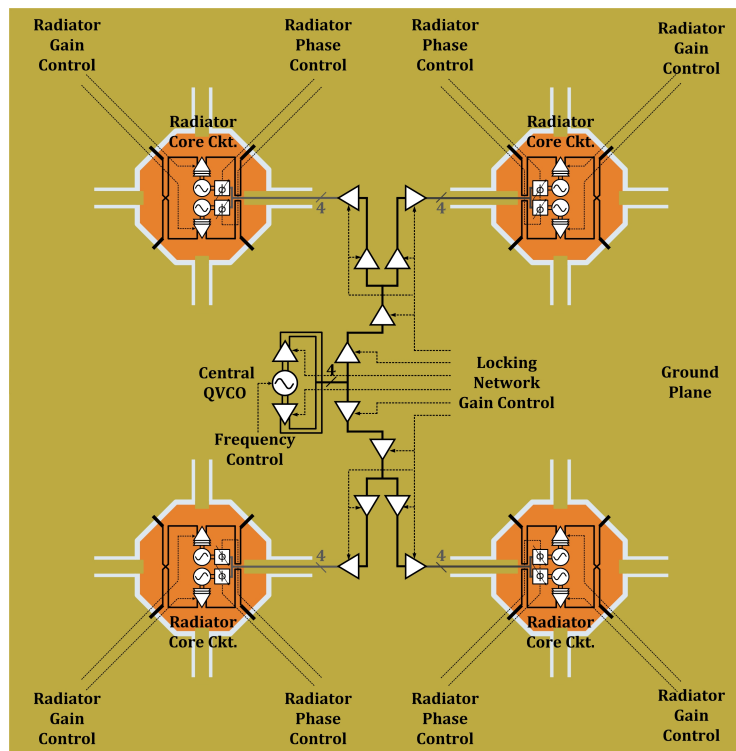


Figure 5.50: Block diagram of the 2x2 slot-based DPC radiator.

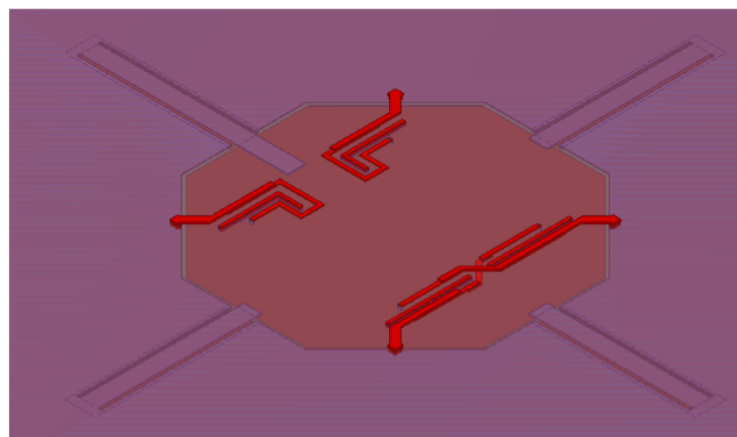


Figure 5.51: Electromagnetic design of the slot-based DPC antenna.

metal plane (inside the antenna, acting as the ground plane for the drive circuitry) and outer metal plane (outside the antenna, serving as the ground plane for the locking network). However, to be able to use the same control scheme as the previous version for the 2x2 slot DPC radiator array, the reference signals from the locking network need to be routed through transmission lines from outer ground plane to the inner ground plane where each antenna's drive circuit is located. The ground

reference for these transmission lines outside the antenna is the outer ground plane while inside the antenna the inner ground plane serves as the ground reference. This means that we need a continuous ground path for these transmission lines in order to properly transfer locking signals to the inside of each element which in turn contradicts the requirement of cutting the ground plane to create the slot antenna itself.

A quarter-wavelength CPW transmission line is used to solve this issue. The inner and outer ground planes are connected to each other through a quarter-wavelength CPW transmission line, shorted at the interface with outer ground plane, as shown in Figure 5.51. This enforces the impedance at the connection to the inner ground plane looking out to be ideally open circuit at RF (assuming the metal losses are negligible). An open circuit at RF means that this transmission line would not affect the slot antenna significantly. It also provides a biasing path from the outer ground plane to the inner ground plane through the “signal line” of the CPW transmission line since now there is a solid piece of metal that connects the two ground planes. At the same time, this unbroken path from the outer ground plane to the inner ground plane is used as the ground plane for microstrip transmission lines that deliver the locking signals to the oscillator inside each antenna. To make the structure symmetric, the $\lambda/4$ CPW transmission line is repeated on all four sides of each slot antenna. It should be noted that since the inner and outer reference planes are connected to each other from a dc standpoint, the feed lines from the final driver stage to the antenna can no longer be directly connected to the outer ground plane and ac coupling capacitors should be used to decouple the dc voltages.

The 2×2 slot-based DPC radiator array is simulated to have +3.6 dBi gain for both linear and circular polarization modes with 18% radiation efficiency (including the feed lines) once the substrate is thinned to $200 \mu\text{m}$. The simulated EM structure and the resulting gain patterns for both modes of operation are shown in Figure 5.52. Based on the measurement results of the wire-based DPC antenna, the EIRP of the 2×2 slot-based DPC radiator array is expected to be +15.5 dBm.

5.4 Polarization Modulation

In the previous sections, we showed that a multi-port driven integrated antenna and its driving circuitry can be designed in such a way to allow transmitting any desired arbitrary polarization (linear at any polarization angle, circular, and elliptical with any axial ratio) to enable dynamic polarization control. Now, we can use the same

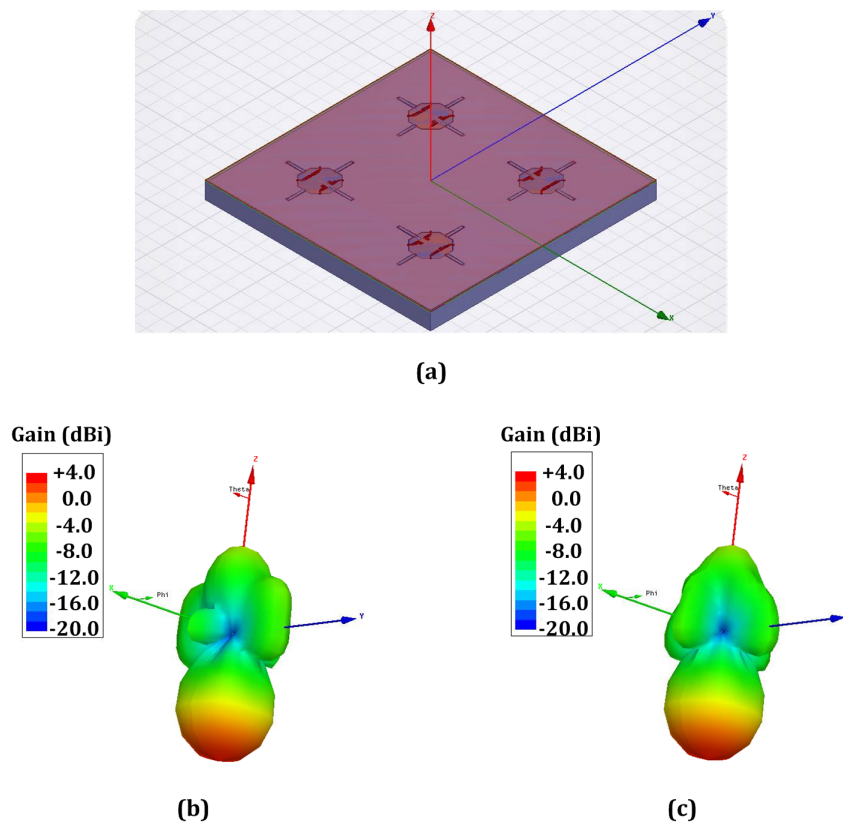


Figure 5.52: (a) HFSS simulation setup for the 2×2 integrated slot-based radiator and the simulated gain patterns for (b) linear polarization mode and (c) circular polarization mode.

DPC antenna to propose a new communication scheme called Polarization Modulation (Pol-M) that augments existing phase and amplitude modulation schemes in wireless communications by an additional degree of freedom. Pol-M substantially enhances the effective channel capacity. This additional feature opens up a new door to a variety of research problems in multiple areas of electromagnetics, communication circuits and systems as well as information theory, where innovative schemes for modulation and channel coding can be investigated. This approach can also be combined with MIMO systems to increase the number of transmit/receive paths without increasing the number of antennas [102].

The DPC feature of multi-port driven integrated antennas can be utilized to encode data in the polarization of EM waves and dynamically switch the transmitted polarization at very high rates; i.e., to “modulate” polarization and transmit polarization “symbols” as data. Figure 5.53 shows an example of such a modulation scheme where the data is encoded in the polarization angle of the linearly polarized transmit-

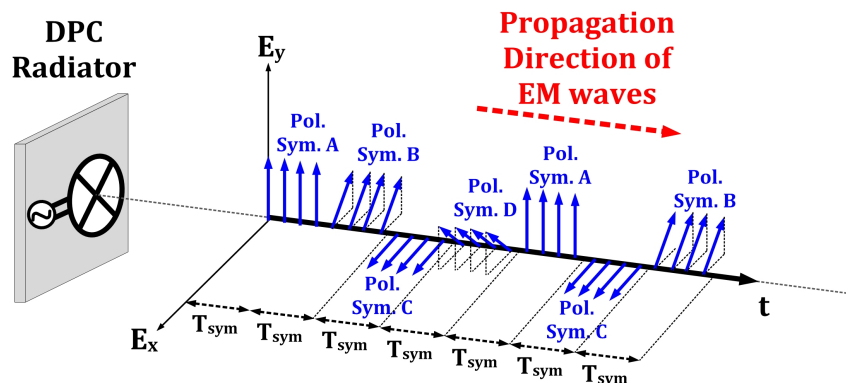


Figure 5.53: DPC radiator can switch between different polarizations at symbol rate, T_{sym} , to transfer data through Polarization Modulation.

ted EM waves and is being transmitted at the rate of $1/T_{sym}$. Here, the polarization symbols are the different polarization angles of the transmitted EM waves over each symbol period, T_{sym} .

When the data is solely transferred in the polarization itself, the security of the data stream would significantly improve too, because in this case the phase and amplitude of the signal can be intentionally adjusted to mask the true data set from undesired receivers. This is due to the fact that only a polarization agile receiver (introduced in [103]) with multi-port antenna or antenna arrays that can detect all polarizations is able to capture the true polarization angle of the received signal and decode the data regardless of the possible misinformation encoded in the phase and amplitude of the received signal. Any single-port receiving antenna or any multi-port antenna whose polarization is fixed cannot distinguish between a signal that has zero amplitude and a signal with finite amplitude that is in the orthogonal polarization with respect to the antenna polarization and thus would not be able to decode the data.

Since Pol-M is a spatial concept, it is completely independent and orthogonal to existing phase and amplitude modulation of the signal's time-domain waveform. Therefore, we can implement transmitter architectures, which incorporate simultaneous phase and amplitude modulations, combined with Pol-M in any two orthogonal polarizations (horizontal and vertical, clock-wise and counter clock-wise, etc.) as independent dimensions for modulation to achieve very high data rate mm-wave communications. As an example consider two orthogonal polarizations, P_x and P_y . Each polarization on its own can accommodate two quadrature components, (I_x, Q_x) for polarization P_x , and (I_y, Q_y) for polarization P_y . The set (I_x, Q_x, I_y, Q_y) creates

an orthogonal basis for a 4-D constellation. Since it is difficult to visualize a 4-D constellation on a 2-D plane, Figure 5.54 shows the projections of such a constellation on the six orthogonal planes of such 4-D space where I_x and Q_x form 16-QAM modulation and I_y and Q_y form a QPSK modulation. It should be noted that such scenario substantially subsumes the previously used scheme [15] where two orthogonal antennas form two channels to send independent data streams with two orthogonal polarizations to double the channel capacity for point-to-point polarization-matched applications by only using two 2-D constellations of the existing 4-D constellation.

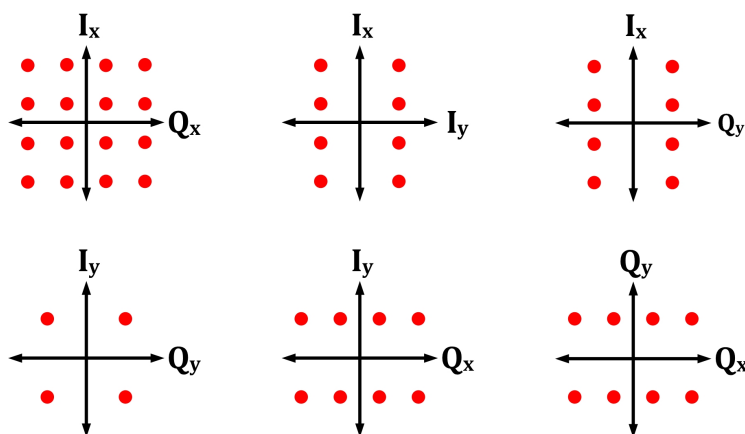


Figure 5.54: Projections of a 4-D constellation on orthogonal planes of the 4-D space for an exemplary 4-D data constellation resulted by performing simultaneous quadrature modulation schemes on two orthogonal polarizations.

Figure 5.55 shows the conceptual block diagram of a transmitter architecture capable of performing simultaneous phase, amplitude, and polarization modulation. In this block diagram, “Signal Modulator” refers to the entire set of blocks, which only modulate amplitude and phase of the signal. However, the signal modulator and the integrated antenna with DPC, as a whole, act as “Signal and Polarization Modulator”. Baseband inputs are fed to the system. Depending on the implementation, either all or different sets of baseband inputs modulate amplitude and phase of the signal and polarization of the transmitted EM waves, thus resulting in simultaneous phase, amplitude, and polarization modulation.

Figure 5.56 illustrates detailed block diagram of one possible implementation of such transmitter that uses our previously discussed DPC antenna. Quadrature LO signals are generated by a quadrature oscillator. The baseband inputs which control the two 360° phase rotators perform two simultaneous tasks: 1) setting the relative phases of the driving ports of the antenna with respect to each other (modulating

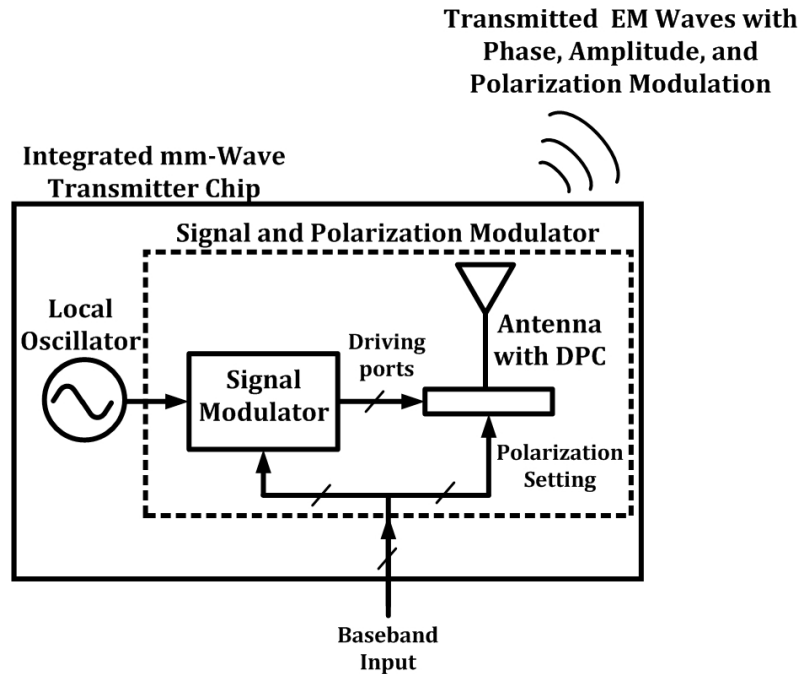


Figure 5.55: Simplified block diagram of a transmitter capable of simultaneous phase, amplitude, and polarization modulation.

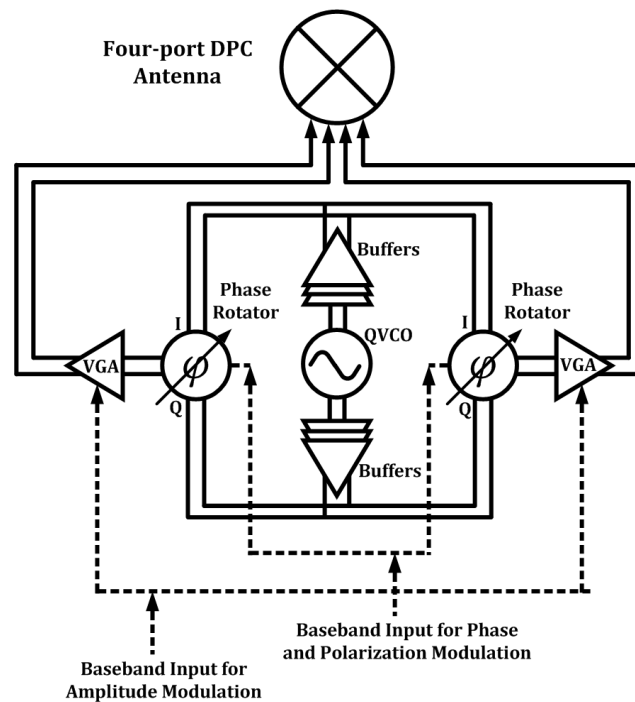


Figure 5.56: One possible implementation of a transmitter capable of performing Pol-M.

the polarization [103]) and 2) setting the relative phases of the driving ports of the antenna with respect to the QVCO phase (modulating signal's phase). In addition, other baseband inputs, which control variable gain amplifiers, modulate the amplitude of the signal resulting in simultaneous modulation of phase, amplitude, and polarization of the transmitted EM waves.

In order to receive the 4-D constellation of such transmitter, similar to the stand-alone Pol-M modulation, a polarization agile receiver with multi-port antenna that can detect all polarizations can simultaneously demodulate phase, amplitude, and polarization information. In these receivers, phases and amplitudes of the received signals at all ports of the receive antenna are used together to extract phase, amplitude, and polarization information.

5.4.1 Prototype: Transmitter and Receiver Architectures for Pol-M

In this section, we present prototype transmitter and receiver architectures for Pol-M, implemented as proof-of-concept printed circuit boards (PCB) for a 2.4 GHz Pol-M link.¹

Any linear polarization of an electric field \mathbf{E} can be expressed as a vector sum of two perpendicular linear polarizations \mathbf{E}_x and \mathbf{E}_y . Our prototype transmitter and receiver architectures for Pol-M utilize this orthogonal decomposition. The transmitter spatially combines two perpendicular linear polarizations of electric field with different gains to generate the desired linear polarization. Figure 5.57(a) shows the conceptual diagram of the architecture for the transmitter. Depending on the desired polarization angle for each symbol, the baseband signal is weighted properly in two independent paths (A_1 and A_2) and is then upconverted. These two paths are then feed to the two ports of a dual-port antenna which can simultaneously radiate orthogonal polarizations \mathbf{E}_x and \mathbf{E}_y . The far-field linearly polarized electric field can thus be expressed as a superposition of the two radiated polarizations:

$$\mathbf{E} = kA_1 \cos(\omega_0 t) \hat{\mathbf{u}}_x + kA_2 \cos(\omega_0 t) \hat{\mathbf{u}}_y \quad (5.8)$$

whose polarization angle is:

$$\text{angle}(E) = \tan^{-1}(A_2/A_1) \quad (5.9)$$

which indicates that depending on the choice for A_1 and A_2 the polarization angle of the transmitted electric field can be controlled. In 5.8, the parameter k

¹This was a joint project with my colleague Kaushik Dasgupta. I was responsible for the electromagnetic design of the transmitter and receiver antennas and Kaushik was in charge of the circuit implementation for both transmitter and receiver units.

indicates the overall gain in the drive and radiation path and is assumed to be the same for both paths. It may also be noted that this architecture is also capable of transmitting/receiving circular polarization if the LO phases are offset by $\pi/2$.

A similar analysis can be performed for the receiver counter-part shown in Figure 5.57(b) that detects the polarization angle of the received signal.

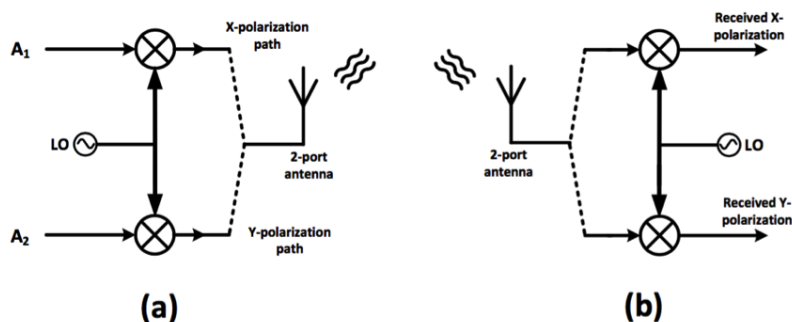


Figure 5.57: System architecture for the prototype polarization modulation (a) transmitter and (b) receiver.

5.4.1.1 Antenna Design

A dual port antenna which is capable of transmitting/receiving two orthogonal polarizations (E_x and E_y) corresponding to the two driving/receiving ports (Port-X and Port-Y) can be used for electromagnetic radiation and reception for both transmitter and receiver in a Pol-M link. Furthermore, it should provide sufficient isolation between the two ports to minimize cross-polarization in both transmitting and receiving modes. Such isolation is also necessary to avoid input impedance variation at Port-X based on how strong the signal Port-Y is and vice versa.

A dual port patch antenna is designed to achieve these goals, as shown in Figure 5.58(a) [104]. The patch is designed to be resonant at 2.4 GHz, and quarter-wave transmission lines are used to match the input impedance of each port to 50 Ω . Figure 5.58(b) shows the simulated radiation pattern and antenna gain while the patch is driven only at one port with the other port shorted to ground. Similar radiation pattern and antenna gain are achieved for both cases of Port-X and Port-Y individual drive. Figure 5.58(c) shows the isolation between the two ports versus frequency. The simulated isolation of 37 dB ensures that in the transmitter each port can be driven almost independently with arbitrary amplitude and phase to transmit

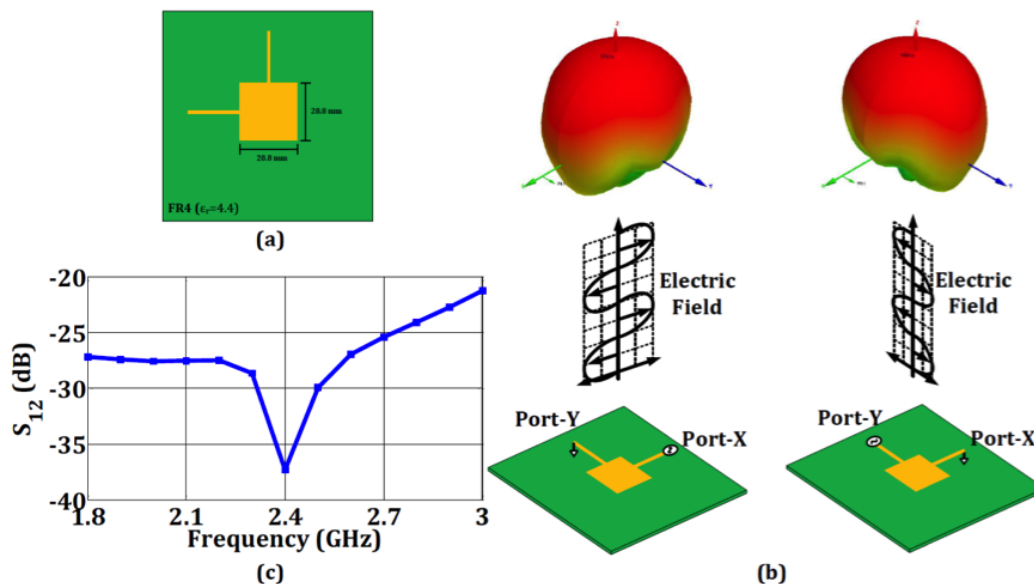


Figure 5.58: Patch antenna simulations showing port isolation as well as gain patterns for X and Y polarizations with maximum gain of 2.7 dB.

any arbitrary polarization and in the receiver each port only picks up part of the polarized electric field that is aligned with it.

5.4.1.2 Circuit Implementation

Figure 5.59(a) shows the circuit block diagram of the transmitter at 2.4 GHz. Variable gain amplifiers (VGAs) (PGA870) provide the necessary weights for polarization control over a 30 dB range. The LO phase shifts are obtained through a weighted summation of in-phase and quadrature-phase LO signals (AD8341). The up-converted signal in each path is then amplified and radiated using the on-board antenna. In this architecture, the response time of the VGA gain-control determines the limit of symbol rate for linear polarization modulation. The receiver circuit block diagram is depicted in Figure 5.59(b), where a TriQuint TQP3M9037 low noise amplifier (LNA) amplifies the received signal in the corresponding polarization, which is then down-converted using a MAX2042 mixer.

5.4.1.3 Measurements

The transmitter and receiver systems are measured as stand-alone systems to verify polarization control and detection capability. Figure 5.60 shows the measurement setup for the system at 2.4 GHz.

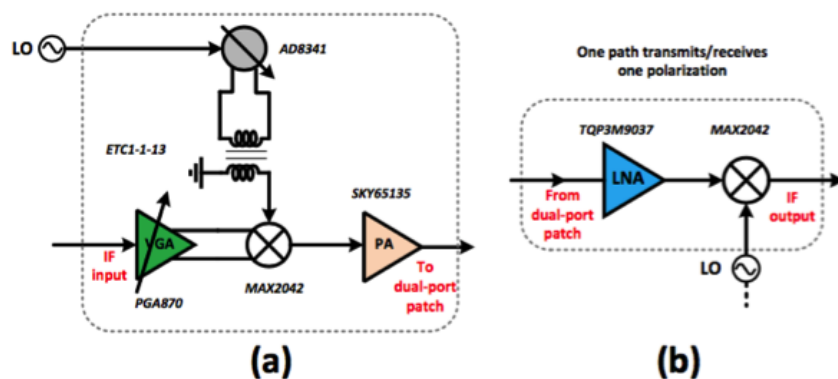


Figure 5.59: Implementation details of (a) transmitter and (b) receiver units for Pol-M.

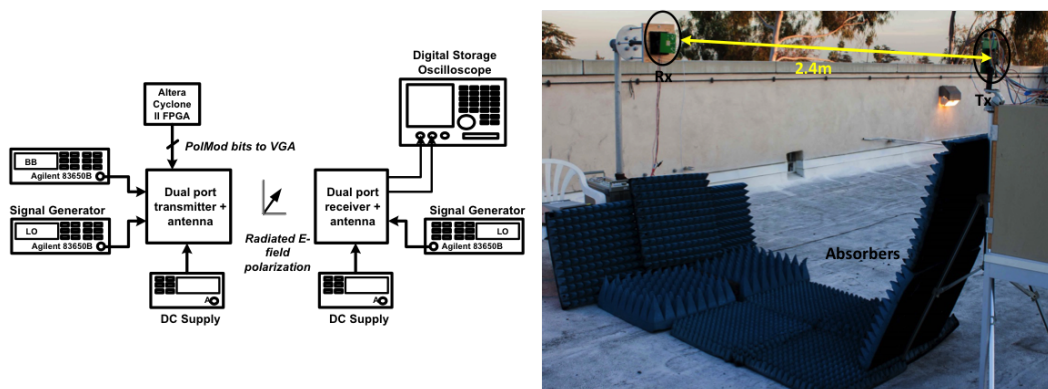


Figure 5.60: Measurement setup for Pol-M transmitter and receiver units.

First, a linearly polarized horn antenna is used to measure the X and Y polarization paths of the transmitter separately. Figure 5.61(a) shows the variation of output power for each path versus orientation of the horn with respect to the transmitter board. As expected, the angles for maximum received power by the horn antenna are 90° apart for the two polarizations paths. Measured isolation between polarizations was 20.1 dB.

To verify the ability to rotate the transmitted linear polarization and tune the polarization angle, both paths are operated with varying VGA settings to ensure constant total output power ($P_x + P_y$). Figure 5.61(b) shows that the total output power variation is less than 1 dB over the polarization angle tuning from 0° to 90° .

The receiver sub-system is also measured using the same horn antenna oriented at different angles as the transmitter to radiate different linear polarizations with

arbitrary polarization angles towards the receiver. Similar to the transmitter, the maximum captured signal from one receiver path corresponds to the minimum signal in the other (Figure 5.62(a)). The measured isolation between the two ports is 23.4 dB with a maximum variation of 1.5 dB in total captured power and the receiver is able to capture the entire power across both polarizations.

A constellation of polarization symbols in E_x - E_y plane similar to that of QPSK modulation is also generated using the transmit horn antenna and resolved into the two receiver paths. The transmitted and recovered polarization constellations are shown in Figure 5.62(b).

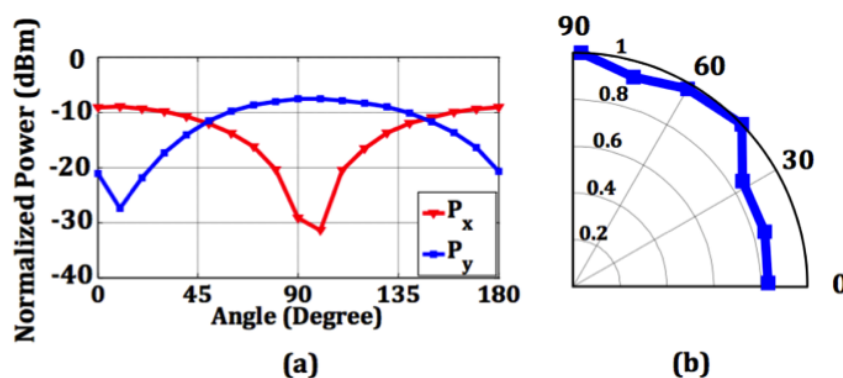


Figure 5.61: Transmitter stand-alone measurements showing (a) power variation across angle of the receiving horn and (b) dynamic polarization control over the first quadrant.

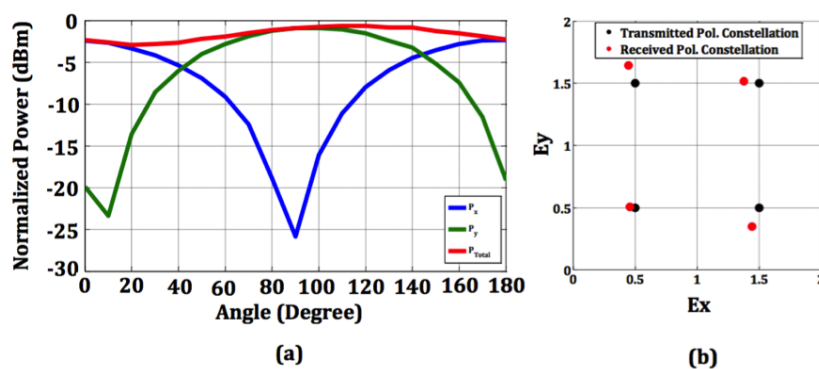


Figure 5.62: Receiver stand-alone measurements showing (a) received power variation across angle of the transmitting horn and (b) received polarizations having different magnitudes as well as angles.

5.4.2 Pol-M with the 2×2 Integrated DPC Radiator Array

The 2×2 integrated DPC radiator array presented in section 5.3.4 is also featured with fast polarization switching capability to enable Pol-M. However, the fast switching capability is restricted to a limited number of pre-loaded polarization settings. A pseudo random binary sequence (PRBS) generator is implemented on-chip and is clocked externally to switch between pre-defined settings for actuators that control relative phases and amplitudes of the drive settings on each DPC antenna. The PRBS block supports four modes of operation, each of which generates a different sequence to be loaded to the actuators. However, these pre-loaded values were not optimized during the design phase to correspond to a well-defined polarization. Figure 5.63, shows the measured polarization symbols that are transmitted by the DPC radiator array in one of the modes of operation of the PRBS block.

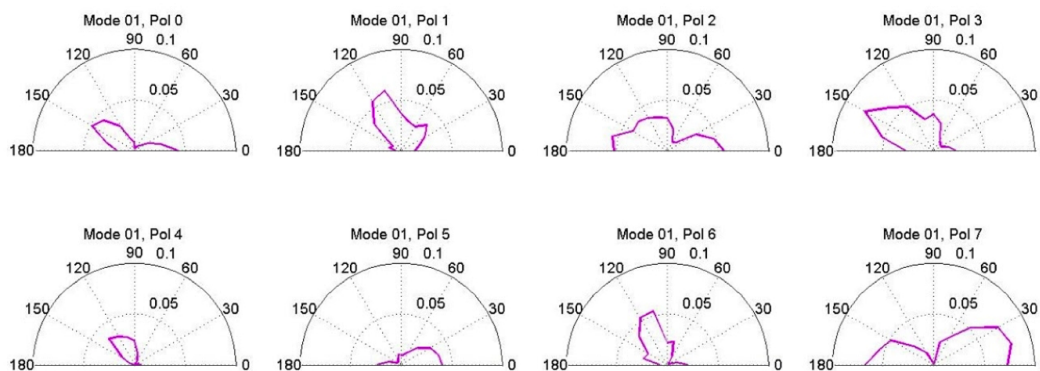


Figure 5.63: Pre-loaded polarization symbols for 2×2 integratd DPC radiator array.

5.5 Conclusions

MPD Antennas enable dynamic control over the electromagnetic polarization of an integrated radiator which in turn allows for polarization matching and maximum coupling between antennas to be maintained regardless of polarization and orientation of the receive antenna in space. Furthermore, if dynamic polarization control of an integrated radiator is combined with the simultaneous ability to steer the radiated beam in two dimensions through 2-D phased arrays of DPC antennas, it ensures polarization matching between the transmitter and receiver antennas in mobile wireless systems in addition to the fixed location systems. In this case, the polarization matching is maintained regardless of the polarization, orientation, and location of the receiving antenna in space, as long as it remains within the 2-D steering range of the 2-D phased array of DPC transmitting antennas. DPC capability of a radiator at very high rates also enables a new feature to encode data in the polarization

itself, introducing Polarization Modulation (Pol-M) as a new modulation scheme. Pol-M increases the security of the wireless link since receivers with single-port or fixed-polarizations would not be able to decode the data. It could also enhance the channel capacity once combined with the existing phase and amplitude modulation schemes.

Chapter 6

CONCLUSIONS

This thesis demonstrated how one of the major challenges in design and performance of integrated antennas may be used as an opportunity to enable extraction of their far-field radiation properties based on in-situ real-time measurements of sensor units that are integrated on the same substrate as the transmitting antenna. We reviewed generation of surface waves in the dielectric substrate of integrated antennas and discussed how these waves get trapped inside the dielectric slab and do not contribute to the efficient radiation. Through a variety of examples, we showed that the excited substrate modes that always exist in the substrate contain valuable information. Then we introduced the concept of Proximal-Field Radiation Sensors (PFRS) as small sensing antennas that are placed strategically in the immediate proximity of the transmitting antennas and extract the information in the substrate modes. Design intuition regarding the type of sensing antennas to use and their placement was provided. We also presented a variety of PFRS data processing schemes with different levels of complexity depending on the affordable detection circuitry and its capability to detect phase and amplitude information. A 5-GHz 2×1 phased array of patch antennas on PCB and a 72-GHz 2×1 phased array of integrated linear-slot antennas in a 55 nm CMOS process, both with four integrated folded-slot PFRS units were presented. For both cases, the data from PFRS was used to successfully measure the far-field radiation patterns of the integrated antenna arrays.

In addition to enabling self-calibration, self-correction, and self-monitoring of the performance for any integrated antenna array equipped with PFRS units, they are of particular interest for implementation on dynamically controllable integrated radiators, where radiation parameters such as polarization and steering angle could be arbitrarily adjusted. Multi-Port Driven (MPD) radiator methodology provides an excellent framework to design such integrated radiators.

We reviewed advantages of MPD antennas over single-port antennas and discussed how electromagnetic duality can be used to design slot-based MPD antennas to reduce the exclusive use area of the antenna on a chip while still benefiting from the same advantages of original wire-based MPD antenna design. A prototype 134.5-GHz integrated slot-based MPD radiator fabricated in 32 nm SOI CMOS

process was presented with a simulated antenna efficiency of 39% and a measured single-element EIRP of +6.0 dBm and a total radiated power of -1.3 dBm. Then we discussed a variety of methods in which a general MPD radiator could be used for dynamic control of radiation properties. Based on that discussion, we introduced the concept of Dynamic Polarization Control (DPC) of integrated radiators as a method to ensure polarization matching of the radiating antenna to receiver antenna in a wireless system, regardless of the polarization and orientation of the receiver in space. MPD design methodology was used to propose a DPC antenna. Several implementations of integrated DPC radiators were presented. The first one was a 105.5-GHz 2×1 integrated DPC radiator array with a maximum EIRP of +7.8 dBm and a total radiated power of 0.9 mW. The radiator was capable of beam steering and controlling the polarization angle across the entire tuning range of 0° to 180° while maintaining axial ratios above 10 dB, and controlling the axial ratio from 2.4 dB (near circular) to 14 dB (linear) in various directions of radiation. We also implemented a 123-GHz 2×2 integrated DPC radiator array to enable two-dimensional beam steering such that it can match the polarization to even to a mobile receiver antenna. The measurement results for this radiator showed a maximum EIRP of +12.3 dBm in the broadside direction and polarization angle control of the radiated linear and elliptical polarizations across the full range of 0° to 180° with tunable axial ratio down to 1.2 dB to achieve circular polarization and the ability to steer the radiated beam up to 15° in both dimensions. The last DPC prototype design was a 120-GHz integrated slot-based DPC radiator array, expected to have a maximum EIRP of +15.5 dBm.

As a result of DPC feature, we also introduced Polarization Modulation (Pol-M) as a new polarization scheme orthogonal to the existing phase and amplitude modulation methods. We discussed how Pol-M could be used to encode information in the polarization itself and improve the security of a wireless communication link and how it could be added on top of phase and amplitude modulation schemes to create 4-D data constellations. We discussed how DPC antenna enables Pol-M and also presented PCB prototypes for transmitter and receiver units operating at 2.4 GHz to support Pol-M.

BIBLIOGRAPHY

- [1] C. A. Balanis, *Antenna Theory: Analysis and Design*. Wiley-Interscience, 2005.
- [2] K. Sengupta and A. Hajimiri, “Distributed active radiation for THz signal generation”, in *IEEE International Solid-State Circuits Conference (ISSCC)*, Feb. 2011, pp. 288–289.
- [3] —, “A 0.28 THz 4×4 power-generation and beam-steering array”, in *IEEE International Solid-State Circuits Conference (ISSCC)*, Feb. 2012, pp. 256–258.
- [4] —, “A 0.28 THz power-generation and beam-steering array in CMOS based on distributed active radiators”, *IEEE Journal of Solid-State Circuits*, vol. 47, no. 12, pp. 3013–3031, Dec. 2012.
- [5] —, “Sub-THz beam-forming using near-field coupling of distributed active radiator arrays”, in *IEEE Radio Frequency Integrated Circuits Symposium (RFIC)*, Jun. 2011, pp. 1–4.
- [6] S. M. Bowers and A. Hajimiri, “Multi-port driven radiators”, *IEEE Transactions on Microwave Theory and Techniques*, vol. 61, no. 12, pp. 4428–4441, Dec. 2013.
- [7] —, “An integrated multi-port driven radiating source”, in *IEEE MTT-S International Microwave Symposium (IMS)*, Jun. 2013, pp. 1–3.
- [8] C. Jiang, A. Mostajeran, R. Han, M. Emadi, H. Sherry, A. Cathelin, and E. Afshari, “A fully integrated 320 GHz coherent imaging transceiver in 130 nm SiGe BiCMOS”, *IEEE Journal of Solid-State Circuits*, vol. 51, no. 11, pp. 2596–2609, Nov. 2016.
- [9] A. Safaripour, S. M. Bowers, K. Dasgupta, and A. Hajimiri, “Dynamic polarization control of two-dimensional integrated phased arrays”, *IEEE Transactions on Microwave Theory and Techniques*, vol. 64, no. 4, pp. 1066–1077, Apr. 2016.
- [10] D. B. Rutledge, D. P. Neikirk, and D. P. Kasilingam, “Integrated-circuit antennas”, *Infrared and Millimeter Waves*, vol. 10, no. part 2, pp. 1–90, 1983.
- [11] G. M. Rebeiz, “Millimeter-wave and terahertz integrated circuit antennas”, *Proceedings of the IEEE*, vol. 80, no. 11, pp. 1748–1770, Nov. 1992.
- [12] A. Babakhani, X. Guan, A. Komijani, A. Natarajan, and A. Hajimiri, “A 77-GHz phased-array transceiver with on-chip antennas in silicon: Receiver and antennas”, *IEEE Journal of Solid-State Circuits*, vol. 41, no. 12, pp. 2795–2806, Dec. 2006.

- [13] D. F. Filipovic, S. S. Gearhart, and G. M. Rebeiz, "Double-slot antennas on extended hemispherical and elliptical silicon dielectric lenses", *IEEE Transactions on Microwave Theory and Techniques*, vol. 41, no. 10, pp. 1738–1749, Oct. 1993.
- [14] R. Han and E. Afshari, "A 260 GHz broadband source with 1.1 mW continuous-wave radiated power and EIRP of 15.7 dBm in 65 nm CMOS", in *IEEE International Solid-State Circuits Conference (ISSCC)*, Feb. 2013, pp. 138–139.
- [15] E. Seok, C. Cao, D. Shim, D. J. Arenas, D. B. Tanner, C. M. Hung, and K. O. Kenneth, "A 410 GHz CMOS push-push oscillator with an on-chip patch antenna", in *IEEE International Solid-State Circuits Conference (ISSCC)*, Feb. 2008, pp. 472–629.
- [16] S. Pan, L. Gilreath, P. Heydari, and F. Capolino, "Investigation of a wideband BiCMOS fully on-chip W-band bowtie slot antenna", *IEEE Antennas and Wireless Propagation Letters*, vol. 12, pp. 706–709, 2013.
- [17] Y. C. Ou and G. M. Rebeiz, "Differential microstrip and slot-ring antennas for millimeter-wave silicon systems", *IEEE Transactions on Antennas and Propagation*, vol. 60, no. 6, pp. 2611–2619, Jun. 2012.
- [18] W. Shin, B. H. Ku, O. Inac, Y. C. Ou, and G. M. Rebeiz, "A 108-114 GHz 4×4 wafer-scale phased array transmitter with high-efficiency on-chip antennas", *IEEE Journal of Solid-State Circuits*, vol. 48, no. 9, pp. 2041–2055, Sep. 2013.
- [19] S. T. Nicolson, A. Tomkins, K. W. Tang, A. Cathelin, D. Belot, and S. P. Voinigescu, "A 1.2 V, 140 GHz receiver with on-die antenna in 65 nm CMOS", in *IEEE Radio Frequency Integrated Circuits Symposium (RFIC)*, Jun. 2008, pp. 229–232.
- [20] J. D. Park, S. Kang, S. V. Thyagarajan, E. Alon, and A. M. Niknejad, "A 260 GHz fully integrated CMOS transceiver for wireless chip-to-chip communication", in *Symposium on VLSI Circuits*, Jun. 2012, pp. 48–49.
- [21] Z. Chen, C. C. Wang, H. C. Yao, and P. Heydari, "A BiCMOS W-band 2×2 focal-plane array with on-chip antenna", *IEEE Journal of Solid-State Circuits*, vol. 47, no. 10, pp. 2355–2371, Oct. 2012.
- [22] N. G. Alexopoulos, P. B. Katehi, and D. B. Rutledge, "Substrate optimization for integrated circuit antennas", *IEEE Transactions on Microwave Theory and Techniques*, vol. 31, no. 7, pp. 550–557, Jul. 1983.
- [23] D. Rutledge and M. Muha, "Imaging antenna arrays", *IEEE Transactions on Antennas and Propagation*, vol. 30, no. 4, pp. 535–540, Jul. 1982.
- [24] P. Katehi and N. Alexopoulos, "On the effect of substrate thickness and permittivity on printed circuit dipole properties", *IEEE Transactions on Antennas and Propagation*, vol. 31, no. 1, pp. 34–39, Jan. 1983.

- [25] D. Pozar, "Considerations for millimeter wave printed antennas", *IEEE Transactions on Antennas and Propagation*, vol. 31, no. 5, pp. 740–747, Sep. 1983.
- [26] M. Kominami, D. Pozar, and D. Schaubert, "Dipole and slot elements and arrays on semi-infinite substrates", *IEEE Transactions on Antennas and Propagation*, vol. 33, no. 6, pp. 600–607, Jun. 1985.
- [27] W. Dou and Z. Sun, "Surface wave fields and power in millimeter wave integrated dipole antennas", *International Journal of Infrared and Millimeter Waves*, vol. 18, no. 3, pp. 711–721, 1997.
- [28] G. V. Eleftheriades and M. Qiu, "Efficiency and gain of slot antennas and arrays on thick dielectric substrates for millimeter-wave applications: A unified approach", *IEEE Transactions on Antennas and Propagation*, vol. 50, no. 8, pp. 1088–1098, Aug. 2002.
- [29] K. Sengupta and A. Hajimiri, "Designing optimal surface currents for efficient on-chip mm-wave radiators with active circuitry", *IEEE Transactions on Microwave Theory and Techniques*, vol. 64, no. 7, pp. 1976–1988, Jul. 2016.
- [30] S. M. Bowers, "Dynamically controllable integrated radiation and self-correcting power generation in mm-wave circuits and systems", PhD thesis, California Institute of Technology, 2014.
- [31] K. Sengupta, "Silicon-based terahertz circuits and systems", PhD thesis, California Institute of Technology, 2012.
- [32] K. Bernstein, D. J. Frank, A. E. Gattiker, W. Haensch, B. L. Ji, S. R. Nassif, E. J. Nowak, D. J. Pearson, and N. J. Rohrer, "High-performance CMOS variability in the 65-nm regime and beyond", *IBM Journal of Research and Development*, vol. 50, no. 4.5, pp. 433–449, Jul. 2006.
- [33] K. Kuhn, C. Kenyon, A. Kornfeld, M. Liu, A. Maheshwari, W.-k. Shih, S. Sivakumar, G. Taylor, P. VanDerVoorn, and K. Zawadzki, "Managing process variation in Intel's 45 nm CMOS technology.", *Intel Technology Journal*, vol. 12, no. 2, 2008.
- [34] T. Mizuno, J. Okumtura, and A. Toriumi, "Experimental study of threshold voltage fluctuation due to statistical variation of channel dopant number in MOSFET's", *IEEE Transactions on Electron Devices*, vol. 41, no. 11, pp. 2216–2221, Nov. 1994.
- [35] A. Asenov, A. R. Brown, G. Roy, B. Cheng, C. Alexander, C. Riddet, U. Kovac, A. Martinez, N. Seoane, and S. Roy, "Simulation of statistical variability in nano-CMOS transistors using drift-diffusion, monte carlo and non-equilibrium green's function techniques", *Journal of Computational Electronics*, vol. 8, no. 3-4, pp. 349–373, 2009.

- [36] S. R. Nassif, N. Mehta, and Y. Cao, “A resilience roadmap”, in *2010 Design, Automation Test in Europe Conference Exhibition (DATE 2010)*, Mar. 2010, pp. 1011–1016.
- [37] O. Hammi, J. Sirois, S. Boumaiza, and F. M. Ghannouchi, “Study of the output load mismatch effects on the load modulation of doherty power amplifiers”, in *IEEE Radio and Wireless Symposium*, Jan. 2007, 393–394a.
- [38] A. Keerti and A. V. H. Pham, “RF characterization of SiGe HBT power amplifiers under load mismatch”, *IEEE Transactions on Microwave Theory and Techniques*, vol. 55, no. 2, pp. 207–214, Feb. 2007.
- [39] R. C. Johnson, H. A. Ecker, and J. S. Hollis, “Determination of far-field antenna patterns from near-field measurements”, *Proceedings of the IEEE*, vol. 61, no. 12, pp. 1668–1694, Dec. 1973.
- [40] A. Yaghjian, “An overview of near-field antenna measurements”, *IEEE Transactions on Antennas and Propagation*, vol. 34, no. 1, pp. 30–45, Jan. 1986.
- [41] J. Brown and E. V. Jull, “The prediction of aerial radiation patterns from near-field measurements”, *Proceedings of the IEE - Part B: Electronic and Communication Engineering*, vol. 108, no. 42, pp. 635–644, Nov. 1961.
- [42] F. Bohn, K. Dasgupta, and A. Hajimiri, “Closed-loop spurious tone reduction for self-healing frequency synthesizers”, in *IEEE Radio Frequency Integrated Circuits Symposium (RFIC)*, Jun. 2011, pp. 1–4.
- [43] S. M. Bowers, K. Sengupta, K. Dasgupta, B. D. Parker, and A. Hajimiri, “Integrated self-healing for mm-wave power amplifiers”, *IEEE Transactions on Microwave Theory and Techniques*, vol. 61, no. 3, pp. 1301–1315, Mar. 2013.
- [44] A. Tang, F. Hsiao, D. Murphy, I. N. Ku, J. Liu, S. D’Souza, N. Y. Wang, H. Wu, Y. H. Wang, M. Tang, G. Virbila, M. Pham, D. Yang, Q. J. Gu, Y. C. Wu, Y. C. Kuan, C. Chien, and M. C. F. Chang, “A low-overhead self-healing embedded system for ensuring high yield and long-term sustainability of 60GHz 4Gb/s radio-on-a-chip”, in *IEEE International Solid-State Circuits Conference (ISSCC)*, Feb. 2012, pp. 316–318.
- [45] A. Stark, U. Johannsen, and A. F. Jacob, “In-situ probes for antenna array calibration”, in *The 40th European Microwave Conference*, Sep. 2010, pp. 465–468.
- [46] B. Rohrdantz, A. Stark, E. Hawamdah, and A. F. Jacob, “A circularly polarized antenna array with integrated calibration probes”, in *IEEE Asia-Pacific Microwave Conference*, Nov. 2014, pp. 462–464.
- [47] R. E. Collin, “Field theory of guided waves”, 1960.
- [48] H. Kogelnik, “Theory of dielectric waveguides”, in *Integrated optics*, Springer, 1975, pp. 13–81.

- [49] S. Bowers, A. Safaripour, and A. Hajimiri, *Sensing radiation metrics through mode-pickup sensors*, US Patent App. 13/766,667, Mar. 2014.
- [50] K. P. F.R.S., “On lines and planes of closest fit to systems of points in space”, *Philosophical Magazine Series 6*, vol. 2, no. 11, pp. 559–572, 1901.
- [51] H. Hotelling, “Analysis of a complex of statistical variables into principal components.”, *Journal of Educational Psychology*, vol. 24, no. 6, p. 417, 1933.
- [52] J. W. Goodman, *Introduction to Fourier optics*. Roberts and Company Publishers, 2005.
- [53] A. Safaripour, M. R. Hashemi, and A. Hajimiri, “Proximal-field radiation sensors”, to appear in *IEEE MTT-S International Microwave Symposium (IMS)*, Jun. 2017.
- [54] A. Rofougaran, J. Rael, M. Rofougaran, and A. Abidi, “A 900 MHz CMOS LC-oscillator with quadrature outputs”, in *IEEE International Solid-State Circuits Conference (ISSCC)*, Feb. 1996, pp. 392–393.
- [55] A. Natarajan, A. Komijani, and A. Hajimiri, “A fully integrated 24-GHz phased-array transmitter in CMOS”, *IEEE Journal of Solid-State Circuits*, vol. 40, no. 12, pp. 2502–2514, Dec. 2005.
- [56] M. Varonen, M. Karkkainen, M. Kantanen, and K. A. I. Halonen, “Millimeter-wave integrated circuits in 65-nm CMOS”, *IEEE Journal of Solid-State Circuits*, vol. 43, no. 9, pp. 1991–2002, Sep. 2008.
- [57] K. Sengupta and A. Hajimiri, “A compact self-similar power combining topology”, in *IEEE MTT-S International Microwave Symposium (IMS)*, May 2010, pp. 244–247.
- [58] S. M. Bowers, K. Sengupta, K. Dasgupta, and A. Hajimiri, “A fully-integrated self-healing power amplifier”, in *IEEE Radio Frequency Integrated Circuits Symposium (RFIC)*, Jun. 2012, pp. 221–224.
- [59] A. Komijani, A. Natarajan, and A. Hajimiri, “A 24-GHz, +14.5-dBm fully integrated power amplifier in 0.18- μm CMOS”, *IEEE Journal of Solid-State Circuits*, vol. 40, no. 9, pp. 1901–1908, Sep. 2005.
- [60] C. H. Doan, S. Emami, A. M. Niknejad, and R. W. Brodersen, “Millimeter-wave CMOS design”, *IEEE Journal of Solid-State Circuits*, vol. 40, no. 1, pp. 144–155, Jan. 2005.
- [61] T. Chi, M. Y. Huang, S. Li, and H. Wang, “A packaged 90-to-300 GHz transmitter and 115-to-325 GHz coherent receiver in CMOS for full-band continuous-wave mm-wave hyperspectral imaging”, in *IEEE International Solid-State Circuits Conference (ISSCC)*, Feb. 2017, pp. 304–305.

- [62] E. Seok, D. Shim, C. Mao, R. Han, S. Sankaran, C. Cao, W. Knap, and K. K. O, “Progress and challenges towards terahertz CMOS integrated circuits”, *IEEE Journal of Solid-State Circuits*, vol. 45, no. 8, pp. 1554–1564, Aug. 2010.
- [63] Z. Feng, W. Zhang, B. Su, K. C. Gupta, and Y. C. Lee, “RF and mechanical characterization of flip-chip interconnects in CPW circuits with underfill”, *IEEE Transactions on Microwave Theory and Techniques*, vol. 46, no. 12, pp. 2269–2275, Dec. 1998.
- [64] T. Krems, W. Haydl, H. Massler, and J. Rudiger, “Millimeter-wave performance of chip interconnections using wire bonding and flip chip”, in *IEEE MTT-S International Microwave Symposium (IMS)*, vol. 1, Jun. 1996, 247–250 vol.1.
- [65] S. M. Bowers, A. Safaripour, and A. Hajimiri, “Dynamic polarization control of integrated radiators”, in *IEEE Radio Frequency Integrated Circuits Symposium (RFIC)*, Jun. 2014, pp. 291–294.
- [66] Y. Tousi and E. Afshari, “A scalable THz 2D phased array with +17 dBm of EIRP at 338 GHz in 65 nm bulk CMOS”, in *IEEE International Solid-State Circuits Conference (ISSCC)*, Feb. 2014, pp. 258–259.
- [67] Z. Wang, P. Y. Chiang, P. Nazari, C. C. Wang, Z. Chen, and P. Heydari, “A 210 GHz fully integrated differential transceiver with fundamental-frequency VCO in 32 nm SOI CMOS”, in *IEEE International Solid-State Circuits Conference (ISSCC)*, Feb. 2013, pp. 136–137.
- [68] S. M. Bowers, A. Safaripour, and A. Hajimiri, “An integrated traveling-wave slot radiator”, in *IEEE Radio Frequency Integrated Circuits Symposium (RFIC)*, Jun. 2014, pp. 369–372.
- [69] C. W. Harrison and D. C. Chang, “Theory of the annular slot antenna based on duality”, *IEEE Transactions on Electromagnetic Compatibility*, vol. EMC-13, no. 1, pp. 8–14, Feb. 1971.
- [70] C. C. Wang, Z. Chen, H. C. Yao, and P. Heydari, “A fully integrated 96 GHz 2×2 focal-plane array with on-chip antenna”, in *IEEE Radio Frequency Integrated Circuits Symposium (RFIC)*, Jun. 2011, pp. 1–4.
- [71] P. Andreani, A. Bonfanti, L. Romano, and C. Samori, “Analysis and design of a 1.8-GHz CMOS LC quadrature VCO”, *IEEE Journal of Solid-State Circuits*, vol. 37, no. 12, pp. 1737–1747, Dec. 2002.
- [72] R. Aparicio and A. Hajimiri, “A noise-shifting differential colpitts VCO”, *IEEE Journal of Solid-State Circuits*, vol. 37, no. 12, pp. 1728–1736, Dec. 2002.
- [73] E. Laskin, P. Chevalier, A. Chantre, B. Sautreuil, and S. P. Voinigescu, “165-GHz transceiver in SiGe technology”, *IEEE Journal of Solid-State Circuits*, vol. 43, no. 5, pp. 1087–1100, May 2008.

- [74] A. Valdes-Garcia, S. T. Nicolson, J. W. Lai, A. Natarajan, P. Y. Chen, S. K. Reynolds, J. H. C. Zhan, D. G. Kam, D. Liu, and B. Floyd, "A fully integrated 16-element phased-array transmitter in SiGe BiCMOS for 60-GHz communications", *IEEE Journal of Solid-State Circuits*, vol. 45, no. 12, pp. 2757–2773, Dec. 2010.
- [75] C. Y. Law and A. V. Pham, "A high-gain 60 GHz power amplifier with 20 dBm output power in 90 nm CMOS", in *IEEE International Solid-State Circuits Conference (ISSCC)*, Feb. 2010, pp. 426–427.
- [76] R. Wanner, R. Lachner, and G. R. Olbrich, "A monolithically integrated 190-GHz SiGe push-push oscillator", *IEEE Microwave and Wireless Components Letters*, vol. 15, no. 12, pp. 862–864, Dec. 2005.
- [77] W. Lee and Y. Yeh, "Polarization diversity system for mobile radio", *IEEE Transactions on Communications*, vol. 20, no. 5, pp. 912–923, Oct. 1972.
- [78] M. R. Andrews, P. P. Mitra, *et al.*, "Tripling the capacity of wireless communications using electromagnetic polarization", *Nature*, vol. 409, no. 6818, pp. 316–318, 2001.
- [79] D. Giuli, "Polarization diversity in radars", *Proceedings of the IEEE*, vol. 74, no. 2, pp. 245–269, Feb. 1986.
- [80] H. A. Zebker and J. J. V. Zyl, "Imaging radar polarimetry: A review", *Proceedings of the IEEE*, vol. 79, no. 11, pp. 1583–1606, Nov. 1991.
- [81] A. G. Andreou and Z. K. Kalayjian, "Polarization imaging: Principles and integrated polarimeters", *IEEE Sensors Journal*, vol. 2, no. 6, pp. 566–576, Dec. 2002.
- [82] M. Sarkar, D. S. S. S. Bello, C. van Hoof, and A. Theuwissen, "Integrated polarization analyzing CMOS image sensor for material classification", *IEEE Sensors Journal*, vol. 11, no. 8, pp. 1692–1703, Aug. 2011.
- [83] P. Nazari, S. Jafarlou, and P. Heydari, "A fundamental-frequency 114 GHz circular-polarized radiating element with 14 dBm EIRP, -99.3 dBc/Hz phase-noise at 1 MHz offset and 3.7% peak efficiency", in *IEEE International Solid-State Circuits Conference (ISSCC)*, Feb. 2017, pp. 322–323.
- [84] T. Chi, F. Wang, S. Li, M. Y. Huang, J. S. Park, and H. Wang, "A 60 GHz on-chip linear radiator with single-element 27.9 dBm psat and 33.1 dBm peak EIRP using multifeed antenna for direct on-antenna power combining", in *IEEE International Solid-State Circuits Conference (ISSCC)*, Feb. 2017, pp. 296–297.
- [85] S. Shahramian, Y. Baeyens, N. Kaneda, and Y. K. Chen, "A 70-100 GHz direct-conversion transmitter and receiver phased array chipset demonstrating 10 Gb/s wireless link", *IEEE Journal of Solid-State Circuits*, vol. 48, no. 5, pp. 1113–1125, May 2013.

- [86] A. Tang, G. Virbila, D. Murphy, F. Hsiao, Y. H. Wang, Q. J. Gu, Z. Xu, Y. Wu, M. Zhu, and M. C. F. Chang, "A 144 GHz 0.76 cm-resolution sub-carrier SAR phase radar for 3D imaging in 65nm CMOS", in *IEEE International Solid-State Circuits Conference (ISSCC)*, Feb. 2012, pp. 264–266.
- [87] A. Natarajan, A. Komijani, X. Guan, A. Babakhani, and A. Hajimiri, "A 77-GHz phased-array transceiver with on-chip antennas in silicon: Transmitter and local LO-path phase shifting", *IEEE Journal of Solid-State Circuits*, vol. 41, no. 12, pp. 2807–2819, Dec. 2006.
- [88] R. Han and E. Afshari, "A CMOS high-power broadband 260-GHz radiator array for spectroscopy", *IEEE Journal of Solid-State Circuits*, vol. 48, no. 12, pp. 3090–3104, Dec. 2013.
- [89] S. M. Bowers, A. Safaripour, and A. Hajimiri, "Dynamic polarization control", *IEEE Journal of Solid-State Circuits*, vol. 50, no. 5, pp. 1224–1236, May 2015.
- [90] Z. Wang, P. Y. Chiang, P. Nazari, C. C. Wang, Z. Chen, and P. Heydari, "A CMOS 210-GHz fundamental transceiver with OOK modulation", *IEEE Journal of Solid-State Circuits*, vol. 49, no. 3, pp. 564–580, Mar. 2014.
- [91] S. M. Bowers, A. Safaripour, and A. Hajimiri, "An integrated slot-ring traveling-wave radiator", *IEEE Transactions on Microwave Theory and Techniques*, vol. 63, no. 4, pp. 1154–1162, Apr. 2015.
- [92] Y. Tousi and E. Afshari, "A high-power and scalable 2-D phased array for terahertz CMOS integrated systems", *IEEE Journal of Solid-State Circuits*, vol. 50, no. 2, pp. 597–609, Feb. 2015.
- [93] R. Han, C. Jiang, A. Mostajeran, M. Emadi, H. Aghasi, H. Sherry, A. Cathelin, and E. Afshari, "A 320 GHz phase-locked transmitter with 3.3 mW radiated power and 22.5 dBm EIRP for heterodyne THz imaging systems", in *IEEE International Solid-State Circuits Conference (ISSCC)*, Feb. 2015, pp. 1–3.
- [94] K. Sengupta, D. Seo, L. Yang, and A. Hajimiri, "Silicon integrated 280 GHz imaging chipset with 4×4 SiGe receiver array and CMOS source", *IEEE Transactions on Terahertz Science and Technology*, vol. 5, no. 3, pp. 427–437, May 2015.
- [95] U. R. Pfeiffer, Y. Zhao, J. Grzyb, R. A. Hadi, N. Sarmah, W. Förster, H. Rucker, and B. Heinemann, "A 0.53 THz reconfigurable source array with up to 1 mW radiated power for terahertz imaging applications in 0.13 μm SiGe BiCMOS", in *IEEE International Solid-State Circuits Conference (ISSCC)*, Feb. 2014, pp. 256–257.
- [96] H. Jalili and O. Momeni, "A 318-to-370 GHz standing-wave 2D phased array in 0.13 μm BiCMOS", in *IEEE International Solid-State Circuits Conference (ISSCC)*, Feb. 2017, pp. 310–311.

- [97] H. Aghasi, A. Cathelin, and E. Afshari, “A 0.92-THz SiGe power radiator based on a nonlinear theory for harmonic generation”, *IEEE Journal of Solid-State Circuits*, vol. 52, no. 2, pp. 406–422, Feb. 2017.
- [98] A. Safaripour, S. M. Bowers, K. Dasgupta, and A. Hajimiri, “A 2×2 dynamic polarization-controlling integrated phased array”, in *IEEE Radio Frequency Integrated Circuits Symposium (RFIC)*, May 2015, pp. 219–222.
- [99] M. K. Fries, M. Grani, and R. Vahldieck, “A reconfigurable slot antenna with switchable polarization”, *IEEE Microwave and Wireless Components Letters*, vol. 13, no. 11, pp. 490–492, Nov. 2003.
- [100] S. Raman and G. M. Rebeiz, “Single- and dual-polarized millimeter-wave slot-ring antennas”, *IEEE Transactions on Antennas and Propagation*, vol. 44, no. 11, pp. 1438–1444, Nov. 1996.
- [101] M. Chua and K. W. Martin, “1 GHz programmable analog phase shifter for adaptive antennas”, in *IEEE Custom Integrated Circuits Conference (CICC)*, May 1998, pp. 71–74.
- [102] L. Dong, H. Choo, R. W. Heath, and H. Ling, “Simulation of MIMO channel capacity with antenna polarization diversity”, *IEEE Transactions on Wireless Communications*, vol. 4, no. 4, pp. 1869–1873, Jul. 2005.
- [103] S. Bowers, K. Dasgupta, A. Safaripour, and A. Hajimiri, *Dynamic polarization modulation and control*, US Patent 9,485,076, Nov. 2016.
- [104] A. Adrian and D. H. Schaubert, “Dual aperture-coupled microstrip antenna for dual or circular polarisation”, *Electronics Letters*, vol. 23, no. 23, pp. 1226–1228, Nov. 1987.